Mechanical Properties of Friction Stir Welded Reduced Activation Ferritic-Martensitic Steel

A thesis

submitted by

Johny Varghese Reg. No.: 12ETMM03

in partial fulfilment of the requirements for the award of the degree of

Doctor of Philosophy

in

Materials Engineering



School of Engineering Sciences and Technology

University of Hyderabad, India

June, 2022

DECLARATION

I, Johny Varghese hereby declare that this thesis work entitled "Mechanical Properties of

Friction Stir Welded Reduced Activation Ferritic-Martensitic Steel" submitted in partial

fulfilment requirements **Doctor Philosophy** of the for the award of of

(in Materials Engineering) in the School of Engineering Sciences and Technology (SEST),

University of Hyderabad is a bonafide record of the work which was carried out by me under

the supervision of Prof. Koteswararao V. Rajulapati. I also declare that the content of this

thesis has not been submitted earlier, as a whole or in part, to this University or any other

University/ Institution for the award of any degree or equivalent.

Johny Varghese

Reg. No.: 12ETMM03

Materials Engineering

School of Engineering Sciences and Technology

University of Hyderabad

CERTIFICATE

This is to certify that the thesis work entitled "Mechanical Properties of Friction Stir Welded Reduced Activation Ferritic-Martensitic Steel", submitted by Johny Varghese bearing Reg. No. 12ETMM03 in partial fulfilment of the requirements for the award of the degree of Doctor of Philosophy in Materials Engineering is a bonafide record of research work that has been carried out by him under my guidance and supervision. The content of this thesis has not been submitted earlier, as a whole or in part, to this or any other University/Institution for the award of any degree or equivalent.

Thesis Supervisor

Prof. Koteswararao V. Rajulapati

Professor

School of Engineering Sciences and Technology

University of Hyderabad

Approved by,

Prof. Dibakar Das

Dean

School of Engineering Sciences and Technology

University of Hyderabad



CERTIFICATE

This is to certify that the thesis entitled "Mechanical Properties of Friction Stir Welded Reduced Activation Ferritic-Martensitic Steel" submitted by Johny Varghese bearing registration number 12ETMM03 in partial fulfilment of the requirements for award of Doctor of Philosophy (in Materials Engineering) in the School of Engineering Sciences and Technology (SEST) is a bonafide work carried out by him under my supervision and guidance.

This thesis is free from plagiarism and has not been submitted previously in part or in full to this or any other University or Institution for award of any degree or diploma.

Johny Varghese was exempted from doing coursework (recommended by Doctoral Committee) on the basis of the following courses passed during his M. Tech. (Integrated M. Tech. /Ph. D) and the M. Tech. Degree was awarded.

Parts of this thesis have been published in the following publications:

- 1. **J. Varghese**, K. V. Rajulapati, K. Bhanu Sankara Rao, Chavan Akash N S.D. Meshram, G. M. Reddy, Characterization of Microstructure and Mechanical Properties of Friction Stir Welded Reduced Activation Ferritic-Martensitic Steel in As-Received, As-Welded and Post Weld Heat Treated States Transaction of Indian Institute of Metals(2022)(https://doi.org/10.1007/s12666-022-02628-z)
- 2. **J. Varghese**, K. V. Rajulapati, S.D. Meshram, G. M. Reddy, K. Bhanu Sankara Rao Strain rate sensitivity and mechanical properties of friction stir welded IN-RAFM steels of thicker sections proceedings of the 13th International Conference on the Mechanical Behaviour of Materials (ICM13), 11-14 June 2019, Melbourne, Australia. (ISBN: 978-1-922016-65-2)
- 3. **J. Varghese** et. al. Tensile Properties and Fracture Characteristics of Friction Stir Welded IN-RAFM Steel Plates of 6mm Thickness in As-Welded and Normalized Conditions at Ambient and High Temperature Atmospheres (under review with MSEA)
- 4. **J. Varghese** et. al. Probing of local mechanical properties of Friction Stir welded IN-RAFM steels of thicker sections in As-Received, As-Welded and post weld Normalized Conditions (manuscript to be communicated)

Course No.	Title	Credits	Pass/ Fail
MT 401	Thermodynamics and Phase Equilibria	4	Pass
MT 402	Characterization of Materials	4	Pass
MT 403	Advanced Engineering Mathematics	4	Pass
MT 404	Seminar	2	Pass
MT 405	Mechanical Behavior of Materials/Selection of Materials	4	Pass
MT 406	Concepts of Material Science	4	Pass
MT 407	Materials Processing and Characterization Laboratory	4	Pass
MT 408	Dislocation and Plasticity	2	Pass
MT 451	Materials and Technologies for Energy Systems	4	Pass
MT 452	Diffusion and Kinetics	2	Pass
MT 453	Modelling and Simulation	4	Pass
MT 454	Powder Metallurgy and Ceramics	4	Pass
MT 455	Surface Engineering	4	Pass
MT 456	Metal Forming Science and Technology	4	Pass
MT 457	Laboratory	4	Pass
MT 458	Seminar	2	Pass
MT 500	Dissertation	18	Pass
MT 601	Research Methodology	4	Pass

Supervisor Dean, SEST

List of Publications

The following papers were published/communicated out of the research work included in this thesis.

- Johny Varghese, K. V. Rajulapati, K. Bhanu Sankara Rao, Chavan Akash N S.D. Meshram, G. M. Reddy, Characterization of Microstructure and Mechanical Properties of Friction Stir Welded Reduced Activation Ferritic-Martensitic Steel in As-Received, As-Welded and Post Weld Heat Treated States Transaction of Indian Institute of Metals(2022)(https://doi.org/10.1007/s12666-022-02628-z)
- 2. **J. Varghese**, K. V. Rajulapati, S.D. Meshram, G. M. Reddy, K. Bhanu Sankara Rao Strain rate sensitivity and mechanical properties of friction stir welded IN-RAFM steels of thicker sections proceedings of the 13th International Conference on the Mechanical Behaviour of Materials (ICM13), 11-14 June 2019, Melbourne, Australia. (ISBN: 978-1-922016-65-2)
- 3. **J. Varghese** et. al. Tensile Properties and Fracture Characteristics of Friction Stir Welded IN-RAFM Steel Plates of 6mm Thickness in As-Welded and Normalized Conditions at Ambient and High Temperature Atmospheres (under review with MSEA)

List of Conferences Attended

The following conference presentations were done out of the research work included in this thesis.

- 1. **Johny Varghese**, S.D. Meshram, G. M. Reddy, K. Bhanu Sankara Rao, Koteswararao V. Rajulapati *Probing of local mechanical properties of friction stir welded IN-RAFM steels of thicker sections* poster presentation at the International Conference on Advanced Materials and Mechanical Characterization (ICAMMC-2021), 02-04 December 2021, Chennai, India.
- 2. **Johny Varghese**, S.D. Meshram, G. M. Reddy, K. Bhanu Sankara Rao, Koteswararao V. Rajulapati *Friction stir welding of IN-RAFM Steels of thicker sections- An overview into the mechanical behavior and effect of welding temperature* oral presentation at the Science, Technology and Innovation Talks (STIN-2021), a national level competition organised as part of the National Science Day 2021 by DST held at ARCI, 25-26 February 2021 Hyderabad, India.
- 3. **J. Varghese**, K. V. Rajulapati, S.D. Meshram, G. M. Reddy, K. Bhanu Sankara Rao *Strain rate sensitivity and mechanical properties of friction stir welded IN-RAFM steels of thicker sections* at the 13th International Conference on the Mechanical Behaviour of Materials (ICM13), 11-14 June 2019, Melbourne, Australia.
- 4. **J. Varghese**, V. L. Manugula, K. V. Rajulapati, G. M. Reddy, K. Bhanu Sankara Rao *Strain rate sensitivity and RT creep behavior of friction stir welded and electron beam welded IN-RAFM steels* poster presentation at Second International Structural Integrity Conference and Exhibition (SICE-2018), 2018, Hyderabad, India.

Acknowledgements

First and foremost, I express my deep gratitude and respect to my research supervisor Professor *Dr. Koteswararao V. Rajulapati*, for his keen interest, valuable guidance, strong motivation and constant encouragement during my research work. I always remember his words "your thesis should speak for you in your future" and I think I have tried my level best to bring the best out of me.

I thank my doctoral committee members Prof. Ing- V. V. S. S. Srikanth and Dr. Swati Ghosh Acharyya for their valuable comments during my DRC meetings. All those have a good part in moulding my doctoral thesis in to the way it is seen now.

I am also thankful to the Dean of School of Engineering Sciences and Technology, *Prof. Dibakar Das* and all other faculties in the department for providing me the facilities and the guidance to carry out my research work.

I wholeheartedly thank *Prof. K. Bhanu Sankara Rao* for his support over the entire span of my work. You are such a sage who has devoted your entire life for research in metallurgy and related topics. I take it as a great privilege to have worked under your guidance as well.

The former Deans of SEST, *Prof. M. Ghanashyam Krishna*, *Prof. M. Sundararaman*, and *Prof. Rajendra Singh* for their help they have rendered during their time in the School.

I would also like to thank the technicians and non-teaching staff of SEST and TEM technicians at Centre for Nanotechnology, University of Hyderabad.

My sincere thanks to *Dr. G. Madhusudan Reddy*, Outstanding Scientist - DMRL Hyderabad for helping me in getting my samples welded in the MJG group. *Dr. Suresh Meshram*, Scientist 'E' for his support throughout the welding and testing part. Thanks to all technicians of DMRL who helped me in tackling different technical hurdles from time to time.

Thanks to *Dr. Shiju Sam*, Scientific Officer 'E' and other scientists at Institute of Plasma Research (IPR), Gandhinagar for their help in getting enough samples for my experiments and related things.

Special Thanks to DAE-BRNS for funding my project and UGC for the financial support through Non-NET BBL fellowship during the rest of the period.

Thanks to my fellow lab mates *Dr. Abhijit, Deekshit, Madhubabu, Hasan, Nanda, Nagalakshmi*, and to my seniors *Dr. Pardhu, Dr. Rahul, Dr. Vijayalakshmi, Dr. Sreedevi, Dr. Ramya, Dr. Paul, Dr. Koushi, Dr. Sunil, Dr. Kamal* etc. and to my classmates as well.

Last but not the least, I would like to thank the GOD almighty for strengthening me and my family till I complete this long journey.

Johny Varghese

Contents

List of Figures	
List of Tables.	
List of Symbols and Abbreviations	
Abstract	VIII
Chapter 1- Introduction	1
1.1. Objectives and scope of the thesis	
1.2. Overview of the thesis	
References	0
Chapter 2- Literature Review	
Introduction	10
2.1 The need for nuclear power	10
2.2 The ITER Program	11
2.3 Reduced Activation Ferritic Martensitic Steels	13
2.4 Physical metallurgy of RAFM steel	14
2.5 India Specific Reduced Activation Ferritic Martensitic Steels (IN-RAFM)	16
2.6 Phase transformations in RAFM steels	18
2.7 Transformation Temperatures in IN-RAFM	18
2.8 Microstructure of Tempered-Martensite	20
2.9 Fabrication technologies in RAFM steels	21
2.10 Welding metallurgy of 9Cr Ferritic-Martensitic steels	21
2.11 Welding of RAFM steel	24
2.12 Solid-state welding	26
2.13 Post Weld Heat Treatment	30
2.14 Mechanical properties of Friction stir welded steels	31
References	34
Chapter 3- Experimental Details	45
Introduction	46
3.1 Material Procurement	46
3.2 As received material	46
3.3 Material composition	47
3.4 Friction Stir Welding	47
3.5 PCBN Tool	49
3.6 As- received material characterization	51
3.7 Mechanical Testings	55

	3.8 Post Weld Heat Treatment	64
	References	66
Cha	apter 4- Results and Discussion	68
4.1.	. Tensile Properties and Fracture Characteristics of Frict	ion Stir Welded IN-RAFM
	Steel Plates of Thicker Section in As-Welded and Norm	nalized Conditions at
	Ambient and High Temperature Atmospheres	70
	4.1.1. Introduction	71
	4.1.2. Experimental Procedure	
	4.1.3. Results.	
	4.1.4. Discussion	91
	4.1.5. Conclusions.	99
	References	101
4 2	Characterization of Microstructure and Mechanical	Properties of Friction Stir
	Welded Reduced Activation Ferritic-Martensitic Steel	_
	and Post Weld Heat Treated States	,
	4.2.1. Introduction	
	4.2.2. Experimental Details	
	4.2.3. Results and Discussion	
	4.2.4. Conclusions	
4.3	Probing of Local Mechanical Properties of Friction Stir	
	Thicker Sections in As-Received, As-Welded Conditions	
	Conditions	136
	4.3.1. Introduction	137
	4.3.2. Experimental Procedure	140
	4.3.3. Results and Discussion	
	4.3.4. Conclusions.	
	References	155
Cha	apter 5 Conclusions and Future Scope	159
	5.1 Conclusions	160
	5.2 Scope of future Work	
	r	

List of Figures

Chapter-2

Figure 2. 1 The ITER assembly.	12
Figure 2. 2 Equilibrium diagram of Fe-Cr with 0.1% Carbon	15
Figure 2. 3 Tempering time-Austenizing temperature-hardness relation in IN-RAFM Steel	18
Figure 2. 4 DSC regime showing ferrite to austenite transformation, $\alpha \rightarrow \gamma$	19
Figure 2. 5 Orientation of M23C6 and MX carbides.	21
Figure 2. 6 Different weld zones and corresponding phase diagram correlation	23
Figure 2. 7 Comparison of mechanical properties of welded IN-RAFM with other RAFM steels	26
Figure 2. 8 Schematic of the Friction Stir Welding process.	28
Figure 2. 9 Different weld zones in FSW cross section.	29
Chapter-3	
Figure 3.1 FSW machine manufactured by MTI.	48
Figure 3.2 Friction stir welded plates of 6mm thickness.	49
Figure 3.3 Schematic drawing of the PCBN tools 6 mm and 12 mm	50
Figure 3.4 PCBN tool.	50
Figure 3.5 X-Ray Diffraction Machine.	51
Figure 3.6 Optical Microscope	53
Figure 3.7 Scanning Electron Microscope.	54
Figure 3.8 Field Emission Scanning Electron Microscope	55
Figure 3.9 Vickers micro hardness Tester.	56
Figure 3.10 Schematic drawing of nanoindentation machine	57
Figure 3.11 Berkovich tip geometry.	58

Figure 3.12 Hysitron Trib	boindenter TI950	59
Figure 3.13 Standard Loa	ad- Displacement curve of a nanoindentation test	59
Figure 3.14 (a) HT Tensi	le sample dimensions and orientation, (b) RT Te	nsile Specimen 60
Figure 3.15 Orientation of	of tensile specimen within weld	61
Figure 3.16 Instron University	ersal Testing Machine (UTM)	62
Figure 3.17 Different geo	ometries of notch tensile sample	63
Figure 3.18 Nabertherm	muffle furnace	65
Chapter-4.1		
Figure 4.1.1. Experiment	al setup and PCBN tool adapted in the current in	vestigation 74
	s of tensile test sample for BM and weld joint. The gauge portion are shown schematically	
Figure 4.1.3 SZ tensile te	st sample orientation and geometry	77
consists of (and MX ty	ure of the as-received (AR: base metal, BM) allows (a) tempered martensite along with M23C6 on grape precipitates in the intralath regions (b&c). Some are shown in b&c	ain and lath boundaries SAD patterns of these
•	sis of the carbides show (a) chromium rich M23C and V containing MX precipitates in the matrix	9
structure an photograph	micrograph of BM in the as-welded state described carbide distribution in the matrix and on grain of BM, (c) SEM microstructure of TMAZ depiction of the state of	boundaries, (b) SEM
undissolved	ographs of SZ in AW state: (a) Intragranular cell MX and freshly formed Fe3C needle particles, (d) SAD of Fe3C needle particles	c) SAD of undissolved
	rostructure showing (a) Base Metal, (b) Thermo I	

_	EBSD image quality maps of (a) as-welded (AW) and (b) PWNT sample from SZ region
Figure 4.1.10	0. Grain size distribution of different zones in as-welded and PWNT conditions
•	. Stress-Strain plots obtained at various temperatures: (a) As-received, (b) As-welded (c) As welded +PWNT (d) Stir Zone sample tested at RT in as-welded and as-welded +PWNT conditions
	. Fractographs of as-received samples tested at different conditions (a) RT, (b) 450 °C, (c) 500 °C, (d) 550 °C respectively
I	Ductile fracture characterized by dimples: (a) As-Welded and tested at 450°C, (b) PWNT tested at 450°C, (c) SZ-alone in as-welded condition and tested at RT, and (d) SZ-alone in PWNT condition and tested at RT
_	4. Large microvoid surrounding chromium rich particle in PWNT state at 450°C
	Schematic of crack initiation and propagation in tensile tests leading to the occurrence of dimples on fracture surface.
Figure 4.1.16.	. Microhardness profile of 6 mm weldment in AW and PWNT states
Figure 4.1.17.	. Contribution of different strengthening mechanisms of RAFM steel employed in the present study
Chapter-4.2	
Figure 4.2.1. ((a) Friction stir welding setup, (b) Geometry of polycrystalline cubic boron nitride tool
•	(a) Various zones in the friction stir welded bead-on-plate of 12mm thickness, (b) Geometry of tensile testing specimen
l I	4.2.3.(a) As-received FE-SEM micrograph showing $M_{23}C_6$ on prior austenitic grain boundaries and both MC and $M_{23}C_6$ precipitates in intragranular regions,(b) TEM micrograph displaying both MC and $M_{23}C_6$ on lath and intra-lath regions and large number of dislocations and dislocation tangles in intra-lath regions.

Figure 4.2.4	martensite structure, (b) Heat Affected Zone showing coarsening and coalescence of M ₂₃ C ₆ , (c) Thermo Mechanically Affected Zone, and (d) Stir Zone. SZ and TMAZ show precipitate-free grain boundaries.
Figure 4.2.5.	TEM micrograph of SZ in AW condition showing freshly formed martensite, Fe ₃ C, cell boundaries, few undissolved MX type precipitates and high dislocation density; (b) Selected area diffraction for Fe ₃ C and MX precipitates
Figure 4.2.6.	Grain size (GS) distribution obtained through EBSD (a) As-welded BM, (b) As-welded Stir Zone, (c) Base metal after PWNT, and (d) Stir Zone after PWNT.
Figure 4.2.7	. Hardness distribution across the transverse cross section in the as-received, as- welded and PWNT states
Figure 4.2.8	. Microstructure in PWNT state (a) Base Metal showing tempered martensite structure, (b) Heat Affected Zone, (c-d) re-appearance of carbides at prior austenite grain boundaries and intragranular precipitates in TMAZ and SZ respectively
Figure 4.2.9.	Tensile Stress-Strain flow curves of the AR, AW and PWNT conditions tested at (a) RT, (b) 450^{0} C, (c) 500^{0} C, (d) 550^{0} C
Figure 4.2.10	D. EBSD image quality maps obtained in as- welded state. These maps illustrate both low and high angle boundaries comprising of cell, sub-grain, lath and grain boundaries in (a) BM, (b) HAZ, (c) TMAZ and (d) SZ. Incorporated table contains angle of boundaries, their fraction, number, and length
Figure 4.2.1	1. EBSD image quality maps obtained in PWNT state. These maps illustrate both low and high angle boundaries comprising of cell, sub-grain, lath and grain boundaries in (a) BM, (b) HAZ, (c) TMAZ and (d) SZ. Incorporated table contains angle of boundaries, their fraction, number, and length
•	2. Hardening/Softening rates for different states at different temperatures 131 3. Fractographs of the samples tested at different conditions (a) AR-500 °C, (b)
	AW-500 °C, (c) PWNT- 500 °C, (d) AW-450 °C

Chapter-4.3

Figure 4.3.1. (a) Nanoindentation system schematic, (b) Berkovich Tip geometry	. 139
Figure 4.3.2. Trapezoidal load function used to study loading rate effect	. 142
Figure 4.3.3. As-received microstructure of IN-RAFM steel	. 143
Figure 4.3.4. Hardness results from CSM tests by nanoindentation (a) 6mm sample, (b) 12	2mm
sample	. 145
Figure 4.3.5. Nanoindentation maps of 6 mm AW plates	. 147
Figure 4.3.6. Nanoindentation maps of 6 mm PWNT plates	148
Figure 4.3.7. Nanoindentation maps of 12 mm AW plates	149
Figure 4.3.8. Nanoindentation maps of 12 mm PWNT plates	150
Figure 4.3.9. SRS estimated from $ln(\sigma)$ vs $ln(\acute{\epsilon})$ plot of the AW sample in the BM re	_
	. 151
Figure 4.3.10. SRS estimated from $ln(\sigma)$ vs $ln(\hat{\epsilon})$ plot of the AW sample in the SZ re	gion
	. 152
Figure 4.3.11. Stress-Strain plots and SRS value of (a) as-received material, (b) as-we	
material	153

List of Tables

Chapter-2	
Table 2.1 Composition of RAFM steels developed by different countries	3
Table 2. 2 Composition of different heats of RAFM steel	5
Table 2. 3 Tensile properties of different grades of RAFM steels	1
Table 2. 4 Impact properties of different RAFM steels)
Chapter-3	
Table 3.1 Chemical composition of the as-received IN-RAFM Steel in weight %47	7
Table 3.2 Machine details and parameters of XRD analysis)
Chapter-4.1	
Table 4.1.1. Composition of RAFM steel (in Wt. %) estimated through optical emission spectroscopy	
Table 4.1.2. Tensile properties derived from the monotonic stress-strain curves obtained a different temperatures in AR, AW and PWNT states	
Table 4.1.3. Phase transformation temperatures of INRAFM steel	3
Table 4.1.4. Strengthening coefficient of substitutional elements	6
Chapter-4.2	
Table 4.2.1. Chemical composition of INRAFM steel used in this investigation	9
Table 4.2.2. Transformation temperatures of INRAFM steel	5
Table 4.2.3. Results of the tensile tests performed on (a) As-Received, (b) AW, (c) PWN samples at RT and HT conditions	
Table 4.2.4. Hardening (+) Softening (-) rates of different sample at different test condition	

List of Symbols and Abbreviations

AS Advancing Side

ASTM American Society for Testing and Materials

BM Base Metal

CCT Continuous Cooling Transformation
DBTT Ductile-to-Brittle Transition Temperature

DSC Differential Scanning Calorimetry EBSD Electron Backscatter Diffraction

EBW Electron Beam Welding EDS Energy Dispersive Spectra

FE-SEM Field-Emission -Scanning Electron Microscopy

FSW Friction Stir Welding

HAGBs High Angle Grain Boundaries

HAZ Heat Affected Zone HV Vickers Hardness

ITER International Thermonuclear Experimental Reactor

ODS Oxide Dispersion Strengthened
LAGBs Low Angle Grain Boundaries
PAGBs Prior Austenite Grain Boundaries
PcBN Polycrystalline Cubic Boron Nitride

PWDT Post Weld Direct Tempering
PWHT Post Weld Heat Treatment

PWNT Post Weld Normalized and Tempered

IN-RAFM India Specific Reduced Activation Ferritic / Martensitic Steel

RS Retreating Side

SAED Selected Area Electron Diffraction

SZ Stir Zone

TBM Test Blanket Module

TEM Transmission Electron Microscopy

TIG Tungsten Inert Gas

TMAZ Thermo-Mechanically Affected Zone TTT Time Temperature Transformation

 $\begin{array}{ccc} A_{c1} & & Austenite \, Start \, Temperature \\ A_{c3} & & Austenite \, Finish \, Temperature \\ M_f & & Martensite \, Finish \, Temperature \\ M_s & & Martensite \, Start \, Temperature \\ UTM & Universal \, Testing \, Machine \\ UTS & Ultimate \, Tensile \, Strength \end{array}$

WM Weld Metal YS Yield Strength

α Low Temperature (Alpha) Ferrite

 $\begin{array}{ccc} \alpha' & & \text{Martensite} \\ \gamma & & \text{Austenite} \\ \delta & & \text{Delta Ferrite} \end{array}$

Abstract

Nuclear Fusion is an alternative method to harvest energy from nuclear methods without the harmful effects as in Fission process. The special purpose steel developed for the structural materials which are reduced activation ferritic-martensitic (RAFM) steel, needs to be joined through different joining methods when it comes to the fabrication part of the components for fusion reactor. The indigenously developed RAFM steel of India is designated as IN-RAFM steel. This forms an integral part of the test blanket module (TBM) of the fusion reactor. Several welding methods like EBW, LBW etc. has been tried on this alloy. But as all of these methods are fusion welding methods the solidification of the weld pool imparts several defects and microstructural changes in the weldment. Hence a solid state welding method like Friction stir welding (FSW) is adopted. The In-RAFM plates of thickness 6 mm and 12 mm were successfully welded using FSW. The welded plates were analysed for the pre weld and post weld characteristics w.r.t the microstructural and mechanical properties. The 6mm welded specimens were subjected to tensile testing at room temperature (RT) and high temperature (HT) and the respective fracture surfaces were also analysed. The fracture surface of the tested samples give a clear idea about the fracture characteristics involved. The tensile samples extracted from the stir zone region gave interesting tensile properties and these results were substantiated with theoretical calculations of the yield strength. EBSD mappings done in the different regions of the weld were able to help the tensile properties of the alloy. Post-weld heat treatments which are meant to homogenize the weldment were proved to have successfully served the purpose in re-establishing the mechanical properties of the material after welding. Nanoindentation mapping of hardness done at different regions of the weld in the as-welded and post-weld normalized and tempered (PWNT) conditions were able to show the homogenization of different phases in the material. 12mm welded plates were also subjected to similar characterizations and the results were found to be matching for both the thicknesses. Strain rate sensitivity of the material was evaluated using nanoindentation tests and were corelated to the bulk behavior of the material. This has given a better insight into the nanomechanical behavior of the alloy and its microstructural co-relation.



CHAPTER 1

Introduction



Introduction

Energy is the driving force behind the progress man has achieved from the time of the agricultural revolution to the time of the industrial revolution and thereafter. Since then, the thrive on finding more and more sources of energy and on using them has to lead the world to invent different forms of generating energy that we rely upon nowadays. Then he realized the need to find sources of energy that are less harmful to the environment and to reduce the use of non-renewable energy resources.

The works for the harnessing of nuclear energy, which began in the mid of 20th century, gained much prominence in many of its specialities like long lifespan, lesser ground area requirement and economic viability. Nuclear fission[1], which involves the splitting of a heavier atom into smaller atoms releasing enormous energy, was the technology used by the world countries. Developed and developing countries started to establish themselves as energy self-sufficient nations with the development of modern nuclear reactors.

Nuclear wastes and the safety issues associated with the disposal of them is a serious issue that is troubling the countries in investing more into this field. The safety issues that have happened in the world in the recent past due to some natural calamities also has posed serious fear among the public also about the safety of nuclear reactors. Still, the world is depending on nuclear power from the fission process for meeting its energy needs to a great extent. Here comes the necessity of harvesting nuclear energy to generate power in a safer and environmentally friendly way.

The fusion process which powers the Sun and the stars involves the joining of lighter atoms to form a heavier atom is much difficult to be made practical because of the tremendous energy that the process will liberate. But if this can be made practical to be employed in an economical way, it will be a revolutionary invention for the entire world to depend upon, considering the aspects like safety, zero carbon emission, and endless energy output. Scientists around the world have been working on this for years, and some of them were successful, but to produce energy in a large scale manner, more research is needed. Hence scientists from different countries have come forward to form a team to put their ideas together to make this big dream come true. Countries like India, European Union, Japan, China, Russia, South Korea and the United States have come forward to form an International Thermonuclear Experimental Reactor (ITER)[2][3] programme, which is a test reactor to be established as a joint effort. The Test Blanket Module (TBM) of this test reactor which encapsulates the high energy neutrons and their collisions, is to be made up of materials that can withstand induced radioactivity and

that needs low activation energy elements to be included in it[4]. Oxide dispersion strengthened alloys (ODS alloys), Ferritic, martensitic Steels etc., have proved to be the best material for structural applications with their performance in these conditions.

The modified 9Cr-1Mo steel, which is one among the family of ferritic – martensitic steels, has been altered by replacing the W and Ta using Mo and Nb so as to enhance the rapid decay of the induced radioactivity through irradiation[5], [6][7]. A combination of 1.4 weight % of W and 0.06 weight % of Tantalum has been found to be the best combination of these elements, which gives the optimum results with respect to the creep, tensile, low cycle fatigue resistance at higher temperature even by keeping its Ductile to Brittle Transition Temperature (DBTT) low[8], [9]. This modification on the conventional Modified 9Cr-1Mo steel has been designated as India Specific RAFM Steel (IN-RAFM).

Joining this RAFM steel is of much importance when it comes to the fabrication side of the components. The fusion joining methods have their inherent microstructural changes associated with solidification and the presence of the deleterious δ -ferrite phase, which can increase the DBTT and decrease the creep and impact strength. Conventional joining methods like Tungsten Inert Gas (TIG) welding, Shielded Metal Arc (SMA) welding have exhibited to have a wider HAZ area and possess high risks of Type IV cracking[10][11]. Electron Beam Welding (EBW) has got a narrow HAZ compared to the above-mentioned methods, but the presence of the undesirable δ -ferrite can lead to premature failure during the service time.

Friction Stir Welding (FSW), which is a solid-state welding process, has been proved to have been employed successfully without bringing the δ -ferrite phase and also with a narrow HAZ[12][13]. Being a solid-state welding method, it doesn't produce the defects associated with cooling of the molten weld pool and inclusions as well. The process involves a rotating tool of suitable material being plunged to a workpiece which creates a local softening due to the frictional heat developed by the rubbing between the tool and the workpiece, and the stirring action moves the material from the advancing side to the retreating side of the tool[14]–[16]. The workpiece is moved forward, and as the tool advances to the next region to be welded, the stirred area cools to form the weld. Even though there are some microstructural and mechanical benefits for this method compared to the conventional ones, the practical hurdles for FSW, including clamping of the workpiece, can't be ignored.

The feasibility of FSW on 6mm thick plates has already been investigated, and the results prove that it is worthy of attracting research interest to be extended to further dimensions as this

technique needs to be established to further thicknesses for its industrial employability[17]. Thicker sections like 12mm have been welded using EBW and FSW techniques, but in-depth property investigations and microstructural characterizations is still a technological lack in the literature[18]–[20]. Mechanical properties need more in depth evaluation in terms of the tensile properties at room temperature and high temperatures.

1.1 Objectives and Scope of thesis:

The motivations that have fuelled in carrying out this thesis work on FSW of IN-RAFM plates of thicker sections can be summarised as,

Objectives:

- Defect free Friction Stir Welding of 6 mm thick plate and its tensile properties study at room temperature and service temperature in the as-welded and PWHT conditions.
- Estimation of strengthening mechanism in the SZ of weldment using tensile testing in SZ region.
- Understanding the tensile behavior with respect to the microstructural changes due to heat treatment.
- FSW of 12mm thick RAFM plate at slower rpm to get a defect free weld and to study its tensile properties at room temperature and service temperature.
- Understanding the effect of section thickness in the evolution of microstructure.
- Explaining the tensile behavior based on the grain refinement during heat treatment.
- Probing local mechanical properties of the weldments from 6 & 12 mm using nanoindentation and its microstructural co-relation.
- Estimation of strain rate sensitivity using nanomechanical testing and its comparison with bulk material testing.

1.2 Overview of the thesis:

Chapter 2. Literature Review

This chapter deals with a brief insight into the history of the RAFM alloy development and the origin of IN-RAFM steel. The process of friction stir welding, which is employed in this work, the related studies done on similar alloys with respect to different joining techniques and microstructural investigations are also discussed. The available literature on tensile testing at RT and HT and Nanoindentation has been summarised.

Chapter 3. Experimental Procedure

The chapter briefly presents the experimental techniques that have been used in carrying out this research work. The machine details, process parameters, and detailed descriptions about the experimental setup of the friction stir welding, tensile and Nanoindentation testing techniques are also being discussed. The different characterization and details about the heat treatment processes have also been briefed as well.

Chapter 4. Results and Discussion

This chapter consists of different sections differentiated based on the investigations done on the alloy.

Section 4.1 deals with the "Tensile properties and fracture characteristics of friction stir welded IN-RAFM steel plates of thicker section in as-welded and normalized conditions at ambient and high-temperature atmospheres", where it describes the tensile tests done on the 6mm FSW specimens at RT and HT both in the as-welded and the post-weld normalized conditions. The results of different microstructural characterizations are also presented in this section.

Section 4.2 describes the friction stir welding of 12mm thick plates using the PcBN tool and its associated microstructural and mechanical characterizations. The process parameters and the characterizations techniques are discussed in detail.

Section 4.3 deals with the high-speed nanoindentation technique carried out on the 6mm and 12mm as-welded and PWNT conditions. Nanoindentation is also used as a tool to estimate the strain rate sensitivity and it is compared with the bulk SRS values obtained from uniaxial tensile testing. The post indentation microstructural investigations and their co-relation with the nanoindentation results are also included.

Chapter 5: Conclusions and future scope

The summary of the entire research work done in this thesis has been included, and the directions for further research on this topic are also proposed.

References

[1] O. Hahn and F. Strassmann, "About the detection and behavior of the alkaline earth metals produced when uranium is irradiated with neutrons," *Nat. Sci.*, vol. 27, no. 1, pp. 11–15, 1939, doi: 10.1007/BF01488241.

- [2] I. A. E. AGENCY, "International Thermonuclear Experimental Reactor (ITER) Engineering Design Activities (EDA) ITER TECHNICAL BASIS," vol. 24, no. 2, pp. 1–816, 2002.
- [3] T. Noda, F. Abe, H. Araki, and M. Okada, "Development of low activation Ferritic steels," *J. Nucl. Mater.*, vol. 141–143, no. PART 2, pp. 1102–1106, 1986, doi: 10.1016/0022-3115(86)90149-2.
- [4] S. Jitsukawa *et al.*, "Development of an extensive database of mechanical and physical properties for reduced-activation martensitic steel F82H," *J. Nucl. Mater.*, vol. 307–311, no. 1 SUPPL., pp. 179–186, 2002, doi: 10.1016/S0022-3115(02)01075-9.
- [5] R. L. Klueh and E. E. Bloom, "The development of ferritic steels for fast induced-radioactivity decay for fusion reactor applications," *Nucl. Eng. Des. Fusion*, vol. 2, no. 3, pp. 383–389, 1985, doi: 10.1016/0167-899X(85)90026-6.
- [6] R. L. Klueh and D. R. Harries, "High-Chromium Ferritic and Martensitic Steels for Nuclear Applications," *High-Chromium Ferritic Martensitic Steels Nucl. Appl.*, 2001, doi: 10.1520/mono3-eb.
- [7] A. A. F. Tavassoli, "Present limits and improvements of structural materials for fusion reactors A review," *J. Nucl. Mater.*, vol. 302, no. 2–3, pp. 73–88, 2002, doi: 10.1016/S0022-3115(02)00794-8.
- [8] B. Raj, K. B. S. Rao, and A. K. Bhaduri, "Progress in the development of reduced activation ferritic-martensitic steels and fabrication technologies in India," *Fusion Eng. Des.*, vol. 85, no. 7–9, pp. 1460–1468, 2010, doi: 10.1016/j.fusengdes.2010.04.008.
- [9] K. Laha *et al.*, "Development of India-specific RAFM steel through optimization of tungsten and tantalum contents for better combination of impact, tensile, low cycle fatigue and creep properties," *J. Nucl. Mater.*, vol. 439, no. 1–3, pp. 41–50, 2013, doi: 10.1016/j.jnucmat.2013.03.073.
- [10] J. A. Francis, W. Mazur, and H. K. D. H. Bhadeshia, "Type IV cracking in ferritic

- power plant steels," *Mater. Sci. Technol.*, vol. 22, no. 12, pp. 1387–1395, 2006, doi: 10.1179/174328406X148778.
- [11] K. Laha, K. S. Chandravathi, P. Parameswaran, and K. Bhanu Sankara Rao, "Type IV cracking susceptibility in weld joints of different grades of Cr-Mo ferritic steel," *Metall. Mater. Trans. A Phys. Metall. Mater. Sci.*, vol. 40, no. 2, pp. 386–397, 2009, doi: 10.1007/s11661-008-9724-x.
- [12] S. K. Albert, M. Matsui, T. Watanabe, H. Hongo, K. Kubo, and M. Tabuchi, "Variation in the type IV cracking behaviour of a high Cr steel weld with post weld heat treatment," *Int. J. Press. Vessel. Pip.*, vol. 80, no. 6, pp. 405–413, 2003, doi: 10.1016/S0308-0161(03)00072-3.
- [13] S. Sam *et al.*, "Delta ferrite in the weld metal of reduced activation ferritic martensitic steel," *J. Nucl. Mater.*, vol. 455, no. 1–3, pp. 343–348, 2014, doi: 10.1016/j.jnucmat.2014.07.008.
- [14] P. T.-S. W.M.Thomas, E.D.Nicholas, J.C.Needham, M.G. Murch and G.J.Dawes, "Friction stir butt welding," 1991.
- [15] R. S. Mishra and Z. Y. Ma, "Friction stir welding and processing," *Mater. Sci. Eng. R Reports*, vol. 50, no. 1–2, pp. 1–78, 2005, doi: 10.1016/j.mser.2005.07.001.
- [16] P. L. Threadgilll, A. J. Leonard, H. R. Shercliff, and P. J. Withers, "Friction stir welding of aluminium alloys," *Int. Mater. Rev.*, vol. 54, no. 2, pp. 49–93, 2009, doi: 10.1179/174328009X411136.
- [17] V. L. Manugula, K. V. Rajulapati, G. Madhusudhan Reddy, R. Mythili, and K. Bhanu Sankara Rao, "A critical assessment of the microstructure and mechanical properties of friction stir welded reduced activation ferritic-martensitic steel," *Mater. Des.*, vol. 92, pp. 200–212, 2016, doi: 10.1016/j.matdes.2015.12.019.
- [18] V. L. Manugula, K. V. Rajulapati, G. M. Reddy, E. Rajendra Kumar, and K. B. S. Rao, "Friction stir welding of thick section reduced activation ferritic-martensitic steel," *Sci. Technol. Weld. Join.*, vol. 23, no. 8, pp. 666–676, 2018, doi: 10.1080/13621718.2018.1467111.
- [19] V. L. Manugula, K. V. Rajulapati, G. M. Reddy, and K. B. S. Rao, "Role of evolving microstructure on the mechanical properties of electron beam welded ferritic-

martensitic steel in the as-welded and post weld heat-treated states," *Mater. Sci. Eng. A*, vol. 698, pp. 36–45, 2017, doi: 10.1016/j.msea.2017.05.036.

[20] V. L. Manugula, K. V. Rajulapati, G. M. Reddy, R. Mythili, and K. Bhanu Sankara Rao, "Influence of Tool Rotational Speed and Post-Weld Heat Treatments on Friction Stir Welded Reduced Activation Ferritic-Martensitic Steel," *Metall. Mater. Trans. A Phys. Metall. Mater. Sci.*, vol. 48, no. 8, pp. 3702–3720, 2017, doi: 10.1007/s11661-017-4143-5.



CHAPTER 2

Literature Review



Literature Review

Introduction

This chapter deals with the insights into the technology of the energy harvesting methods from nuclear sources and the research carried out across the world in this field. The chapter also discusses the history of alloy development for nuclear applications, the possible challenges on the application side, and the research carried out to expand the database of the alloy.

2.1 The need for nuclear power

For decades, the world's energy needs were met from natural sources like water, fossil fuels, wind, etc. The energy needs of the growing world were so huge that researchers started thinking of better and cheaper energy harvesting methods. Even though Albert Einstein's mass-energy relation was coined in 1905[1], it took another forty years for the scientists to bring the application of the equation to harvest energy from radioactive materials. The first man-made nuclear research reactor Chicago Pile-1 was made as part of the Manhattan project in 1942. But the first nuclear reactor to generate electricity was the EBR-1 made in 1951. Since then, the research done by several scientists across the world has resulted in the evolution of the advanced and safe nuclear reactors that the world is currently depending upon.

Nuclear fission, which involves splitting a heavier nucleus to a lighter one emitting energy, is currently used to generate energy/electricity. The by-products of a fission process are radioactive and are difficult to be disposed of safely. The hazards associated with a significant accident is fatal to humans and animals. Considering these demerits, scientists started thinking about making the next forbidden mode of nuclear reaction; the Fusion process.

Fusion is a reverse process that is happening in fission. Two lighter nuclei, mostly the isotopes of Hydrogen, Deuterium and Tritium, fuse to give a heavier nucleus and enormous energy. The sun that gives heat and light and the stars that flicker are all working with the principle of nuclear fusion. When Deuterium undergoes fusion with Tritium releases a Helium nucleus along with a free neutron and an energy equivalent to 17.6 MeV. This released energy sustains the reaction, and the released fast-moving free neutrons released in all directions are the source of energy from a fusion reactor. Even though fusion is a process that existed in nature from the beginning, the concept of fusion was first discussed by A.S Eddington in 1920[2]. Compared to fission, fusion is less harmful to the environment, and the end products are not radioactive. There is no risk related to the failure of a fusion plant as well. Considering these, there is much research happening to make the fusion process usable for harnessing energy commercially.

Materials for Fusion Reactors

The challenge in selecting a suitable material for the fusion reactor application is associated with the induced radioactivity on the material being used. When the material is subjected to prolonged exposure to high energy neutron atmosphere, the internal composition within the nucleus of the component elements changes, and it may lead to induced radioactive decay of the material. So the materials selected should be such that there won't be any such occurrence of induced radioactivity. Such elements are called low activation elements. Elements like Cr, V, Ti, Mn, Fe, W, Ta are of this kind.

2.2 The ITER Program

With the view of making a fusion reaction happen in a controlled atmosphere and to investigate the scientific and technical feasibility, and for harnessing energy for peaceful purposes countries across the world viz., India, European Union, USA, China, Russia, Japan and South Korea joined hands to set up an experimental reactor called International Thermonuclear Experimental Reactor (ITER) program[3], [4]. The experimental setup is arranged in France, where the magnetic confinement is obtained using a Tokamak. The main parts of the Tokamak where the plasma is confined are the first wall and the breeding blanket. These parts are continuously exposed to high energy neutrons and are subjected to plasma and radiations. This will result in structural changes in the materials used to manufacture the first wall and breeding blanket. Hence these components need to have sufficient strength to withstand the irradiation embrittlement. Certain alloys of Titanium, Nickel, Copper Chromium and some austenitic stainless steels have their properties meeting to be used in these conditions. Among these, void swelling and helium embrittlement are major problems concerning the austenitic stainless steels used in fast breeder reactors (FBR). Other promising materials include vanadium alloys, Ferritic-Martensitic Steels etc. Among these, Ferritic-Martensitic Steels hold a much superior position because of the extensive research on it and the advantage of an extensive scientific database. Another material that can be used is SiC composites; this material and Vanadium alloys have better high-temperature properties when considering the working temperature conditions, but it lacks the methods by which it can be joined when it comes to manufacturing side.

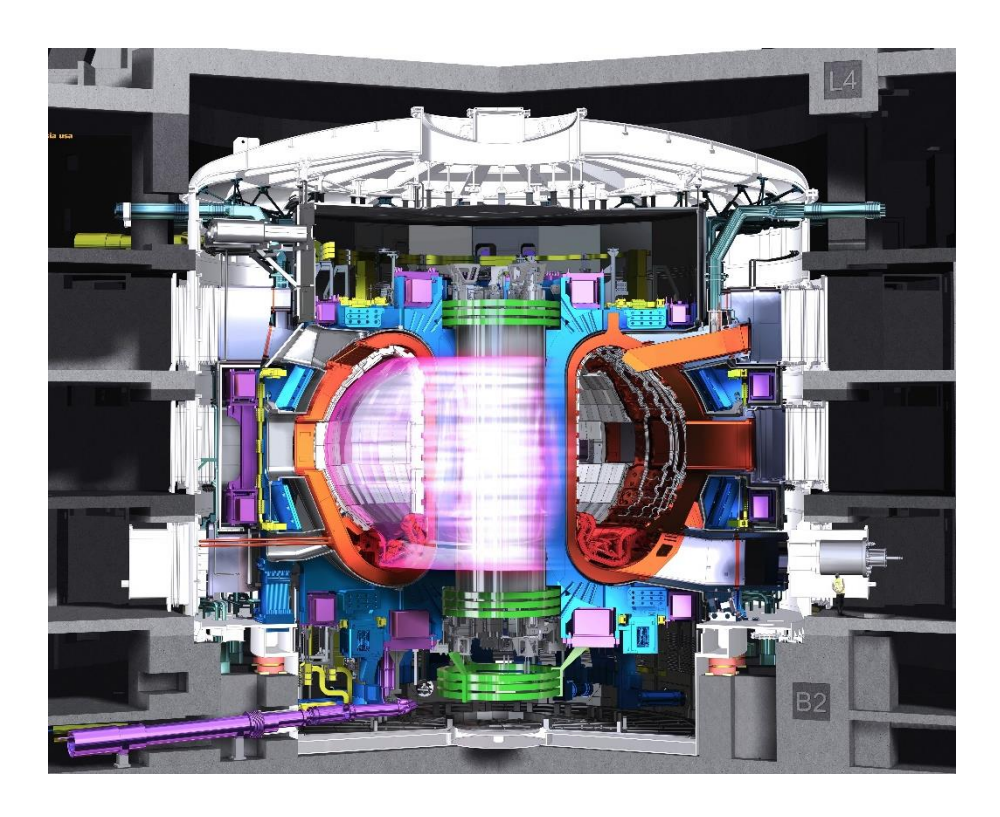


Figure 2.1 The ITER assembly [5]

The joining processes of the ferritic-martensitic steels also are much studied, and EBW, TIG, FSW etc., has been proved to be much satisfying when compared to the standard requirements demanded by the ITER. Among the steels with ferritic-martensitic phase structure, the modified 9Cr-1Mo steel acronymed as P91, T91 etc. [5], [6]. is an established grade in the nuclear sector. This steel is being used in fast breeder reactors for a long time because of its high creep strength, high-temperature stability, fracture toughness, and weldability, making it suitable for manufacturing steam generator parts. The microstructure of this steel is rich in carbides which are of M23C6 and MX type, which are rich in Chromium and Vanadium or Niobium Respectively. The as-cast alloy is subjected to a series of heat treatments which includes a solutionizing process in which the carbides are dissolved into the austenite phase. Then it is air-cooled, which gives enough time for the martensite phase to be formed. Subsequently, this brittle martensitic phase is taken through a tempering process at a temperature range between 650-760°C. This produces a tempered martensitic structure that has the carbide precipitates and a ferritic matrix[6][7], [8].

2.3 Reduced Activation Ferritic Martensitic Steels

The superior properties of the ferritic-martensitic steels compared to the other suitable ones for nuclear applications have lead it to be adopted by the ITER design body. The main criterion to be possessed by the material for a nuclear application is its reduced activation property. That will make the disposal of the material after service time easier. Even though these materials gain induced activation due to prolonged exposure to irradiation atmosphere, they will lose their acquired radioactivity quickly (radioactive decay). This will reduce the environmental impact on disposal as well[4], [9], [10]. This induced radioactivity is an indirect contribution of the component alloying elements. So, these elements with the induced radioactivity property need to be strictly avoided for this to be eliminated. For example, the presence of Molybdenum (Mo) and Niobium (Nb) in the Mod. 9Cr-1Mo steel leads to induced radioactivity which decays very slow. So, such tramp elements that are radioactive in nature (viz. Cu, B, Ti, Nb, Mo, Al, Ni, Co) must be avoided while alloying to the least possible level.

Participant countries started their research on modifying this Mod. 9Cr-1Mo steels. Tungsten (W) and Tantalum (Ta) which are low activation elements, were placed instead of Mo and Nb. Along with this, the elements that enhance the embrittlement like Zr, O, P, Sb, As, Sn was also limited to ppm levels to enhance the reduced activation property[11]. Besides the reduced activation property of this RAFM steels derived from Mod. 9Cr-1Mo steel, its properties with respect to the structural application side like the defiance to void swelling, Helium embrittlement, strength, weldability and other mechanical properties are also possessed by RAFM steels[12]–[17]. The operating temperature range of RAFM steels is in the range of 350-550 °C. Below this range, the risks associated with embrittlement and above this range, the strength deterioration issues arise[12].

Several countries associated with ITER developed their versions of RAFM steels. Table 2.1 shows the composition of different steels developed.

Country	Steel		Composition								
	Designa tion	С	Si	N	Cr	W	Та	V	Mn	Fe	Ref.
USA	9Cr2W VTa	0.11	0.0	0.02	8.8	1.9 7	0.06 5	0.1	0.3 9	Bal	[4], [18]

Table 2.1 Composition of RAFM steels developed by different countries

F82H	F82H	0.093	0.0	0.00	7.6	2.0	0.04	0.2	0.4	Bal	[19],
			9	2	5				9		[20]
	JLF-1	0.1	0.2	0.05	9.0	2.0	0.07	0.2	0.5	Bal	[21]-
								3	4		[23]
China	CLAM	0.092	0.0	0.02	8.8	1.4	0.12	0.2	0.4	Bal	[24]-
			1		7	8			7		[27]
Europe	EUROF	0.1	0.0	0.03	8.5	1.0	0.08	0.2	0.5	Bal	[20],
	ER		5					5			[28],
											[29]

As part of the ITER program, India has also developed its own RAFM steel for the Test Blanket Module (TBM). It is designated as India Specific RAFM, abbreviated as IN-RAFM. The history behind its development and other metallurgical aspects will be discussed subsequently.

2.4 Physical metallurgy of RAFM steel

The physical metallurgy of RAFM steel is a tailored product for the specific application purpose considering its specific requirements. Figure 2.2 represents the equilibrium diagram of Fe-Cr with a carbon concentration of 0.1%. When the Cr content of the steel is high in 9-12% range, it can either have a dual-phase like Austenite + Ferrite, or it can be completely austenite in the temperature regime of 850-1200 °C. The Cr content is limited to 12%, beyond which the γ -Fe loop ends. Being in BCC structure, ferrite forming property is enhanced by the addition of elements like Cr, V, W, Si as it is easier for the α -ferrite (BCC) to dissolve more than γ -austenite. This limits the Cr content to 12%, whereas the presence of Mn, which is an austenite stabilizer, tends to enhance it. Hence the normalizing heat treatment temperature is fixed below 1200 °C to limit the structure to only the γ phase[30]–[32]. At a temperature range of 1100 °C, the increased Cr content in steel can lead to the development of the δ -ferrite phase during the austenitization process. This is also eliminated by the addition of the austenite stabilizer, Mn. However, the δ -ferrite can still be formed in the steel during specific joining processes depending on the cooling rate[33]. The austenitic start temperature, A_{c1} is influenced by the presence of Ni in the composition. By avoiding Ni, this has been increased by 30-50

 $^{\circ}$ C[33]. The tempering temperature for the martensitic phase is to be carried out below A_{c1} temperature to avoid re-austenitizing of the steel and to gain better strength and toughness.

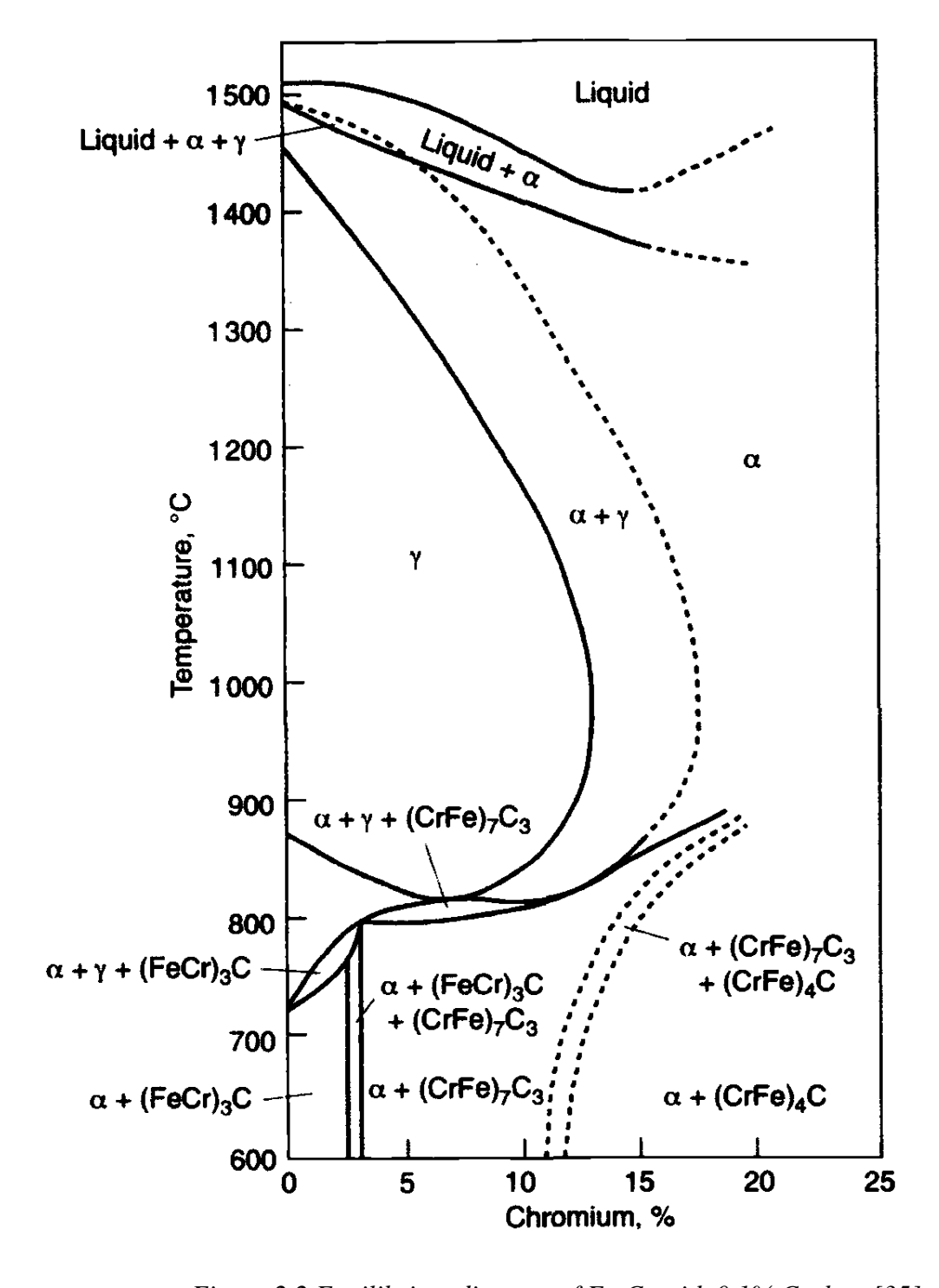


Figure 2.2 Equilibrium diagram of Fe-Cr with 0.1% Carbon [35]

As the A_{c1} temperature is enhanced by the elimination of Ni, this higher tempering temperature decreases the Ductile to Brittle Transition Temperature (DBTT).

2.5 India Specific Reduced Activation Ferritic Martensitic Steels (IN-RAFM)

Being an integral partner in the ITER program, India has also done extensive research on developing its own RAFM steel. M/s. Mishra Dhatu Nigam (MIDHANI) Hyderabad, India, has played a pivotal role in developing India's RAFM steel. MIDHANI produced four heats of steel with slight variations in the compositions of W and Ta, which has close resemblances to EUROFER of Europe. The composition of these four heats are given in Table 2.2. A highly homogenized alloy was able to be manufactured through a series of melting processes, including vacuum induction melting and vacuum arc refining. Tramp elements and other impurities were strictly eliminated by using highly pure alloying elements.

Table 2.2 Composition of different heats of RAFM steel[34]

Element	Designation				
	1W-0.06Ta	1.4W-0.06Ta	2W-0.06Ta	1W-0.14Ta	
Cr	8.98	9.03	8.99	9.13	
С	0.09	0.126	0.12	0.12	
Mn	0.51	0.56	0.65	0.57	
V	0.23	0.24	0.24	0.22	
W	0.99	1.38	2.06	0.94	
Та	0.07	0.06	0.06	0.135	
N	0.0266	0.03	0.02	0.033	
0	0.0019	0.002	0.0024	0.0041	
Р	0.002	0.002	0.002	0.002	
S	0.0008	0.001	0.0014	0.0015	
В	0.0003	0.0005	0.0005	0.0005	
Ti	0.004	0.005	0.005	0.005	

Nb	0.0019	0.001	0.001	0.001
Мо	0.002	0.002	0.002	0.002
Ni	0.005	0.005	0.004	0.005
Cu	0.001	0.002	0.002	0.002
Al	0.005	0.0035	0.00	0.002
Si	0.069	0.06	0.06	0.06
Со	0.004	0.005	0.005	0.005
As+Sn+Sb+Zr	0.005	0.004	0.001	0.001

Of these, the 1.4W, 0.06Ta combination has proved to deliver better mechanical properties and toughness as per the ITER requirements for TBM fabrication. This steel is denominated as India Specific Reduced Activation Ferritic Martensitic (IN-RAFM) Steel. This steel is intended to be used after normalizing followed by tempering, and the microstructure is that of tempered martensite. The prior austenite grain size and hardness is dependent on the austenitizing temperature and the tempering duration. This was varied, and the optimum normalizing temperature was estimated to be 1253K (980 °C) for a duration of 30min and tempering temperature to be 983K (710 °C) for 60min. Figure 2.3 shows the Tempering time-Austenizing temperature-hardness relation [35].

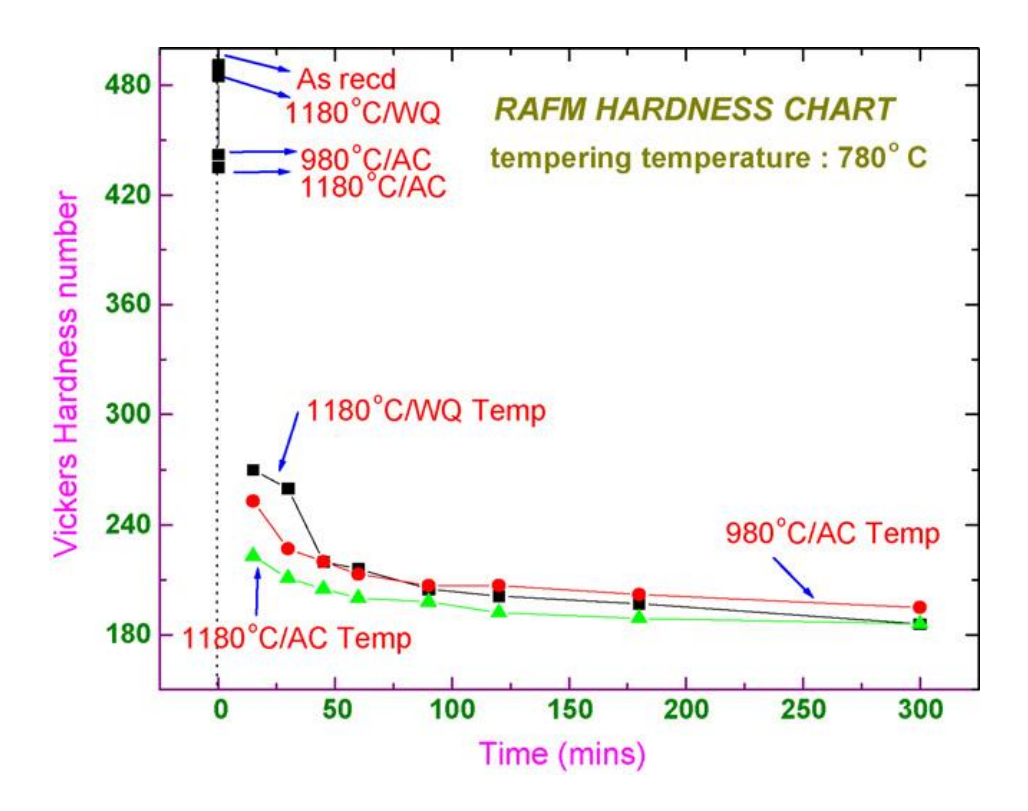


Figure 2.3 Tempering time-Austenizing temperature-hardness relation in IN-RAFM Steel[35]

2.6 Phase transformations in RAFM steels

The various alloying elements in RAFM steels have considerable influence on the phase transformations. The studies conducted by A. Alamo et al. establish that the ferrite stabilizers like W and Ta increase the transformation temperatures[31]. Martensitic start temperature (M_s) is the temperature at which the austenite starts to transform to martensite, and Martensitic finish temperature (M_f) is the temperature at which the transformation is completed. Alamo has found that the M_S temperature is highly influenced by the C content and follows an inverse relation[31]. It was also found that martensite can be formed by air cooling also which is of the range 50-60K.min⁻¹.

2.7 Transformation Temperatures in IN-RAFM

Using Differential Scanning Calorimetry(DSC), Ravikirana et al. has done an extensive study on the phase transformation temperatures of IN-RAFM steel[36]. DSC works based on a program set in such a way that a reference sample and the specimen to be measured are heated in different aluminium crucibles, and their response to the temperature is recorded as a function of temperature. When the specimen to be tested undergoes a phase change, the corresponding difference can be observed in the heat input, which will also be recorded in a graphical format.

The IN-RAFM steel was estimated to have a martensitic start temperature of 645K and martensitic finish temperature of 583K with an error of ±5K[36]. The austenitic start and austenitic finish temperatures designated as Ac1 and Ac3 respectively were found from the DSC thermogram shown in Figure 2.4. [37]. [38]–[40]

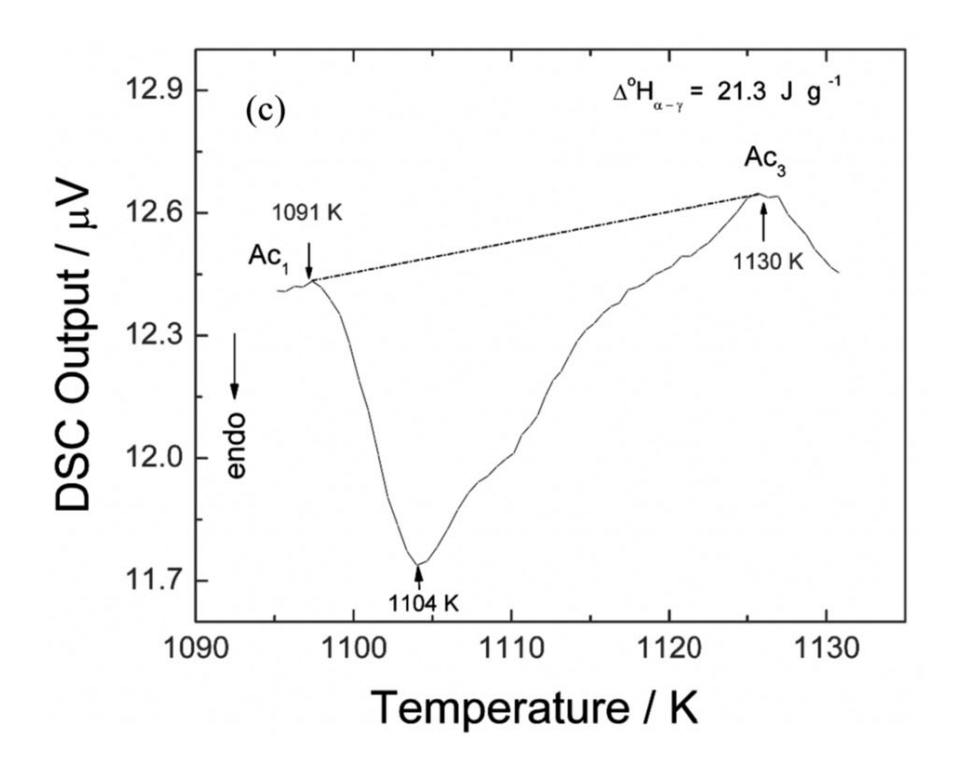


Figure 2.4 DSC regime showing ferrite to austenite transformation, $\alpha \rightarrow \gamma[37]$ The transformation sequence of IN-RAFM at slow heating and cooling rate or 3K.min⁻¹ is as follows.

a-ferrite (ferromagnetic) + $M23C6 + MX \rightarrow \alpha$ -ferrite (paramagnetic) + $M23C6 + MX \rightarrow \gamma$ austenite + $M23C6 + MX \rightarrow \gamma + MX \rightarrow \delta + \gamma + MX \rightarrow \gamma + \delta \rightarrow \gamma + \delta + L \rightarrow \delta + L \rightarrow Liquid$ [36], [40]. The corresponding transformation temperatures of each stage is as given below[36].

- i. α -ferrite (ferromagnetic)+ $M_{23}C_6$ + $MX \rightarrow \alpha$ -ferrite (paramagnetic)+ $M_{23}C_6$ +MX; T_c =1027 \pm 5 K
- ii. α -ferrite (paramagnetic) + $M_{23}C_6$ + $MX \rightarrow \alpha$ -ferrite + $M_{23}C_6$ + MX + γ austenite; $A_{c1} = 1091 \pm 5 \ K$
- iii. α -ferrite + $M_{23}C_6$ + MX + γ -austenite \rightarrow $M_{23}C_6$ + MX + γ -austenite; A_{c3} = 1130 \pm 5 K
- iv. iv. $M_{23}C_6+MX+\gamma$ -austenite $\rightarrow \gamma$ -austenite $+MX;\,T_d,\,M_{23}C_6=1342\pm 5\,\,K$ (T_d- Dissolution temperature)
- v. γ -austenite + MX $\rightarrow \delta$ -ferrite + γ -austenite + MX ; 1494 \pm 10 K

```
vi. \gamma-austenite + \delta-ferrite + MX \rightarrow \gamma-austenite + \delta-ferrite; T_d, MX= 1563 \pm 5 K
```

- vii. γ -austenite + δ -ferrite $\rightarrow \gamma$ -austenite + δ -ferrite + Liquid; 1762 \pm 5 K
- viii. γ -austenite + δ -ferrite+ Liquid $\rightarrow \delta$ -ferrite + Liquid; 1767 \pm 15 K
- ix. δ -ferrite + Liquid \rightarrow Liquid; T_L = 1791 \pm 15K

2.8 Microstructure of Tempered-Martensite

The microstructure of RAFM steels is tempered-martensitic as the alloy will be in a normalized and tempered condition[23], [33]. As martensite being a structure that is highly strengthened due to the high density of dislocations and the presence of several precipitates of the alloying elements, long-range diffusions of substitutional atoms lead to carbide formation. This is highly dependent on tempering temperature and the duration. These carbides are mainly of the form M23C6 and MX (where M is the metal part). Prior austenite grain boundaries (PAGB) in the tempered martensitic structure serve as the nucleation points for the Cr rich M23C6 carbides[41]. The PAGB's coarsen with an increase in austenitizing temperature[42]. The V and Ta rich MX carbides are distributed within the grains, at the martensitic laths and also at the PAGB's. Even though the MX carbides also coarsen with increasing tempering temperature, they are comparatively thermally stable compared to M23C6[42]. Hence the MX carbides are relatively small in size. The coarsening of M23C6 carbides is much higher at the PAGB's due to the greater diffusion at the PAGB's[43]. This is a serious risk when considering the creep strength of the steel[44]. This phenomenon is called Oswald ripening. Figure 2.4 shows the orientation of carbides in the grains and grain boundaries.

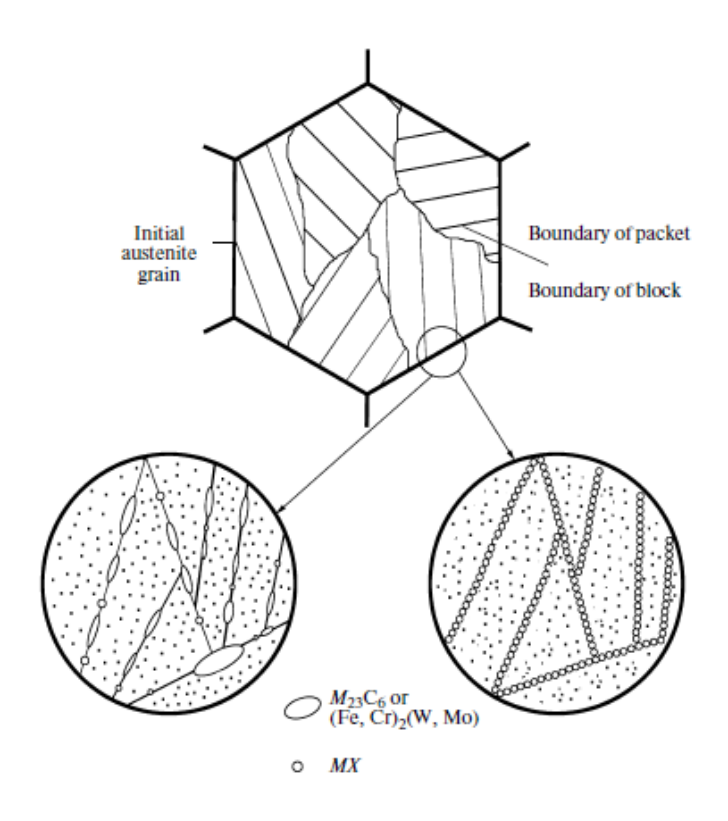


Figure 2.5 Orientation of $M_{23}C_6$ and MX carbides [43]

2.9 Fabrication technologies in RAFM steels

Joining methods adopted in the fabrication side of the TBM is very important as the tailored properties of the RAFM steel can be changed during the joining process. It has already been proved that the RAFM steels are suitable in their weldability[16], [33], [45], [46]. The design of the TBM is in such a way that it can withstand the plasma and prolonged irradiation atmospheres. The first wall that is directly exposed to the heat due to plasma accommodates special cooling jackets for heat absorption, making it a complex design[47]–[49]. The conventional joining methods like Tungsten Inert Gas welding (TIG)[50], Electron Beam Welding (EBW), LASER Beam Welding (LBW) [51]–[62] and Hot Isostatic Pressing (HIP)etc. [53], [54], [60]–[63] have been already tried on the alloy, and a substantial database is also available.

2.10 Welding metallurgy of 9Cr Ferritic-Martensitic steels

The post-weld metallurgy of the RAFM steels depends on the type of welding method used. Welding methods (viz: EBW [26], [29], [33], [58], LBW, TIG[26], [50], [64], [65]) with high heat input will have broader region where phase and microstructure variations are there because of heat. Studies conducted by Klueh et al. M. Vijaya et al., P. Vasantharaja et.al.[3][33], [50]

shows that the welded RAFM steels have three zones. The region where the molten parent metal solidifies is called the Fusion Zone (FZ), the nearby region which is affected by the heat during welding is called Heat Affected Zone (HAZ), and the region away from the fusion zone which is unaffected by the welding process is called the Base Metal (BM) zone.

The fusion zone is the region where the welding temperature exceeds the melting point of the alloy ($T > T_m$). The phases formed in the fusion zone depends on the cooling rate. For fast welding methods like EBW, the cooling rate will increase, and the chances of formation of δ -ferrite is high. Further cooling leads to the formation of austenite, and if the cooling rate favours martensitic formation below M_s temperature, then the martensite phase is also formed. The δ -ferrite phase will be retained in some welding processes like EBW[33].

R.L. Klueh et. al.[3] studied the microstructural differences in the HAZ with respect to distance from the FZ and with phase diagram correlations. Figure 2.6 shows the different zones of the 9Cr weld joints. The formation of different phases like martensite, ferrite, delta ferrite etc., on solidification from the austenitic phase, is dependent upon the Cr equivalent and Ni equivalent in these steels. This has been studied by A.L Schaeffler[66], and H. Schneider[67] have formulated a graph called Schaeffler- Schneider Diagram, which illustrates the formation of these phases with respect to different Cr equivalent and Ni equivalent values. Other than Schalfer and Scheinder, the equation to estimate the Cr equivalent has also been formulated by researchers like Kalthauser and Newhouse.[30].

The equation given by Newhouse [68] is given below.

Cr equivalent (wt%) =
$$(\%Cr) + 6(\%Si) + 4(\%Mo) + 1 l(\%V) + 5(\%Nb) + 1.5(\%W) + 8(\%Ti) + 12(\%A1) - 4(\%Ni) - 2(\%Co) - 2(\%Mn) - (\%Cu) - 40(\%C) - 30(\%N)$$

For 9Cr steels, this Cr equivalent value is kept below 13.5, and the difference in Cr and Ni equivalent is less than 8 so that complete transformation to martensite takes place[30].

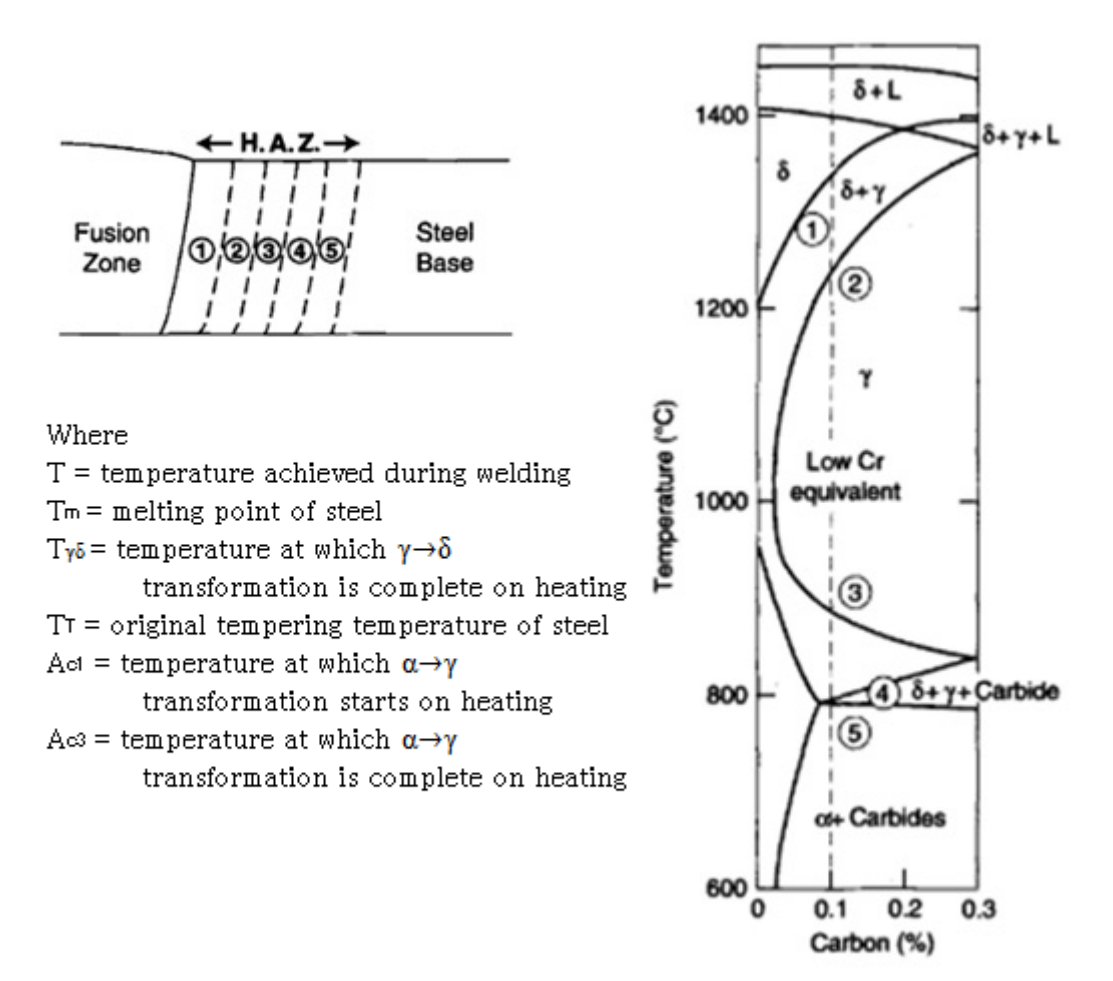


Figure 2.6 Different weld zones and corresponding phase diagram correlation[3]

The Heat Affected Zone (HAZ), where the average temperature (T<T_m) is not exceeding the melting point, has distinct microstructural properties due to the temperature gradient that is experienced as it moves away from the Fusion Zone.

Region 1, which is adjacent to the FZ, experience a temperature less than the melting temperature of the alloy but higher than the transformation temperature of austenite to δ -ferrite $(T_m > T > T_{\gamma - \delta})$. As the temperature is not enough for the complete martensite transformation, a two-phase structure (martensite+ δ -ferrite) exist in this region with δ -ferrite along the PAGB's. The extent of this region depends on the heat generated during the welding process. Depending on the further cooling rate, the δ -ferrite can remain retained at the FZ boundary.

Region 2 next to region 1 will have a temperature less than the transformation temperature of austenite to δ -ferrite ($T_{\gamma-\delta}>T>A_{c3}$), but still it will be in the upper-temperature side of the γ phase and hence causes the dissolution of the initially existing carbides which leads to a

coarsened prior austenitic grain structure and finally it leads to a fully transformed martensitic lath structure on further cooling.

The region 3 will also have a martensitic microstructure like the adjacent region 2, but the grain size will be less because of the lower γ phase temperature prevailing ($T_{\gamma-\delta}>T>A_{c3}$). This lesser temperature inhibits the dissolution of the carbides, and it will resist the grain coarsening.

Region 4 will be a combination of an under-tempered and over-tempered martensitic structure. This happens as the temperature in this region will be in an inter-critical region of the M_s and M_f temperatures ($A_{c3}>T>A_{c1}$). Hence there will be only a partial austenite transformation, and parent steel which was already in a tempered martensitic condition will again get tempered at this temperature.

Region 5 will have a temperature below the transformation temperatures but above that of the tempering temperature of the base metal (Ac1>T> T_T). This region will be narrow and will be nearly similar to the parent metal regardless of the additional tempering happening to the already tempered martensitic structure[3].

2.11 Welding of RAFM steel

Joining of RAFM steels come into much use when it comes to the fabrication side of TBM. Out of the various joining methods, welding holds the superior hand due to the strength of the joint, stable microstructure, easiness of operation, reduced distortion and versatility. As discussed in section 2.9, different welding methods have been tried in the joining of RAFM steels across the world by the countries that have designed their own RAFM varieties. EBW, TIG, LBW, FSW etc. are some of them. Of these, there are fusion welding methods and solid-state welding methods. The welding process, which involves the melting of the parent metal and joining, is called Fusion welding, e.g. EBW, TIG, LBW[26], [50], [64], [69]. Here the temperature developed will be higher than the melting point of the parent metal (T>T_m).

In a study conducted by Qiang Zhu et. al.[64], on the TIG welding of CLAM steels, it has been reported that the weldment or the Fusion Zone is of a width of 10 mm, and the hardness values of the weldment (WM) is much higher than the HAZ and Base Metal (BM). It was also observed that the HAZ had undergone a little softening also. These were brought near to the values of the BM by giving post-weld heat treatment (PWHT). It was found that the hardness of the WM decreased with an increase in PWHT temperature. The presence of δ -ferrite was also observed in the tempered martensitic WM.

Similar studies on thicker sections of CLAM steel by Zhizhong Jiang et.al.[26], employing higher welding current and voltage has yielded a WM or nearly the same width (10 mm) as obtained by Qiang Zhu. A similar higher hardness at the WM and softening at the HAZ region was observed. PWHT was performed to homogenize the weld. The presence of ferrite in the HAZ, along with the martensitic lath structure, has caused the softening after weld. Even though PWHT helped to lower the hardness of the WM, the tensile properties remained superior to that of HAZ and BM, and hence all the tensile specimens failed at the BM side.

Conventional TIG welding being a narrow penetration technique, a modified version of it called the Activated Tungsten Inert Gas welding (A-TIG), which enables to weld thicker sections in a single pass, was employed on LAFM steels by P. Vasantharaja et.al.[50]. This study was able to perform sound welds on samples of thickness 6mm in a single pass. He also studied the welding of a 10mm thick sample using a double pass. The hardness of the WM resembled the early cited behaviour of the steel, and this has been homogenized using a PWHT process. Tensile testing of the samples failed in the BM region as in the previous studies.

Narrow Gap TIG welding (NG-TIG) and Electron Beam Welding (EBW) was studied on IN-RAFM steels by S.K. Albert et.al. [65]. The study was able to propose a suitable filler wire for the NG-TIG process. The DBTT values of the EBW and TIG were similar; however toughness of the EB welds was less compared to the BM. The scattered presence of δ -ferrite was detected in the WM. Creep properties of the EB welded samples were also studied in the as-welded and PWHT conditions.

T. Jayakumar et. al.[55] did an extensive study on different welding methods on IN-RAFM steels which employed TIG, EBW, LASER and HYBRID welding. The comparison of mechanical properties of welded IN-RAFM shown in Figure 2.7 proves that IN-RAFM holds comparable performance with other varieties of RAFM steels.

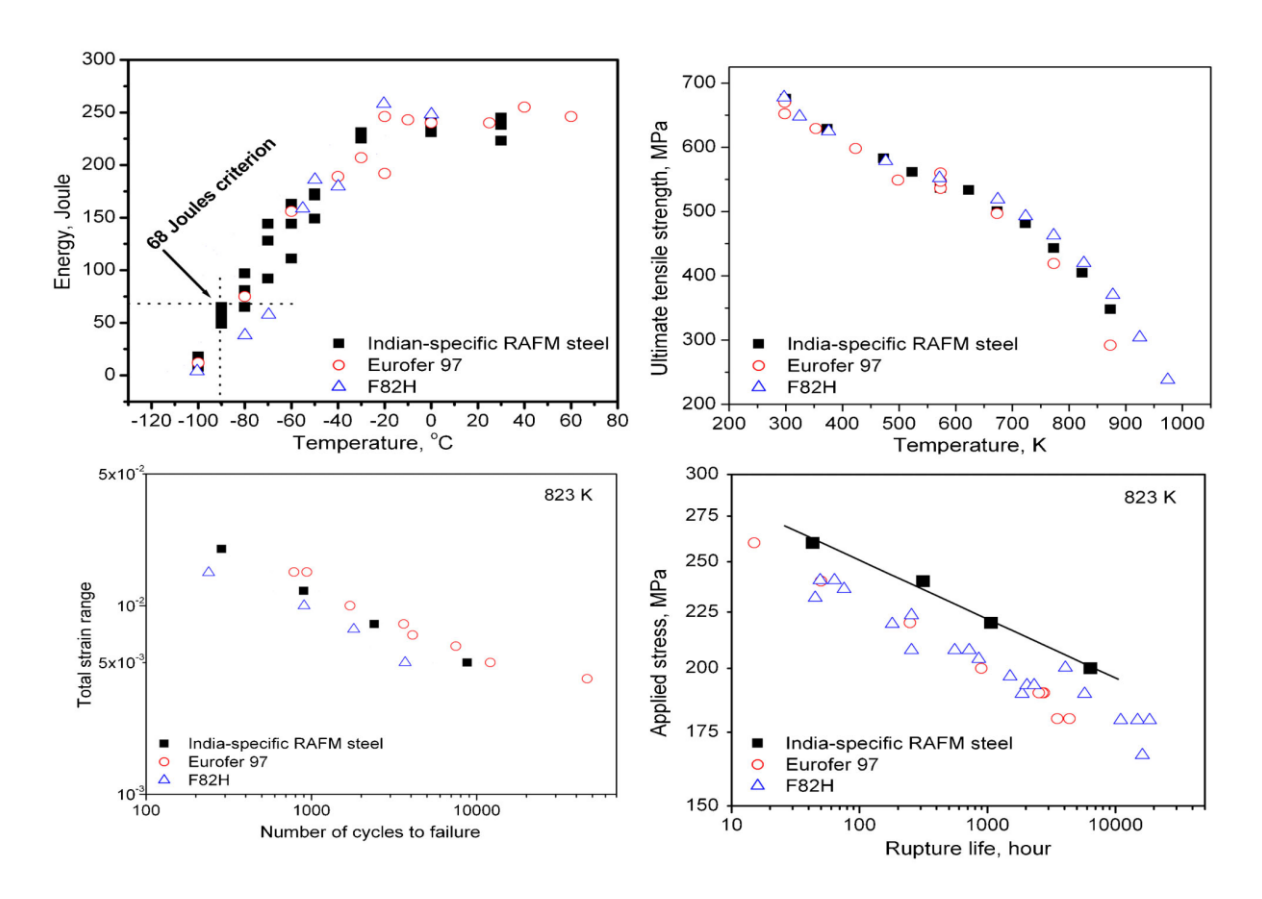


Figure 2.7 Comparison of mechanical properties of welded IN-RAFM with other RAFM steels[55]

Similar studies with EBW, LASER welding etc., were performed on IN-RAFM by Hemant Kumar et. al.[70], S.K. Albert et. al.[71] and T. Jayakumar et. al.[72].

In all these fusion welding processes, as it involves the melting of the parent metal and the subsequent solidification, there are the inherent defects associated with solidification and the chances of δ -ferrite formation, which is a deleterious phase.

2.12 Solid-state welding

This is the welding process that doesn't involve coalescence due to the melting of the parent metal. So the welding temperature will be lower than the melting point of the parent metal. As the parent metal or the welding tool is not melted, the chances of contamination of the weldment by foreign particles from the tool, flux or the welding atmosphere is avoided. Cooling of the weldment is from lesser temperatures when compared to the fusion welding techniques, and hence δ -ferrite can also be eliminated.

The Welding Institute (TWI), Cambridge, UK[73] invented the Friction Stir Welding (FSW) process in 1991. In this method, a suitable tool in the shape of a cylinder with a reduced diameter tip at the end is rotated and plunged onto a workpiece clamped firmly using suitable

fixtures. The frictional heat generated between the tip and the workpiece creates a local softening of the material to be welded. Once this softening is attained, the workpiece/tool is traversed along the region to be welded. The rotating tool moves the softened material from its advancing side to the retreating side. This stirring action will exchange the material on both sides of the weld joint, and the pressure applied to the tool prevents the escape of any material from the welding line. As the tool travels forward, the retreating side cools to get a weld. Figure 2.8 shows a schematic of the friction stir welding process.

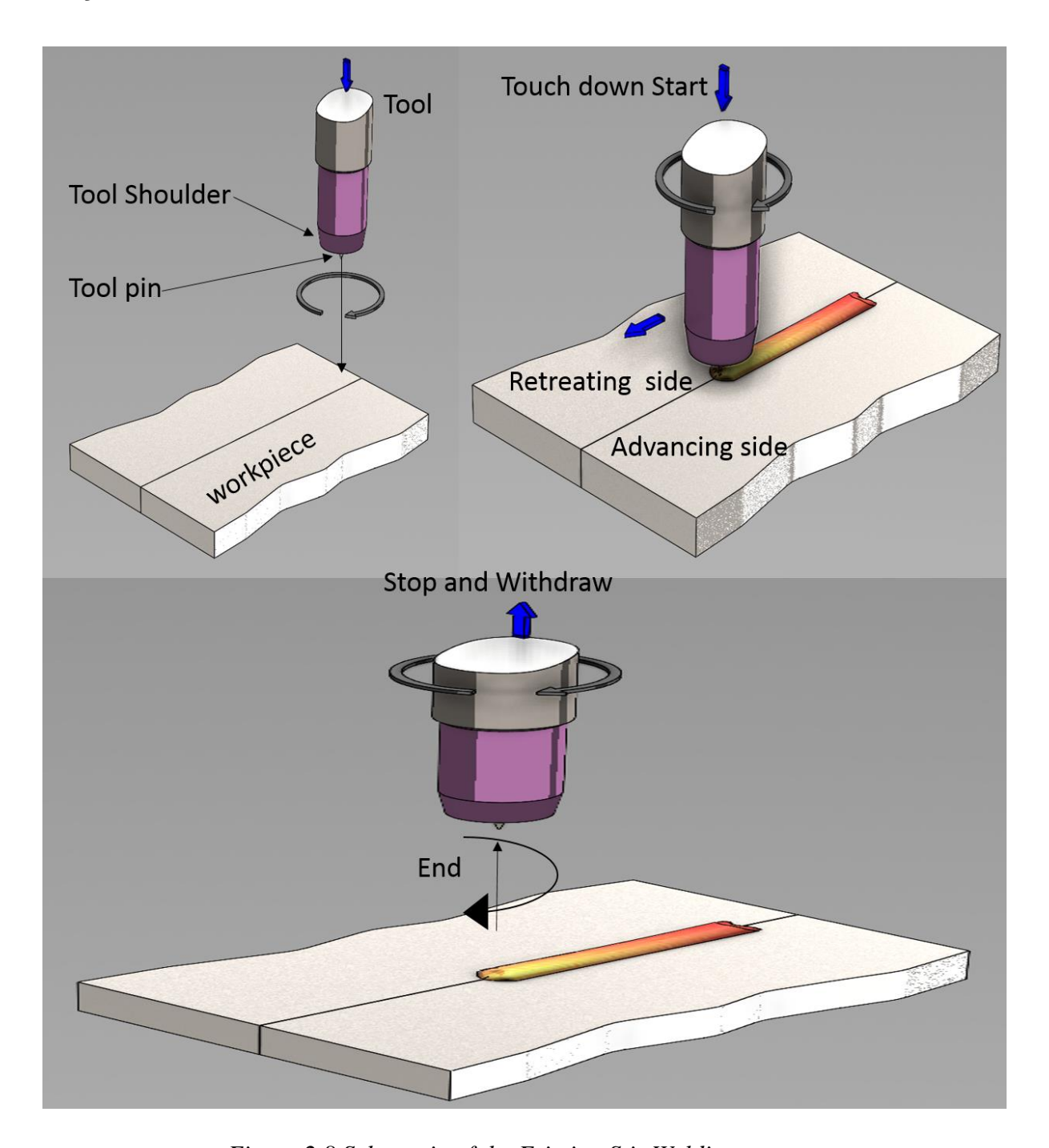


Figure 2.8 Schematic of the Friction Stir Welding process

The achievement of a successful defect-free is dependent on various parameters. The tool material should be made of a material that is strong enough to penetrate the workpiece without wear. The frictional heat created between the shoulder of the tool, pin and workpiece should be high enough to soften the workpiece. The tool material should have high-temperature strength and oxidation resistance so that the tool material will not wear and contaminate the weldment while welding. The length of the pin should be enough to get a full penetration weld. The tool tilt should be enough to produce the least flash. The tool geometry should be such that it helps the stirring action while welding. R.S. Mishra et. al.[74] has done a detailed study on

these parameters on aluminium alloys. Several other studies have also been carried out to have an extensive database about friction stir welding.

The weld zone of the FSW process can be divided into four regions based on the microstructural changes and the heat input. Figure 2.9 shows the different zones in an FSW cross-section.

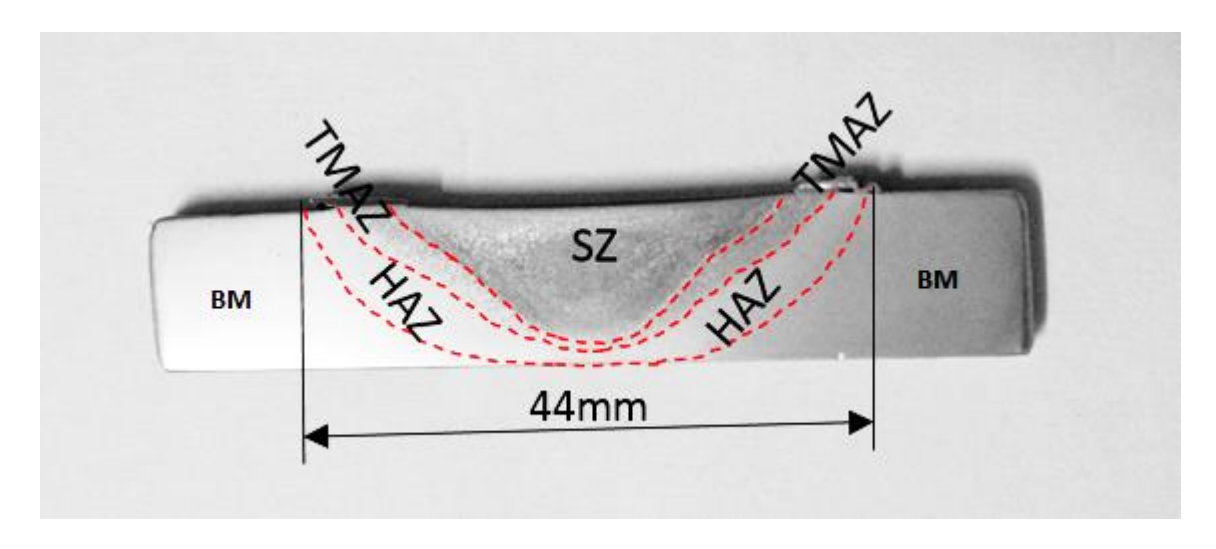


Figure 2.9 Different weld zones in FSW cross section[75]

Stir Zone (SZ) or the weld nugget is the region where the pin of the tool rotates, and the material movement takes place. This region will be subjected to heavy plastic deformation, and due to the heat, a recrystallized fine grain structure exist. The shape of the nugget is depended on several parameters like the tool geometry, tool speed etc. Improper choice of the process parameters can result in wormhole like defects in the nugget zone.

The region next to the stir zone is the Thermo Mechanically Affected Zone (TMAZ). This region will have highly deformed grains due to mechanical shear from the nugget zone. The temperature experienced in this region will lead to microstructural changes as well.

The Heat Affected Zone is the region between the TMAZ and the Base Metal (BM) and is void of any plastic deformation. But the prolonged exposure to the heat due to welding will result in considerable microstructural changes [74].

Choice of suitable tool material

The choice of suitable tool material is very important for a defect-free weld, as discussed above. Soft metals like aluminium, copper etc., were welded using hardened steel as the tool material[76], [77]. It was seen that the tool is worn considerably after multiple passes of welding. K. Colligan [78] used Tungsten-Carbide tools for welding 6XXX and 7XXX series

of aluminium alloys. Dissimilar butt welding of aluminium and steel was performed by T. Yasui et. al.[79] using WC-12Co tool.

The tool material should be harder than the workpiece. This made the welding of high strength materials difficult.

Welding of steels using FSW was first proposed by the founding institute of FSW. W.M. Thomas et.al.[80] produced a defect-free weld on 12 and 15 mm thick low carbon 12Cr steel plates. In a study done by A. P. Reynolds et.al.[81], The tungsten tool was used for welding of 0.18%C steel. Polycrystalline Cubic Boron Nitride (PCBN) tool with a profiled pin which is a much hard material, was used by W.N. Tracy et al. [82] for welding of X-65 steel. The tool profile and shoulder geometry also play an important role in getting a good weld. The force applied to keep the softened nugget zone in place is applied through the shoulder. A concave shoulder used in this study aided this.

The PCBN tool has several properties which help it to be used for FSW of high strength materials. Its high thermal conductivity helps to be fixed to tool holders with a cooling jacket. The layered structure of the boron nitride acts as a lubricant as well. Its least co-efficient of frictions aids to produce a smooth weld surface[83]. Its higher production cost makes it an expensive consumable for FSW of high strength superalloys and steels. M/s. Mazak Megastir technologies is a global manufacturer of PCBN tools of superior quality.

2.13 Post Weld Heat Treatment

Friction stir welding leads to a highly hard weldment which is not acceptable for application purposes. The recrystallized microstructure in the stir zone also contradicts the base metal region. Hence the studies which were carried out on the FSW on steels have proposed the need for a Post Weld Heat Treatment (PWHT) to be carried out on the welded specimens to homogenize the hardness and microstructure with the base metal properties.

PWHT involves heating the welded sample to austenitizing temperature or near austenitizing temperature and air cooling followed by a tempering process as originally done for the parent metal.

In the study conducted by B. Mazumdar et.al.[84], ferritic steel was welded using FSW employing a PCBN tool, and the weld was homogenized to the parent metal properties by giving a PWHT at 1123 K (850 °C). Similarly, in a work by W. Tang et. al.[85], the ferritic-

martensitic steel, EUROFER-97, was welded using a PCBN tool, and the PWHT was done by tempering at 760 °C, which is the original tempering process done for EUROFER-97.

In the friction stir welding studies done on IN-RAFM by M. Vijaya et al. [86] using the PCBN tool, two heat treatment strategies were followed and compared. The samples were subjected to a direct tempering at 760 °C for 90 mins (PWDT) followed by air cooling and another set by a re-austenitization at 980 °C for 30 mins/air cooling followed by tempering at 760 °C for 90 mins/air cooling (PWNT). It was found that the microstructure and the hardness were homogenized by following this procedure. Better mechanical properties were exhibited by the PWNT process[86].

2.14 Mechanical properties of Friction stir welded steels

Several aspects related to the mechanical properties of FSW steels were studied by many researchers, and the results are quite interesting. The welding parameters like tool speed, tool tilt and the tool profile affect the microstructure of weld zones. The tool rotation speed and traverse speed are the weld temperature governing factors. When the weld temperature exceeds the transformation temperatures, considerable phase changes also occur in the weld nugget [87]. Most of the researchers have studied the mechanical properties in the as-welded and PWHT conditions to ensure the effectiveness of homogenization of the weld.

Tensile Properties

The base metal tensile properties of RAFM steels have been studied by several people. They are summarised in Table 2.3.

		0 00	· ·	
Steel	Yield	UTS	%	Reference
grade	Strength	(MPa)	Elongation	
	(MPa)	(ivii a)		
Eurofer-97	543	659	21	[88]–[91]
F82H	554	673	22.5	[92]–[95]
JLF-1	520	625	15	[96]
CLAM	508	665	19	[96]–[99]

Table 2. 3 Tensile properties of different grades of RAFM steels

IN-RAFM	550	666	21	[35], [55],
				[65], [71],
				[72], [100],
				[101]

Tensile properties of FSW plates were studied by machining samples along the cross-section of the weld such that the weld zone comes within the gauge length. M. Vijaya et. al.[33] has conducted FSW on IN-RAFM steels of 6mm thick plates using PCBN tools and has reported that the tensile strength of as-received steel has increased due to FSW, and the tensile elongation has decreased. Post weld heat treatments were applied on the welded specimens by which the tensile strength was restored to nearly the as-received condition with improved elongation. However, the high-temperature tensile properties and fractography are a technological gap in the case of IN-RAFM steels.

Impact Properties

Impact properties of RAFM steels were also studied by researchers. Some of them have investigated the DBTT also by doing impact tests at low temperatures. The outcomes are summarised in Table 2.4.

Table 2. 4 Impact properties of different RAFM steels

Steel Grade	Impact Energy	DBTT	Reference
	(1)	(°C)	
Eurofer-97	255	-70	[89][90]
F82H	140	-60	[89][15][92][54]
JLF-1	294	-86	[102]–[104]
CLAM	258	-102	[52][24][26]
IN-RAFM	248	-80	[35], [55], [65],
			[100], [101]

Impact properties and DBTT of friction stir welded IN-RAFM steels of thicker sections is still an interesting field to be investigated.

Nanohardness

Nanohardness of RAFM steels was studied by a limited number of researchers only. A study on the EUROFER-97 steel done by M. Roldan et. al.[105], has reported that the hardness values to be 3.5GPa, and he has observed that the hardness increased to nearly double after irradiation in high energy He-ion atmosphere. Another study by Y. Takayama et. al.[106], on F82H steels in the as-received and irradiated conditions shows that the as-received nanohardness, which was 4 GPa increased considerably with the single and dual ion beam irradiation. Investigations on CLAM steels by Y. Chang et. al.[107] reported that the as-received hardness of 4.9 GPa increased to 5.8 GPa with an irradiation dose of 10 dpa.

IN-RAFM lacks a database on nanoscale response to indentation testings.

References

[1] A. Einstein, "Does the Inertia of a Body Depend Upon its Energy-Content?" *Ann. Phys.*, vol. 18, pp. 639–641, 1905.

- [2] A. S. Eddington, "Internal Constitution of the Stars," *Obs.*, vol. XLIII, pp. 341–358, 1920.
- [3] R. L. Klueh and D. R. Harries, "High-Chromium Ferritic and Martensitic Steels for Nuclear Applications," *ASTM Monogr. ASTM Int. 3*, pp. 71–80, 2001.
- [4] R. L. Klueh and E. E. Bloom, "The development of ferritic steels for fast induced-radioactivity decay for fusion reactor applications," *Nucl. Eng. Des. Fusion*, vol. 2, no. 3, pp. 383–389, 1985.
- [5] S. N. Rosenwasser, P. Miller, J. A. Dalessandro, J. M. Rawls, W. E. Toffolo, and W. Chen, "The application of martensitic stainless steels in long lifetime fusion first wall/blankets," *J. Nucl. Mater.*, vol. 85–86, no. PART 1, pp. 177–182, 1979.
- [6] R. L. Klueh and A. T. Nelson, "Ferritic/martensitic steels for next-generation reactors," *J. Nucl. Mater.*, vol. 371, no. 1–3, pp. 37–52, 2007.
- [7] V. K. Sikka, "DEVELOPMENT OF MODIFIED 9 Cr-1 Mo STEEL FOR ELEVATED-TEMPERATURE SERVICE.," pp. 317–327, 1984.
- [8] J. M. Vitek and R. L. Klueh, "Precipitation reactions during the heat treatment of ferritic steels," *Metall. Trans. A*, vol. 14, no. 6, pp. 1047–1055, 1983.
- [9] G. J. Butterworth, "Objectives and prospects for low-activation materials," *J. Nucl. Mater.*, vol. 179–181, no. PART 1, pp. 135–142, 1991.
- [10] L. Giancarli, "IMPURITY ACTIVATION AND SURFACE y-DOSE LEVELS IN FIRST WALL STRUCTURAL MATERIALS," vol. 139, pp. 1–10, 1986.
- [11] G. J. Butterworth and L. Giancarli, "Some radiological limitations on the compositions of low-activation materials for power reactors," *J. Nucl. Mater.*, vol. 155–157, no. PART 2, pp. 575–580, 1988.
- [12] R. L. Klueh, D. J. Alexander, and M. Rieth, "Effect of tantalum on the mechanical properties of a 9Cr-2W-0.25V-0.07Ta-0.1C steel," *J. Nucl. Mater.*, vol. 273, no. 2, pp. 146–154, 1999.

[13] R. L. Klueh and P. J. Maziasz, "REDUCED-ACTIVATION FERRITIC STEELS: A COMPARISON WITH Cr-Mo STEELS," *J. Nucl. Mater.*, vol. 155–157, pp. 602–607, 1988.

- [14] C. A. Wang, R. L. Klueh, and B. A. Chin, "The weldability of low activation Cr-W steels," *J. Nucl. Mater.*, vol. 191–194, no. PART B, pp. 831–835, 1992.
- [15] S. Jitsukawa *et al.*, "Development of an extensive database of mechanical and physical properties for reduced-activation martensitic steel F82H," *J. Nucl. Mater.*, vol. 307–311, no. 1 SUPPL., pp. 179–186, 2002.
- [16] S. Jitsukawa *et al.*, "Recent results of the reduced activation ferritic/martensitic steel development," *J. Nucl. Mater.*, vol. 329–333, no. 1-3 PART A, pp. 39–46, 2004.
- [17] H. Kayano, H. Kurishita, A. Kimura, M. Narui, M. Yamazaki, and Y. Suzuki, "Charpy impact testing using miniature specimens and its application to the study of irradiation behavior of low-activation ferritic steels," *J. Nucl. Mater.*, vol. 179–181, no. PART 1, pp. 425–428, 1991.
- [18] R. L. Klueh, D. S. Gelles, and T. A. Lechtenberg, "Development of ferritic steels for reduced activation: The US program," *J. Nucl. Mater.*, vol. 141–143, no. PART 2, pp. 1081–1087, 1986.
- [19] T. Noda, F. Abe, H. Araki, and M. Okada, "Development of low activation Ferritic steels," *J. Nucl. Mater.*, vol. 141–143, no. PART 2, pp. 1102–1106, 1986.
- [20] M. Tamura, H. Hayakawa, M. Tanimura, A. Hishinuma, and T. Kondo, "Development of potential low activation ferritic and austenitic steels," *J. Nucl. Mater.*, vol. 141–143, no. PART 2, pp. 1067–1073, 1986.
- [21] S. Jitsukawa *et al.*, "FT/1-4 Progress of Reduced Activation Ferritic/Martensitic Steel development in Japan."
- [22] Y. De Carlan, A. Alamo, M. H. Mathon, G. Geoffroy, and A. Castaing, "Effect of thermal ageing on the microstructure and mechanical properties of 7-11 CrW steels," *J. Nucl. Mater.*, vol. 283–287, no. PART I, pp. 672–676, 2000.
- [23] F. Abe, T. Noda, H. Araki, and S. Nakazawa, "Alloy composition selection for improving strength and toughness of reduced activation 9Cr-W steels," *J. Nucl. Mater.*, vol. 179–181, no. PART 1, pp. 663–666, 1991.

[24] J. Yu, Q. Huang, and F. Wan, "Research and development on the China low activation martensitic steel (CLAM)," *J. Nucl. Mater.*, vol. 367-370 A, no. SPEC. ISS., pp. 97–101, 2007.

- [25] B. Zhong *et al.*, "Creep deformation and rupture behaviour of CLAM steel at 823 K and 873 K," *J. Nucl. Mater.*, vol. 455, no. 1, pp. 640–644, 2014.
- [26] Z. Jiang *et al.*, "Microstructure and mechanical properties of the TIG welded joints of fusion CLAM steel," *Fusion Eng. Des.*, vol. 85, no. 10–12, pp. 1903–1908, 2010.
- [27] Q. Huang *et al.*, "Progress in development of China Low Activation Martensitic steel for fusion application," *J. Nucl. Mater.*, vol. 367-370 A, no. SPEC. ISS., pp. 142–146, 2007.
- [28] N. Baluc, R. Schäublin, C. Bailat, F. Paschoud, and M. Victoria, "Mechanical properties and microstructure of the OPTIMAX series of low activation ferritic-martensitic steels," *J. Nucl. Mater.*, vol. 283–287, no. PART I, pp. 731–735, 2000.
- [29] B. Van Der Schaaf *et al.*, "Progress and critical issues of reduced activation ferritic/martensitic steel development," *J. Nucl. Mater.*, vol. 283–287, no. PART I, pp. 52–59, 2000.
- [30] J. Oñoro, "Martensite microstructure of 9-12%Cr steels weld metals," *J. Mater. Process. Technol.*, vol. 180, no. 1–3, pp. 137–142, 2006.
- [31] A. Alamo, J. C. Brachet, A. Castaing, C. Lepoittevin, and F. Barcelo, "Physical metallurgy and mechanical behaviour of FeCrWTaV low activation martensitic steels: Effects of chemical composition," *J. Nucl. Mater.*, vol. 258–263, no. PART 2 B, pp. 1228–1235, 1998.
- [32] F. B. Pickering and A. D. Vassiliou, "Effect of austenitizing temperature on constitution, transformation, and tempering of 9Cr–1Mo steel," *Met. Technol.*, vol. 7, no. 1, pp. 409–413, 1980.
- [33] V. L. Manugula, K. V. Rajulapati, G. M. Reddy, and K. B. S. Rao, "Role of evolving microstructure on the mechanical properties of electron beam welded ferritic-martensitic steel in the as-welded and post weld heat-treated states," *Mater. Sci. Eng. A*, vol. 698, pp. 36–45, 2017.
- [34] Ravikirana et al., "Effect of alloy content on microstructure and microchemistry of

phases during short term thermal exposure of 9Cr-W-Ta-0·1C reduced activation ferritic/martensitic (RAFM) steels," *Bull. Mater. Sci.*, vol. 37, no. 6, pp. 1453–1460, 2014.

- [35] B. Raj, K. B. S. Rao, and A. K. Bhaduri, "Progress in the development of reduced activation ferritic-martensitic steels and fabrication technologies in India," *Fusion Eng. Des.*, vol. 85, no. 7–9, pp. 1460–1468, 2010.
- [36] Ravikirana, "Study of transformation characteristics and microstructural evolution in 9Cr reduced activation ferritic martensitic steel using electron microscopy calorimetry and computational methods," *Ph.D. Thesis*, *Dep. Eng. Sci. Homi Bhabha Natl. Inst.*, 2014.
- [37] R. Kirana, S. Raju, R. Mythili, S. Saibaba, T. Jayakumar, and E. Rajendra Kumar, "High-Temperature Phase Stability of 9Cr-W-Ta-V-C Based Reduced Activation Ferritic-Martensitic (RAFM) Steels: Effect of W and Ta Additions," *Steel Res. Int.*, vol. 86, no. 7, pp. 825–840, 2015.
- [38] Ravikirana, R. Mythili, S. Raju, S. Saroja, T. Jayakumar, and E. Rajendra Kumar, "Decomposition modes of austenite in 9Cr-W-V-Ta reduced activation ferritic-martensitic steels," *Mater. Sci. Technol. (United Kingdom)*, vol. 31, no. 4, pp. 448–459, 2015.
- [39] V. Shankar *et al.*, "Effect of tungsten and tantalum on the low cycle fatigue behavior of reduced activation ferritic/martensitic steels," *Fusion Eng. Des.*, vol. 87, no. 4, pp. 318–324, 2012.
- [40] B. Jeya Ganesh *et al.*, "Differential scanning calorimetry study of ffusional and martensitic phase transformations in some 9 wt-%Cr low carbon erritic steels," *Mater. Sci. Technol.*, vol. 27, no. 2, pp. 500–512, 2011.
- [41] L. Tan, J. T. Busby, P. J. Maziasz, and Y. Yamamoto, "Effect of thermomechanical treatment on 9Cr ferritic-martensitic steels," *J. Nucl. Mater.*, vol. 441, no. 1–3, pp. 713–717, 2013.
- [42] B. Yan *et al.*, "The effect of precipitate evolution on austenite grain growth in RAFM steel," *Materials (Basel).*, vol. 10, no. 9, pp. 1–11, 2017.
- [43] R. O. Kaybyshev, V. N. Skorobogatykh, and I. A. Shchenkova, "New martensitic

steels for fossil power plant: Creep resistance," *Phys. Met. Metallogr.*, vol. 109, no. 2, pp. 186–200, 2010.

- [44] F. Abe, "Precipitate design for creep strengthening of 9% Cr tempered martensitic steel for ultra-supercritical power plants," *Sci. Technol. Adv. Mater.*, vol. 9, no. 1, 2008.
- [45] H. Serizawa *et al.*, "Influence of friction stir welding conditions on joinability of oxide dispersion strengthened steel / F82H ferritic/martensitic steel joint," *Nucl. Mater. Energy*, vol. 9, pp. 367–371, 2016.
- [46] A. Kimura, "Current status of reduced-activation ferritic/martensitic steels R&D for fusion energy," *Mater. Trans.*, vol. 46, no. 3, pp. 394–404, 2005.
- [47] Y. Poitevin *et al.*, "Tritium breeder blankets design and technologies in Europe: Development status of ITER Test Blanket Modules, test & qualification strategy and roadmap towards DEMO," *Fusion Eng. Des.*, vol. 85, no. 10–12, pp. 2340–2347, 2010.
- [48] M. Akiba, M. Enoeda, and S. Tanaka, "Overview of the TBM R&D activities in Japan," *Fusion Eng. Des.*, vol. 85, no. 10–12, pp. 1766–1771, 2010.
- [49] H. Tanigawa *et al.*, "Technical issues of reduced activation ferritic/martensitic steels for fabrication of ITER test blanket modules," *Fusion Eng. Des.*, vol. 83, no. 10–12, pp. 1471–1476, 2008.
- [50] P. Vasantharaja and M. Vasudevan, "Studies on A-TIG welding of Low Activation Ferritic/Martensitic (LAFM) steel," *J. Nucl. Mater.*, vol. 421, no. 1–3, pp. 117–123, 2012.
- [51] C. Li *et al.*, "Welding techniques development of CLAM steel for Test Blanket Module," *Fusion Eng. Des.*, vol. 84, no. 7–11, pp. 1184–1187, 2009.
- [52] J. Zhang *et al.*, "Overview on the welding technologies of CLAM steel and the DFLL TBM fabrication," *Nucl. Mater. Energy*, vol. 9, pp. 317–323, 2016.
- [53] P. F. Fu, Z. Y. Mao, Y. J. Wang, Z. Y. Tang, and C. J. Zuo, "Fatigue properties of heavy-thickness Ti6.5Al2Zr1Mo1V alloy with oscillation EBW," *Vacuum*, vol. 121, pp. 230–235, 2015.

[54] T. Hirose, M. Enoeda, H. Ogiwara, H. Tanigawa, and M. Akiba, "Structural material properties and dimensional stability of components in first wall components of a breeding blanket module," *Fusion Eng. Des.*, vol. 83, no. 7–9, pp. 1176–1180, 2008.

- [55] T. Jayakumar *et al.*, "Reduced activation ferritic martensitic steel and fabrication technologies for the Indian test blanket module in ITER," *Fusion Sci. Technol.*, vol. 65, no. 2, pp. 171–185, 2014.
- [56] P. Aubert, F. Tavassoli, M. Rieth, E. Diegele, and Y. Poitevin, "Review of candidate welding processes of RAFM steels for ITER test blanket modules and DEMO," *J. Nucl. Mater.*, vol. 417, no. 1–3, pp. 43–50, 2011.
- [57] X. Chen, Y. Huang, B. Madigan, and J. Zhou, "An overview of the welding technologies of CLAM steels for fusion application," *Fusion Eng. Des.*, vol. 87, no. 9, pp. 1639–1646, 2012.
- [58] S. Cho, D. H. Kim, and M. Y. Ahn, "Development of low activation ferritic/martensitic steel welding technology for the fabrication of KO HCSB TBM," *J. Nucl. Mater.*, vol. 386–388, no. C, pp. 491–494, 2009.
- [59] M. Rieth and J. Rey, "Specific welds for test blanket modules," *J. Nucl. Mater.*, vol. 386–388, no. C, pp. 471–474, 2009.
- [60] Q. Huang *et al.*, "Progress in development of CLAM steel and fabrication of small TBM in China," *J. Nucl. Mater.*, vol. 417, no. 1–3, pp. 85–88, 2011.
- [61] H. Hayakawa, A. Yoshitake, M. Tamura, S. Natsume, A. Gotoh, and A. Hishinuma, "Mechanical properties of welded joints of the reduced-activation ferritic steel: 8% Cr-2% W-0.2% V-0.04% Ta-Fe," *J. Nucl. Mater.*, vol. 179–181, no. PART 1, pp. 693–696, 1991.
- [62] Y. Zhai, B. Huang, J. Zhang, B. Zhang, S. Liu, and Q. Huang, "Effect of weld spacing on microstructure and mechanical properties of CLAM electron beam welding joints," *Fusion Eng. Des.*, vol. 112, pp. 440–449, 2016.
- [63] T. Hirose, M. Enoeda, and H. Ogiwara, "Fabrication of First Wall Component of ITER Test Blanket Module by HIPping Reduced Activation Ferritic / Martensitic Steel," pp. 2–7, 2011.
- [64] Q. Zhu, Y. C. Lei, X. Z. Chen, W. J. Ren, X. Ju, and Y. M. Ye, "Microstructure and

mechanical properties in TIG welding of CLAM steel," *Fusion Eng. Des.*, vol. 86, no. 4–5, pp. 407–411, 2011.

- [65] S. K. Albert, K. Laha, A. K. Bhaduri, T. Jayakumar, and E. Rajendrakumar, "Development of IN-RAFM steel and fabrication technologies for Indian TBM," *Fusion Eng. Des.*, vol. 109–111, pp. 1422–1431, 2016.
- [66] A. L. Schaeffler, "Welding dissimilar metals with stainless electrodes," *Iron Age*, vol. 162, no. 7, pp. 72–79, 1948.
- [67] H. Schneider, "Investment casting of high-hot strength 12% chrome steel," *Foundry Trade*, vol. 108, p. 562, 1960.
- [68] P. Patriarca, S. D. Harkness, J. M. Duke, and L. R. Cooper, "U.S. advanced materials development program for steam generators," *Nucl. Technol.*, vol. 28, no. 3, pp. 516–536, 1976.
- [69] N. Baluc *et al.*, "Status of reduced activation ferritic/martensitic steel development," *J. Nucl. Mater.*, vol. 367-370 A, no. SPEC. ISS., pp. 33–41, 2007.
- [70] H. Kumar *et al.*, "Development of laser welding process for reduced activation ferritic martensitic steel for indian test blanket module," *Fusion Sci. Technol.*, vol. 66, no. 1, pp. 192–199, 2014.
- [71] S. K. Albert *et al.*, "Mechanical properties of similar and dissimilar weldments of RAFMS and AISI 316L (N) SS prepared by electron beam welding process," *Fusion Eng. Des.*, vol. 89, no. 7–8, pp. 1605–1610, 2014.
- [72] T. Jayakumar and E. Rajendra Kumar, "Current status of technology development for fabrication of Indian Test Blanket Module (TBM) of ITER," *Fusion Eng. Des.*, vol. 89, no. 7–8, pp. 1562–1567, 2014.
- [73] D. G. Thomas WM, Nicholas ED, Needham JC, Murch MG, Temple-Smith P, "Friction Stir Butt Welding (1991)," GB Pat. No. 9125978.8, Int. Pat. No. PCT/GB92/02203., vol. 14, no. 1, pp. 3–7, 1991.
- [74] R. S. Mishra and Z. Y. Ma, "Friction stir welding and processing," *Mater. Sci. Eng. R Reports*, vol. 50, no. 1–2, pp. 1–78, 2005.
- [75] J. Varghese, K. V Rajulapati, S. D. Meshram, G. M. Reddy, and K. B. S. Rao, "Strain

Rate Sensitivity and Mechanical Properties of Friction Stir Welded IN-RAFM Steels of Thicker Sections 1 Introduction 2 Experimental Details," *ISBN 978-1-922016-65-2*, no. June, pp. 11–14, 2019.

- [76] R. A. Prado, L. E. Murr, K. F. Soto, and J. C. McClure, "Self-optimization in tool wear for friction-stir welding of Al 6061+20% Al2O3 MMC," *Mater. Sci. Eng. A*, vol. 349, no. 1–2, pp. 156–165, 2003.
- [77] W. B. Lee and S. B. Jung, "The joint properties of copper by friction stir welding," *Mater. Lett.*, vol. 58, no. 6, pp. 1041–1046, 2004.
- [78] K. Colligan, "Material flow behavior during friction stir welding of aluminum," *Weld. J. (Miami, Fla)*, vol. 78, no. 7, pp. 229-s, 1999.
- [79] T. Yasui, Y. Shimoda, M. Tsubaki, and M. Fukumoto, "Welding of aluminum and steel by friction stir diffusion process," *Mater. Sci. Forum*, vol. 449–452, no. I, pp. 433–436, 2004.
- [80] W. M. Thomas, P. L. Threadgill, and E. D. Nicholas, "Feasibility of friction stir welding steel," *Sci. Technol. Weld. Join.*, vol. 4, no. 6, pp. 365–372, 1999.
- [81] A. P. Reynolds, W. Tang, M. Posada, and J. DeLoach, "Friction stir welding of DH36 steel," *Sci. Technol. Weld. Join.*, vol. 8, no. 6, pp. 455–461, 2003.
- [82] N. W. Tracy, S. J. Anderson, and D. J. Segrera, "Friction Stir Welding of Steel," *Int. J. Res. Eng. Technol.*, vol. 03, no. 09, pp. 286–289, 2014.
- [83] R. Rai, A. De, H. K. D. H. Bhadeshia, and T. DebRoy, "Review: Friction stir welding tools," *Sci. Technol. Weld. Join.*, vol. 16, no. 4, pp. 325–342, 2011.
- [84] B. Mazumder *et al.*, "Effect of friction stir welding and post-weld heat treatment on a nanostructured ferritic alloy," *J. Nucl. Mater.*, vol. 469, pp. 200–208, 2016.
- [85] W. Tang, J. Chen, X. Yu, D. A. Frederick, and Z. Feng, "Heat input and post weld heat treatment effects on reduced-activation ferritic/martensitic steel friction stir welds," *Frict. Stir Weld. Process. VIII*, pp. 83–87, 2016.
- [86] V. L. Manugula, K. V. Rajulapati, G. M. Reddy, R. Mythili, and K. Bhanu Sankara Rao, "Influence of Tool Rotational Speed and Post-Weld Heat Treatments on Friction Stir Welded Reduced Activation Ferritic-Martensitic Steel," *Metall. Mater. Trans. A*

- Phys. Metall. Mater. Sci., vol. 48, no. 8, pp. 3702–3720, 2017.
- [87] V. L. Manugula, K. V. Rajulapati, G. Madhusudhan Reddy, R. Mythili, and K. Bhanu Sankara Rao, "A critical assessment of the microstructure and mechanical properties of friction stir welded reduced activation ferritic-martensitic steel," *Mater. Des.*, vol. 92, pp. 200–212, 2016.
- [88] E. Gaganidze, F. Gillemot, I. Szenthe, M. Gorley, M. Rieth, and E. Diegele, "Development of EUROFER97 database and material property handbook," *Fusion Eng. Des.*, vol. 135, no. June, pp. 9–14, 2018.
- [89] M. Rieth *et al.*, "EUROFER 97 Tensile, charpy, creep and structural tests," p. 68, 2003.
- [90] P. Fernandez, A. M. Lancha, J. Lapena, D. Gomez-Briceno, M. Serrano, and M. Hernandez-Mayoral, "Reduced Activation Ferritic/Martensitic Steel Eurofer'97 as Possible Structural Material for Fusion Devices. Metallurgical Characterization on As-Received Condition and After Simulated Service Conditions.," p. 73, 2004.
- [91] A. Puype, L. Malerba, N. De Wispelaere, R. Petrov, and J. Sietsma, "Effect of processing on microstructural features and mechanical properties of a reduced activation ferritic/martensitic EUROFER steel grade," *J. Nucl. Mater.*, vol. 494, pp. 1– 9, 2017.
- [92] E. Wakai, M. Sato, T. Sawai, K. Shiba, and S. Jitsukawa, "Mechanical Properties and Microstructure of F82H Steel Doped with Boron or Boron and Nitrogen as a Function of Heat Treatment," *Mater. Trans.*, vol. 45, no. 2, pp. 407–410, 2004.
- [93] S. Zinkle, J. Robertson, and R. Klueh, "Thermophysical And Mechanical Properties Of Fe-(8-9)%cr Reduced Activation Steels," 1998.
- [94] M. Ando, H. Tanigawa, H. Kurotaki, and Y. Katoh, "Mechanical properties of neutron irradiated F82H using micro-tensile testing," *Nucl. Mater. Energy*, vol. 16, no. August, pp. 258–262, 2018.
- [95] N. Yamanouchi, M. Tamura, H. Hayakawa, A. Hishinuma, and T. Kondo, "Accumulation of engineering data for practical use of reduced activation ferritic steel: 8%Cr2%W0.2%V0.04%TaFe," *J. Nucl. Mater.*, vol. 191–194, no. PART B, pp. 822–826, 1992.

[96] Y. Li, T. Nagasaka, and T. Muroga, "Microstructure and mechanical properties of JLF-1 and CLAM steels exposed to thermal aging with stress," *Plasma Fusion Res.*, vol. 6, no. 1 SPECIAL ISSUE, pp. 2–6, 2011.

- [97] & W. Y. Li. Yanfen, Huang Qunying, "Study on impact and tensile properties of CLAM steel," *Nucl. Phys. Rev.*, vol. 23, no. 2, pp. 151–154, 2006.
- [98] H. Ge, L. Peng, Y. Dai, Q. Huang, and M. Ye, "Tensile properties of CLAM steel irradiated up to 20.1 dpa in STIP-V," *J. Nucl. Mater.*, vol. 468, no. 96, pp. 240–245, 2016.
- [99] W. Xue, J. Zhou, Y. Shen, W. Zhang, and Z. Liu, "Micromechanical behavior of a fine-grained China low activation martensitic (CLAM) steel," *J. Mater. Sci. Technol.*, vol. 35, no. 9, pp. 1869–1876, 2019.
- [100] B. Raj and T. Jayakumar, "Development of Reduced Activation Ferritic-Martensitic Steels and fabrication technologies for Indian test blanket module," *J. Nucl. Mater.*, vol. 417, no. 1–3, pp. 72–76, 2011.
- [101] C. R. Das et al., "Mechanical properties of 9Cr-1W reduced activation ferritic martensitic steel weldment prepared by electron beam welding process," Fusion Eng. Des., vol. 89, no. 11, pp. 2672–2678, 2014.
- [102] R. Kasada, H. Ono, H. Sakasegawa, T. Hirose, A. Kimura, and A. Kohyama, "Mechanical properties of JLF-1 reduced-activation ferritic steels," *Fusion Sci. Technol.*, vol. 44, no. 1, pp. 145–149, 2003.
- [103] T. Nagasaka, H. Yoshida, K. Fukumoto, T. Yamamoto, and H. Matsui, "Mechanical Properties of a High Purity Fe-9Cr-2W-0.1C Model Alloy for Low Activation Ferritic Steels for Fusion Reactors." pp. 170–177, 2000.
- [104] Y. Li, Q. Huang, Y. Wu, T. Nagasaka, and T. Muroga, "Mechanical properties and microstructures of China low activation martensitic steel compared with JLF-1," J. Nucl. Mater., vol. 367-370 A, no. SPEC. ISS., pp. 117–121, 2007.
- [105] M. Roldán, P. Fernández, J. Rams, F. J. Sánchez, and A. Gómez-Herrero, "Nanoindentation and TEM to study the cavity fate after post-irradiation annealing of he implanted EUROFER97 and EU-ODS EUROFER," *Micromachines*, vol. 9, no. 12, 2018.

[106] Y. Takayama *et al.*, "Nanoindentation hardness and its extrapolation to bulk-equivalent hardness of F82H steels after single- and dual-ion beam irradiation," *J. Nucl. Mater.*, vol. 442, no. 1-3 SUPPL.1, 2013.

[107] P. Hosemann, D. Kiener, Y. Wang, and S. A. Maloy, "Issues to consider using nano indentation on shallow ion beam irradiated materials," *J. Nucl. Mater.*, vol. 425, no. 1–3, pp. 136–139, 2012.



CHAPTER 3

Experimental Details



Introduction

This chapter discusses the material details and the experimental procedures executed in carrying out this research. The composition of the as-received material, the initial characterization techniques, the microscopic techniques and the mechanical property measurements are discussed. The friction stir welding is done on the material, and the mechanical characterizations, including the test setup of the tensile tests at room temperature and high temperature, the sample making procedures and also the nanoindentation, are also explained in different sections.

3.1 Material Procurement

The material for the present study, IN-RAFM, was supplied by the Institute of Plasma Research (IPR) Gandhinagar, Gujarat. The as-received material was in the form of plates of thicknesses 6 and 12mm. Three plates of each thickness were provided by IPR.

3.2 As received material

The as-received sample of IN-RAFM steel was in the cold-rolled condition as plates of thickness 6mm and 12mm. The supplied material was produced at M/s. Midhani, Hyderabad by a series of melting and remelting using vacuum induction melting and purified to ensure homogeneity using vacuum arc refining. The basic thumb of alloy design is; the pure you feed, the pure you get. This has been followed very strictly in manufacturing this IN-RAFM Steel, even in stringent restrictions of the Molybdenum (Mo) and Niobium (Nb) which are tramp elements that can cause radioactivity, and Sulphur and Phosphorus, which can lead to embrittlement. The big chunk of the cast product known as the ingots were hot forged and subjected to hot rolling to form plates of the desired thickness. In order to relieve the stress during these processes, the plates were subjected to a normalizing heat treatment at 980°C (1253K) for a duration of 30 minutes, followed by a tempering process at 760 °C (1033K) for up to 90 minutes[1].

These plates were sectioned in different orientations using the EDM wire cutting method to extract samples for the initial characterizations. The sectioned samples were polished using silicon carbide waterproof emery papers starting from 400 grit size in intervals up to 1200 grit size and then with the Grade A and Grade B of levigated polishing Alumina powder suspended in water. Great care was given while polishing to ensure that the polishing process is not imposing any internal stresses on the sample. Mirror finished scratch-free surface was obtained by giving the final polishing using the diamond lapping compound starting from grade 1-3 with

an average micron size of 2 up to grade 0-1/2, which has an average grain size of 1/4 microns. Hifin fluid in aerosol form was used while polishing with the diamond lapping compound on the velvet cloths. The polished samples were examined in the optical microscope to ensure that there are no scratches on the surface.

3.3 Material composition

The composition of the as-received material was analysed using the Optical Emission Spectroscopy technique according to the IS 9879-1998 standards. It uses a spark generated between an electrode and the workpiece (sample whose composition is to be analysed) to vaporize atoms to create a discharge plasma that is capable of creating an emission spectrum unique to its component elements[2], [3]. The results of the composition analysis are shown in Table 3.1.

Composition (wt. %) Composition (wt. %) Element **Element** С 0.077 Ni 0.018 Mn 0.537 Мо 0.002 0.021 Si Cu 0.001 ٧ S 0.002 0.246 Ρ 0.004 W 1.36 Cr 9.13 Fe 88.602

Table 3.1 Chemical composition of the as-received IN-RAFM Steel in weight %

3.4 Friction Stir Welding

The present study deals with the mechanical properties of the friction stir welded plates of 6mm thickness at various conditions and also the feasibility of welding a 12mm thick plate.

Friction stir welding is a solid-state welding process that does not involve the melting of the parent metal. Welding was done on an FSW machine with a vertical load capacity of 200kN manufactured by M/s. Manufacturing Technology Inc. (MTI), USA. The machine has a tool holder with a cooling jacket in which pressurised water is circulated. This tool holder enables the machine to weld a wide variety of materials from harder materials like Titanium, steels, high strength alloys to soft alloys of aluminium, also using appropriate tools. The bed of the

machine is big enough to accommodate bigger workpieces to small plates, and it also has an additional swivel base attachment to be mounted so as to weld circular workpieces. The user interphase of the machine is by a computer connected to it, which enables the input and recording of the welding parameters. Figure 3.1 shows the FSW machine



Figure 3.1 FSW machine manufactured by MTI

The rotating tool made of PCBN is plunged over the plates of size 300x300 mm with thicknesses of 6 and 12mm, which creates a local softening, and the plate is traversed, keeping the tool stationary to get a bead on plate weld along a straight line.

The tool speed was chosen to be 200 rpm, and the tool tilt was 2° from the normal of the plate based on the earlier studies done by V.L. Manugula et. al.[4] on plates of the same thickness. The tool traverse speed was set to be 30 mm. min⁻¹. The parameters were chosen to be these because of the optimised properties of the weld owing to the interphase temperature being kept below A_{c1} while using these parameters. Two welds were performed on the 300 mm wide plate at a distance of 150 mm between both welds. Figure 3.2 shows the orientation of the welds on the 6mm thick plate. The length of welds was limited to 150mm so as to avoid overheating of the tool holder.

Bead on plate welds on 12mm thick plates at 200 rpm and a tool traverse speed of 15mm.min⁻¹ with a tool tilt of 2°. The welds were limited to a maximum length of 50mm to avoid the tool getting heated up. Four sets of welds were made on the 12mm thick plate with 50 mm length.



Figure 3.2 Friction stir welded plates of 6mm thickness

3.5 PCBN Tool

The selection of the tool material is very important in a sound weld. The PCBN tools of grade Q70 used were supplied by M/s. Megastir Technologies, USA. The schematic drawing of the tool is shown in Figure 3.3, and Figure 3.4 shows the picture of the 6mm and 12mm tool. The tool with a pin length of 5.85 mm was used for welding the 6mm thick plate, and 11.75 mm pin length was used for the 12mm thick plate. The shank geometry and sizes are based on the tool holder to which it is to be inserted.

The projecting pin is the first part to touch the workpiece. The rotating pin will pierce the workpiece until the shoulder touches the workpiece, and the frictional heat generated between the pin, shoulder and the workpiece will act as the onset of the local softening of the workpiece. The stirring process done by the profiled pin chips the material locally at a much faster rate that there won't be a time gap for the material to relieve the heat generated. This is nothing but an adiabatic shearing process[5] that softens the material without melting.

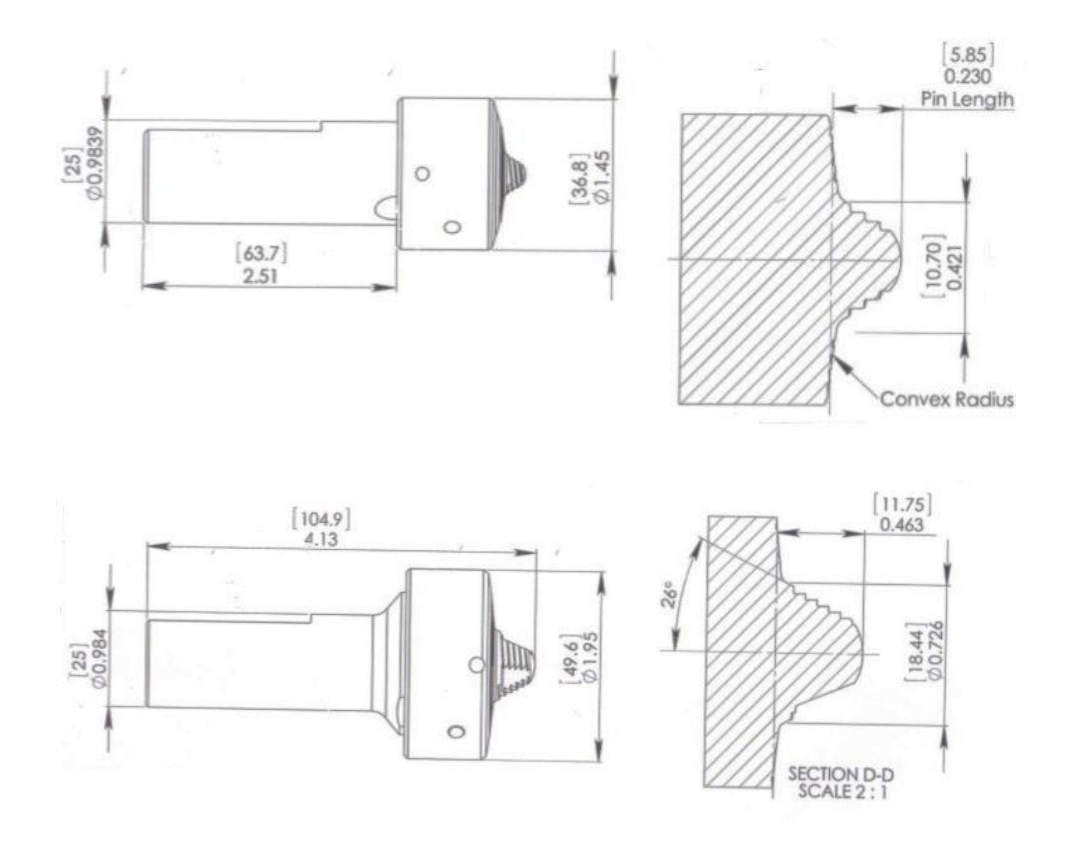


Figure 3.3 Schematic drawing of the PCBN tools 6 mm and 12 mm



Figure 3.4 PCBN tool

3.6 As- received material characterization

As mentioned in section 3.1, the mirror-finished sample was subjected to the following initial characterization methods, which includes both optical and mechanical methods.

3.6.1 X-Ray diffraction

It is one of the most commonly used techniques to analyse the crystal structure of a material [6]. The polished sample surface is impinged with a beam of X-rays of known wavelength from a source exited using a high voltage. The waves get scattered, and the constructive interference caused by each plane of atoms will be in relation to the wavelength (λ) of the beam, lattice spacing (d) between planes and the angle of incidence of the beam (θ), which is called the Bragg's law given as $n\lambda=2d\sin\theta$. The details of the XRD machine and the parameters used for this study are given below in Table 3.2.

The XRD machine of Bruker (Model: D8 Advance) was used to do the analysis (Figure 3.5).



Figure 3.5 X-Ray Diffraction Machine

Bruker Make Model D8 Advance X-Ray source Cu-Kα Wavelength (λ) 1.54Å Max Voltage 40kV Max Current 30mA Scan Angle (2θ) 20-120° Step Size 0.01° Time/step 0.5 s

Table 3.2 Machine details and parameters of XRD analysis

Microstructural Characterization

3.6.2 Optical Microscopy

Light microscopy is the basic technique to study surface morphology and grain orientations. Optical microscopic observations were conducted using an OLYMPUS GX-51 inverted microscope (Figure 3.6). The mirror-finished samples were etched using freshly prepared Villella's reagent (100 ml Ethyl alcohol, 5 ml Hydrochloric acid (HCl), 1g picric acid) to reveal the grain boundaries and the phases.

Optical microscopy uses an array of simple optical lenses to magnify the object by different folds to produce the final image on a real plane. The objective and the condenser lenses are the main components of the arrangement. A light source is used to illuminate the sample surface. The magnification of the image is governed by the equation, $M_{\text{final}} = M_{\text{obj}} * M_{\text{con}}$. The resolution of the image is dependent on the wavelength of the light source used. Optical microscopy was performed on the samples in the as-received, as-welded and PWNT conditions.



Figure 3.6 Optical Microscope

3.6.3 Electron Microscopy

Scanning Electron Microscopy

The SEM, which uses an electron beam to fall on the sample surface, is capable of producing images with better resolution as the electron beam is of comparatively less wavelength to visible light. An electron beam is produced using an electron gun placed in a cooling chamber. The incident electron beam on the sample surface splits into secondary electrons, backscattered electrons, characteristic x-rays and some photons. Out of this, secondary electrons which carry surface information are captured using appropriate detectors to get the secondary image, and backscattered electrons, which carry compositional data, are captured by a BSE detector to get the backscattered image[3].

Scanning electron microscope of M/s. HITACHI (Model: S 3400N), which uses a tungsten filament as the source of the electron beam, was used for this study (Figure 3.7). The polished sample surface was etched with Villella's reagent and was sonicated in ethanol to remove the etch debris before imaging. Great care was given to avoid any sort of contaminations on the sample surface after etching.



Figure 3.7 Scanning Electron Microscope

Field Emission Scanning Electron Microscopy

The working of an FE-SEM is similar to an SEM apart from the principle which is used to generate the electron beam. In an SEM, thermionic emission is used to generate the electron beam, whereas, in an FE-SEM, it is electromagnetic, which enables it to generate a high energy electron beam and thereby better resolution and can also work at low operating voltages.

Field emission scanning electron microscope of M/s. FEI Nova NanoSEM was used for imaging (Figure 3.8). The machine had attachments to detect secondary electrons (through lens detector), backscattered electrons, characteristic X-rays to perform compositional analysis using electron dispersive spectroscopy (EDS detector of M/s. EDAX) and electron backscattered diffraction(EBSD) detector to study the crystal orientations. FESEM imaging was performed on the samples in the as-received, as-welded and PWNT conditions.



Figure 3.8 Field Emission Scanning Electron Microscope

3.7 Mechanical Testings

3.7.1 Vickers Micro Hardness

The hardness of a material can be defined as the resistance to indentation. Indentation hardness testings use a tip of defined geometry to be penetrated onto the mirror-finished sample surface. A Vickers microhardness tester uses a square pyramidal-shaped tip made of diamond with an included angle of $136\,^{\circ}$ as the indenter. The Vickers hardness number (VHN) is calculated based on the area of the tip that has penetrated to the sample surface and the average length of the diagonals given by

$$A = \frac{d^2}{(2\sin\frac{136}{2})} \approx \frac{d^2}{1.8544}$$

Where,

A is the area

d is the average length of the diagonals of the indent (mm)

And the Vickers Hardness Number,

$$VHN = \frac{Force}{Area}$$
$$= 1.8544 \frac{P}{a^2}$$

Where,

P is the applied load (kg)

The Vickers microhardness was tested using a Tinius Olsen (FH-006 series) automated indentation machine. A load of 500g was applied on the tested samples, and the holding time was 10 s. The samples were tested at ten different locations, and the average value has been reported. This machine is capable of doing indentations in a matrix and profile manner. The weldment was indented in a linear profile at regular intervals to get the hardness profile across the weld. Microhardness studies were performed on the samples in the as-received, as-welded and PWNT conditions.



Figure 3.9 Vickers microhardness Tester

3.7.2 Nanoindentation

Nanoindentation is a novel technique to study the mechanical behaviour of the material in near-atomic length scales. A Nanosized tip is penetrated onto the mirror-finished sample surface. The machine is capable of measuring the depth of penetration and the load experienced on the tip with respect to the time. The area of contact of the tip with the sample is calculated based on the depth of penetration from a standard area function specific for each tip used. The commonly used tips are Berkovich tip, conical tip, flat punch tip etc. The tip applies a load to the sample based on a pre-set load function. A capacitive type transducer attached to the tip measures the load with an accuracy coming to $\pm 5\mu N$. Figure 3.10 shows the schematic of the machine setup, and figure 3.11 shows the Berkovich tip geometry. Nanoindentation was performed on the samples in the as-received, as-welded and PWNT conditions.

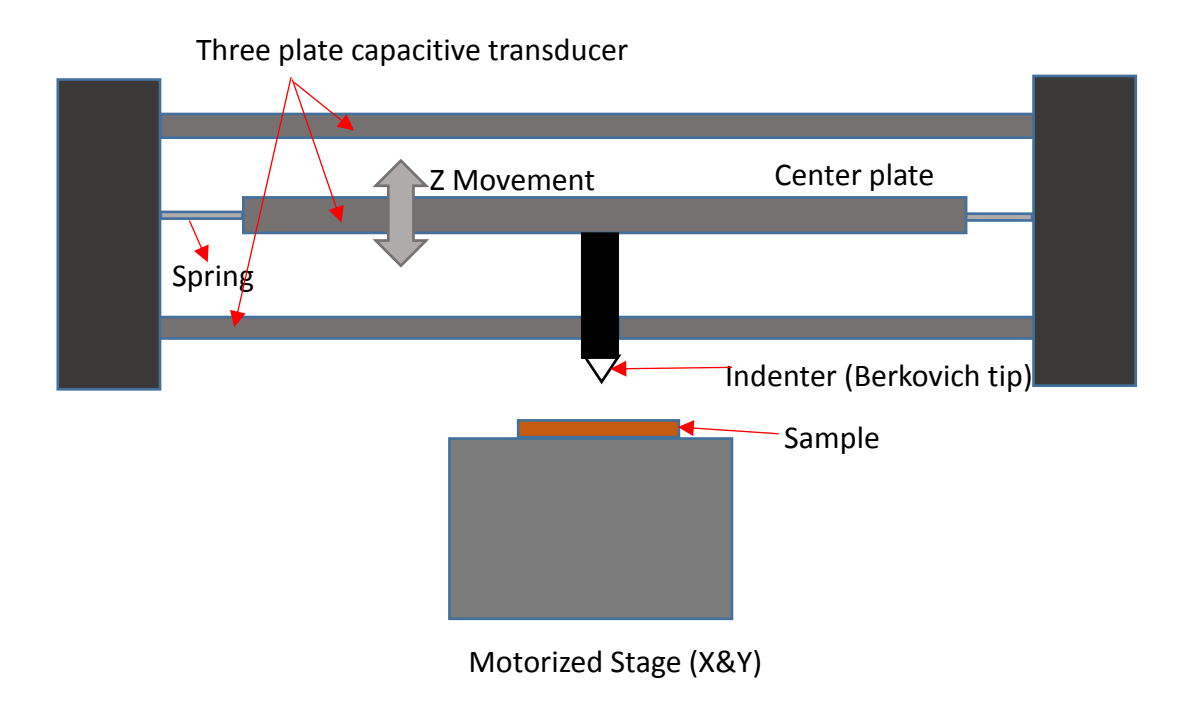


Figure 3.10 Schematic drawing of nanoindentation machine

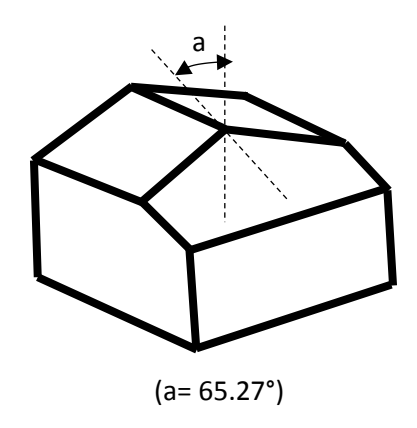


Figure 3.11 Berkovich tip geometry

The nanoindentation tests were performed on a Hysitron Triboindenter TI 950 (Figure 3.12) with a standard transducer that can measure a load up to $10000\mu N$. A trapezoidal load function was used throughout the tests. A maximum load of $8000\mu N$ was applied, and a holding time (dwell time) of 30 s was given. Loading rates varying from $1000~\mu N.s^{-1}$ to $8000~\mu N.s^{-1}$ were used. Figure 3.13 shows a standard Load-Displacement curve of a nanoindentation test. The hardness is calculated by fitting a straight line to the slope of the unloading curve based on the Oliver-Pharr method and using the equations mentioned below[7].

Hardness,
$$H = P_{\text{max}} / 24.5 h_c^2$$

Young's modulus,
$$\frac{1}{E_r} = \frac{1 - v_r^2}{E_i} + \frac{1 - v_s^2}{E_s}$$

Where,

Pmax - Peak load

E_r - Reduced young's modulus

h_c - Contact depth

E_i - Indenters young's modulus

E_s - Sample's young's modulus

 v_i - Poisons ratio of the indenter

 v_s - Poisons ratio of the sample



Figure 3.12 Hysitron Triboindenter TI950

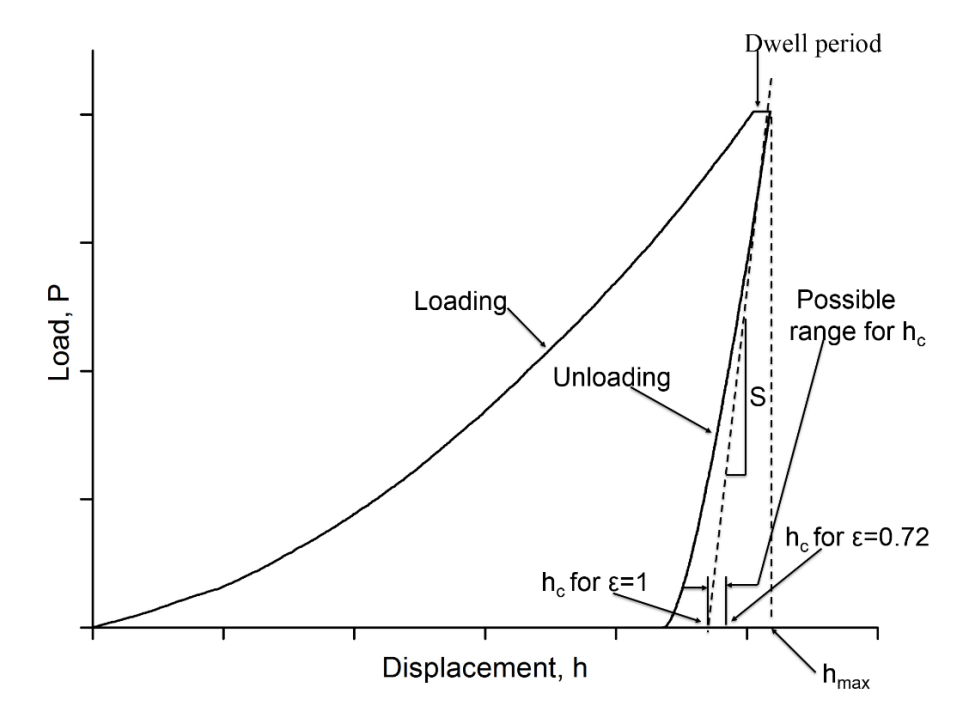


Figure 3.13 Standard Load- Displacement curve of a nanoindentation test

At each condition, a minimum of 49 indents was performed by giving an automated matrix program to perform indents in 7 rows and 7 columns at a spacing of 5 μm. The average values of these indents after eliminating the outliers are reported.

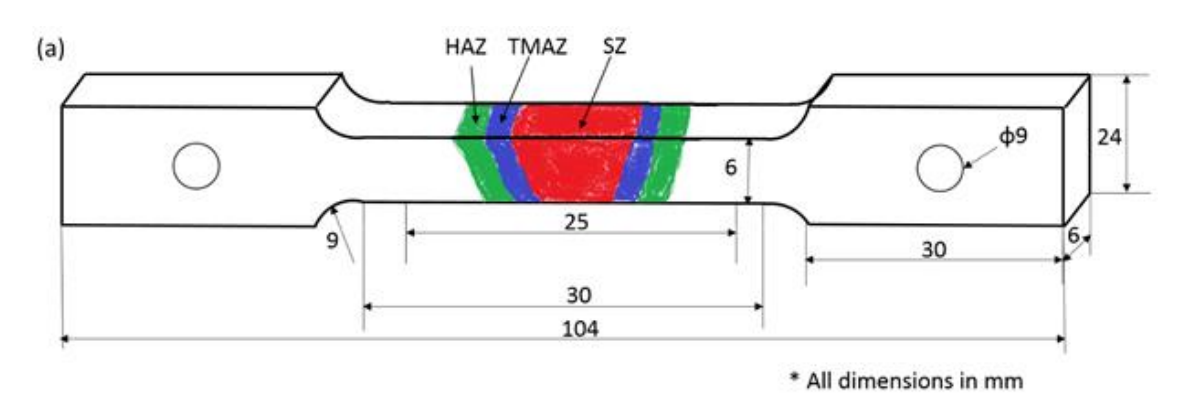
Flow stress during nanoindentation is given by the Tabor's relation, Stress, $\sigma = \frac{H}{3}$ [8]. Strain rate is calculated by dividing the maximum load by loading rate. Strain rate sensitivity (m) is calculated by estimating the slope of the logarithmic plot of flow stress vs. strain rate.

Strain rate sensitivity,
$$m = \frac{\partial ln\sigma}{\partial ln\acute{\epsilon}}$$

Different loading rates of 1000, 2000, 4000, 5000, 7000 μ N.s⁻¹ while keeping the maximum load at 8000 μ N were applied in the present study[9].

3.7.3 Uniaxial Tensile Test

Uniaxial tensile tests are done to estimate the mechanical properties like yield strength, ultimate tensile strength, tensile elongation etc., of the bulk samples. These tests are usually done using a Universal Testing Machine (UTM). This machine is capable of doing almost all mechanical property estimation tests and hence holds the name universal. The machine consists of a stationary head and a movable head. The specimen to be tested is fixed between these two heads using appropriate fixtures. The movable head moves up or down to apply load on the specimen. The load cell attached to the movable head measures the load experienced on the specimen. Extensometers are attached to the specimens to measure the elongation precisely. A high-temperature furnace arrangement attached to the machine enables the machine to do high-temperature tests also.



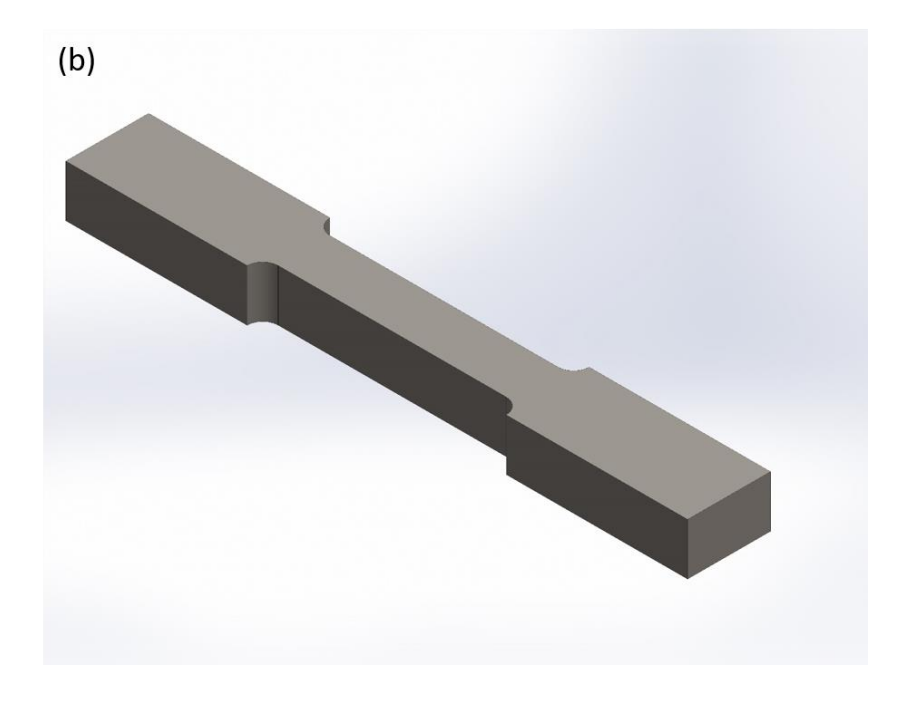


Figure 3.14 (a) HT Tensile sample dimensions and orientation, (b) RT Tensile Specimen Specimens, as shown in Figure 3.14, were designed based on the ASTM E-8 standards[10] and were machined using the EDM wire cut method. Samples were machined from 6mm, and 12mm welded plates. The gauge length was chosen such that the entire weld region, including the different weld zones, will be occupied within the gauge length. Figure 3.15 shows the orientation of the tensile specimen within the weld.

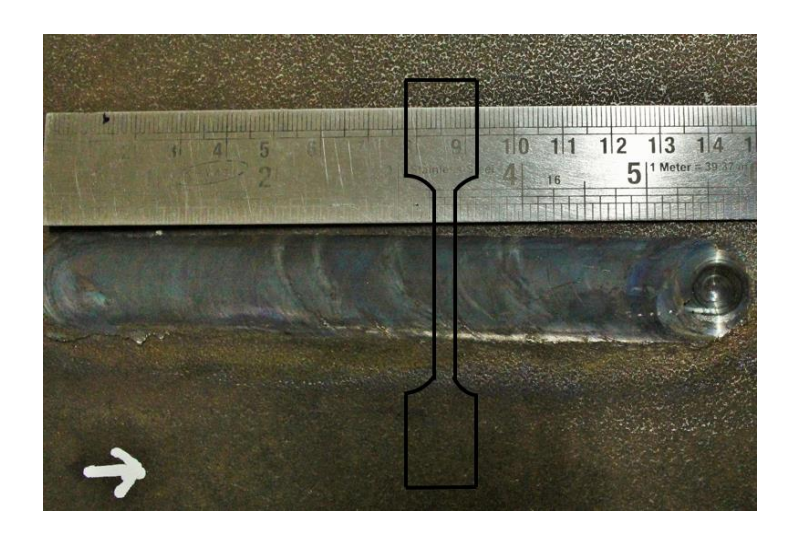


Figure 3.15 Orientation of tensile specimen within the weld



Figure 3.16 Instron Universal Testing Machine (UTM)

Tensile properties were studied using a UTM manufactured by M/s. INSTRON (Model: 5982) with a capacity of 100kN is shown in figure 3.16. The machine has a high-temperature furnace attached to it, which enables the tests at elevated temperatures. The extensometer attached to the sample measures the elongation precisely. The software interphase of the machine BLUE HILL 3 enables the data acquisition. Crosshead speeds of 1 mm.min⁻¹ were applied to the samples.

Room Temperature Tensile Test

Room temperature tensile tests were performed on the samples to study the RT behaviour of the weld and for comparison with the parent material. Samples were made from 6 mm and 12 mm thick plates in the as-received, as-welded and PWNT conditions for the RT test. The samples were gripped using the wedge grips, and an RT extensometer was attached to measure the elongation precisely. The samples were tested at a crosshead speed of 1 mm.min⁻¹.

3.7.4 Notch Tensile Test

The welded samples were breaking at the region outside the weld region in the as-welded and PWNT conditions. So in order to confine the failure at the weld region, notches were given on the samples at the centre of the weld region. Different notch geometries, as shown in Figure 3.17 with varied notch depth and angle, were experimented to get the fracture at the weld region.

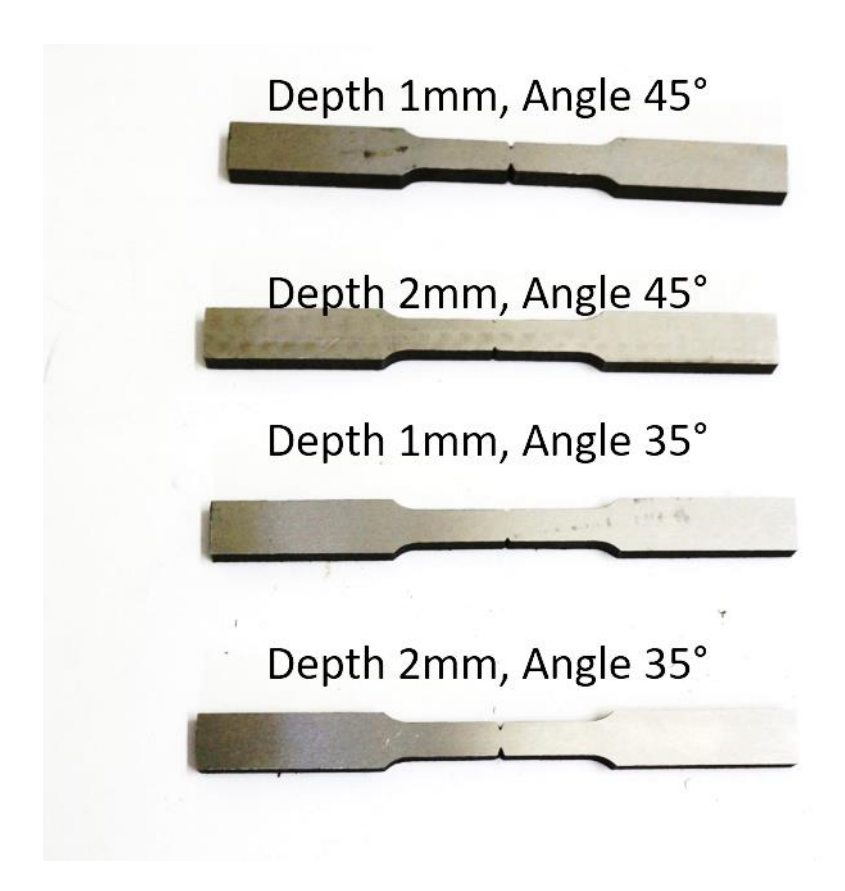


Figure 3.17 Different geometries of notch tensile sample

3.7.5 Elevated Temperature Tensile Test

The elevated temperature tensile tests were performed at 450, 500 and 550 °C, which are the working atmosphere temperatures of the RAFM steel. The specimens to be tested at high temperature were given a modification (Figure: 3.14 (a)) in the grip region so as to insert the

locking pin of the specimen holder for HT tests according to the ASTM E-21 standards[11]. Samples were made from 6 mm and 12 mm thick plates in the as-received, as-welded and PWNT conditions for the HT test. HT extensometer with alumina chisel legs was used to measure the elongation.

3.7.6 Strain Rate Jump Test

The crosshead speed was varied to study the effect of different strain rates on the material and thereby strain rate sensitivity (SRS). This was done by giving jumps in the crosshead speed by giving values of 1, 0.5, 0.1, 0.05 mm. min⁻¹.

3.8 Post Weld Heat Treatment

The PWHT's are important in FSW, as in the case of any welding operation. The properties of the weldment, which might have changed after the heating and cooling operations after welding, can be deleterious in-service time. This needs to be homogenised. The heat treatment cycle needs to be chosen based on the phases that were formed after the welding process. Post weld normalizing and tempering (PWNT) treatment which involves heating the material to austenitizing temperature (980 °C), holding there for 30 min and then cooling to room temperature followed by heating to tempering temperature (760 °C) and holding there for 90 min followed by air cooling to room temperature has proved to be giving the best mechanical and microstructural properties for the weld. This heat treatment cycle was optimized after considering that there should be ample heating beyond the A_{c3} temperature (857 °C) for the MX type carbides which are present in the matrix to dissolve completely[1]. Studies done on IN-RAFM by V. Manugula et al. has proved that the mechanical properties have improved after PWNT, and the microstructure has homogenised and resembles the prior welding condition of the parent metal[12].

PWHT were carried out in a muffle furnace manufactured by M/s. Nabertherm (Model: LT 15/13) (Figure 3.18) has a temperature accuracy of ± 3 °C.



Figure 3.18 Nabertherm muffle furnace

References

- [1] B. Raj, K. B. S. Rao, and A. K. Bhaduri, "Progress in the development of reduced activation ferritic-martensitic steels and fabrication technologies in India," *Fusion Eng. Des.*, vol. 85, no. 7–9, pp. 1460–1468, 2010.
- [2] B. of I. Standards, *Indian Standard METHOD FOR EMISSION SPECTROMETRIC ANALYSIS OF AUSTENITIC AND FERRITIC STAINLESS STEELS POINT TO PLANE TECHNIQUE*. 1998.
- [3] Armin P. Langheinrich and D. Blair Roberts, "optical emission spectroscopy (OES)," *Mod. Methods Geochemical Anal. Plenum Press New York*, pp. 169–170, 1971.
- [4] V. L. Manugula, K. V. Rajulapati, G. Madhusudhan Reddy, R. Mythili, and K. Bhanu Sankara Rao, "A critical assessment of the microstructure and mechanical properties of friction stir welded reduced activation ferritic-martensitic steel," *Mater. Des.*, vol. 92, pp. 200–212, 2016.
- [5] T. Childs, "Adiabatic Shearing in Metal Machining Tom," *CIRP Encycl. Prod. Eng.*, 2016.
- [6] B D Cullity, *Elements of X-Ray Diffraction*. USA: Addison-Wesley Publishing Company Inc., 1956.
- [7] W. C. Oliver and G. M. Pharr, *Journal of Materials Research*, vol. 7, no. 06. pp. 1564–1583, 1992.
- [8] P. Zhang, S. X. Li, and Z. F. Zhang, "General relationship between strength and hardness," *Mater. Sci. Eng. A*, vol. 529, no. 1, pp. 62–73, 2011.
- [9] J. Alkorta, J. M. Martínez-Esnaola, and J. Gil Sevillano, "Critical examination of strain-rate sensitivity measurement by nanoindentation methods: Application to severely deformed niobium," *Acta Mater.*, vol. 56, no. 4, pp. 884–893, 2008.
- [10] W. C. ASTM International, "A. Standard, Standard Test Methods for Tension Testing of Metallic Materials, E8/E8M," *ASTM Int. West Conshohocken, PA, 2013a*, no. C, pp. 1–27, 2013.
- [11] A. E21, "Standard Test Methods for Elevated Temperature Tension Testing of Metallic Materials." ASTM Internationa, West Conshohocken, PA.

- [12] V. L. Manugula, K. V. Rajulapati, G. M. Reddy, R. Mythili, and K. Bhanu Sankara Rao, "Influence of Tool Rotational Speed and Post-Weld Heat Treatments on Friction Stir Welded Reduced Activation Ferritic-Martensitic Steel," *Metall. Mater. Trans. A Phys. Metall. Mater. Sci.*, vol. 48, no. 8, pp. 3702–3720, 2017.
- [13] A. E23, "Standard Test Methods for Notched Bar Impact Testing of Metallic Materials E23," *ASTM Int. West Conshohocken, PA, 2013a*, vol. 14, no. C, p. 28, 2015.



CHAPTER 4

Results and Discussion





CHAPTER 4.1

Ambient, Elevated Temperature Tensile Properties and Origin of Strengthening in Friction Stir Welded 6 mm thick Reduced Activation Ferritic-Martensitic Steel Plates in As-Welded and Post-Weld Normalized Conditions



4.1.1 Introduction

The emphasis on electricity generation by nuclear fusion has thrown several unanticipated and new challenges in the development of suitable materials and fabrication technologies for critical components of fusion reactors within the prevalent operating environment. The engineering and technical co-operation between the European Community, United States, Russia, Japan, China, Korea and India is being pursued towards realizing the construction and operation of the International Thermonuclear Experimental Reactor (ITER) in France. The ITER project is conceived with major objectives of conducting feasibility studies on the generation of fusion energy and examining the different concepts proposed by the participating countries using the test blanket modules (TBMs) for tritium breeding. The materials and fabrication technology issues are prominent in the components of the first wall, diverter, limiters, and blankets of ITER. These components are subjected to intense fluxes of highenergy neutrons, reactive chemicals, and also experience a combination of mechanical and thermal stresses, and electromagnetic loadings under both static and transient conditions. Therefore, the composition of candidate structural materials are to be tailored to have a very low induced radioactivity from the consideration of nuclear waste disposal in a reasonable time period and decommissioning at the end of service; and are also required to possess a reasonable combination of initial microstructure and mechanical properties and their stability in the operating conditions of fusion environment to ensure the structural integrity. The TBM materials development and fabrication technologies in the ITER partner countries received an unprecedented emphasis with respect to lowering ductile-to-brittle transition temperature (DBTT), ensuring adequate creep and fatigue resistance at elevated temperatures against the loss of ductility upon exposure to irradiation under fusion reactor environment [1]. As a result, several Reduced Activation Ferritic-Martensitic (RAFM) steels have emerged as the most promising candidates for TBMs of ITER. The highly creep resistant Modified 9Cr-1Mo Ferritic-Martensitic steel [2], which has been used for many high temperature components in steam generators of nuclear fission reactor power plants, fossil-fired power plants and chemical process industries, served as the basis in the RAFM steels development. Though, the high temperature mechanical properties, forming and welding characteristics of Mod.9Cr-1Mo are good for fusion reactor applications, it has been found deficient as a structural material for construction of first wall and TBM of ITER due to high dose of residual radioactivity, emanating from the long lived transmutation nuclides of Mo, Nb and Nitrogen. In view of this, RAFM steels of various countries have been principally designed by substituting W and Ta for

Mo and Nb respectively with the intention of achieving rapid decay of radioactivity after irradiation in the fusion environment [3-11]. The promising RAFM steels that are reckoning in the fabrication of TBMs consisted of Eurofer-97(Europe), CLAM (China), F82H (Japan), 9Cr2WTa (USA) and INRAFM Steel (India). In spite of the differences noticed in their chemical composition to a certain extent, all these RAFM steels were considered for TBM application, only in the normalised plus tempered condition.

The majority of the structural components in TBM would be fabricated by advanced joining technologies. The fusion welding techniques that received considerable attention towards fabrication of TBM parts consisted of tungsten inert gas (TIG), electron beam (EBW), laser beam (LSW), shielded metal arc (SMAW) and narrow gap tungsten inert gas (NG-TIG) welding [8, 12-14]. In case of Ferritic-Martensitic steels, the high heat input TIG and SMAW processes were found to portray a very wide heat affected zone (HAZ) with varying and gradient microstructures across HAZ depending upon the temperatures experienced during multipass weld thermal cycles. The soft microstructure developed as a consequence of thermal cycling in the intercritical zone of HAZ was found to promote accelerated creep deformation, damage and failure in the vicinity of outer edge of HAZ adjoining the base metal. The soft region in HAZ was found its origin in the coarsening of dislocation substructures and M₂₃C₆ precipitates. Another issue is that, the fusion zone in high heat input welding processes was noticed to have delta-ferrite which contributed to the raise in DBTT, poor impact toughness and low creep resistance of weld joints [12-14]. The delta-ferrite is undesirable in the fusion weld zone because of its tendency for transforming to brittle sigma-phase on exposure to elevated temperatures during service. The nucleation and growth of delta-ferrite results during solidification of molten weld metal in TIG, SMAW and EBW processes. Very recently, the role of delta-ferrite in EBW process on RAFM steel has been explored in detail [12, 15].

Delta-ferrite can be completely eliminated by employing a potential solid state welding process known as Friction Stir Welding (FSW), since it will not create the molten metal in the weld zone [16, 17]. In FSW process a rotating tool containing the shoulder and pin is plunged into the joint between the two flat plates which generate heat due to friction and plastic deformation. The work piece is softened around the tool and material is transported from advancing side to retreating side. The major parameters that control the heat input in FSW are tool rotational speed, tool traverse speed, axial force, shape of tool and tool material [16-20]. The tool rotational speed is the key parameter that determines the peak temperature attained and the

cooling rates achieved during FSW of RAFM steels [18-20]. The proper combination of tool rotational and traverse speeds can be employed for reducing the width of HAZ of RAFM steels. Several researchers have demonstrated that the FSW weld joint of RAFM steels is composed of Stir Zone (SZ), Thermo-mechanically affected zone (TMAZ), HAZ and base metal (BM). These zones have been found to have different micro structural constituents and exhibited enormous variation in hardness across the weld joint. SZ depicted very high hardness while the narrow HAZ possessed a dip in hardness which is lower than that of base metal (BM) [18-20]. It is absolutely necessary that all the zones shall exhibit similar microstructure and mechanical properties to prevent the pre-mature failures in the components; this requires the adaptation of appropriate post weld heat treatment (PWHT). The present study deals with the microstructure and mechanical properties of the Indian RAFM steel plate of 6mm thickness by executing full penetration bead-on-plate FSW experiments. Studies are carried out in the as-received, aswelded and post-weld normalised and tempered condition. The tensile properties, deformation and fracture behaviour are critically assessed. The tensile properties of stir zone in the aswelded and PWHT conditions are also examined. An attempt is also made to predict the strengthening mechanisms operating in SZ and correlated with the data obtained experimentally.

4.2.2 Experimental Procedure

The Indian RAFM steel was manufactured by M/s MIDHANI, Hyderabad, India, and supplied to Institute of Plasma Research (IPR), Gandhinagar. The chemical composition of the steel is shown in Table 4.1.1. The steel has been processed by using pure raw materials and by employing vacuum induction melting and vacuum arc re-melting methods. Strict control was exercised during thermo-mechanical processing on the parameters influencing forging, rolling and heat treatments. The as-received BM has undergone a normalising (980 °C/30min./air cooling) plus a tempering (760 °C/90min./air cooling) treatment.

The blanks of 300x300x6 mm were used in FSW experiments. The full penetration bead-on-plate welds were made on a machine procured from Manufacturing Technology Inc., USA, by using a Polycrystalline Cubic Boron Nitride (PCBN) cylindrical tool with a pin height of 5.85 mm, Figure 4.1.1 shows the experimental setup of the machine (Fig 4.1.1.(a)) and the PCBN tool (Fig 4.1.1.(b)). The tool rotational speed of 200 rpm, a traverse speed 30 mm.min⁻¹ and a tool tilt angle of 2 degrees were employed. These were established parameters in order to

obtain the defect-free welds for India RAFM steel [18, 20]. Argon gas shielding has been used during the progression of welding to prevent the surface oxidation of FSW welds.



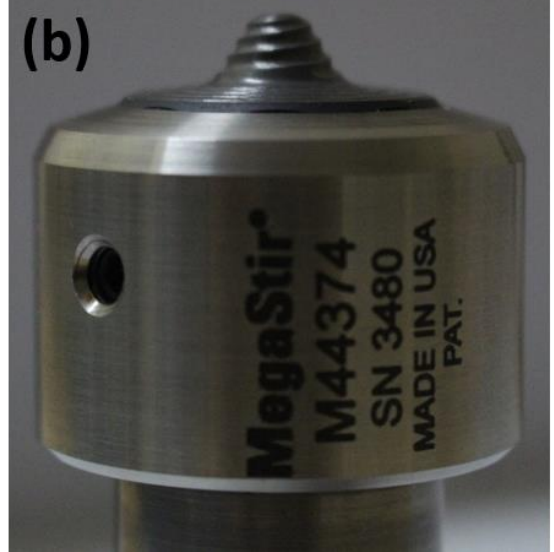


Figure 4.1.1. Experimental setup and PCBN tool adapted in the current investigation.

The metallographic investigations were performed at different locations in the transverse cross section of FSW joint in the as-received (AR), as-welded (AW) and PWHT states by optical and field emission scanning electron microscopy techniques. Villella's reagent (100ml Ethanol, 5ml HCl and 1g picric acid) has been used to etch the polished samples to reveal the

microstructure. The optical microstructure was observed using an Olympus GX 51 microscope, and electron micrographs were taken using FESEM manufactured by FEI (Model: Nova NanoSEM 450). TEM investigation was carried out in the BM and stir zone (SZ) region to observe the microstructural features. The samples were polished to a thickness of 100 microns, and 3 mm discs were punched. These discs were subjected to dimpling using a dimple grinder manufactured by M/s. Gatan Inc (Model: 623). The dimpled discs were perforated using a Gatan precision ion polishing system (PIPS). The perforated discs were imaged using a TECNAI FEI G2 S-Twin Transmission Electron Microscope at an accelerating voltage of 200 keV.

Some of the welded samples were subjected to PWNT treatment comprising of reaustenitization normalising treatment (980°C/30min./air cooling) followed by tempering (760°C/90min./air cooling) to explore its effect on evolving microstructure and mechanical properties. This heat treatment cycle was same as that given to the alloy in the as-supplied condition. The heat treatments were carried out in a Nabertherm LT 15/13 muffle furnace which has a temperature control accuracy of ± 1 °C. Tensile test samples were machined from the AR, AW and PWNT plates using EDM wire-cut method. These samples were ground for better surface finish and dimensional homogeneity. The specimen shown in Figure 4.1.2 illustrates the dimensions of the test specimen as per the ASTM E8-M standard and schematically describes the positioning of various zones in the transverse cross section of the FSW joint and in the gauge portion of the tensile test specimen in the AW state (Fig.4.1.2). Some of the samples were fabricated entirely from SZ (Fig.4.1.3) in order to assess the tensile properties of SZ in AW and PWHT states. Tensile testing was carried out employing Instron 5982 UTM with a maximum capacity of 100kN. Three specimens were tested in each condition to ensure the repeatability of the tests. An extensometer was used in all the tests to measure the deformation in the gauge length region accurately. The samples were tested employing a strain rate of 6.67 x 10^{-4} s⁻¹ at room temperature and at 450 °C, 500 °C, and 550 °C in AR, AW and PWNT states. The fractured samples were observed under SEM in order to obtain the information on the mechanism of failure. In order to obtain the information on crystallographic orientation of the different regions of the weld, EBSD analysis was carried in the FE-Scanning electron microscope equipped with an EBSD detector manufactured by M/s. EDAX (Digi View). The weld regions were polished up to mirror finished condition and then subjected to vibratory polishing in colloidal silica medium of 0.05-micron particle size for about 14 hours.

The tensile behaviour of the SZ region in the AW and PWNT condition was explained using theoretical estimation of different strengthening mechanisms and their contribution to yield strength. Dislocation density was calculated from XRD analysis carried out in a BRUKER D8 ADVANCE XRD machine having a Cu K α radiation (λ =1.5418 Å). A scan range (2 θ) of 20-120°, with a step size 0.02° and a scan time of 4s/step were used.

Table 4.1.1. Composition of RAFM steel (in Wt.%) estimated through optical emission spectroscopy

Element	Composition (wt. %)	Element	Composition (wt. %)
C	0.077	Ni	0.018
Mn	0.537	Mo	0.002
Si	0.021	Cu	0.001
S	0.002	V	0.246
P	0.004	W	1.36
Со	0.007	Cr	9.13
Ta	0.066	Fe	88.602

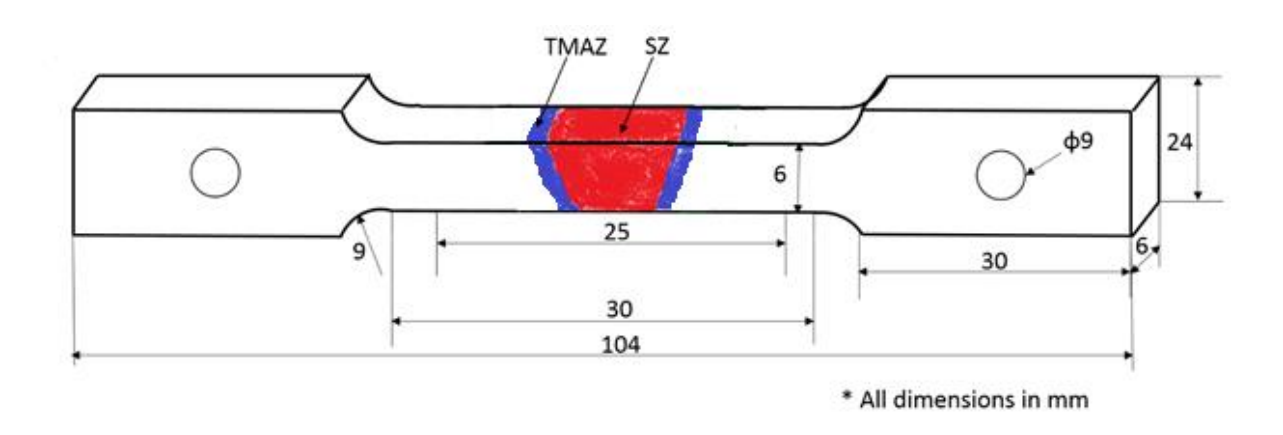


Figure 4.1.2. Dimensions of tensile test sample for BM and weld joint. The location of SZ and TMAZ in the gauge portion are shown schematically.

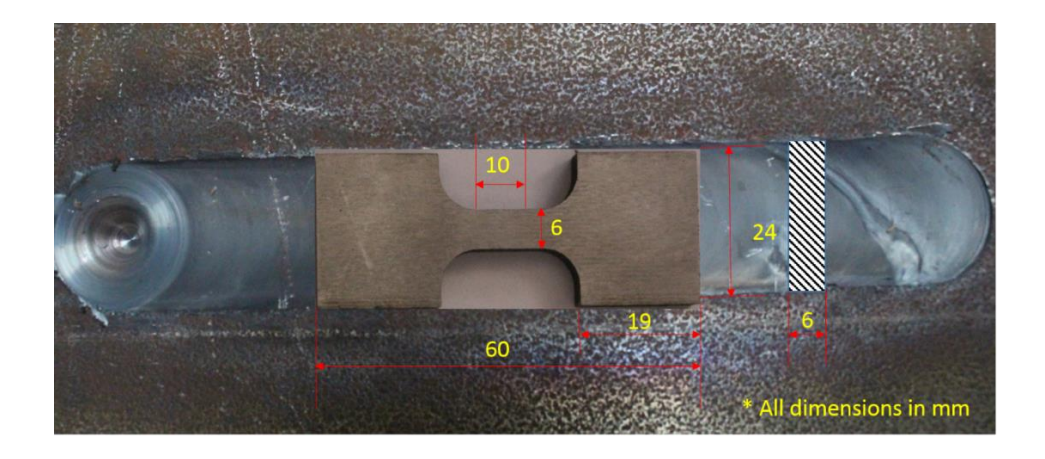


Figure 4.1.3. SZ tensile test sample orientation and geometry

4.1.3 Results

(A) Microstructure of as-received material (base metal, BM)

The BM microstructure was made up of a tempered martensite (Fig.4.1.4). The prior austenite grain boundaries and martensite lath boundaries contained discrete and relatively coarse chromium and tungsten rich $M_{23}C_6$ precipitates. Very fine MX type particles rich in Ta and V were found in the intra-lath regions, as depicted in Fig.4.1.4a. The bright field TEM photographs and selective area diffraction analysis presented in Figs.4.1.4b&c indeed confirm the occurrence of $M_{23}C_6$ and MX at aforementioned sites. The EDS analysis shown in Fig.4.1.5a&b confirmed the presence of Cr and W in $M_{23}C_6$ and Ta and V in MX type of carbides. The size of $M_{23}C_6$ and MX precipitates were found to be in the range of 60-130nm and 20-40nm respectively. The average prior austenite grain size of BM is $7\pm0.67~\mu m$, and the width of the lath martensite structure is ~500±80 nm. Multiple micrographs from TEM and FE-SEM were used to determine grain size and lath size. Presence of dislocations and dislocation tangles can also be observed in the intra lath regions (Figures 4.1.4b&c).

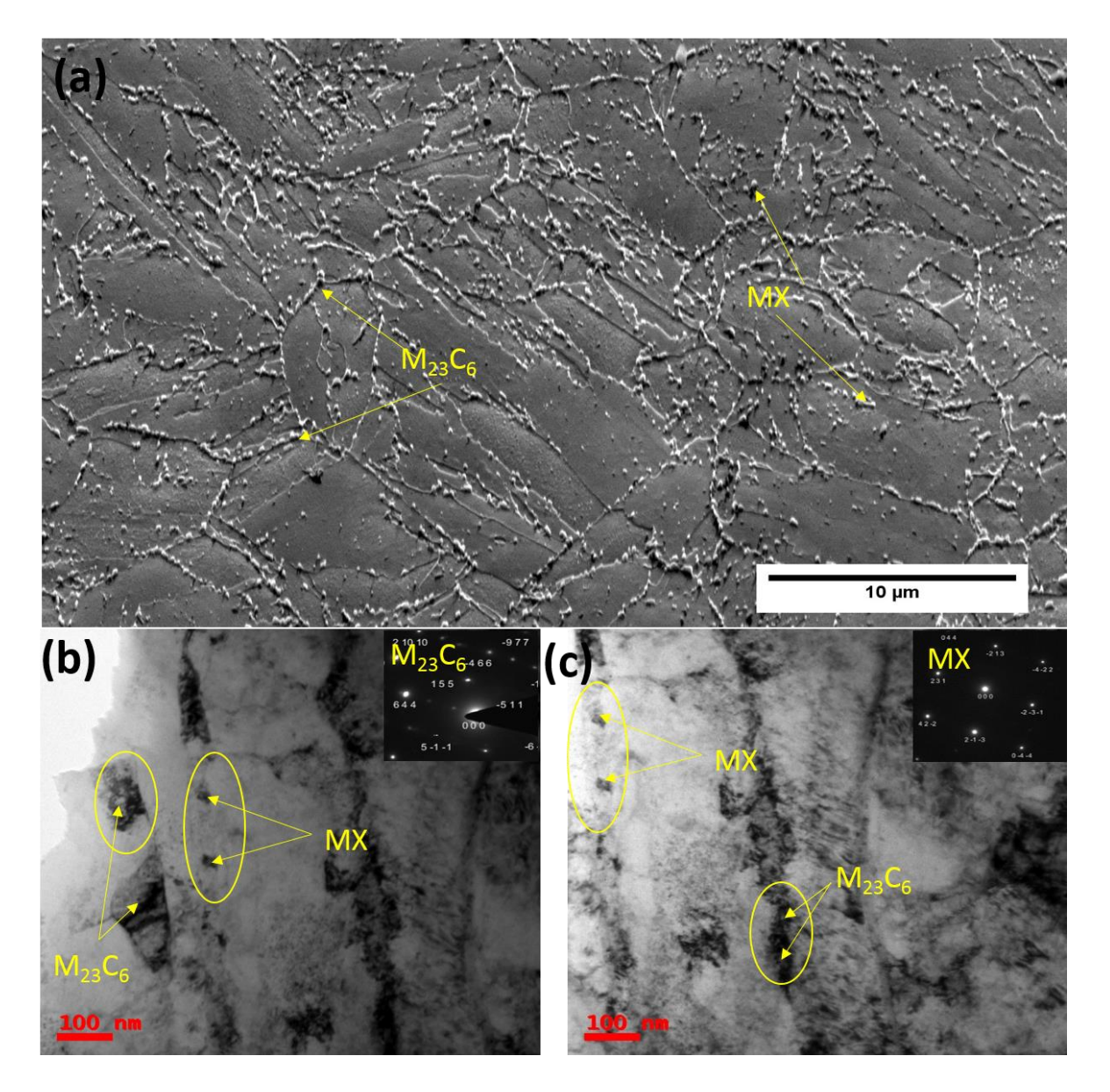


Figure 4.1.4. Microstructure of the as-received (AR: base metal, BM) alloy. The microstructure consists of (a) tempered martensite along with $M_{23}C_6$ on grain and lath boundaries and MX type precipitates in the intralath regions (b&c). SAD patterns of these precipitates are shown in b&c.

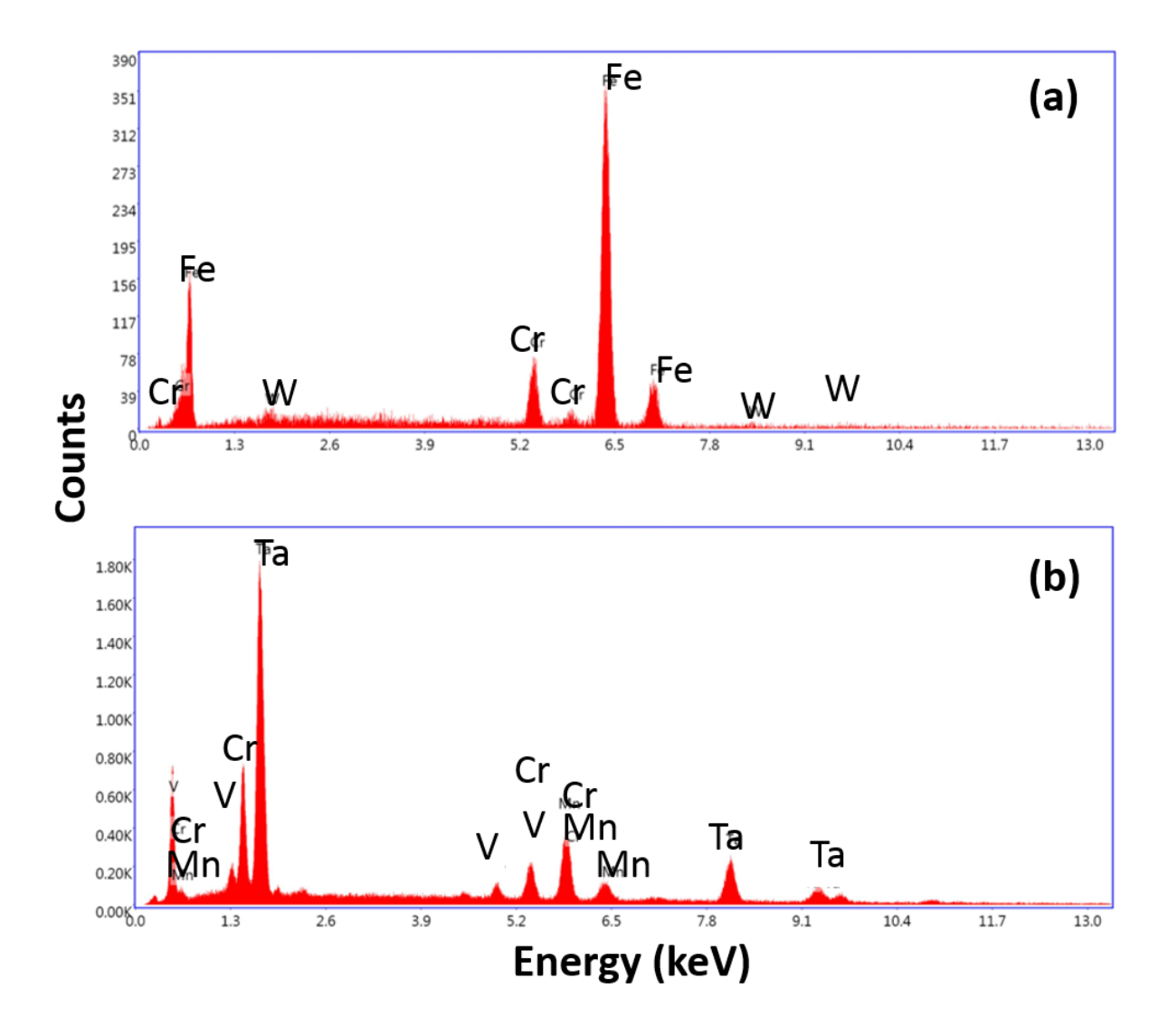


Figure 4.1.5. EDS analysis of the carbides show (a) chromium rich $M_{23}C_6$ on grain boundaries and (b) Ta and V containing MX precipitates in the matrix.

(B) Constituents of weld joint and their microstructure

The transverse-cross section of FSW joints clearly indicated the full penetration and sound welds without occurrence of any type of defects, which was confirmed by radiographic analysis. In the as-welded state, the joint revealed SZ, TMAZ and unaffected BM. The HAZ which normally reported to occur at high rotational speeds and in thick sections [19] was found non-existent at 200 rpm rotational speed employed in this research work. The BM in as-welded joint contained equiaxed grains (Figure 4.1.6a&b). The type of carbides and their distribution was found almost identical to that displayed in the as-received material. Figures 4.1.6c&6d describe the FE-SEM micrographs of the TMAZ and SZ respectively. Microstructure in SZ

was noticed to be very complex and reflected the changes that occur due to thermomechanical deformation during solid state FSW process. The salient features of SZ microstructure include: majority of the grain boundaries in SZ contained reduced number of (i) particles(Fig.4.1.6d) compared to that present in BM, while some of them were found free from M₂₃C₆ precipitates (Fig.4.1.6d) suggesting their dissolution, (ii) matrix is free from intragranular M₂₃C₆ (iii) large number of dislocations generated during friction stirring process have been re-organised into a lower energy configuration in the form of elongated cells with randomly distributed dislocations in cell interiors, which acts as a pointer to the occurrence of dynamic recovery (Figure 4.1.7), (iv) the presence of very few and fine MX precipitates in the intragranular regions which escaped destruction and dissolution during FSW (Figure 4.1.7b), and (v) the occurrence of very small needle type of precipitates in ferrite grains (Figure 4.1.7c) ; the SAD pattern (Figure 4.1.7d) from these precipitates indicated that these precipitates possess stoichiometry of Fe₃C and occur along [-423] zone axis. The microstructure of the TMAZ (Fig.4.1.6c) was significantly different than that observed in SZ (Fig.4.1.6d). TMAZ contained less number of grain boundaries that are free from M₂₃C₆ precipitates and found to have clustered areas of M₂₃C₆ in intragranular regions (Fig.4.1.6c). The peak temperature and frictional force experienced by the material decreases on moving from SZ into TMAZ resulting in the observed variation in the microstructure in AW state.

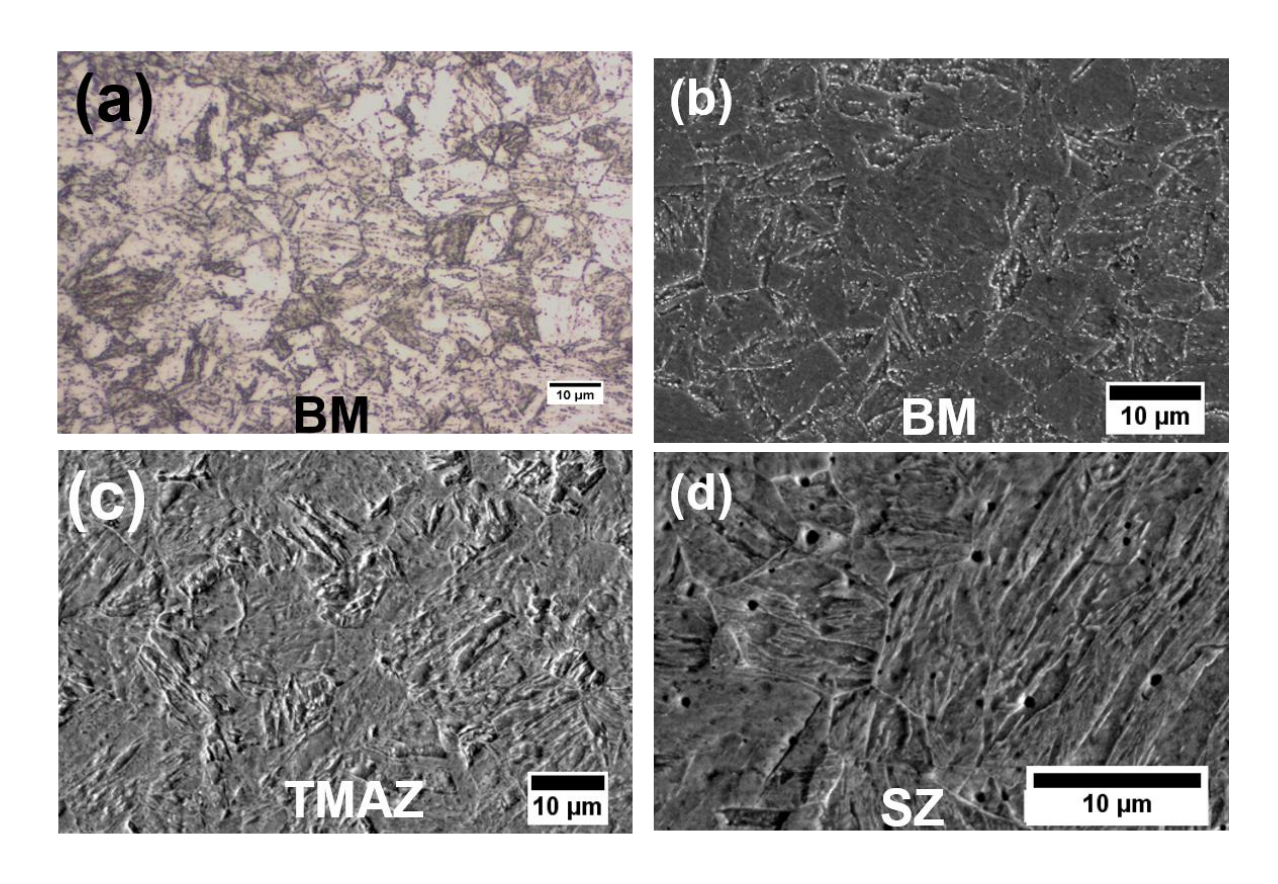


Figure 4.1.6. (a) Optical micrograph of BM in the as-welded state describing equiaxed grain structure and carbide distribution in the matrix and on grain boundaries, (b) SEM photograph of BM, (c) SEM microstructure of TMAZ depicting clustered zones of M₂₃C₆ precipitates and and (d) SEM microstructure of SZ.

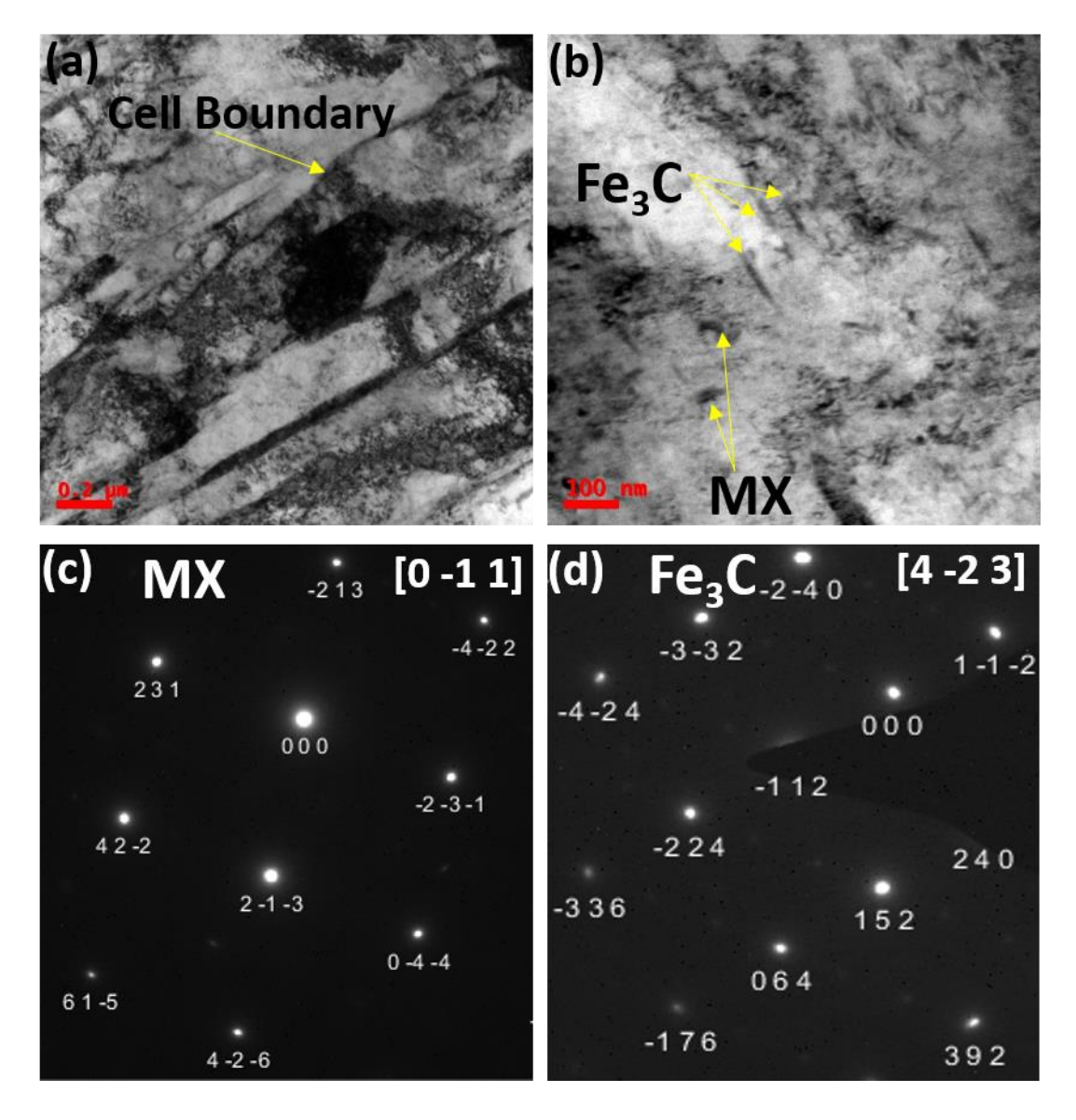


Figure 4.1.7. TEM micrographs of SZ in AW state: (a) Intragranular cells and dislocations, (b) undissolved MX and freshly formed Fe₃C needle particles, (c) SAD of undissolved MX precipitates, (d) SAD of Fe₃C needle particles.

(C) Post weld normalising and tempering (PWNT) heat treatment

The presence of some undissolved MX precipitates in the SZ indicate the need of a heat treatment process above the Ac₃ temperature. As the dissolution of these precipitates in y-

austenite are governed by the diffusional mobility of substitutional solutes like W, Ta and V, it is important to provide sufficient heating above the Ac₃ temperature. The heat treatment is also aimed at dissolution of the Fe₃C formed in the SZ. The post weld normalizing and tempering (PWNT) treatment was chosen considering these aspects. The AW samples have been subjected to PWNT treatment comprising of re-austenitizing at 980 °C/30min/air cooling plus tempering at 760°C/90min/air cooling. Figure 4.1.8 illustrates that the grain boundary M₂₃C₆ was restored after PWNT and fine intragranular precipitates in the SZ were reprecipitated (Fig.4.1.8c). The clusters of M₂₃C₆ in TMAZ disappeared and further resulted in very fine precipitation of M₂₃C₆ in the matrix (Fig.4.1.8b).

Figure 4.1.9 depicts the EBSD image quality figures of SZ in AW and PWNT conditions. Microstructure in AW state revealed a large variation in grain size (Fig.4.1.9a) which was narrowed down after PWNT (Fig.4.1.9b). The SZ revealed the existence of both low angle (defined by $2\text{deg} \leq \text{theta} \min \leq 15 \text{ deg}$) and high angle boundaries (defined by misorientation angle theta $\min \geq 15 \text{ deg}$) in both the states. AW state contained higher fraction of high angle boundaries while the fraction of low angle boundaries significantly increased after PWNT. The PWNT promoted an equiaxed grain structure (Fig.4.1.9b). Figure 4.1.10 illustrates the grain size distribution and variation that was seen in different zones of AW and PWNT states. The grain size distribution in BM narrows down after PWNT with an average size of 7 μ m though few grains appeared to have been coarsened during re-austenitization solution treatment. Remarkable change in the grain size distribution was noticed after PWNT in the SZ and TMAZ with the occurrence of fresh nucleation due to the recovery and recrystallization of the plastic deformation induced dislocation substructure. The increased number of low angle boundaries serve as an evidence for this observation.

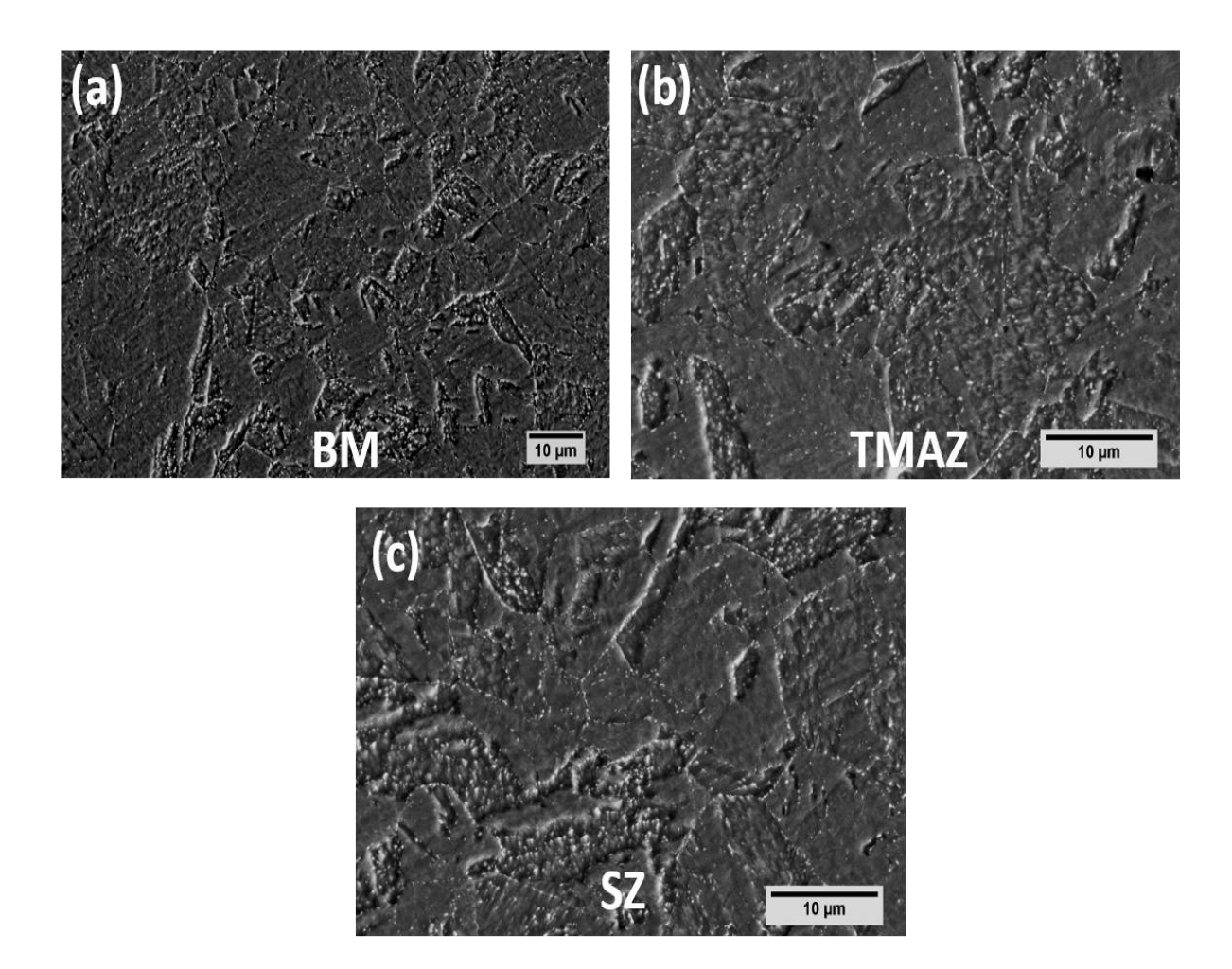


Figure 4.1.8. PWNT microstructure showing (a) Base Metal, (b) Thermo Mechanically Affected Zone, (c) Stir Zone

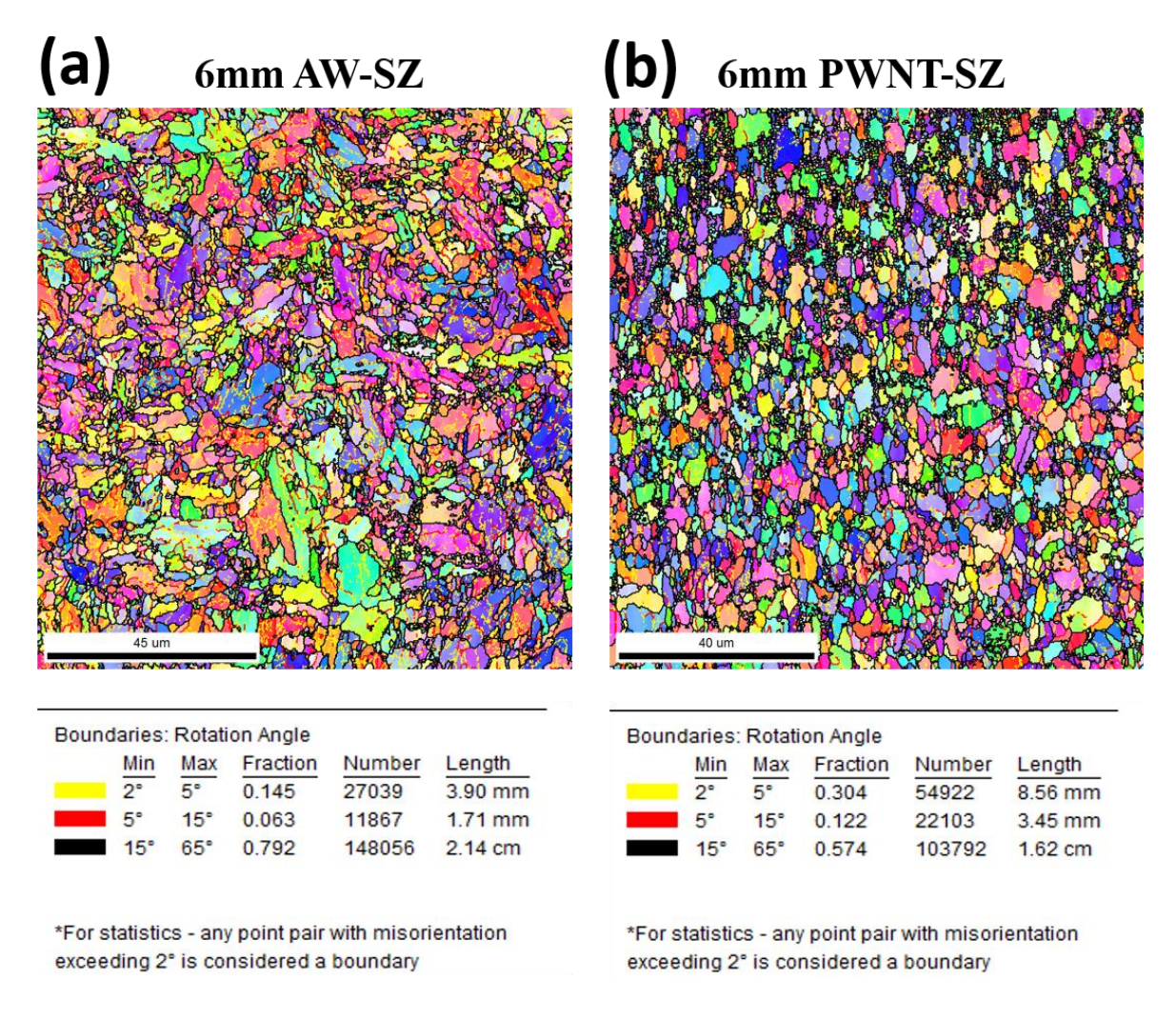


Figure 4.1.9. EBSD image quality maps of (a) as-welded (AW) and (b) PWNT sample from SZ region

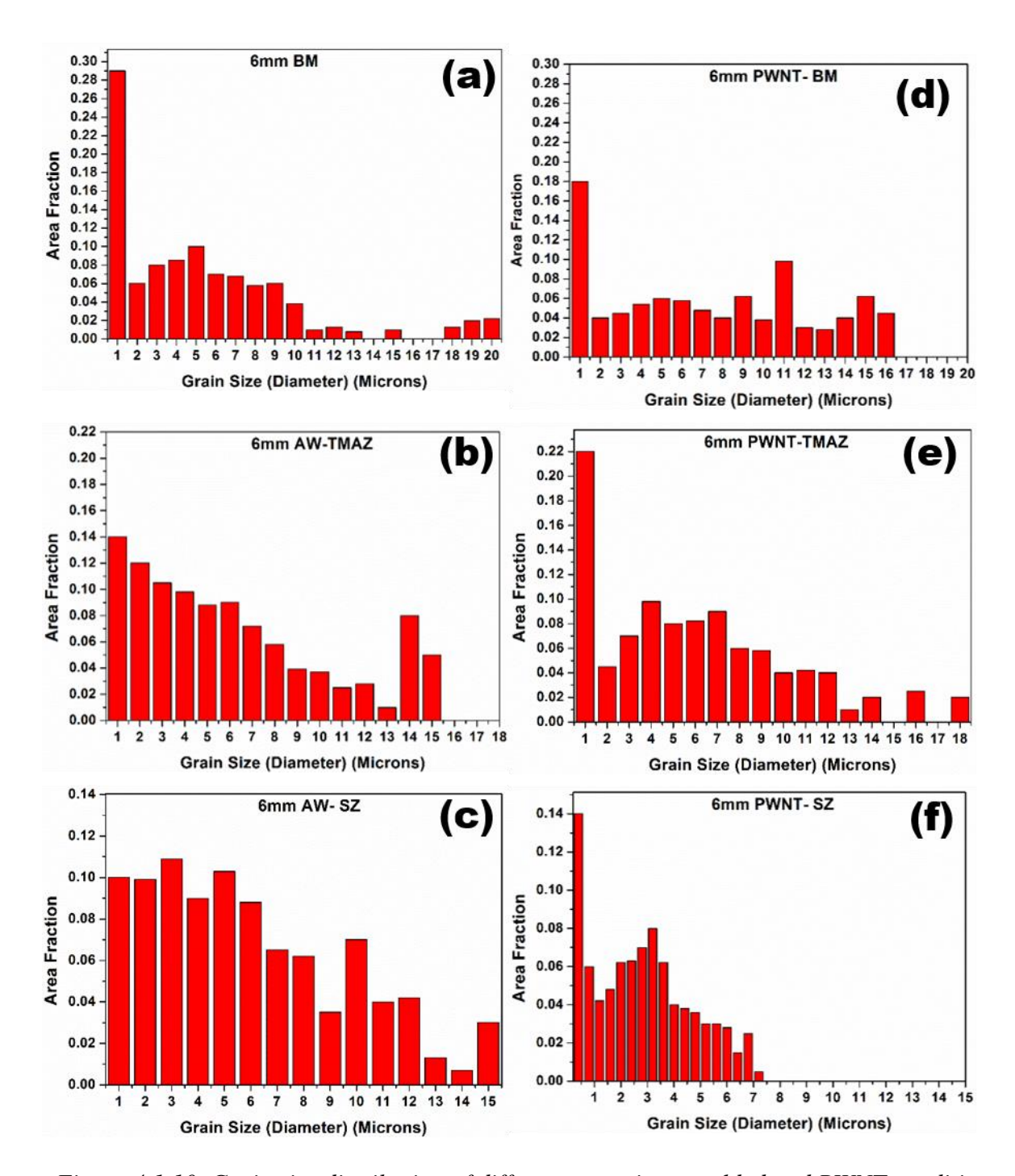


Figure 4.1.10. Grain size distribution of different zones in as-welded and PWNT conditions

(D) Tensile properties and stress-strain curves

The monotonic tensile stress-strain curves obtained at a nominal strain rate of 6.67 x 10^{-4} s⁻¹ at room temperature and at 450 °C, 500 °C, 550 °C in AR, AW and PWNT states are shown in Figure 4.1.11. In all the states, irrespective of the temperature employed, the stress-strain curves remained smooth without evidence of serrated flow. The derived tensile properties from the stress-strain curves are given in Table 4.1.2. In general, the

0.2% offset yield strength and ultimate tensile strength decreased on increasing the temperature up to 550 °C in all the states; the percentage elongation exhibited a minimum at 450 °C. AW state displayed lower elongation compared to BM and PWNT states at identical tensile test temperatures. Base material revealed a rapid fall in strength during the progression of the test at 450 °C leading to reduced ductility (Fig.4.1.11a). The temperature dependent fall in strength was found similar in AW and PWNT states (Fig.4.1.11 b&c). The rate of fall in strength was lower in case of AW-FSW joint. Samples fabricated with SZ alone revealed very high tensile strength (Fig.4.1.11d) with rapid softening beyond UTS. PWNT treatment to samples containing SZ-alone caused substantial decrease in UTS with considerable gain in percentage elongation at room temperature (Fig.4.1.11d). The SZ either in AW joint specimen or in PWNT treatment did not improve the elongation to a greater extent as depicted by SZ-alone (Figure 4.1.11b, 11c &11d).

Table 4.1.2. Tensile properties derived from the monotonic stress-strain curves obtained at different temperatures in AR, AW and PWNT states

Sa	ample Condition	Test	Elongation	UTS	0.2% YS
		Temperature	(%)	(MPa)	(MPa)
		(°C)			
(a)	AR	RT	24 ± 1.0	610 ± 4.2	470 ± 5.5
	AR	450	17 ± 1.2	535 ± 9.3	450 ± 8.8
	AR	500	25 ± 1	436 ± 8.5	368 ± 7.6
	AR	550	28 ± 1.3	353 ± 7.7	286 ± 8.1
(b)	AW	RT	15 ± 1.3	641 ± 4.2	487 ± 5.1
	AW	450	14 ± 2.2	522 ± 5.5	468 ± 6.3
	AW	500	13 ± 1.5	482 ± 4.8	460 ± 5.9
	AW	550	16 ± 1.9	422 ± 4.9	407 ± 6.6
(c)	PWNT	RT	21 ± 1.6	610 ± 4.1	461 ± 3.9
	PWNT	450	18 ± 1.2	460 ± 5.0	410 ± 4.2

PWNT	500	20 ± 1.9	422 ± 4.6	376 ± 5.0
PWNT	550	21 ± 2.1	381 ± 5.4	348 ± 5.4

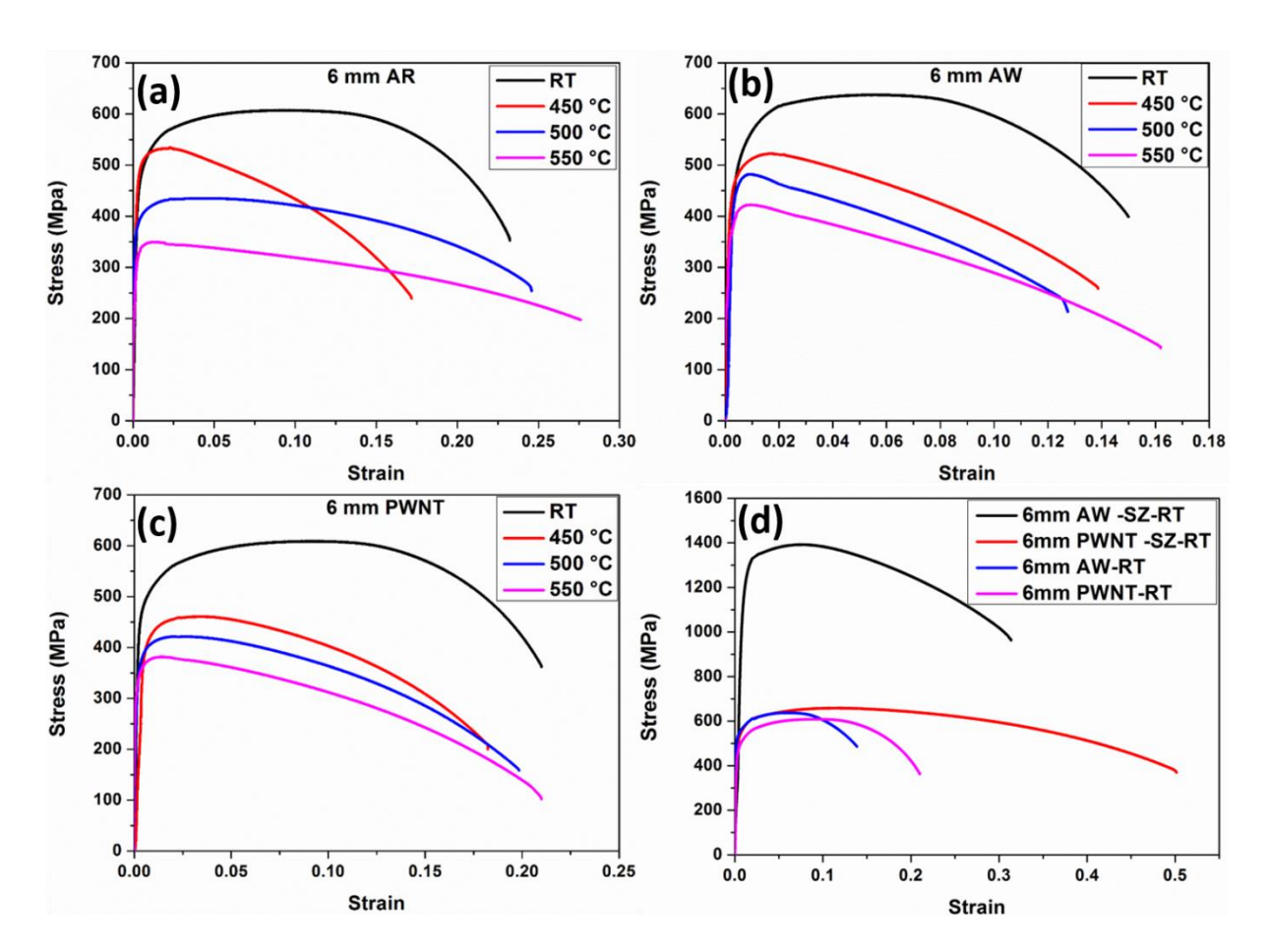


Figure 4.1.11. Stress-Strain plots obtained at various temperatures: (a) As-received, (b) As-welded (c) As welded +PWNT (d) Stir Zone sample tested at RT in as-welded and as-welded +PWNT conditions

(E). Fracture Modes

Irrespective of the material state, fracture at all the temperatures was in ductile transgranular mode characterized by the presence of dimples (micro voids) on the fracture surface. Failure in BM took place in the middle portion of the gauge length. Typical fracture surfaces of BM samples failed at RT, 450 °C, 500 °C and 550 °C are illustrated in Fig. 4.1.12. The size of dimples increased with increasing temperature. The same trend continued in AW and PWNT states except that the fracture in these cases occurred at the interface between the TMAZ and BM within the gauge length. There were no intergranular cavities or cracks in any of the material and test conditions. Figure 4.1.13 demonstrates the prevalence of ductile fracture mode

at 450 °C under conditions that promoted low ductility at intermediate temperatures in AW (Fig.4.1.13a) and PWNT (Fig.4.1.13b) states. The fracture features that prevailed in SZ-alone tests at room temperature in AW and PWNT states are show in Figures 4.1.13c &d. In the base metal where the inclusions are non-existent, microvoids initiated in the areas surrounding the fine carbides of <1 µm. The occasional presence of very few large particles (Figure 4.1.14) acted predominantly as microvoid promoting sites in AW and PWNT states. The EDS analysis of one such particle revealed that these are rich in Cr. Once the cavities were nucleated, deformation assisted growth and their linkage gets established in the necked region as illustrated in Figure 4.1.15.

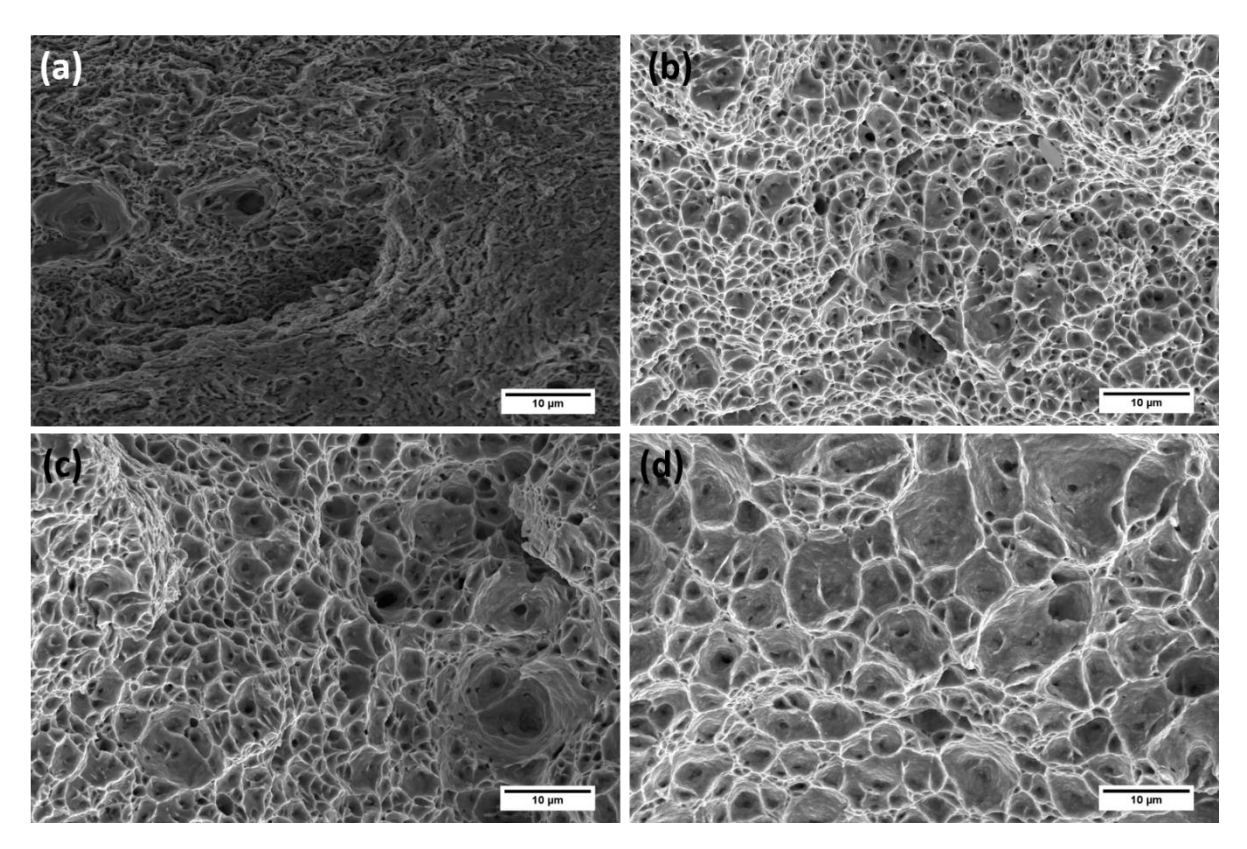


Figure 4.1.12. Fractographs of as-received samples tested at different conditions (a) RT, (b) $450 \, ^{\circ}\text{C}$, (c) $500 \, ^{\circ}\text{C}$, (d) $550 \, ^{\circ}\text{C}$ respectively

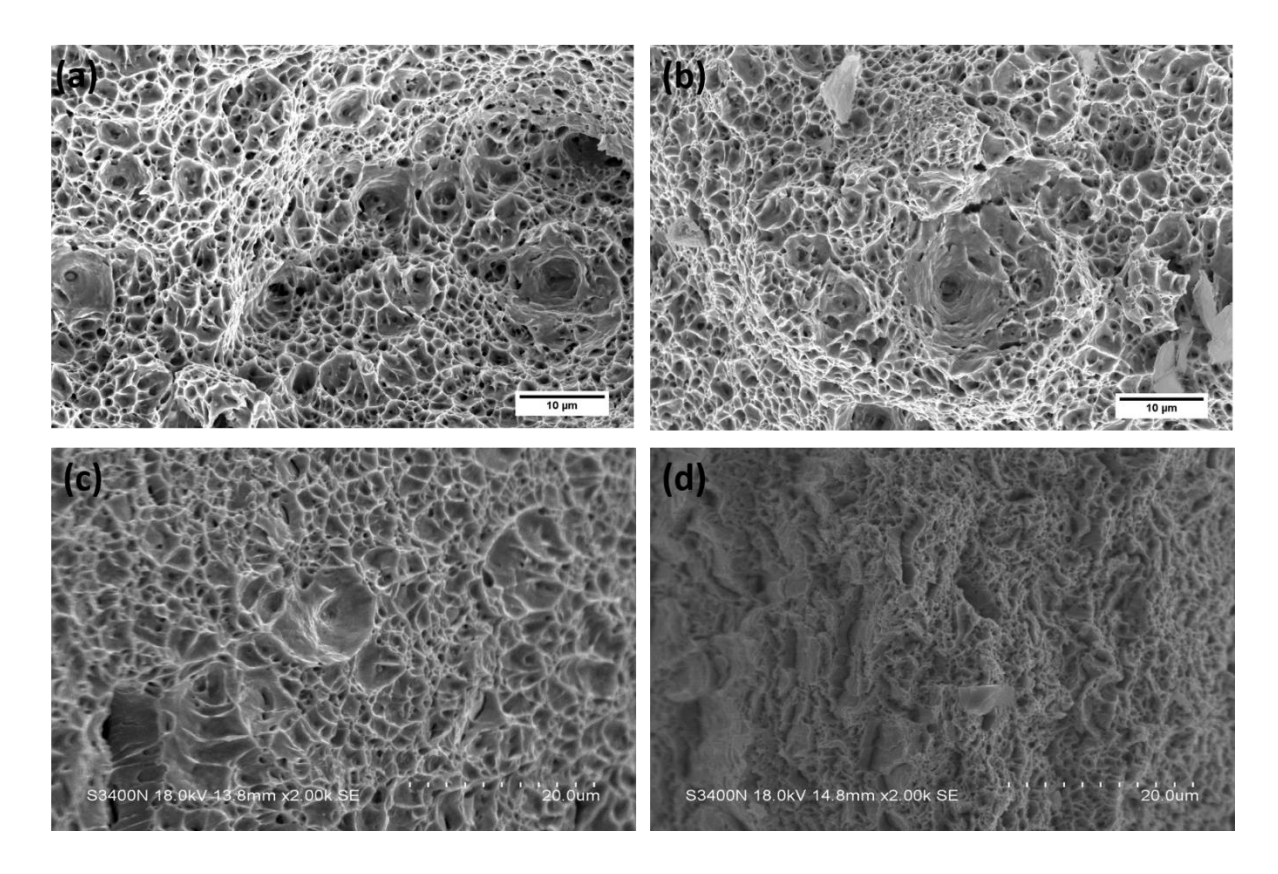


Figure 4.1.13: Ductile fracture characterized by dimples: (a) As-Welded and tested at 450°C, (b) PWNT tested at 450°C, (c) SZ-alone in as-welded condition and tested at RT, and (d) SZ-alone in PWNT condition and tested at RT.

89

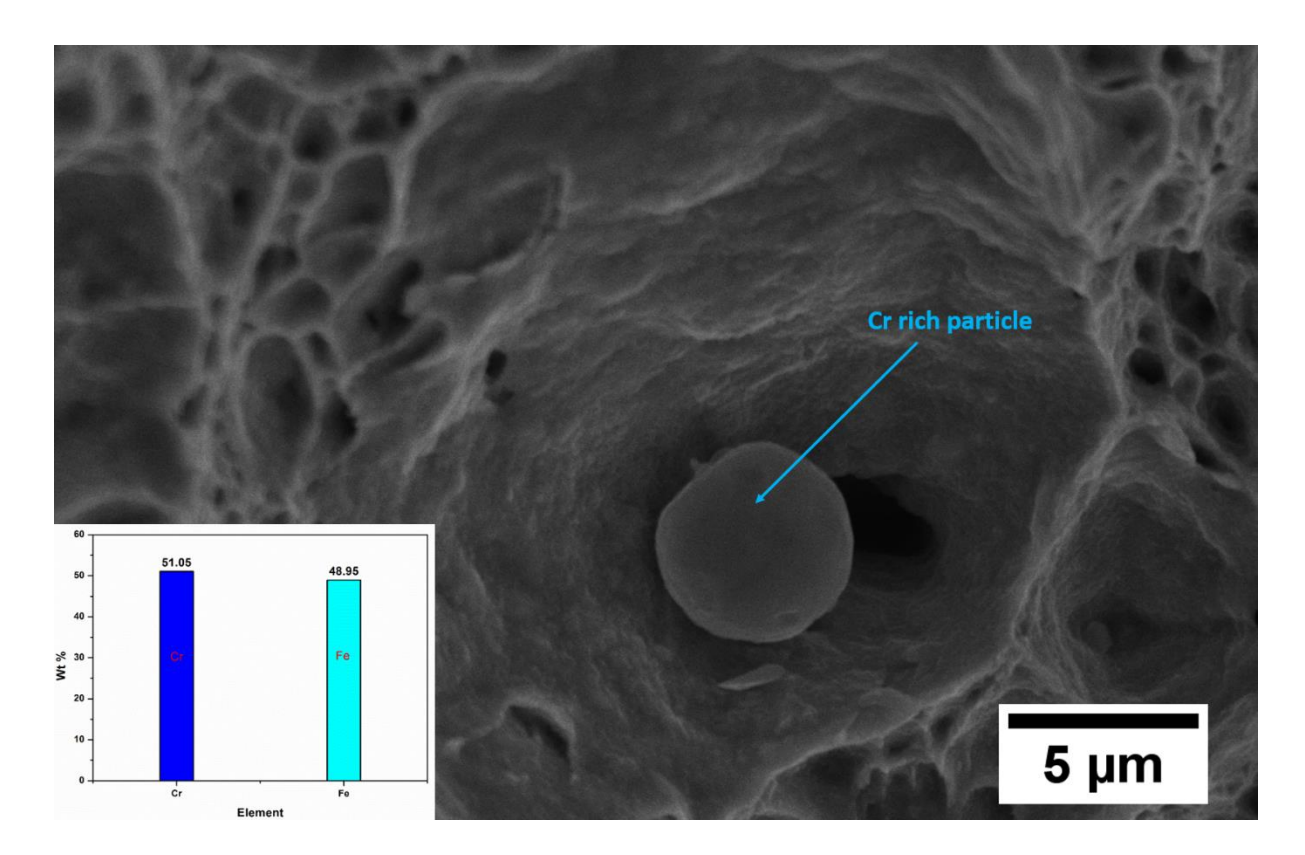


Figure 4.1.14: Large microvoid surrounding chromium rich particle in PWNT state at 450°C.

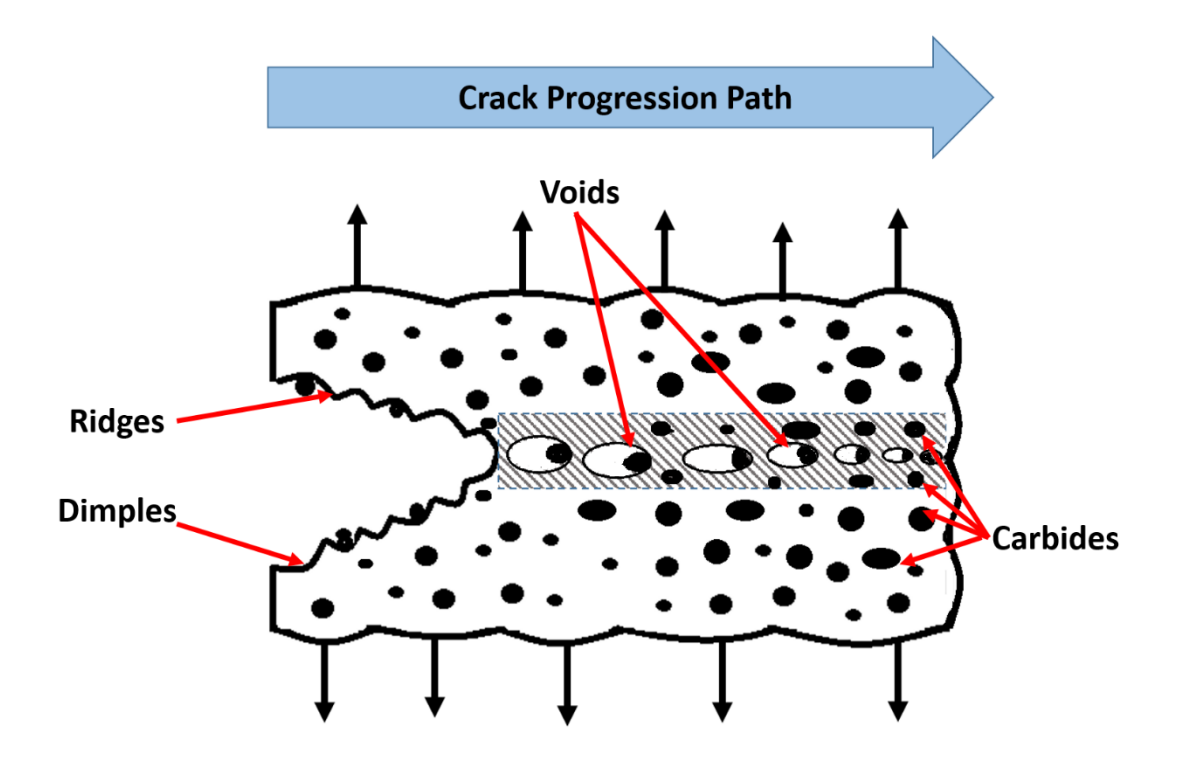


Figure 4.1.15. Schematic of crack initiation and propagation in tensile tests leading to the occurrence of dimples on fracture surface. (Redrawn based on the schematic given in [30])

4.1.4 Discussion

(A). Evolution of microstructure and its impact

RAFM steels derive strength from the combined effects of solid solution strengthening, precipitation hardening from the intra- and intergranular carbides, transformation induced relatively stable martensite lath structure, dislocation-dislocation and dislocation-particle interactions. Very fine MX particles appears to have inherent resistance against coarsening and act as barriers for dislocation movement in the matrix at elevated temperatures and also beneficial for imparting the impact toughness [18, 20]. The disappearance of M₂₃C₆ on prior austenite grain boundaries in SZ of AR state is detrimental. The non-existence of grain boundary carbides could accelerate grain boundary sliding, and as a consequence may develop intergranular cavities and cracks promoting intergranular fracture. As a result, the AW alloy can suffer from poor high temperature ductility, creep and creep-fatigue interaction resistance during service.

It is necessary to understand the factors contributing to the dissolution of M₂₃C₆ particles in SZ and its consequence. Investigations conducted earlier on this steel employing Differential Scanning Calorimeter established various phase transformation temperatures as detailed in Table 4.1.3 [11]. The most important parameter that determines the microstructure in SZ is the peak temperature seen during FSW, which in turn would depend upon the tool rotational speed. Detailed investigations performed by Manugula et.al [18] by non-contact in-line thermography enabled to determine the interface temperature between the bottom surface of the tool shoulder and top surface of the work piece. The peak temperature seen at the interface corresponds to the near-surface temperature of the work piece. The similar microstructures found in the surface-near regions at the top and bottom as well as in the middle locations of the 6 mm plate confirmed that the peak temperature in SZ is almost same and further no temperature gradient existed from top to bottom of the 6 mm thick plate. The interface temperatures for 200, 300 and 500, and 700 rpm conditions were respectively below Ac₁, between Ac₁ and Ac₃, and above Ac₃ [18, 20]. From these observations it is inferred that, the temperature experienced by the SZ at 200 rpm employed in this study is around 500 °C. This temperature is much lower than the dissolution temperature of M₂₃C₆ and therefore the disappearance of these precipitates in SZ should not be expected. It seems that M₂₃C₆ precipitates during FSW deformation undergo fragmentation, causing them to be sub-critical and leading to solid state dissolution, thereby leaving behind a matrix enriched with chromium and carbon, and simultaneously making grain boundaries devoid of these carbides. The inelastic deformation involved during FSW creates a

large number of dislocations and non-equilibrium vacancies in the SZ. These vacancies and other lattice defects would cause the accelerated diffusion of interstitial carbon atoms promoting Fe₃C nucleation on the dislocations. In order to further understand microstructure development in AW state across the weld joint, microhardness measurements were made on transverse cross section in the mid thickness zone (Figure 4.1.16). The SZ exhibited very high hardness. In the past, the high hardness in the SZ has been attributed to the presence of the lath martensite in conjunction with coarsened prior austenite grains [18-20]. Such a microstructure would result at tool rotational speeds higher than 700 rpm, where the peak temperatures in SZ exceed Ac₃. Air cooling from austenite phase field (above Ac₃) promotes lath martensite. At 200 rpm, the peak temperature attained in SZ is much below Ac₁, hence no transformation to austenite and subsequently the transformation to lath martensite is expected during FSW. However, the increased dislocation density, the fine dispersion of Fe₃C and MX type carbides that have escaped destruction and dissolution, and matrix enriched with substitutional and interstitial elements appears to contribute to high hardness in SZ. Since the high hardness would degrade toughness and creep resistance in the AW structure, PWNT is indeed needed to restore the microstructure and mechanical properties in the weld zone to the level shown by BM. As the distance from SZ increased, a rapid fall in hardness occurred in TMAZ until it touched the hardness profile of unaffected BM (Figure 4.1.16). The decreasing peak temperature experienced in the TMAZ, as it moves from SZ towards BM, determines the rapid reduction in hardness. It is to be pointed out that there is no dip in hardness at the interface between TMAZ and BM, which confirms the absence of HAZ [Figure 4.1.16]. The pronounced HAZ with hardness much less than 200 VPN has been reported at rotational speeds higher than 300 rpm. The HAZ gets pronounced when the temperature seen by BM is in the intercritical temperature range (between Ac₃ and Ac₁), leading to a mixture of ferrite and martensite in HAZ. In some cases, when the peak temperature lies just below Ac₁, over tempering of M₂₃C₆ can occur with associated coarsening in the HAZ adjoining the BM. These microstructural changes promote a soft HAZ which get reflected in the form of a dip in hardness between TMAZ and BM. Since at 200 rpm, the peak temperature is much below Ac₁, none of the above mechanisms operated and therefore HAZ was absent. The base metal region in AW samples, which is not affected by the heat of the welding or the mechanical deformations of the stirring, has a microstructure that is similar to that of the material in the AR condition. At the end of PWNT treatment the alloy generated slightly finer microstructural constituents (Figures 4.1.8-10) with narrow distribution of grain size and restored the hardness across the transverse cross section to the level of BM (Figure 4.1.16). The carbides on grain and lath boundaries re-appeared after PWNT, which is considered to be a desirable phenomenon.

Sl. No.	Transformation Temperature with reference to Fe-C diagram	Centigrade, °C
1	Melting Temperature	1518 ± 5
2	Martensite Start, M _s	367 ± 5
3	Martensite Finish, M _f	310 ± 5
4	Recrystallization Temperature (0.4 Tm)	443 ± 5
5	Austenite Start, Ac ₁	818 ± 5
6	Austenite Finish, Ac ₃	857 ± 5

Table 4.1.3: Phase transformation temperatures of INRAFM steel [11]

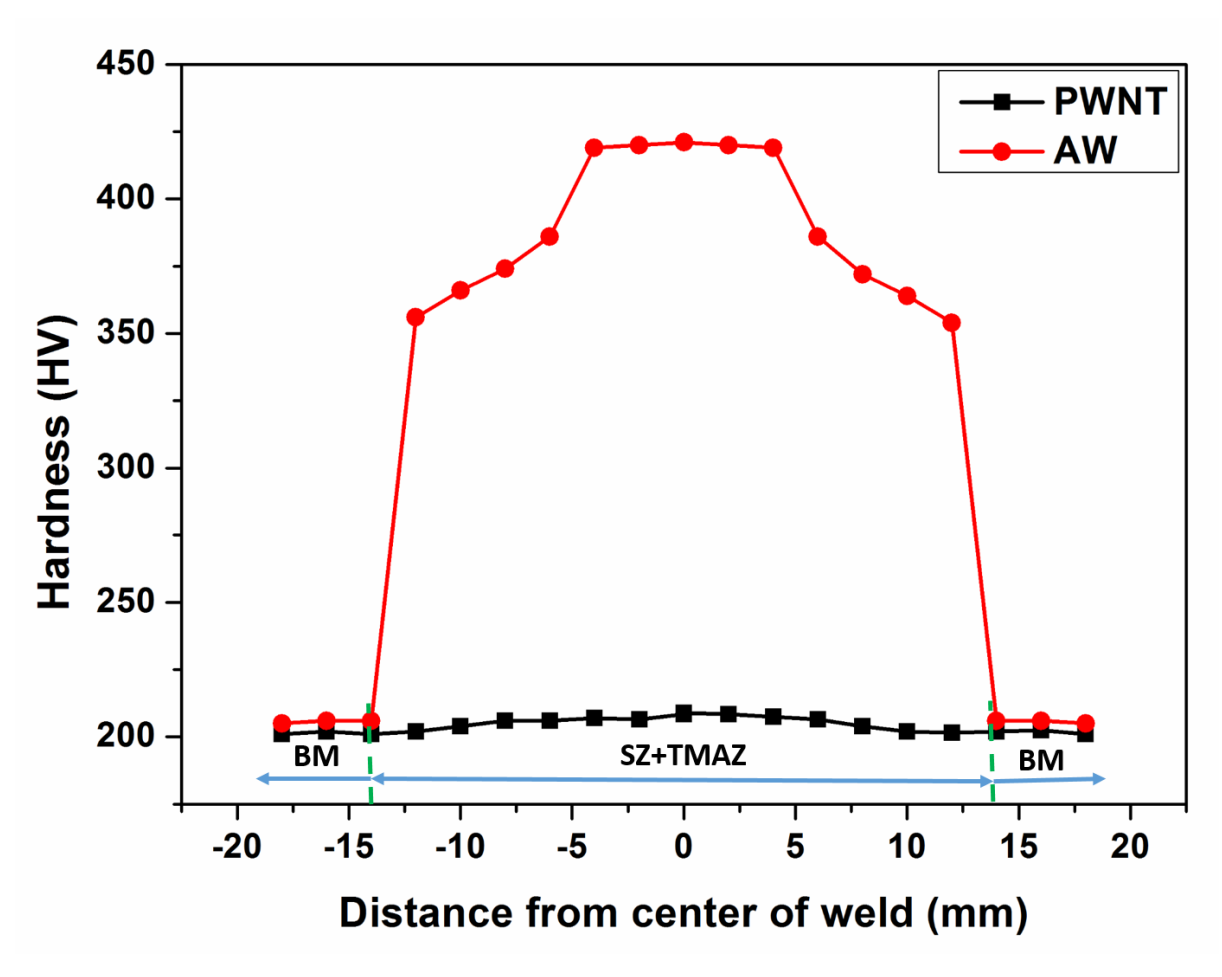


Figure 4.1.16: Microhardness profile of 6 mm weldment in AW and PWNT states

(B) Tensile deformation and properties

In all the states at RT, the alloy exhibited monotonic strain hardening in the early stages followed by a regime of nearly stable saturation stress which continued till the softening commenced towards the end of test (Figure 4.1.11). At temperatures ≥450 °C, the tensile stress−

strain flow curves displayed a relatively short period of rapid strain hardening until UTS is reached, followed by a prolonged period of softening. RAFM steels in the normalised and tempered state contain high dislocation density. The stress response during the progression of tensile deformation at a given temperature depends critically on the evolving microstructure. The main microstructural features in INRAFM steel that can influence the stress response include the dislocation density, lath size of tempered martensite, size and distribution of carbides. The initial strain hardening at all the temperatures can be attributed to dislocationdislocation and dislocation-precipitate interactions. The carbides are considered to be very effective in pinning the dislocations when their size is extremely small. The tensile tests performed at ≤ 550 °C are not so conducive to coarsening of fine carbides. However, at ≥ 450 °C, as the tensile test progresses, the density of dislocations appears to decrease due to either annihilation of dislocations or recovery and recrystallization effects. The later get manifested by the occurrence of cells and sub-grains at temperatures ≥450 °C explaining the softening effect. It may be noted that the elevated temperature tensile tests are above the recrystallization temperature (443±5 °C, Table 4.1.3). At room temperature, the balance between the strain hardening effects and annihilation of dislocations leads to the saturation stress response until the microvoid generation and their linkage sets in towards the end of tensile test.

The alloy exhibited reduction in ductility at intermediate temperatures. Based on the detailed investigations conducted on temperature dependence of tensile properties in the range 25–650 °C in the AR state [21], the loss of ductility at intermediate temperatures has been ascribed to the operation of dynamic strain ageing (DSA) process. DSA has been considered to result from the attractive interaction between diffusing solute species in the alloy and mobile dislocations during the deformation [22, 23]. Ageing of mobile dislocations by solute atmospheres would occur either during quasi viscous type of dislocation motion [24] or during the period when the dislocations are temporarily held up at local obstacles in the glide plane [25, 26]. In this investigation, the alloy displayed smooth stress-strain curves at all the temperatures without evidence for serrated flow, which is considered to be one of the generally observed manifestations of DSA. The non-existence of serrated flow has also been reported earlier in the tensile tests performed over a wide temperature range on this RAFM steel [21, 27]. The reduction in the tensile strength at high temperatures with reduction in tensile elongation at intermediate temperatures (200-500 °C) and the subsequent increase at higher temperature have also been observed earlier in RAFM steels [10,21,27,28]. The temperature dependence of tensile properties exhibited similar trends in Mod.9Cr-1Mo steel [29, 30] from which INRAFM

steel was coined. In case of ferritic-martensitic steels which show prolonged period of softening at elevated temperatures, it can be presumed that the serrated flow the characteristic feature of DSA will not be displayed. In spite of minimum ductility due to DSA, the fracture mode remained transgranular.

(C) Origin of strengthening

The detailed study of various strengthening mechanisms which contribute to the yield strength of the material in the AW and PWNT states has been attempted. The strengthening mechanisms operating in the SZ region was investigated by calculating the contribution of each mechanism to the strengthening process. Since TMAZ is small, no attempt has been made to fabricate the tensile test samples by incorporating TMAZ region alone. The main strengthening mechanisms that affect the deformation behaviour include solid solution strengthening, Precipitation hardening, grain boundary strengthening, dislocation strengthening and the Peierls –Nabarro strengthening [31]. Martensitic lath boundaries are the major component that contributes to the boundary strengthening in RAFM steels with respect to the yield strength [32]. The following equation which considers the width of the lath boundary and the Burgers vector, is used to calculate the grain boundary strengthening [33].

$$\sigma_{\rm gb} = \text{M.G.b/}\lambda_{\rm ml}$$
(1)

M is the Taylor factor (M=3)

G is the shear modulus of pure iron (81GPa)

b is the magnitude of the Burgers vector of SZ (0.312 nm)

 λ_{ml} is the average width of martensite laths (AW=700nm, PWNT=900nm).

Two types of carbides, $M_{23}C_6$ and MX are the types of precipitates that contribute to the precipitation strengthening process. The following equation was used to calculate the precipitation strengthening according to the Orowan bypass mechanism model [33].

$$\sigma_p = 0.8 \text{ x M.G.b/}\lambda p \dots (2)$$

Where,

M is the Taylor factor (M=3)

G is the shear modulus of pure iron (81GPa)

b is the magnitude of the Burgers vector of SZ(AW=0.312 nm, PWNT=0.340)

 λ_p is the average spacing of precipitates in the slip plane.

Chapter 4.1

$$\lambda_p = 1/\sqrt{N_i}$$

Where N_i is the number density of all precipitates (AW=4.681 μ m-2, PWNT=19.84 μ m-2)

Solid solution strengthening is a combined contribution of the interstitial elements and the substitutional elements. For interstitial elements like C, N the following equation can be used [34].

$$\sigma_i$$
= 1722.5 $X_i^{1/2}$ (3)

Where,

 X_i is the concentration of interstitial elements at equilibrium in wt % (C=0.077).

For substitutional elements the following equation can be used [34].

$$\sigma_s = 0.00689 \text{ k}_s.X_s^{3/4} \dots (4)$$

Where,

 X_s is the concentration of substitutional elements at equilibrium in atomic %.

 K_s is the strengthening coefficient of different substitutional elements.

$$\sigma_{ss} = \sigma_{i+} \sigma_{s} \ldots (5)$$

The different substitutional elements and their strengthening coefficients are given in Table 4.1.4 [35]. Elements with negligible concentration are omitted.

Table 4.1.4. Strengthening coefficient of substitutional elements

Sl.No.	Element	Atomic %	Strengthening
			coefficient
1	Mn	0.537	7000
2	Si	0.021	11000
3	Cr	9.13	1400
4	Ni	0.018	6100
5	Mo	0.002	9600
6	V	0.246	4000
7	W	1.36	11000

Dislocation strengthening is estimated by considering the dislocation density of the SZ region. This has been done using a fine XRD analysis using a step size of 0.02°/s. The Taylor method was used to estimate the dislocation strengthening using the following equation [36-38].

$$\sigma_d = \alpha_2 M.G.b.\sqrt{\rho_d}$$
 (6)

Where,

 α_2 is the material-dependent constant (0.38 for polycrystalline iron)

M is the Taylor factor (M=3)

G is the shear modulus of pure iron (81GPa)

b is the magnitude of the Burgers vector of SZ(0.312 nm)

 ρ_d is the dislocation density (7.7 x 10^{13} nm⁻²)

Dislocation density was calculated from XRD done at the SZ region using equation (7) [39].

$$\rho = \frac{2\sqrt{3}.\varepsilon}{d.b} \qquad (7)$$

Where,

 ε is the lattice strain

d is the grain size

The Peierls-Nabarro stress (σ_0) or the frictional stress can be defined as the friction stress experienced while trying to move the dislocations along the ideal lattice. Its value is adopted to be 53.9 MPa according to previous studies in RAFM steels [35, 40-42].

The contribution from each of the above strengthening mechanism to the yield strength of the SZ region in the AW and PWNT conditions was calculated and is shown graphically in Figure 4.1.17. The yield strength of the AW condition estimated theoretically is 1217 MPa and it matches closely with the experimental result of 1154 MPa (Fig.4.1.11d). In the PWNT condition the theoretical value is 688 MPa and experimental value is 659 MPa (Fig.4.1.11d). It can be seen that in the AW condition where there are dissolved carbides the contribution of the solid solution strengthening (σ_{ss}) is the highest. After the PWNT process where the dissolved carbides re-precipitate, the strength contribution due to solid solution strengthening declined. The high tensile elongation of the PWNT condition is derived from the combined effects of decreased dislocation density and the decreased solid solution strengthening.

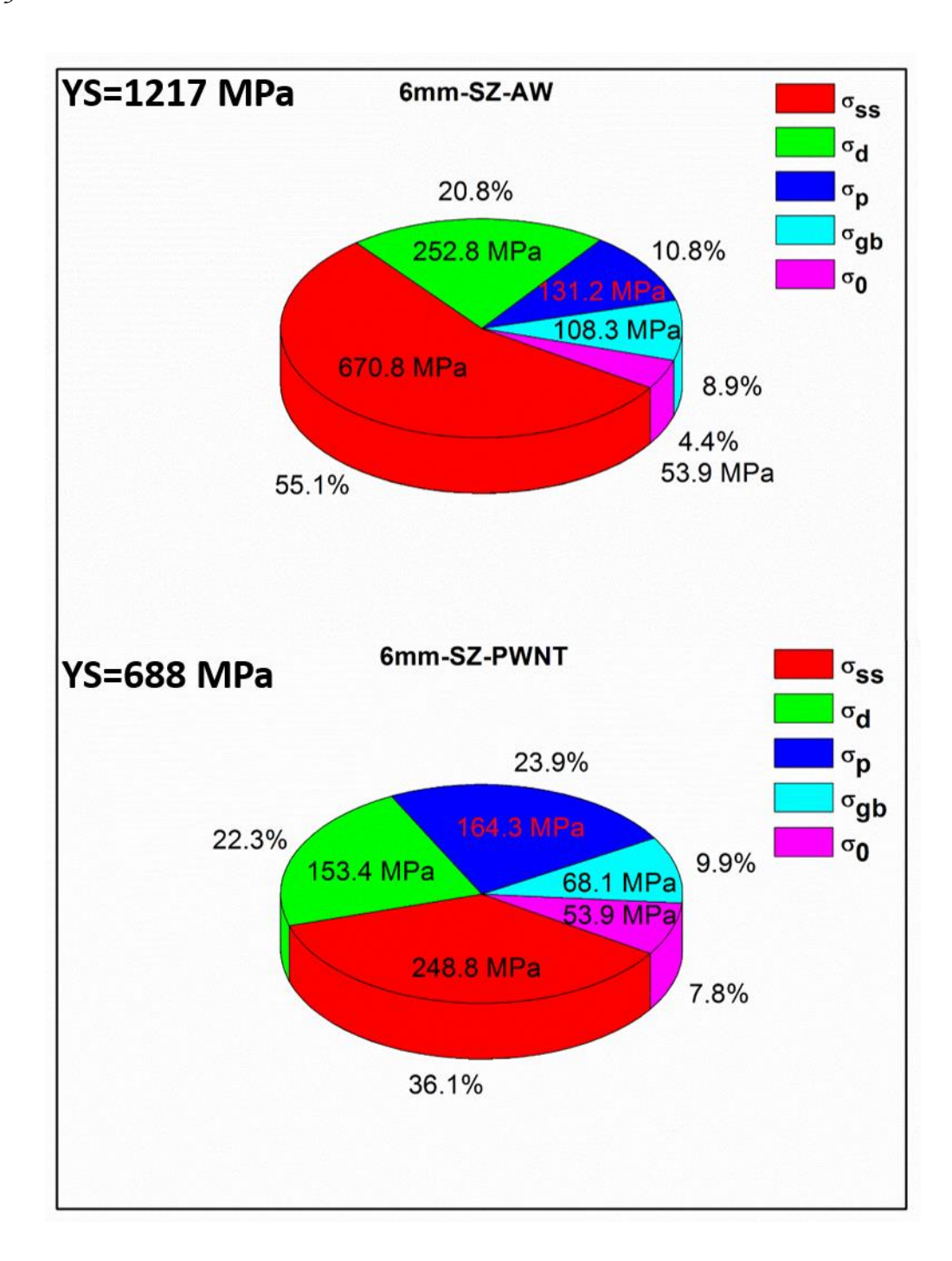


Figure 4.1.17. Contribution of different strengthening mechanisms of RAFM steel employed in the present study.

5. Conclusions

- The friction stir welding of a reduced activation ferritic-martensitic steel has been successfully performed on 6 mm thick plates employing PcBN tool. At the tool rotational speed of 200 rpm defect-free bead-on-plate welds were obtained.
- The as-received base metal microstructure revealed tempered martensite (alpha-ferrite + carbides) comprising of prior austenite grain boundaries and martensite lath boundaries decorated with discrete M₂₃C₆ particles in addition to very fine MX precipitates in intragranular regions.
- FSW joint contained SZ, TMAZ and unaffected BM. In the SZ and TMAZ significant changes in microstructure occurred; solid state dissolution of M₂₃C₆ and precipitation of brittle Fe₃C took place. No fresh martensite could be found in SZ in the as-welded state though the dislocation density is high. BM structure remained unaffected in the as-welded state.
- In the as-welded state, the FSW joint displayed very high hardness in SZ with a rapid fall in hardness across TMAZ. Both SZ and TMAZ were softened to the level of BM by post weld normalising and tempering treatment. This treatment enabled the reprecipitation of desirable carbides on grain and martensite lath boundaries in SZ and TMAZ, with complete elimination of Fe₃C from SZ. The microstructure after PWNT was more homogeneous and resembled that of BM with perceptible change in grain size distribution in SZ due to the impact of recrystallization process.
- Tensile tests performed at room temperature and at 450 °C, 500 °C and 550 °C in AR, AW and PWNT states indicated the decrease in 0.2% offset yield strength and ultimate tensile strength with raise in temperature. Alloy showed higher strength in the AW state due to high dislocation density and the presence of Fe₃C in SZ. The ductility was low in AW state but improved after PWNT treatment. The low ductility in all the states at an intermediate temperature has been ascribed due to intervention of dynamic strain ageing effects. Alloy displayed transgranular ductile fracture with signature of dimples irrespective of temperature and material state.
- In order to study the tensile behavior of the SZ specifically, tensile specimens were extracted separately from the stir zone region. The SZ-alone showed higher strength in AW state and high ductility (~50%) in the PWNT state at room temperature. The deformation in weld joint at room temperature was constrained by other constituents

and the recovery and recrystallization effects contributing to high ductility of SZ-alone have not been fully realised.

• The yield strength of the SZ region was estimated using mathematical calculations of the operating strengthening mechanisms. These results match with the experimental results obtained.

^{*}This section is communicated as a manuscript to MSEA and is under review (MSEA-D-22-00102).

References

- [1] H. Tanigawa, K. Shiba, A. Möslang, R.E. Stoller, R. Lindau, M.A. Sokolov, G.R. Odette, R.J. Kurtz, S. Jitsukawa, Status and key issues of reduced activation ferritic/martensitic steels as the structural material for a DEMO blanket, J. Nucl. Mater. 417 (2011) 9–15. https://doi.org/10.1016/j.jnucmat.2011.05.023.
- [2] V.K. Sikka, Development of modified 9Cr-1Mo steel for elevated temperature service, Proc.AIME topical Conf.Ferritic Alloys for use in Nuclear Energy Technologies, Snowbird, Utah (1983), Eds.Davies JW, Michael DJ, 317-327
- [3] N. Baluc, D.S. Gelles, S. Jitsukawa, A. Kimura, R.L. Klueh, G.R. Odette, B. van der Schaaf, J. Yu, Status of reduced activation ferritic/martensitic steel development, J. Nucl. Mater. 367-370 A (2007) 33–41. https://doi.org/10.1016/j.jnucmat.2007.03.036.
- [4] H. Tanigawa, T. Hirose, K. Shiba, R. Kasada, E. Wakai, H. Serizawa, Y. Kawahito, S. Jitsukawa, A. Kimura, Y. Kohno, A. Kohyama, S. Katayama, H. Mori, K. Nishimoto, R.L. Klueh, M.A. Sokolov, R.E. Stoller, S.J. Zinkle, Technical issues of reduced activation ferritic/martensitic steels for fabrication of ITER test blanket modules, Fusion Eng. Des. 83 (2008) 1471–1476. https://doi.org/10.1016/j.fusengdes.2008.07.024.
- [5] J. Yu, Q. Huang, F. Wan, Research and development on the China low activation martensitic steel (CLAM), J. Nucl. Mater. 367-370 A (2007) 97–101. https://doi.org/10.1016/j.jnucmat.2007.03.236.
- [6] Q. Huang, C. Li, Y. Li, M. Chen, M. Zhang, L. Peng, Z. Zhu, Y. Song, S. Gao, Progress in development of China Low Activation Martensitic steel for fusion application, J. Nucl. Mater. 367-370 A (2007) 142–146. https://doi.org/10.1016/j.jnucmat.2007.03.153.
- [7] B. Van Der Schaaf, D.S. Gelles, S. Jitsukawa, A. Kimura, R.L. Klueh, A. Möslang, G.R. Odette, Progress and critical issues of reduced activation ferritic/martensitic steel development, J. Nucl. Mater. 283–287 (2000) 52–59. https://doi.org/10.1016/S0022-3115(00)00220-8.
- [8] B. Raj, K.B.S. Rao, A.K. Bhaduri, Progress in the development of reduced activation ferritic-martensitic steels and fabrication technologies in India, Fusion Eng. Des. 85

- (2010) 1460–1468. https://doi.org/10.1016/j.fusengdes.2010.04.008.
- [9] J.F. Salavy, I.V. Boccaccini, P.Chaudhuri, S.Cho, M.Enoeda, L.M.Ginacarli, R.J. Kurtz, T.Y. Luo, K. Bhanu Sankara Rao, C.P.C. Wong, Must we use ferritic steel in TBM?, Fus.Eng.Des. 85 (2010) 1896-1902
- [10] K. Laha, S. Saroja, A. Moitra, R. Sandhya, M.D. Mathew, T. Jayakumar, E. Rajendra Kumar, Development of India-specific RAFM steel through optimization of tungsten and tantalum contents for better combination of impact, tensile, low cycle fatigue and creep properties, J. Nucl. Mater. 439 (2013) 41–50. https://doi.org/10.1016/j.jnucmat.2013.03.073.
- [11] S. Raju, B. Jeya Ganesh, A.K. Rai, R. Mythili, S. Saroja, E. Mohandas, M. Vijayalakshmi, K.B.S. Rao, B. Raj, Measurement of transformation temperatures and specific heat capacity of tungsten added reduced activation ferritic-martensitic steel, J. Nucl. Mater. 389 (2009) 385–393. https://doi.org/10.1016/j.jnucmat.2009.02.030.
- [12] V.L. Manugula, K. V. Rajulapati, G.M. Reddy, K.B.S. Rao, Role of evolving microstructure on the mechanical properties of electron beam welded ferriticmartensitic steel in the as-welded and post weld heat-treated states, Mater. Sci. Eng. A. 698 (2017) 36–45. https://doi.org/10.1016/j.msea.2017.05.036.
- [13] S. Sam, C.R. Das, V. Ramasubbu, S.K. Albert, A.K. Bhaduri, T. Jayakumar, E. Rajendra Kumar, Delta ferrite in the weld metal of reduced activation ferritic martensitic steel, J. Nucl. Mater. 455 (2014) 343–348. https://doi.org/10.1016/j.jnucmat.2014.07.008.
- [14] P.Aubert, F.Tavassoli, M.Rieth, E.Diegele, Y.Poitevin, Review of candidate welding processes of RAFM steels for ITER test blanket modules and DEMO, J. Nucl. Mater. 417 (2011) 43-50
- [15] C.R. Das, S.K. Albert, S. Sam, P. Mastanaiah, G.M.S.K. Chaitanya, A.K. Bhaduri, T. Jayakumar, C.V.S. Murthy, E.R. Kumar, Mechanical properties of 9Cr-1W reduced activation ferritic martensitic steel weldment prepared by electron beam welding process, Fusion Eng. Des. 89 (2014) 2672–2678. https://doi.org/10.1016/j.fusengdes.2014.07.001.

- [16] R.S. Mishra, Z.Y. Ma, Friction stir welding and processing, Mater. Sci. Eng. R Reports. 50 (2005) 1–78. https://doi.org/10.1016/j.mser.2005.07.001.
- [17] P.L. Threadgill, A.J. Leonard, H.R. Shercliff, P.J. Withers, Friction stir welding of aluminium alloys, Int. Mater. Rev. 54 (2009) 49–93. https://doi.org/10.1179/174328009X411136.
- [18] V.L. Manugula, K. V. Rajulapati, G.M. Reddy, R. Mythili, K. Bhanu Sankara Rao, Influence of Tool Rotational Speed and Post-Weld Heat Treatments on Friction Stir Welded Reduced Activation Ferritic-Martensitic Steel, Metall. Mater. Trans. A Phys. Metall. Mater. Sci. 48 (2017) 3702–3720. https://doi.org/10.1007/s11661-017-4143-5.
- [19] V.L. Manugula, K. V. Rajulapati, G.M. Reddy, E. Rajendra Kumar, K.B.S. Rao, Friction stir welding of thick section reduced activation ferritic–martensitic steel, Sci. Technol. Weld. Join. 23 (2018) 666–676. https://doi.org/10.1080/13621718.2018.1467111.
- [20] V.L. Manugula, K. V. Rajulapati, G. Madhusudhan Reddy, R. Mythili, K. Bhanu Sankara Rao, A critical assessment of the microstructure and mechanical properties of friction stir welded reduced activation ferritic-martensitic steel, Mater. Des. 92 (2016) 200–212. https://doi.org/10.1016/j.matdes.2015.12.019.
- [21] J. Vanaja, K. Laha, S. Sam, M. Nandagopal, S. Panneer Selvi, M.D. Mathew, T. Jayakumar, E. Rajendra Kumar, Influence of strain rate and temperature on tensile properties and flow behaviour of a reduced activation ferritic-martensitic steel, J. Nucl. Mater. 424 (2012) 116–122. https://doi.org/10.1016/j.jnucmat.2012.02.020.
- [22] K. Bhanu Sankara Rao, M.G. Castelli, J.R. Ellis, On the LCF deformation of Haynes 188 superalloy in the dynamic strain ageing regime, Scripta Metall Mater 33 (1995) 1005.-1012
- [23] K. Bhanu Sankara Rao, M.G. Castelli, G.P. Allen, J.R. Ellis, A critical assessment of the mechanistic aspects in Haynes 188 during LCF in the range 25 C to 1000 C, Metall Mater Trans A 28 (1997) 347-361, https://doi.org/10.1007/s11661-997-0137-z.
- [24]. A.H. Cottrell, Philos Mag 44(1953) 829. https://doi.org/10.1080/ 14786440808520347.
- [25]. A.Van Den Beukel, U.F. Kocks, Acta Metall 30 (1982) 1027. https://doi.org/10.1016/0001-6160(82)90211-5.

- [26] A. Van. Den Beukel, Acta Metall, 28 (1980) 965.
- [27] P. Prakash, J. Vanaja, D.P. Rao Palaparti, G. V. Prasad Reddy, K. Laha, G.V.S. Nageswara Rao, Tensile flow and work hardening behavior of reduced activation ferritic martensitic steel subjected to thermo-mechanical treatment, J. Nucl. Mater. 520 (2019) 19–26. https://doi.org/10.1016/j.jnucmat.2019.04.009.
- [28] M.D. Mathew, J. Vanaja, K. Laha, G. Varaprasad Reddy, K.S. Chandravathi, K. Bhanu Sankara Rao, Tensile and creep properties of reduced activation ferritic-martensitic steel for fusion energy application, J. Nucl Materials, 417(2011)77-80
- [29] B.K. Choudhary, V.S. Srinivasan, M.D. Mathew, Influence of strain rate and temperature on tensile properties of 9Cr-1Mo ferritic steel, Mater. High Temp. 28 (2011) 155–161. https://doi.org/10.3184/096034011X13072941275843.
- [30] B.K. Choudhary, K. Bhanu Sankara Rao, S.L. Mannan, B.P. Kashyap, Serrated yielding in 9Cr-1Mo ferritic steel, Mater. Sci. Technol. 15 (1999) 791–797. https://doi.org/10.1179/026708399101506580.
- [31] J. hua Zhou, Y. feng Shen, and N. Jia, "Strengthening mechanisms of reduced activation ferritic/martensitic steels: A review," *Int. J. Miner. Metall. Mater.*, vol. 28, no. 3, pp. 335–348, 2021.
- [32] K. Maruyama, K. Sawada, and J. I. Koike, "Strengthening mechanisms of creep resistant tempered martensitic steel," *ISIJ Int.*, vol. 41, no. 6, pp. 641–653, 2001.
- [33] L. Tan, L. L. Snead, and Y. Katoh, "Development of new generation reduced activation ferritic-martensitic steels for advanced fusion reactors," *J. Nucl. Mater.*, vol. 478, pp. 42–49, 2016.
- [34] B. C H Young, "Strength of martensite and bainite," *Materials Science and Technology*, vol. 10. pp. 209–214, 1994.
- [35] H. L. Shengli Li, Xinqi Yang, Napat Vajragupta, Wenshen Tang, Alexander Hartmaier, "The influence of post-weld tempering temperatures on microstructure and strength in the stir zone of friction stir welded reduced activation ferritic / martensitic steel," *Mater. Sci. Eng. A*, vol. 814, no. May, 2021.
- [36] G.I. Taylor, "Plastic strain in metals," J. Inst. Met., vol. 62, pp. 307–324, 1938.
- [37] C. Zhu, T. Harrington, G. T. Gray, and K. S. Vecchio, "Dislocation-type evolution in quasi-statically compressed polycrystalline nickel," *Acta Mater.*, vol. 155, no. August, pp. 104–116, 2018.
- [38] G. I. Taylor, "The mechanism of plastic deformation of cystals. Part-1 Theoretical," *Proc. Phys. Soc. A*, vol. 145, no. 855, pp. 362–387, 1934.

- [39] R. S. Ganji, P. Sai Karthik, K. Bhanu Sankara Rao, and K. V. Rajulapati, "Strengthening mechanisms in equiatomic ultrafine grained AlCoCrCuFeNi high-entropy alloy studied by micro- and nanoindentation methods," *Acta Mater.*, vol. 125, pp. 58–68, 2017.
- [40] J. Shen *et al.*, "Microstructural characterization and strengthening mechanisms of a 12Cr-ODS steel," *Mater. Sci. Eng. A*, vol. 673, pp. 624–632, 2016.
- [41] A. Chauhan *et al.*, "Microstructure characterization and strengthening mechanisms of oxide dispersion strengthened (ODS) Fe-9%Cr and Fe-14%Cr extruded bars," *J. Nucl. Mater.* vol. 495, pp. 6–19, 2017.
- [42] N. Kamikawa *et al.*, "Stress-strain behavior of ferrite and bainite with nano-precipitation in low carbon steels," *Acta Mater.*, vol. 83, pp. 383–396, 2015.



CHAPTER 4.2

Characterization of Microstructure and
Mechanical Properties of Friction Stir
Welded Reduced Activation FerriticMartensitic Steel in As-Received, As-Welded
and Post Weld Heat Treated States



4.2.1 Introduction

The research for harvesting energy on a commercial basis from the fusion reactors is being pursued very intensively worldwide. International Thermonuclear Experimental Reactor (ITER) is currently under construction for conducting feasibility studies on the production of fusion energy and screening different concepts utilizing test blanket modules for tritium breeding in a fusion environment. The components of the first wall, diverter, limiters and blanket modules are subjected to high neutron irradiation, in addition to strong thermal, mechanical and electromagnetic loadings. The structural materials also should have the least activation from the consideration of nuclear waste disposal and decommissioning at the end of service. The main task in materials programme for TBMs is to comply with safety conditions by developing reduced activation materials. Several alloys have been suggested to be used in these situations out of which, Reduced Activation Ferritic/Martensitic (RAFM) Steels have been proved to be much propitious because of their proven ability to meet the required microstructure and mechanical properties at operating temperatures of ITER. Majority of the participating countries have developed their own compositions for RAFM steels [1-5]. India has pursued a systematic and comprehensive investigations and frozen the composition of its RAFM steel, and designated it as IN-RAFM steel [6–9]. The composition of IN-RAFM steel was derived from the conventional modified 9Cr-1Mo steel by replacing the highly radiation-sensitive elements Mo, Nb by W and Ta, and exercising strict control over C, N, S, P and other trace and tramp elements [10]. Such control over chemistry was necessary for lowering induced radioactivity [10]. The careful choice of virgin materials with low impurities and melting by VIM and VAR enabled to achieve very low ductile-to-brittle transition temperature, and also parent improved the creep-rupture strength and ductility at elevated temperatures.

The RAFM steel which will be used to manufacture the first wall and blanket structure of a fusion reactor needs to be joined by an appropriate joining method during the manufacturing process. This joining method should not be harming the base metal properties for which the RAFM steel is tailor-made. The conventional fusion welding methods like TIG, MIG, EBW etc., have been investigated and there is considerable change in the microstructure and mechanical properties of the weld compared with the base metal. Moreover, as these welding techniques involve the melting of the parent metal, the presence of δ -ferrite which is a deleterious phase was reported in most of the weldments. Therefore, there is a need for a welding method that can avoid these issues. Friction stir welding (FSW) holds a better promise in this regard. FSW is a solid-state welding process that

doesn't involve the melting of the parent metal. Coalescence is produced by the frictional heat developed between the rotating welding tool and workpiece[11–13]. Obtaining a defect-free weld depends upon the proper choice of tool material, optimization of welding parameters like tool rotation speed, tool traverse speed, tool tilt angle etc.

Studies were carried out [14–16] on the feasibility of FSW of RAFM steel and has optimised the process parameters for 6 mm thick plates. The welding of thicker plates (>6mm) using FSW is a challenging task as the tool rotation speeds required are high in order to create the local softening in thick plates for facilitating the material transport while stirring. Successful FSW joints between 12 mm thick plates have been realized by employing tool rotation speeds of 500 and 900 rpm at a traverse speed of 20 mm.min⁻¹; at these high rotational speeds the heat input was found high and led to higher width of the very soft and undesirable Heat Affected zone (HAZ) [15,17]. The tensile properties of such type of FSW welds have not been explored yet.

In order to avoid very wide and soft HAZ, an attempt has been made in this investigation for producing sound bead-on-plate welds on 12 mm thick RAFM steel at a slow tool rotational speed of 200 rpm. The microstructures in the as-received (AR), as-welded (AW) and Post Weld Heat Treatment (PWHT) conditions in various zones of FSW joint have been evaluated and correlated with the hardness. Changes that occurred in the grain size and substructure evolution in various zones have been studied in detail and reported. The tensile properties of AW and PWHT states at various temperatures on RAFM plates of 12 mm thickness are being reported for the first time.

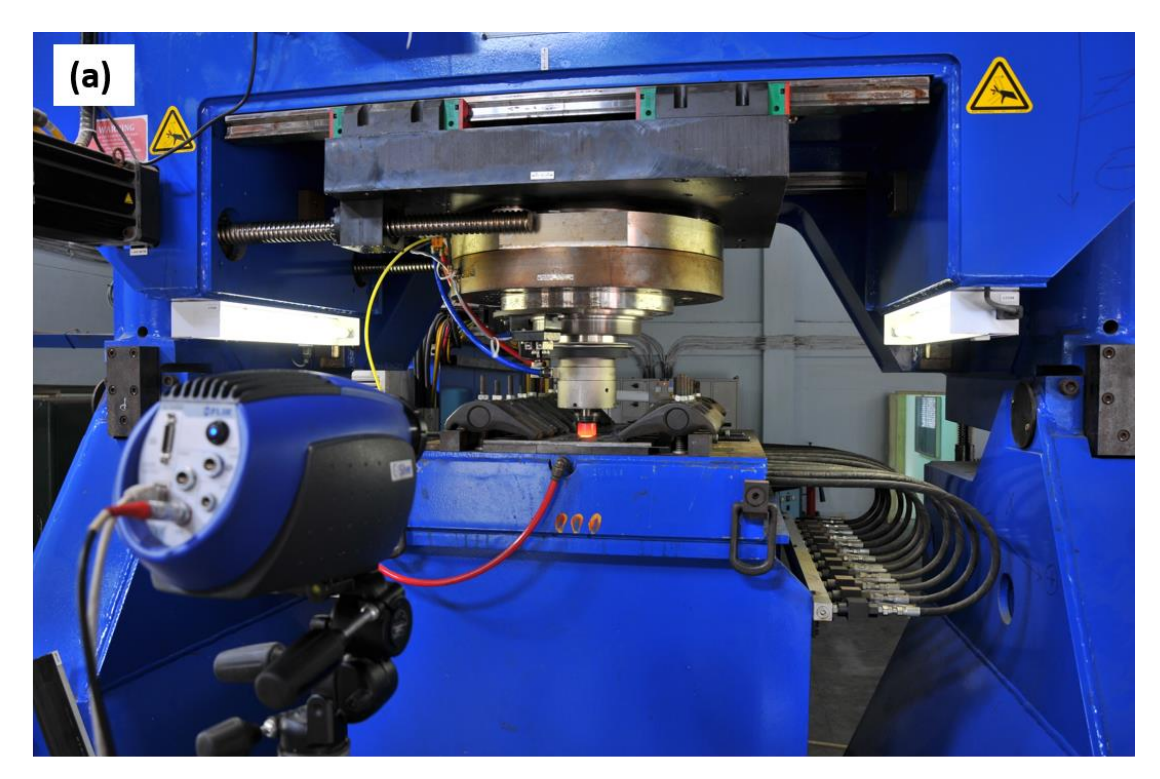
4.2.2 Experimental Details

RAFM steel plates of 12 mm thickness were manufactured at MIDHANI, Hyderabad, India and supplied in bulk to Institute of Plasma Research (IPR) Gandhinagar, India. In the current investigation, 300x300 mm square blanks of 12 mm thickness procured from IPR were utilised. The steel was supplied in normalized (980°C/30 minutes + air cooling) and tempered (760°C/90 minutes + air cooling) condition. The chemical composition of the alloy determined by optical emission spectroscopy technique is shown in Table 4.2.1.

Table 4.2.1: Chemical composition of INRAFM steel used in this investigation

Element	Weight %	Element	Weight %
С	0.077	Ni	0.018
Mn	0.537	Mo	0.002
Si	0.021	Cu	0.001
S	0.002	V	0.246
P	0.004	W	1.360
Со	0.007	Cr	9.130
Та	0.066	Fe	88.602

FSW was carried out with the equipment supplied by Manufacturing Technology Inc., USA in the position control mode (Figure 4.2.1a). Bead-on-plate FSW experiments were performed employing polycrystalline cubic boron nitride tool; the geometry and dimensions of PCBN tool are given in Figure 4.2.1b. All FSW beads were obtained by employing the tool rotating speed of 200 rpm, with a tool traverse speed of 15 mm.min⁻¹ and tilt angle of 2°. The chosen tool traverse speed produced welds without defects and also ensured no damage to the tool. The FSW bead surface was protected during welding by providing argon gas shielding. Figure 4.2.2a depicts a macrograph revealing various zones (SZ, TMAZ, HAZ and BM) in the transverse cross section of FSW joint.



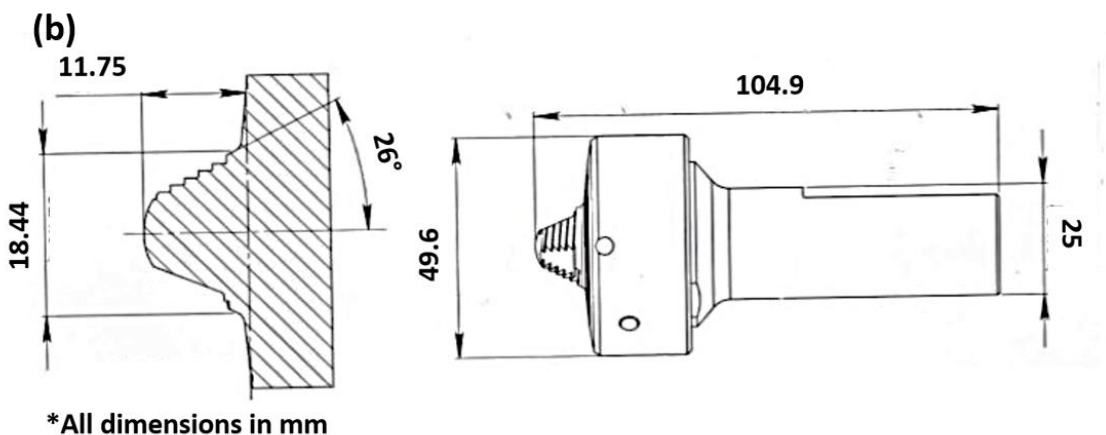


Figure 4.2.1: (a) Friction stir welding setup, (b) Geometry of polycrystalline cubic boron nitride tool

Etching was performed using Villela's reagent (100ml Ethanol, 5ml HCl, 1g picric acid) on mirror polished samples to observe the post-weld microstructure using optical and FESEM techniques. Electron micrographs were obtained using FEI- Nova nano-SEM 450 machine. The Vickers hardness of the weldment was studied using a machine manufactured by M/s. Tinus Olsen. Indents at regular intervals towards both sides from the centre of the weld were taken. TEM samples were prepared by polishing the weldment to a thickness of 100 microns using emery papers of different

grit sizes. The thinned weldment was punched to discs of 3 mm diameter, and were subjected to dimpling using a GATAN dimple grinder (Model: 623). The dimpled discs were milled in a GATAN precision ion polishing system (PIPS). These discs were subjected to Transmission Electron Microscopy (TECHNAI FEI G2 S-Twin) at an accelerating voltage of 200keV.

The welded plates were subjected to Post Weld Normalizing followed by Tempering (PWNT) heat treatment; in which the plates are heated to the solutioning temperature of 980° C and soaked for 30 minutes and then air-cooled. After this, a tempering treatment at 760° C is given for 90 minutes followed by air cooling. The optimum parameters for PWNT were established earlier for this alloy [14]. Nabertherm muffle furnace (Model: LT 15/13) which has a temperature accuracy of $\pm 1^{\circ}$ C was used for the heat treatments.

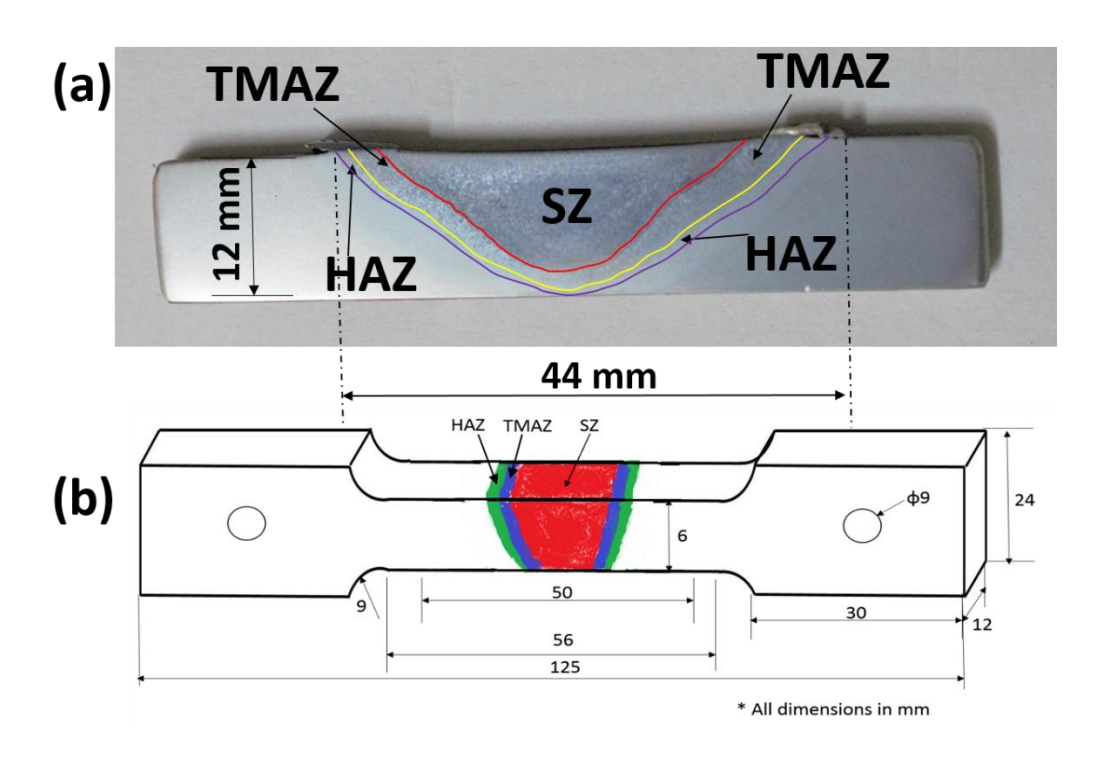


Figure 4.2.2. (a) Various zones in the friction stir welded bead-on-plate of 12mm thickness,

(b) Geometry of tensile testing specimen

Tensile specimens according to the ASTM E8-M standard were machined from the AR, AW and PWNT plates using EDM wire-cut method. The machined specimens were ground for better surface finish and dimensional homogeneity. Figure 4.2.2b shows the dimensions of the tensile specimen used in this study. The gauge portion of tensile samples was composed of SZ, TMAZ, HAZ and

BM. Tensile testing was carried out employing Instron 5982 UTM with a maximum capacity of 100kN. Appropriate extensometers were used to accurately measure the elongation in the gauge length region. Tensile tests were carried out at room temperature and at 450, 500, 550 °C in AR, AW and PWNT states. The fractured samples were observed under SEM in order to obtain the information on the characteristics of failure.

EBSD analysis was done on the samples in the AW and PWNT states in the constituent zones. FE-SEM equipped with an EBSD detector manufactured by EDAX was used for this study. The samples were hot mounted using Bakelite powder and vibratory polishing using colloidal silica of particle size 0.05 microns was given for 14 hours in a vibratory polishing machine manufactured by QATM, Germany; before EBSD mapping. Fraction of high angle grain boundaries and low angle grain boundaries were deduced in the AR, AW, and PWNT conditions in different zones; the variation in these fractions between BM, AW and PWNT were analysed to explain the mechanical property variations.

4.2.3 Results and Discussion

(A) Initial Microstructure

The microstructure in AR state consisted of tempered lath martensite as revealed in Figure 4.2.3. The discrete precipitates on grain boundaries were identified as chromium rich $M_{23}C_6$ type carbides while the intragranular regions displayed both $M_{23}C_6$ type carbides and fine MC or carbonitrides rich in V or Ta (Figure 4.2.3 a &b). In general, the lath boundaries in intragranular regions were found decorated with $M_{23}C_6$. The high creep resistance of tempered lath martensite structure has been attributed to its stability over very long durations and results from combined influence of homogeneous distribution of the nanoscale precipitates within the tempered martensite matrix as MC type carbides and as discrete $M_{23}C_6$ particles precipitated on the boundaries of prior austenitic grains and laths. Intra lath regions have also contained individual dislocations and dislocation tangles. The grain boundary carbides provide the desired creep resistance by impeding the grain boundary sliding at operating temperature of the steel. In the AR state, the steel displayed an average linear intercept grain size of approximately 7 microns. The width of the tempered martensite laths varied between $\sim 480\pm70$ nm.

(B) Microstructure in Different Zones After FSW

The macrostructure of the weld comprising of different zones is schematically described in Figure 4.2.2a. The centre of the weldment where the tool pin rotates is SZ. The region next to the SZ is TMAZ. This region can be attributed to the area where the mechanical effects of the stirring action of the tool and the temperature effects due to the frictional heat developed by the rotating tool have jointly prevailed. The region next to the TMAZ is HAZ. In this region, there is no mechanical effect of the rotating tool, but the heat experienced would promote microstructural changes in HAZ. The region that is far from the centre of the weld and is next to the HAZ is the unaffected BM. The welded blanks for tensile samples were machined in transverse direction; the orientation of tensile sample was perpendicular to the tool traverse direction.

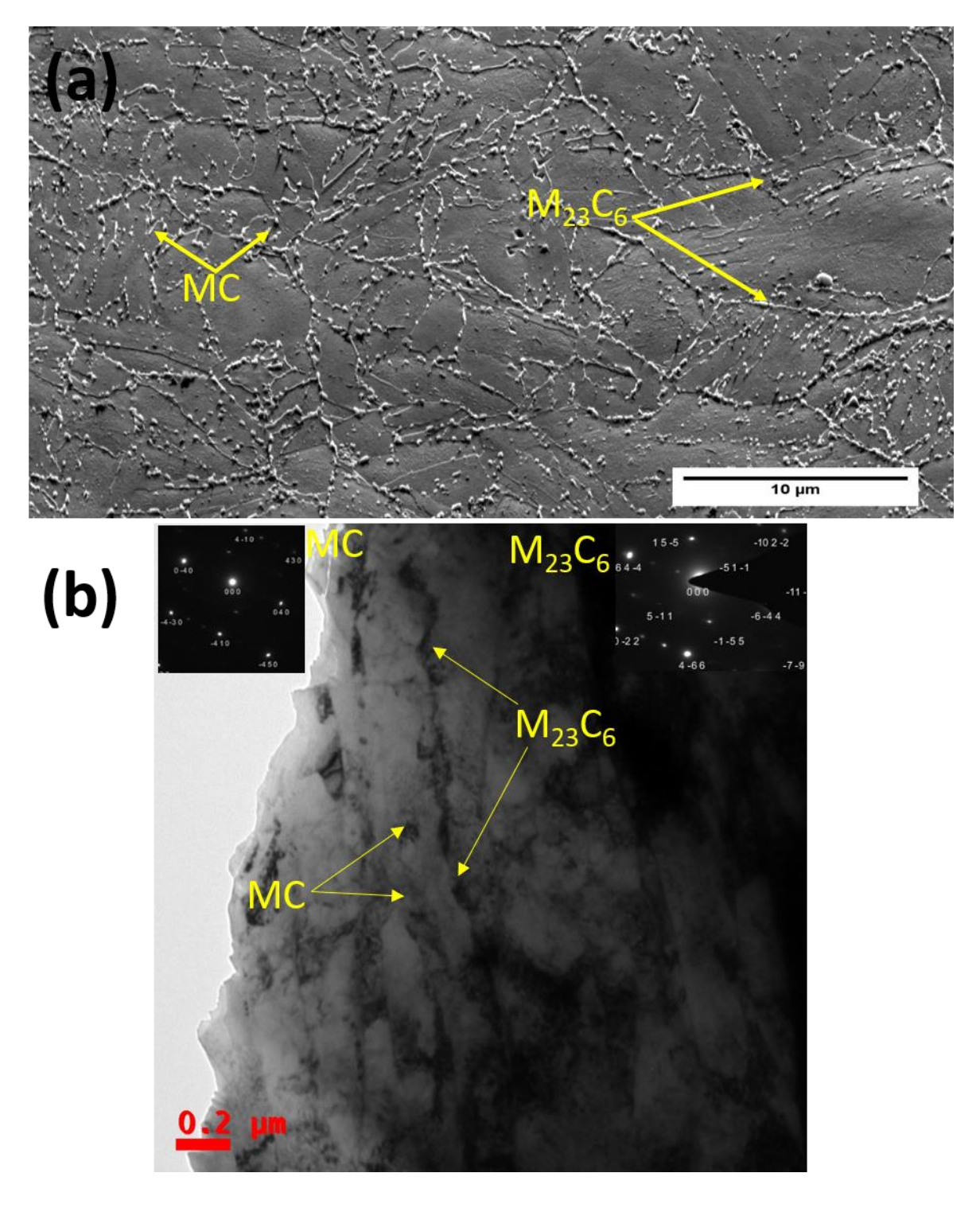


Figure 4.2.3.(a) As-received FE-SEM micrograph showing $M_{23}C_6$ on prior austenitic grain boundaries and both MC and $M_{23}C_6$ precipitates in intragranular regions,(b) TEM micrograph displaying both MC and $M_{23}C_6$ on lath and intra-lath regions and large number of dislocations and dislocation tangles in intra-lath regions.

The FE-SEM microstructures in different zones of the weld are depicted in Figure 4.2.4. The microstructure of the BM region resembles that of the initial material's (AR) microstructure. It is noticed that most of the grain boundary carbides which were present in the base metal (Figure 4.2.4a) have disappeared in the TMAZ (Figure 4.2.4c) and SZ (Figure 4.2.4d). There has not been much change in the prior austenite grain size between BM and SZ; the inference from this observation is that the temperature in stir zone has not attained to a level where it can cause rapid grain growth.

Evaluation of microstructure by TEM in SZ in the AW state indicated the presence of freshly formed martensite plates in the alpha-ferrite matrix, few undissolved MC particles, dislocation cell structure, high dislocation density in cell interiors and Fe₃C which formed along {0-31} zone axis (Figure 4.2.5). The occurrence of these features can be rationalised based on the interface temperature experienced between the top surface of the plate and bottom surface of the tool shoulder. In detailed investigations performed on this steel of 6 mm plate thickness, the interface temperature has been shown to depend upon heat input dictated by tool rotational speed [16]; the tool rotational speeds of 200, 300-500 and 700 rpm recorded interface temperatures below Ac₁ (lower critical temperature), between Ac₁ and Ac₃, and above Ac₃ (upper critical temperature) respectively with reference to Fe-C phase diagram. Various transformation temperatures for RAFM steel that have been determined earlier [9] are given in Table 4.2.2.

Table 4.2.2. Transformation temperatures of INRAFM steel [9].

Sl. No.	Transformation Temperature with reference to Fe-C diagram	Kelvin, K	Centigrade, °C
1	Melting Temperature	1791±5	1518 ± 5
2	Martensite Start, M _s	640±5	367 ± 5
3	Martensite Finish, M _f	583±5	310 ± 5
4	Recrystallization Temperature (0.4 Tm)	716±5	443 ± 5
5	Austenite Start, Ac ₁	1091±5	818 ± 5
6	Austenite Finish, Ac ₃	1130±5	857 ± 5

In general, phase transformation occurs by heating above the Ac_1 transformation temperature at which austenite begins to form on heating. Since the prior austenite grain size of SZ and BM are

similar, it can be presumed that, in the SZ of 12 mm thick plate, the interface temperature has not exceeded above Ac_3 . The occurrence of fresh martensite (Figure 4.2.5) suggests that the minimum temperature attained in SZ was above Ac_1 . This observation acts as a pointer to that, in 12 mm thick plate, the interface temperature is in intercritical zone bounded by Ac_1 and Ac_3 . This observation leads to a conclusion that the interface temperature can also be a function of the section thickness of the steel. The nucleation of austenite takes place at alpha grain boundaries in SZ, when the interface temperature is in the intercritical zone. Subsequently, on cooling, the freshly formed austenite undergoes phase transformation leading to the occurrence of martensite, as detailed in Figure 4.2.5. It has been opined that the major driving force for Fe₃C precipitation in SZ is carbon supersaturation [14, 16]; an increase in the carbon concentration in the matrix would favour this type of carbide. Majority of the $M_{23}C_6$ precipitates in the SZ during FSW deformation would be fragmented to a size which makes them to be subcritical. These subcritical particles undergo a solid state dissolution thereby leading to a matrix facilitating supersaturation of carbon. In fact, the fragmentation and dissolution of $M_{23}C_6$ could also be credited for the development of precipitate-free grain boundaries in the SZ and in TMAZ.

The grain size distributions in the AW state in BM and SZ are shown in Figures 4.2.6 a&b. There was no obvious change in the grain size distribution in the AR material and unaffected BM region in AW state which was remote from the centre of SZ. However, there has been substantial increase in the area fraction of very fine grains in SZ (Figure 4.2.6b). These fine grains correspond to low angle boundaries, which could result from the reorganisation of plastic deformation induced dislocations in SZ into a low energy configuration comprising of cells and sub-grains. The dynamic recovery process that promotes these features occur more quickly in the SZ matrix that is depleted with carbides.

At the employed rotational speed of 200 rpm, TMAZ in 12 mm plates appear to develop temperatures between Ac_1 and Ac_3 , whereas in case of 6 mm plates the TMAZ and HAZ have seen temperatures less than Ac_1 [16]. In this study, in 12 mm thick plates, the coarsening and coalescence of $M_{23}C_6$ particles were noticed in the HAZ (Figure 4.2.4b). Ripening of $M_{23}C_6$ would result when the peak temperature experienced in HAZ is below Ac_1 (818°C) but much above that of tempering temperature employed (760 °C) in AR state. In this investigation, no alpha-ferrite was found in HAZ at 200 rpm. However, transformation to alpha-ferrite was reported earlier in 12 mm plates when the

rotational speeds employed were 500 and 900 rpm [15]; at these higher rotational speeds the HAZ had seen temperatures in the intercritical zone.

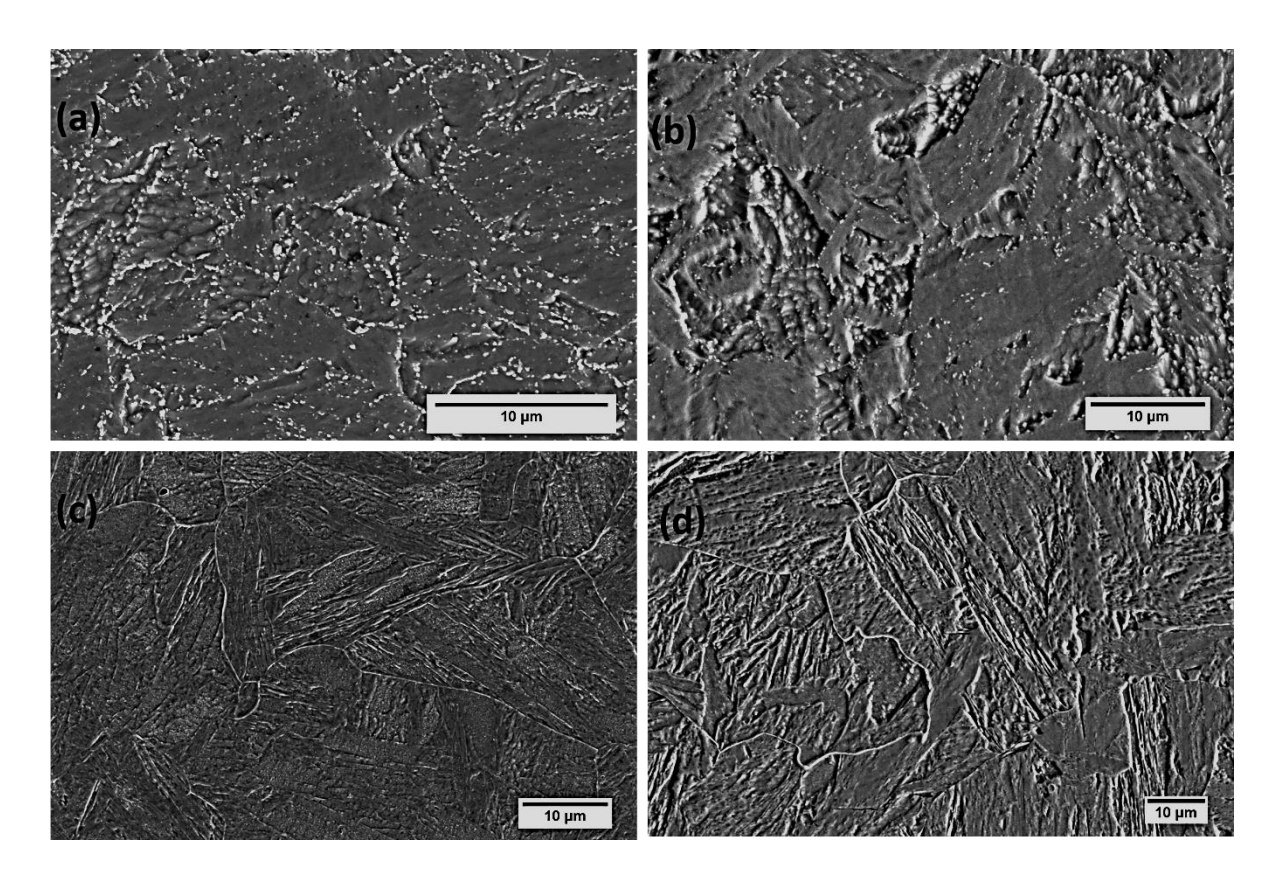


Figure 4.2.4. FE-SEM micrographs of AW 12 mm plate (a) Base Metal showing tempered martensite structure, (b) Heat Affected Zone showing coarsening and coalescence of M₂₃C₆, (c) Thermo Mechanically Affected Zone, and (d) Stir Zone. SZ and TMAZ show precipitate-free grain boundaries.

The drastic variation in microstructure in the AW condition across various zones was also reflected in the form of an inhomogeneous distribution of hardness (Figure 4.2.7). The hardness in BM is around 200 HV. The SZ region is very hard due to the presence of martensite, very fine MC, high dislocation density and Fe₃C. There was a drastic drop in hardness as the distance from SZ was increased towards unaffected BM. A significant decrease in hardness was seen in HAZ with a value less than 200 HV. The low hardness in HAZ could be associated with the over tempering of

microstructure which portrayed in the form of coarsening and coagulation of $M_{23}C_6$ particles (Figure 4.2.4b).

The occurrence of carbide-free grain boundaries in SZ and TMAZ are undesirable; these boundaries could act as preferential sites for the promotion of grain boundary sliding and creation of intergranular cavities and cracks leading to intergranular fracture under creep conditions. It shall be recapitulated that RAFM steels were designed to have adequate creep resistance. Therefore, there is a necessity to restore the grain boundary M₂₃C₆ in the SZ and TMAZ of FSW welds and homogenise the microstructure across the weld joint by designing appropriate post-weld heat treatments. These heat treatments should also be aimed at eliminating Fe₃C in SZ and promoting the re-precipitation of M₂₃C₆ on grain boundaries, and also cause the dissolution of coarse and coagulated M₂₃C₆ precipitates in HAZ and re-precipitation of these at appropriate locations in the desired shape and size. Thus, PWHT is mandatory for AW material to obtain the microstructure and mechanical properties similar to those possessed in AR material, and it is crucial to minimize the impact of mechanical property variation associated with FSW.

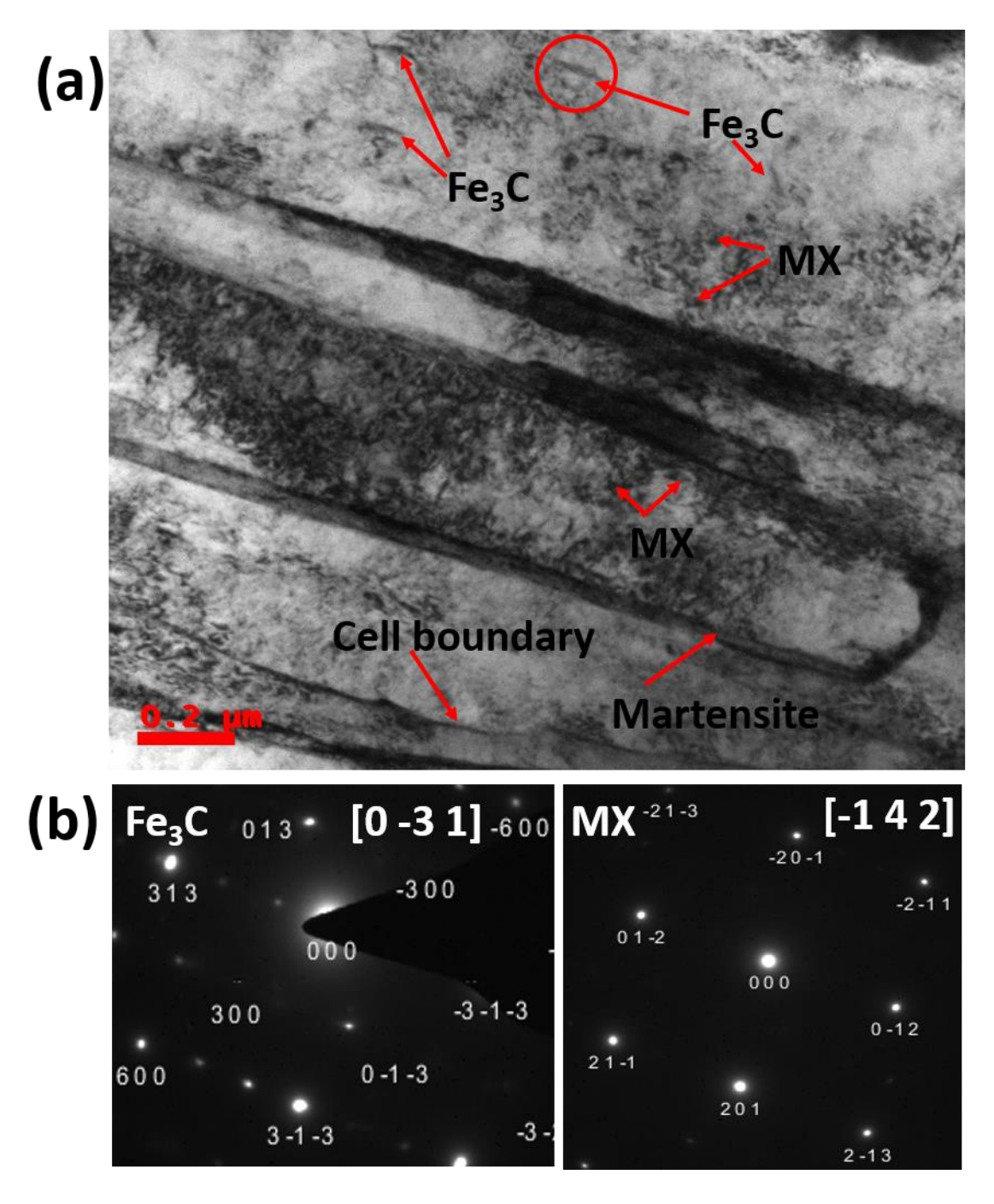


Figure 4.2.5. TEM micrograph of SZ in AW condition showing freshly formed martensite, Fe_3C , cell boundaries, few undissolved MX type precipitates and high dislocation density; (b)

Selected area diffraction for Fe_3C and MX precipitates.

(C) Post Weld Heat Treatment

A critical assessment of microstructure conducted on as-welded 6 mm thick plates after PWHT's led to a clear indication that the PWNT treatment is beneficial in providing uniform microstructure within the weld zones as compared to that obtained after post weld direct tempering. In view of this, the AW 12 mm thick plates were subjected to PWNT treatment comprising of soaking at 980°C for 30 minutes followed by air-cooling to room temperature and subsequently given a tempering treatment at 760°C for 90 minutes and air cooling. The solutioning temperature (980°C) was set much above the Ac₃ temperature (857°C) in order to facilitate the complete reaustenization process and enabling the complete dissolution of the coarse and coagulated M₂₃C₆ in HAZ, martensite and Fe₃C in SZ. Tempering temperature and duration were identical as those adopted in AR state for BM. PWNT re-precipitated M₂₃C₆ on grain and martensite lath boundaries and proved to be instrumental in creating more homogeneous and uniform microstructure within SZ, TMAZ and HAZ zones (Figure 4.2.8). The microstructure in these zones became very similar to the AR base metal microstructure. As a consequence, a very uniform hardness distribution was achieved after PWNT and the hardness in the welded region is very much comparable to BM (Figure 4.2.7). Grain size distribution of BM and SZ regions in PWNT state are incorporated in Figure 4.2.6.

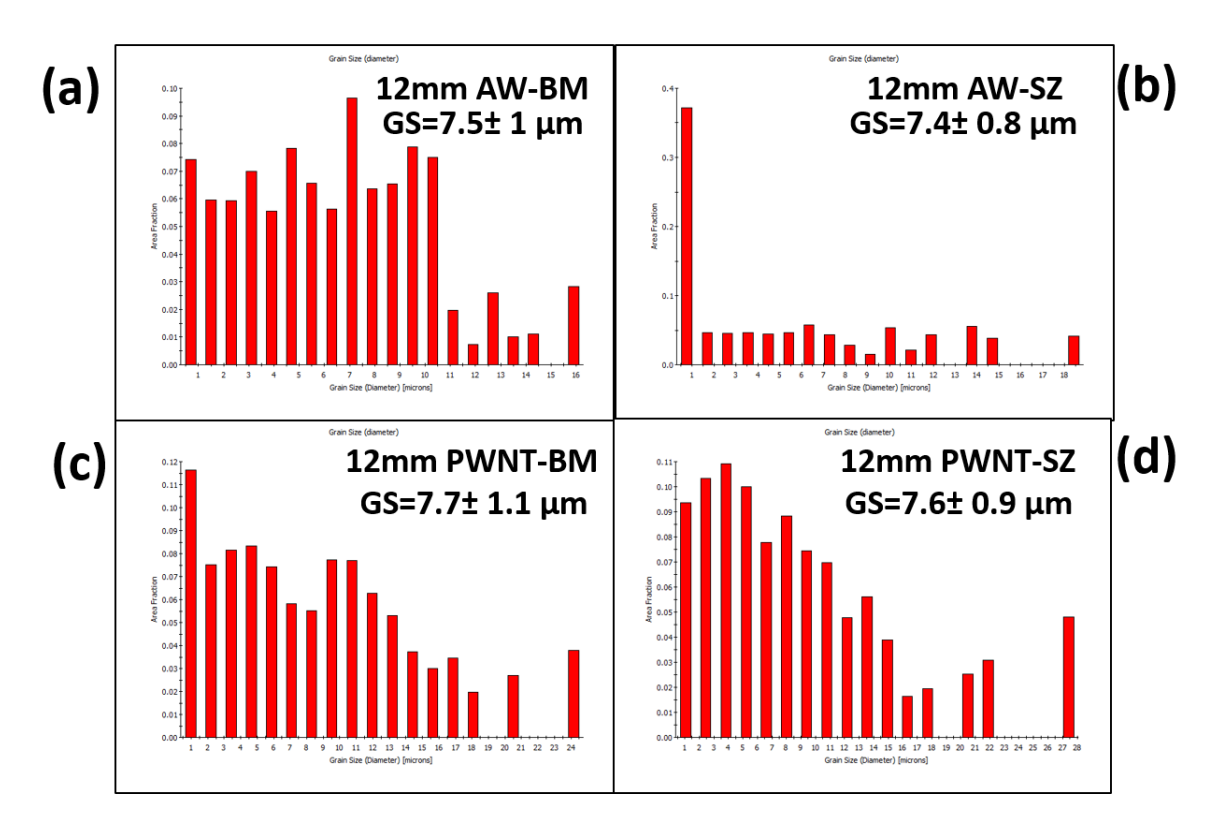


Figure 4.2.6. Grain size (GS) distribution obtained through EBSD (a) As-welded BM, (b) As-welded Stir Zone, (c) Base metal after PWNT, and (d) Stir Zone after PWNT.

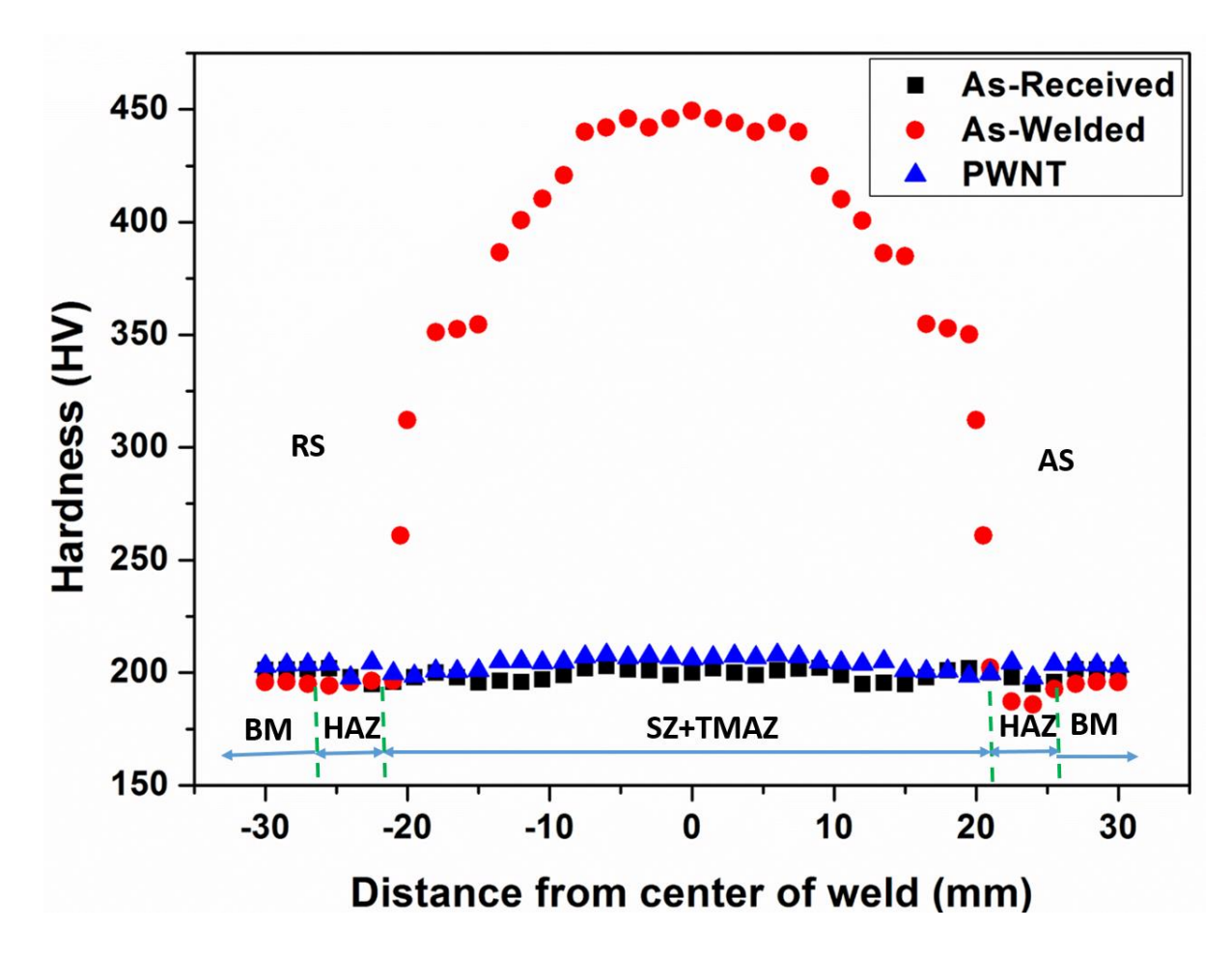


Figure 4.2.7. Hardness distribution across the transverse cross section in the as-received, aswelded and PWNT states

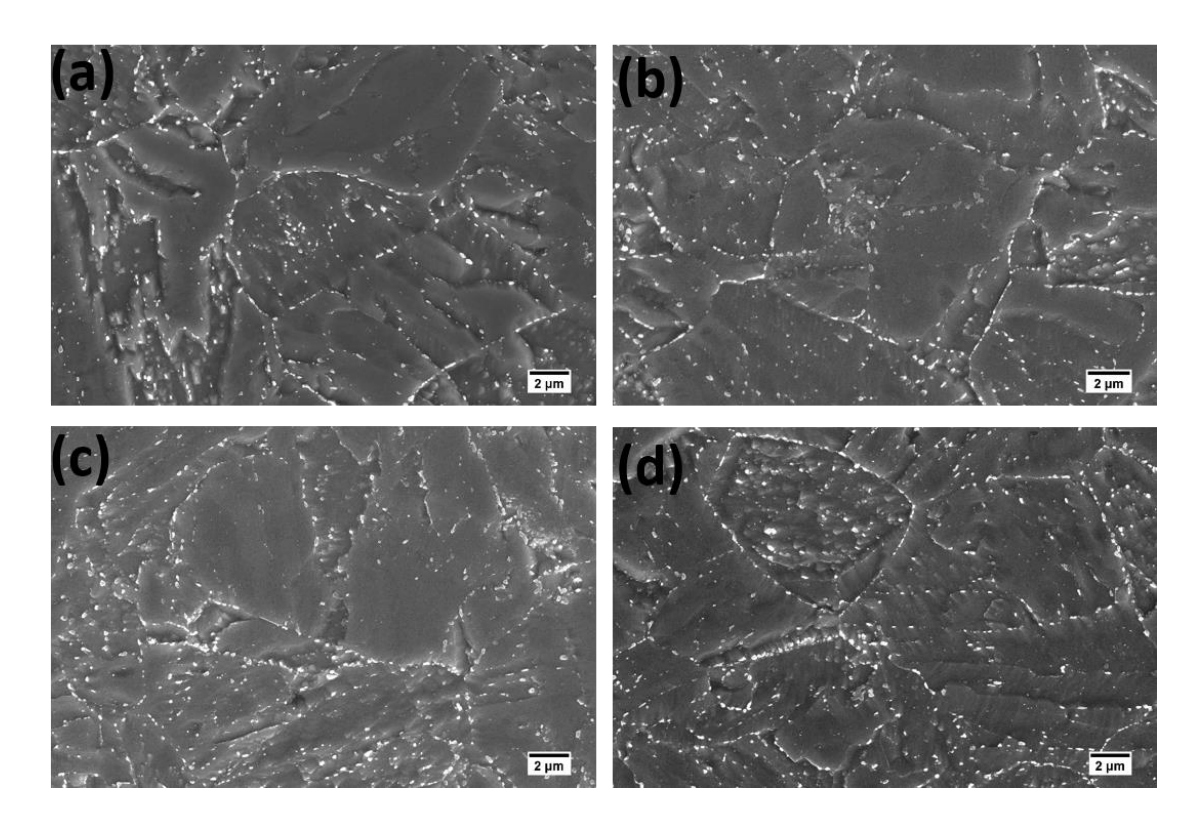


Figure 4.2.8. Microstructure in PWNT state (a) Base Metal showing tempered martensite structure, (b) Heat Affected Zone, (c-d) re-appearance of carbides at prior austenite grain boundaries and intragranular precipitates in TMAZ and SZ respectively

(D) Tensile Properties of As-Received, Friction Stir Welded and Post Weld Heat Treated RAFM Steel

At a nominal strain rate of 3.33x10⁻⁴ s⁻¹, the tensile properties of the alloy determined in AR, AW and PWHT states at various temperatures are given in Table 4.2.3. The monotonic tensile stress-strain curves evolved in AR, AW and PWNT states at different temperatures are shown in Figure 4.2.9. The salient features pertaining to tensile properties, deformation and fracture are: (i) Irrespective of the state prevailing, RAFM steel shows a decrease in 0.2% YS and UTS as the testing temperature increased, (ii) Strength of the alloy in AW state is higher at all the temperatures, (iii) Strength after PWNT treatment is very close or marginally higher than in AW state depending on the temperature, (iv) Ductility in the form of the percentage elongation exhibits a minimum at 450 °C in all the states, (v) Ductility in AR state is better than in PWNT state at RT, 500 °C and 550 °C, (vi) Percentage elongation in PWNT condition is unusually higher compared to AW state at 450°C, (vii) Tensile stress-strain flow curves in all the states exhibit a relatively short period of rapid strain

hardening until UTS is reached followed by very long period of softening at elevated temperatures, and (viii) In all the states at RT, the alloy exhibits monotonic strain hardening in the early stages followed by a regime of nearly stable peak stresses until the softening commences towards the end.

Based on the detailed investigations conducted on temperature dependence of tensile properties in the range 25 to 650 °C in the AR state, the loss of ductility at intermediate temperatures has been reported to result from the operation of dynamic strain ageing (DSA) process [17]. DSA is generally reported to occur due to the attractive interaction between diffusing solute species in the alloy and mobile dislocations during the deformation [18,19]. Ageing of mobile dislocations by solute atmospheres would occur either during quasi viscous type of dislocation motion [20] or during the period when the dislocations are temporarily held up at local obstacles in the glide plane [21,22]. The generally seen manifestation of DSA is the occurrence of serrations in the tensile flow curves and has been attributed to either locking or unlocking of mobile dislocations with the solute atmos. In this investigation, the alloy displayed smooth stress-strain curves at all the temperatures without evidence for serrated flow. The non-existence of serrated flow has also been reported earlier in the tensile tests performed over a wide temperature range on this RAFM steel [17]. If DSA is the predominant process operating at a particular temperature, one would also expect an instantaneous negative strain rate sensitivity (SRS) of tensile flow stress; this negative SRS manifests itself through a decrease in flow stress with an increase in strain rate at a given temperature during the progression of the tensile deformation. Vanaja et.al [17] have examined the SRS at room temperature and 300°C; these studies clearly indicated that the SRS was positive at room temperature, and negative at 300 °C where DSA prevailed. In the domain where DSA was absent the positive strain rate sensitivity resulted. Negative strain rate sensitivity was considered as a potent indicator of DSA than the display of serrated flow [19]. The low ductility observed at 450 °C in this investigation could be credited to DSA.

In general, many of the solution annealed stainless steels and superalloys exhibit rapid strain hardening in DSA regime. On the other hand, the ferritic-martensitic steels exhibit strain softening predominantly at elevated temperatures as displayed in Figure 4.2.9. This type of softening was akin to that reported earlier during low cycle fatigue of cold-worked 304 stainless steel [23], and modified 9Cr1Mo steel [24] from which RAFM steel has been derived. Softening of RAFM steels having high initial dislocation densities could result when the annihilation rate of dislocations is greater than the generation rate causing a net decrease in dislocation density, or when the

rearrangement of dislocations takes place into a cell or sub-grain structure resulting in an increase in the mean free path for dislocations. Annihilation of lath boundaries can also occur due to interaction between martensite lath boundary dislocations and mobile dislocations generated during tensile deformation. Softening may also result from the coarsening of $M_{23}C_6$ precipitates. However, the observed softening in all the states cannot be attributed to coarsening of precipitates since the tensile tests were conducted at much lower temperatures than those mentioned to be conducive for coarsening of $M_{23}C_6$.

The EBSD analysis of the grain boundary maps taken from different zones of AW and PWNT samples can be used judiciously to explain the variation in tensile properties. Figures 4.2.10 and 4.2.11 respectively describe EBSD image quality figures in AW and PWNT states and depict the volume fraction of low angle grain boundaries (defined by misorientation angle 2 deg. ≤ theta minute ≤ 15 deg.) and high angle grain boundaries (misorientation angle theta minute ≥ 15 deg.). In the AW state, the volume fraction of LAGBs is very low in SZ compared to the values recorded in BM, HAZ, and TMAZ. After PWNT treatment LAGBs have increased in SZ and TMAZ. The increase of tensile elongation from the AW to PWNT condition can be attributed to the increase in the LAGB concentration owing to ease in dislocation movement. As the misorientation between adjacent grains are less, dislocation movement will be easier in regions having higher fraction of LAGBs and they contribute to increased ductility. The variation in the tensile behaviour of the AW and PWNT condition can be explained by this change in the fraction of LAGBs and HAGBs. LAGBs are considered as Read and Shockley dislocation arrays and annihilation of such boundaries would occur by impingement of mobile dislocations [25]. At elevated temperatures, dislocation climb, and cross slip enhances the annihilation mechanism and promotes the coarsening of laths, cells and sub-grains leading to much higher softening rates. At room temperature, the reorganisation of dislocations into low energy configurations would be sluggish in the initial stages of deformation and therefore the flow stress response curves show an initial period of strain hardening as revealed in Figure 4.2.9

The hardening (+)/softening (-) rates in the tensile tests conducted at various temperatures in AR, AW and PWNT states are summarised in Table 4.2.4 and Figure 4.2.12. The hardening/softening rates are defined as: (true stress corresponding to 0.1 strain- true stress at 0.05 strain) / 0.05]. The total contribution to total elongation results from the combined action of deformation induced modifications in substructure and localisation of deformation due to necking towards the end of

tensile testing; the later gets depicted in the form of transgranular ductile fracture (Figure 4.2.13). The hardening/softening ratio described here predominantly portray the changes occurring during tensile deformation and eliminates the contribution from the fracture process. The softening observed in tensile tests in all the states at elevated temperatures could be attributed to the cumulative effects of dislocation annihilation, or coarsening of laths, cells, and sub-grains. The rapid softening in AW state that was described in Figure 4.2.9 could also be considered to result partially from the annihilation of dislocations at HAGBs in SZ.

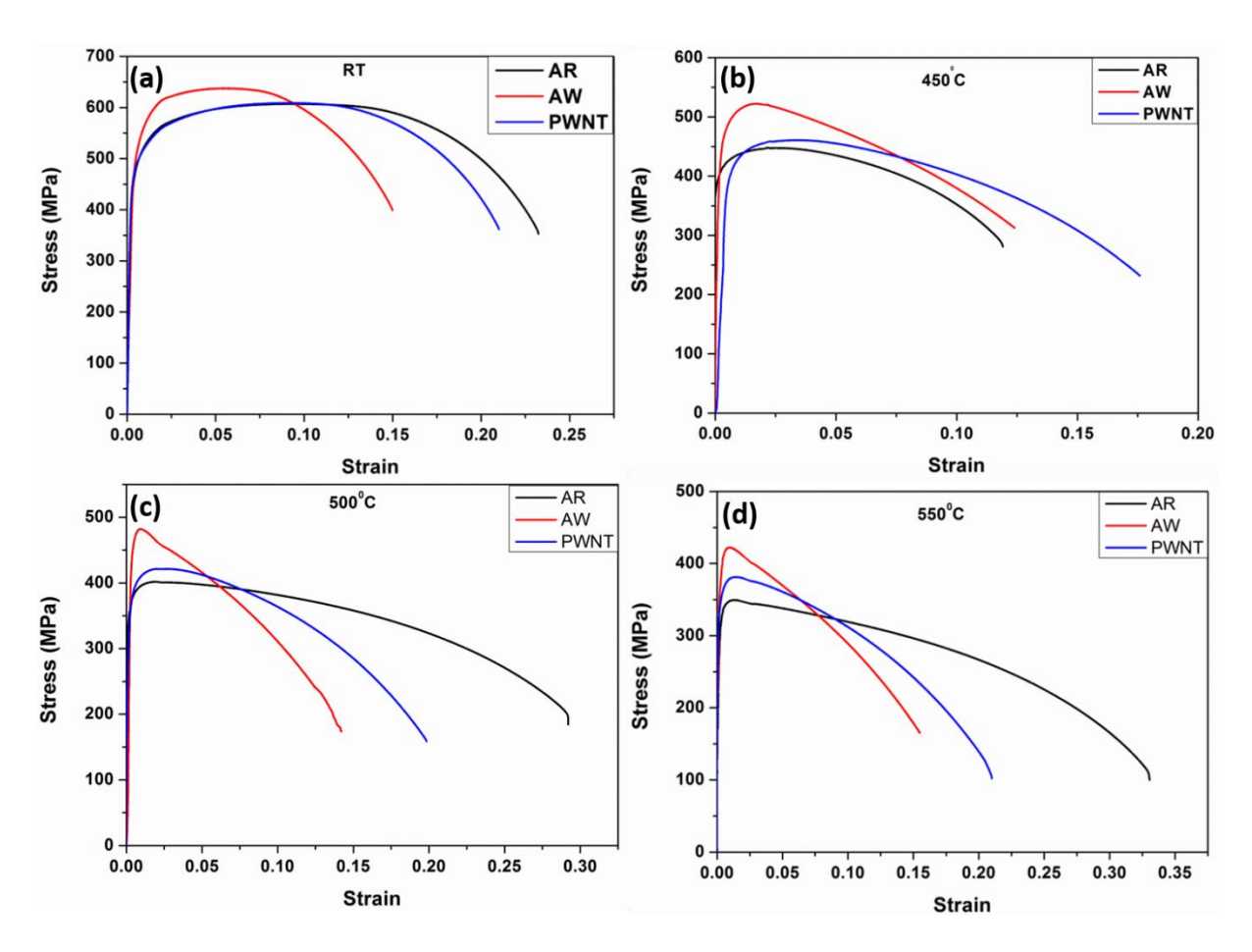


Figure 4.2.9. Tensile Stress-Strain flow curves of the AR, AW and PWNT conditions tested at (a) RT, (b) $450\,^{0}$ C, (c) $500\,^{0}$ C, (d) $550\,^{0}$ C

Table 4.2.3. Results of the tensile tests performed on (a) As-Received, (b) AW, (c) PWNT samples at RT and HT conditions

Sample Condition	Test Temperature (°C)	Yield Strength (MPa)	UTS (MPa)	% Elongation
(a) AR	RT	476 ± 5.2	607 ± 8	23 ± 1.8
	450	397 ± 3.1	448 ± 4.2	12 ± 1.2
	500	367 ± 4.1	402 ± 5.8	29 ± 1.9
	550	329 ± 4.6	349 ± 5.1	33 ± 2.1
(b) AW	RT	513 ± 3.9	637 ± 4.9	15 ± 1.4
	450	473 ± 3.1	525 ± 4.2	12 ± 1.8
	500	418 ± 2.9	484 ± 5.1	14 ± 2.3
	550	368 ± 3.4	424 ± 4.3	15 ± 1.7
(c) PWNT	RT	473 ± 4.4	611 ± 5.9	21 ± 1.8
	450	410 ± 5.1	460 ± 6.1	18 ± 1.1
	500	376 ± 4.4	422 ± 5.1	20 ± 1.7
	550	348 ± 4.8	381 ± 6.4	21 ± 2.3

Table 4.2.4. Hardening (+) Softening (-) rates of different sample at different test conditions

Sample	Hardening (+)/Softening(-) Rates at Test Temperatures				
Condition	RT	450 °C	500 °C	550 °C	
AR	+817	-1391	-46	-80	
AW	+265	-1720	-1895	-1412	
PWNT	+839	-711	-644	-717	

(E) Fracture Modes

Irrespective of the material state fracture at all the temperatures was in ductile transgranular mode characterized by the presence of dimples (micro voids) on the fracture surface. Typical fracture surfaces of samples failed at 500 0 C in the AR, AW and PWNT states are illustrated in Figure 4.2.13 a, b & c respectively. The fracture in all weld and PWNT samples occurred at the interface between the HAZ and base metal. Figure 4.2.13.d represents the features on the fracture surface of AW sample tested at 450 0 C, where the failure has been found in the vicinity of microstructurally altered BM (HAZ) region of low hardness. In spite of low ductility at 450 0 C, no intergranular cavities or cracks were noticed in any of the states. The insert in Figure 4.2.13d represents the low magnification view of the fracture surface.

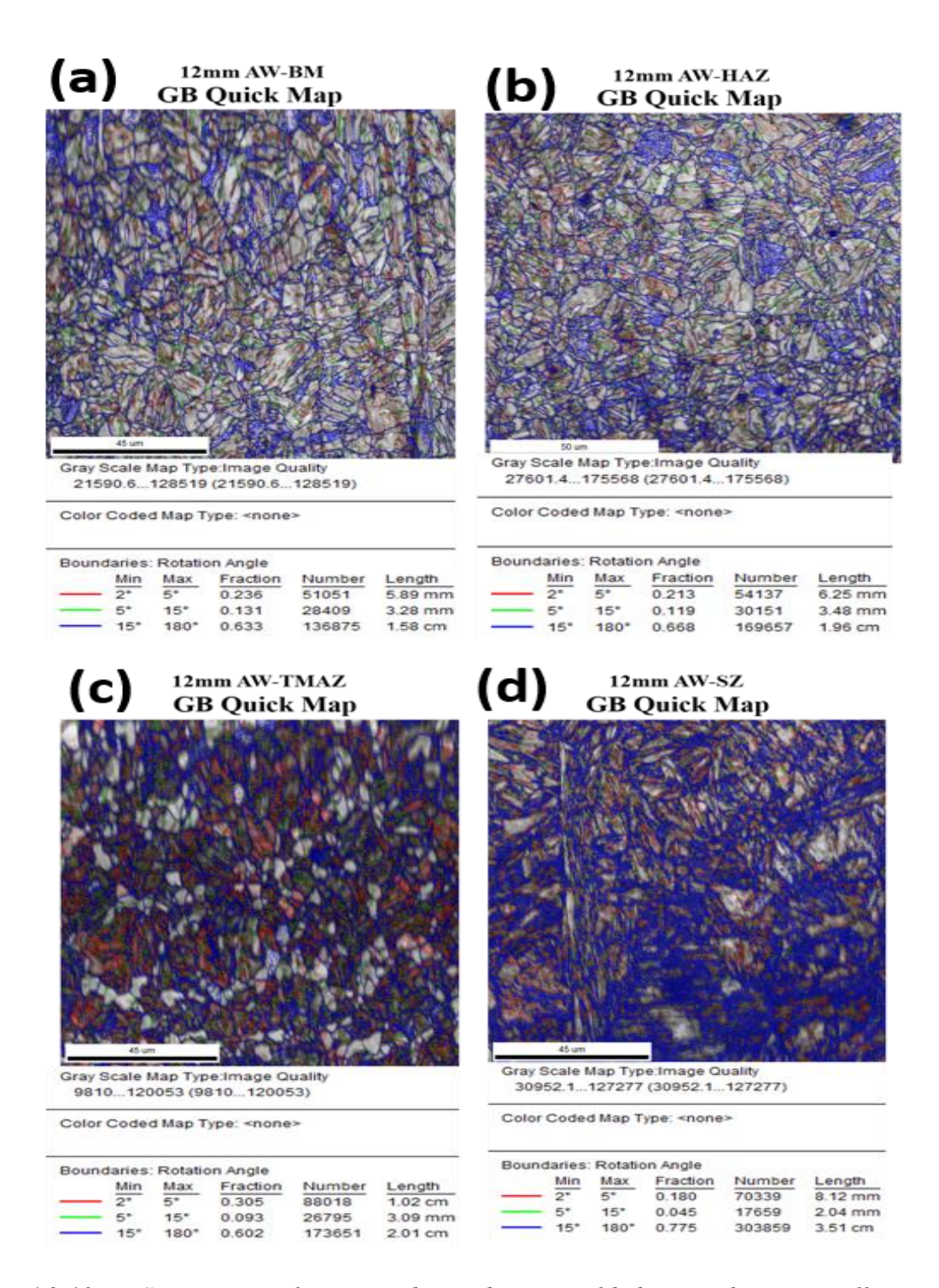


Figure 4.2.10. EBSD image quality maps obtained in as-welded state. These maps illustrate both low and high angle boundaries comprising of cell, sub-grain, lath and grain boundaries in (a) BM, (b) HAZ, (c) TMAZ and (d) SZ. Incorporated table contains angle of boundaries, their fraction, number, and length

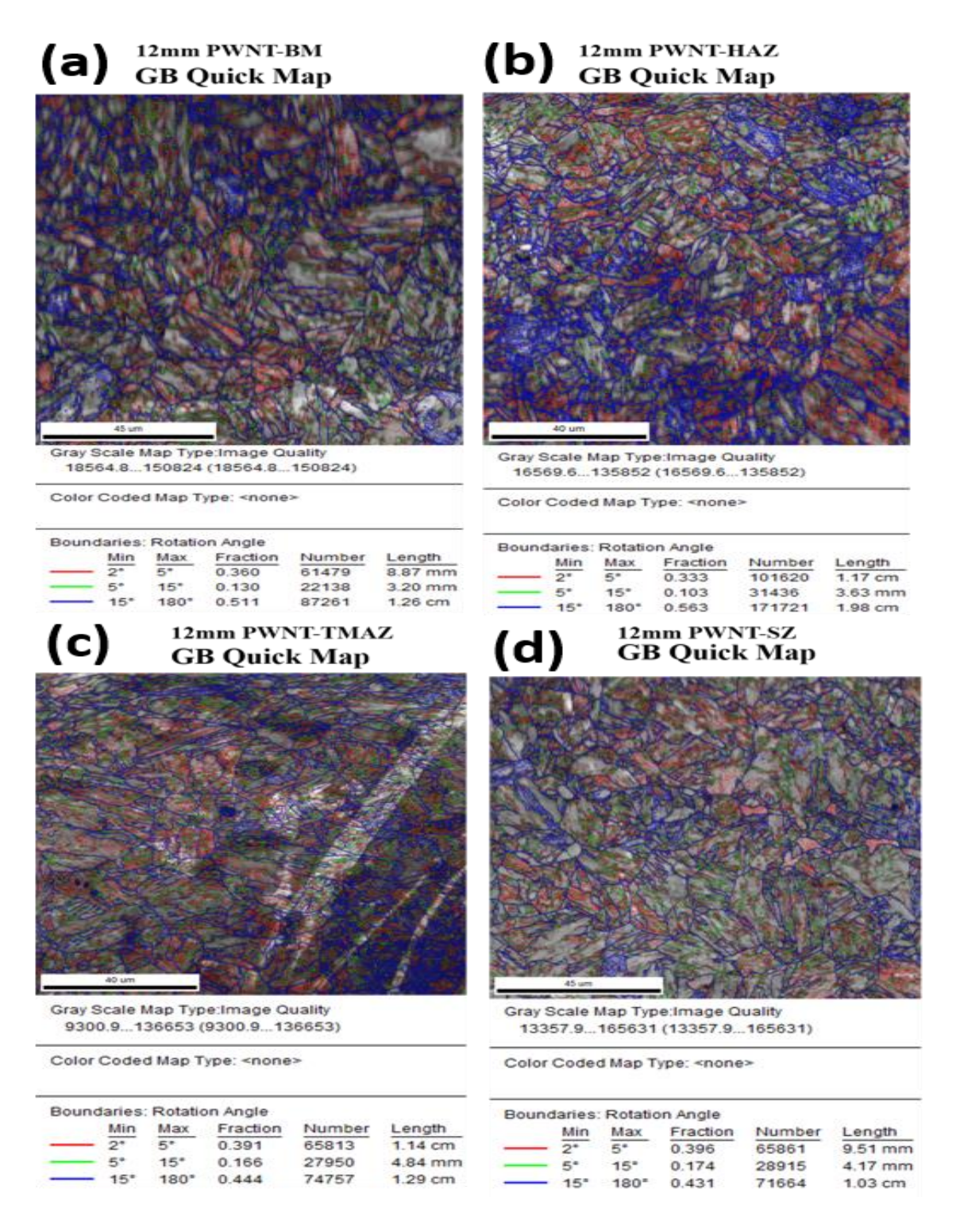


Figure 4.2.11. EBSD image quality maps obtained in PWNT state. These maps illustrate both low and high angle boundaries comprising of cell, sub-grain, lath and grain boundaries in (a) BM, (b) HAZ, (c) TMAZ and (d) SZ. Incorporated table contains angle of boundaries, their fraction, number, and length

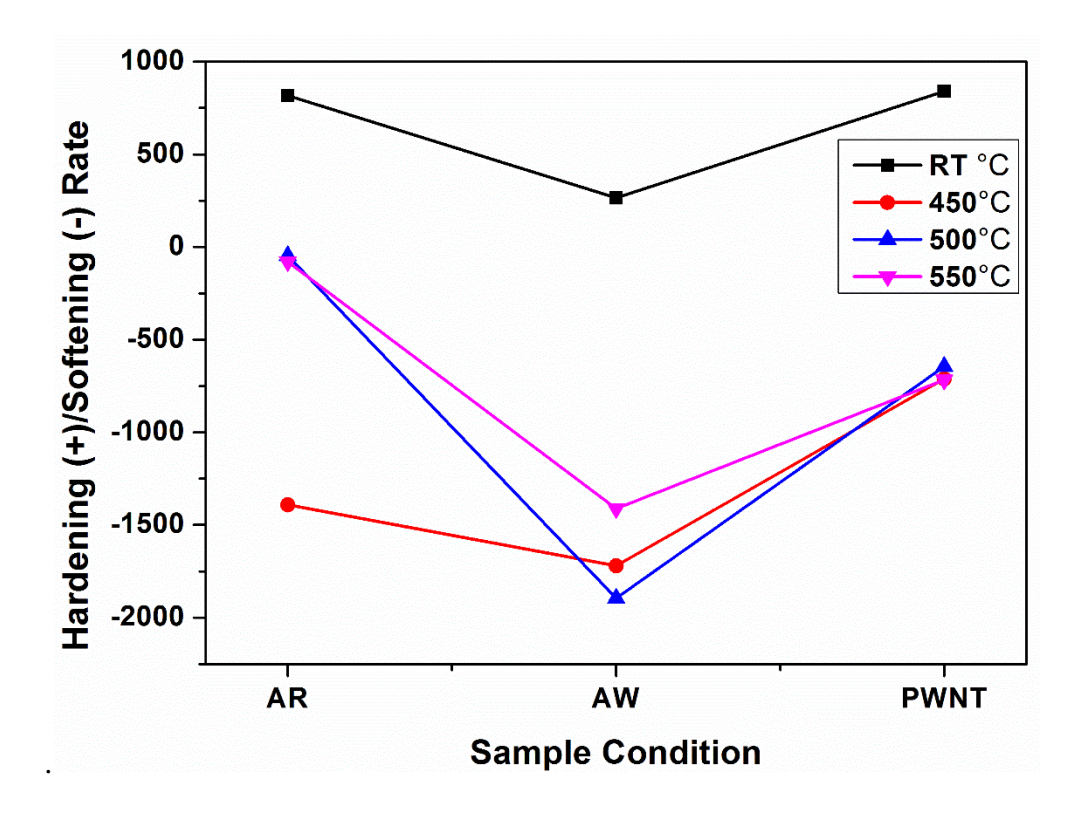


Figure 4.2.12: Hardening/Softening rates for different states at different temperatures

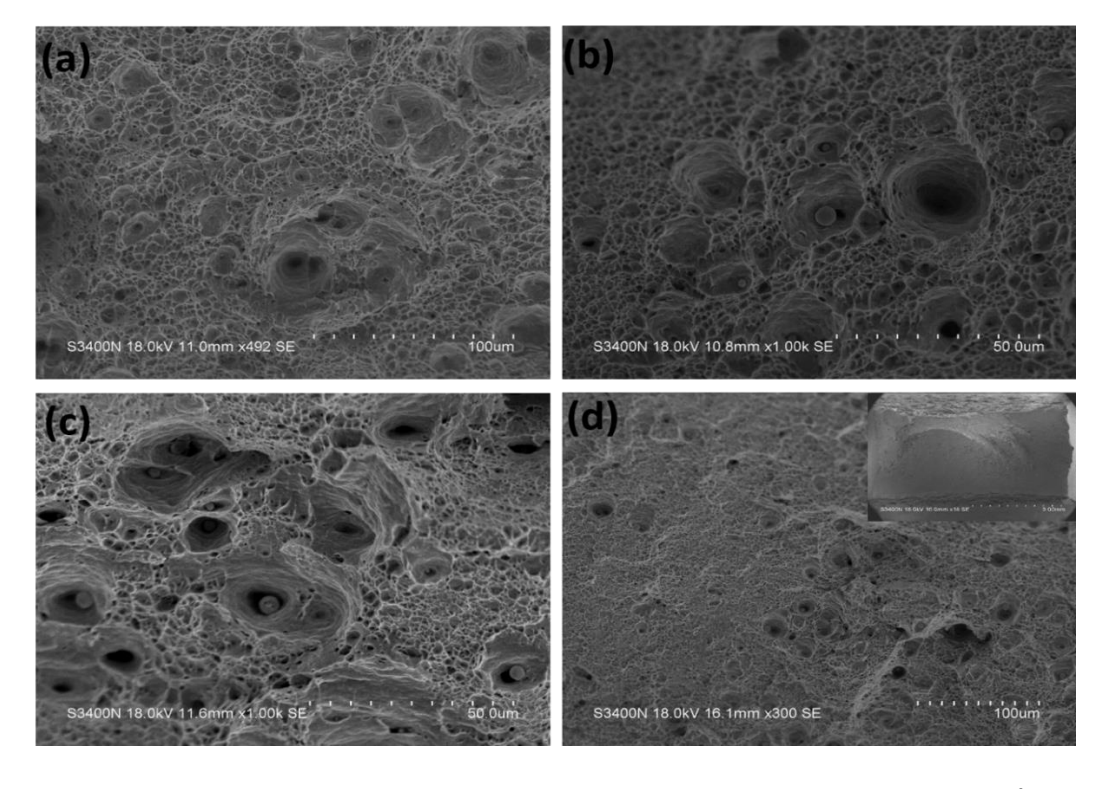


Figure 4.2.13. Fractographs of the samples tested at different conditions (a) AR-500 0 C, (b) AW-500 0 C, (c) PWNT- 500 0 C, (d) AW-450 0 C

4.2.4 Conclusions:

The 12mm thick as-received RAFM steel displayed a tempered martensite microstructure. (i) TEM studies revealed M₂₃C₆ type carbides on prior austenite grain and martensite lath boundaries. The finer particles in the intra-lath regions were identified as Ta and V rich MX type of carbides and carbonitrides. (ii) Bead-on-Plate FSW was successfully accomplished by employing PCBN tool with a rotational speed of 200 rpm. In the as-welded state, the weld joint was composed of SZ, TMAZ, HAZ and unaltered base metal. (iii) SZ displayed very high hardness due to the presence of martensite, Fe₃C and high dislocation density. The SZ and TMAZ exhibited precipitate- free prior austenite grain boundaries which can act as preferential sites for the occurrence of grain boundary damage under creep conditions, while HAZ displayed ripening and agglomeration of carbides with concomitant decrease in hardness. (iv) The as-welded microstructure was completely modified and restored to the parent metal microstructure by PWNT treatment. The non-uniformity in hardness across the transverse section was also eliminated. (v) Tensile tests conducted in different states over the wide temperature range indicated UTS to be in the order AW> PWNT>AR while ductility in the form of the percentage elongation is in the order AW<PWNT <AR. An exception to this generalisation was shown at 450 °C, where the ductility was in order AR<AW<PWNT. (vi) Irrespective of the state, the minimum in ductility was displayed at 450 °C owing to the prevalence of dynamic strain ageing. In all the states and at all the temperatures ductile fracture prevailed. (vii) Tensile flow stress-strain response revealed a brief period of monotonic hardening in all the states at room temperature followed by softening. Elevated temperatures were found conducive for rapid The variation in monotonic tensile stress response was rationalised on the basis of softening. evolving substructure during tensile deformation. (viii) The tensile test samples were taken from the central portion of the bead-on-plate welds and represent the full penetration welds, as would also be expected from welding of two plates in a configuration of a butt joint. Thick sections may require FSW from both the sides when two plates joining is contemplated in butt configuration at very low rotational speeds; this is essential since tools of larger length would fail at low heat inputs associated with low rotational speeds.

^{*}This section is published in Transactions of Indian Institute of Metals (https://doi.org/10.1007/s12666-022-02628-z)

References:

- [1] N. Baluc, D.S. Gelles, S. Jitsukawa, A. Kimura, R.L. Klueh, G.R. Odette, B. van der Schaaf, J. Yu, Status of reduced activation ferritic/martensitic steel development, J. Nucl. Mater. 367-370 A (2007) 33–41. https://doi.org/10.1016/j.jnucmat.2007.03.036.
- [2] H. Tanigawa, K. Shiba, A. Möslang, R.E. Stoller, R. Lindau, M.A. Sokolov, G.R. Odette, R.J. Kurtz, S. Jitsukawa, Status and key issues of reduced activation ferritic/martensitic steels as the structural material for a DEMO blanket, J. Nucl. Mater. 417 (2011) 9–15. https://doi.org/10.1016/j.jnucmat.2011.05.023.
- [3] J. Yu, Q. Huang, F. Wan, Research and development on the China low activation martensitic steel (CLAM), J. Nucl. Mater. 367-370 A (2007) 97–101. https://doi.org/10.1016/j.jnucmat.2007.03.236.
- [4] Q. Huang, C. Li, Y. Li, M. Chen, M. Zhang, L. Peng, Z. Zhu, Y. Song, S. Gao, Progress in development of China Low Activation Martensitic steel for fusion application, J. Nucl. Mater. 367-370 A (2007) 142–146. https://doi.org/10.1016/j.jnucmat.2007.03.153.
- [5] B. Van Der Schaaf, D.S. Gelles, S. Jitsukawa, A. Kimura, R.L. Klueh, A. Möslang, G.R. Odette, Progress and critical issues of reduced activation ferritic/martensitic steel development, J. Nucl. Mater. 283–287 (2000) 52–59. https://doi.org/10.1016/S0022-3115(00)00220-8.
- [6] S. Saroja, A. Dasgupta, R. Divakar, S. Raju, E. Mohandas, M. Vijayalakshmi, K. Bhanu Sankara Rao, Baldev Raj, Development and characterization of advanced (Cr ferritic/martensitic steels for fission and fusion reactors, J. Nucl. Mater. 1 (2011) 53.
- [7] B. Raj, T. Jayakumar, Development of Reduced Activation Ferritic-Martensitic Steels and fabrication technologies for Indian test blanket module, J. Nucl. Mater. 417 (2011) 72–76. https://doi.org/10.1016/j.jnucmat.2011.02.032.
- [8] B. Raj, K.B.S. Rao, A.K. Bhaduri, Progress in the development of reduced activation ferritic-martensitic steels and fabrication technologies in India, Fusion Eng. Des. 85 (2010) 1460–1468. https://doi.org/10.1016/j.fusengdes.2010.04.008.
- [9] S. Raju, B. Jeya Ganesh, A.K. Rai, R. Mythili, S. Saroja, E. Mohandas, M. Vijayalakshmi,

- K.B.S. Rao, B. Raj, Measurement of transformation temperatures and specific heat capacity of tungsten added reduced activation ferritic-martensitic steel, J. Nucl. Mater. 389 (2009) 385–393. https://doi.org/10.1016/j.jnucmat.2009.02.030.
- [10] R.L. Klueh, Ferritic-martensitic steels for advanced nuclear reactors, Trans. Indian Inst Met. 62 (2009) 81–87.
- [11] R.S. Mishra, Z.Y. Ma, Friction stir welding and processing, Mater. Sci. Eng. R Reports. 50 (2005) 1–78. https://doi.org/10.1016/j.mser.2005.07.001.
- [12] P.L. Threadgill, A.J. Leonard, H.R. Shercliff, P.J. Withers, Friction stir welding of aluminium alloys, Int. Mater. Rev. 54 (2009) 49–93. https://doi.org/10.1179/174328009X411136.
- [13] D.G. Thomas WM, Nicholas ED, Needham JC, Murch MG, Temple-Smith P, Friction Stir Butt Welding (1991), GB Pat. No. 9125978.8, Int. Pat. No. PCT/GB92/02203. 14 (1991) 3–7. https://doi.org/10.1093/tropej/14.1.3.
- [14] V.L. Manugula, K. V. Rajulapati, G.M. Reddy, R. Mythili, K. Bhanu Sankara Rao, Influence of Tool Rotational Speed and Post-Weld Heat Treatments on Friction Stir Welded Reduced Activation Ferritic-Martensitic Steel, Metall. Mater. Trans. A Phys. Metall. Mater. Sci. 48 (2017) 3702–3720. https://doi.org/10.1007/s11661-017-4143-5.
- [15] V.L. Manugula, K. V. Rajulapati, G.M. Reddy, E. Rajendra Kumar, K.B.S. Rao, Friction stir welding of thick section reduced activation ferritic–martensitic steel, Sci. Technol. Weld. Join. 23 (2018) 666–676. https://doi.org/10.1080/13621718.2018.1467111.
- [16] V.L. Manugula, K. V. Rajulapati, G. Madhusudhan Reddy, R. Mythili, K. Bhanu Sankara Rao, A critical assessment of the microstructure and mechanical properties of friction stir welded reduced activation ferritic-martensitic steel, Mater. Des. 92 (2016) 200–212. https://doi.org/10.1016/j.matdes.2015.12.019.
- [17] J. Vanaja, K. Laha, S. Sam, M. Nandagopal, S. Panneer Selvi, M.D. Mathew, T. Jayakumar, E. Rajendra Kumar, Influence of strain rate and temperature on tensile properties and flow behaviour of a reduced activation ferritic-martensitic steel, J. Nucl. Mater. 424 (2012) 116–122. https://doi.org/10.1016/j.jnucmat.2012.02.020.

- [18] K, Bhanu Sankara Rao, Castelli, M. G., Ellis J. R., On the low cycle fatigue deformation of haynes 188 superalloy in the dyn amic strain aging regime., Scr. Metall. Mater. 33 (1995) 1005–1012.
- [19] K. Bhanu Sankara Rao, M.G. Castelli, G.P. Allen, J.R. Ellis, A critical assessment of the mechanistic aspects in HAYNES 188 during low-cycle fatigue in the range 25 °C to 1000 °C, Metall. Mater. Trans. A. 28 (1997) 347–361. https://doi.org/10.1007/s11661-997-0137-z.
- [20] A.H. Cottrell, A note on the Portevin-Le Chatelier effect, Philos. Mag. 44 (1953) 829–832. https://doi.org/doi.org/10.1080/14786440808520347.
- [21] A. Van Den Beukel, U.F. Kocks, The strain dependence of static and dynamic strain-aging, Acta Metall. 30 (1982) 1027–1034. https://doi.org/10.1016/0001-6160(82)90211-5.
- [22] A. den Beukel, On the mechanism of serrated yielding and dynamic strain ageing, Acta Metall. 28 (1980) 965–969.
- [23] K.B.S. Rao, M. Valsan, R. Sandhya, S.L. Mannan, P. Rodriguez, An assessment of cold work effects on strain-controlled low-cycle fatigue behavior of type 304 stainless steel, Metall. Trans. A. 24 (1993) 913–924. https://doi.org/10.1007/BF02656512.
- [24] A. Nagesha, R. Kannan, G.V.S. Sastry, R. Sandhya, V. Singh, K. Bhanu Sankara Rao, M.D. Mathew, Isothermal and thermomechanical fatigue studies on a modified 9Cr-1Mo ferritic martensitic steel, Mater. Sci. Eng. A. 554 (2012) 95–104. https://doi.org/10.1016/j.msea.2012.06.021.
- [25] M. Sauzay, H. Brillet, I. Monnet, M. Mottot, F. Barcelo, B. Fournier, A. Pineau, Cyclically induced softening due to low-angle boundary annihilation in a martensitic steel, Mater. Sci. Eng. A. 400–401 (2005) 241–244. https://doi.org/10.1016/j.msea.2005.02.092



CHAPTER 4.3

Probing of Local Mechanical Properties of Friction Stir Welded IN-RAFM Steels of Thicker Sections in As-Received, As-Welded Conditions and Post Weld Normalized Conditions



4.3.1 Introduction:

The energy demand of the world is currently met by some conventional energy harvesting methods and nuclear fission method. The increased current demand can be met only with expanding the extent of energy production from nuclear sources. Nuclear fission is the process which is currently used to harvest energy from radioactive materials. But if nuclear fusion can also be made practical, the harmful effects of fission reactors can be avoided. The materials used in the fabrication of a nuclear fusion reactor demands the reduced activation property to be used in environments of irradiation [1]. Special steels have been designed for meeting these criteria and are named as Reduced Activation Ferritic Martensitic (RAFM) Steels [2–7]. India has also developed its own RAFM steel as part of the International Thermonuclear Experimental Reactor (ITER) program and is designated as IN-RAFM steel[8–10]. This has been designed by eliminating the elements which are having induced radioactivity property out of the conventional nuclear grade Mod. 9Cr-1Mo steel. This steel is having similar composition and properties as that of the other steels viz. CLAM, EUROFER-97, F82H, 9Cr2WTa developed by other collaborating countries like China, Europe, Japan and USA respectively[3–6]. High temperature creep resistance, stable mechanical behavior in irradiation environments and reduced DBTT were the factors which were given major consideration while designing these steels. The currently investigating IN-RAFM steel is a product of continuous research done by India in this field over a period of time[9–11].

The mechanical properties of this alloy has already been investigated by many researchers and the alloy possess good strength at high temperatures as well. The weldability of this alloy has been studied mainly using Electron Beam Welding (EBW) and Friction Stir Welding (FSW) and the results are quite interesting[12–16]. In EBW the phase change because of the high heat input and faster cooling rate had led to the formation of delta-ferrite which is a deleterious phase. FSW was tried for the first time on IN-RAFM plates of 6 mm thickness and defect free welds were obtained[14]. The study was also able to optimize the process parameters for FSW to get the best mechanical properties out of the weldment. Considerable increase in hardness was observed at the weld center which was homogenized using post weld heat treatment. The dissolution of carbides at the weld center due to the high heat during FSW was the reason for the increased hardness

In the study done by M. Vijayalakshmi et. al.[16] in which EBW has been carried out followed by the microstructural and mechanical properties investigation, it has been observed that the weld zone was comprised of delta ferrite which is a deleterious phase in case of steels when the mechanical properties are considered. The weld zone processed higher hardness compared to the base metal region which was not able to be homogenized using the PWDT process but was successfully homogenized using the PWNT process. Solid state welding - Friction Stir Welding (FSW) was reported for the first time in which a bead-on-plate weld on thicker plates were performed successfully without any defect and without the presence of any delta ferrite phase in the weldment by M. Vijayalakshmi et. al. [13–15]. Thermographic measurements have established the interphase temperatures experienced in the weldment while welding and was helpful in establishing the optimized welding speed for better mechanical and microstructural properties. For 6mm thick plates a tool rotational speed of 200 rpm and tool traverse speed of 30 mm.min⁻¹ was established as a best combination of these two parameters. 12mm thick plates were welded at speeds of 500 and 900 rpm at a traverse speed of 20 mm.min⁻¹ and could establish defect free welds. Preliminary mechanical property studies were performed in both these thicknesses.

In a previous study performed on the same alloy of 12mm thickness by J. Varghese et. al., where tensile tests on friction stir welded specimens are performed at room temperature and high temperature, dynamic strain ageing (DSA) is observed. The reduction of tensile elongation at an intermediate temperature regime in the range of study has been explained based on the phenomenon of DSA which was observed without the occurrence of serrations in the tensile flow curve. The study also established that the interphase temperature during FSW is a function of section thickness also[17].

Nanoindentation is a technique established by the end of the 21st century by Oliver and Pharr [18] as a novel technique to evaluate the hardness and modulus of a material using a load and depth sensing indentation method. Figure 4.3.1(a) shows the schematic of a nanoindentation setup. The Indenter or the tip mounted on a spring loaded plate placed between a capacitive transducer applies load on to the sample mounted on a movable stage. The resistance offered by the sample to indentation alters the plate spacing in the capacitive arrangement which in turn reflects in the voltage output. This is calibrated and the load applied on the sample and the depth of penetration is estimated. The tip used in this study is Berkovich tip which is having a three sided pyramidal shaped geometry as shown in Figure 4.3.1(b).

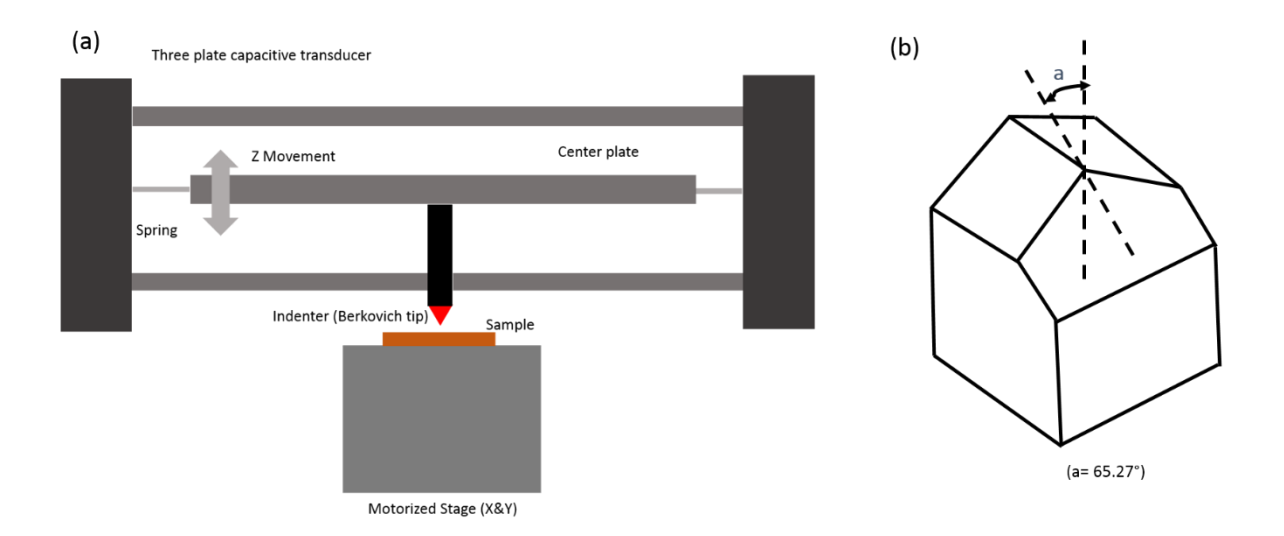


Figure 4.3.1(a) Nanoindentation system schematic, (b) Berkovich Tip geometry

Nanoindentation studies on RAFM steels has been carried out mainly to study the irradiation effects on hardness and nanomechanical properties of the material. The studies conducted on EUROFER [19,20] and F82H[21] studies show the increase in the nanohardness values after irradiation to different extents. The effect of indentation size effect (ISE) and the mechanisms behind it are also discussed.

Strain rate sensitivity being estimated from nanomechanical testing has been attempted by several researchers. A study on strain rate sensitivity using nanoindentation on arc welded SM490 steel showed the depth dependent variation of SRS and hardness values. The weldment exhibited reduced SRS compared to the base metal region[22]. Another study on a dual phase steel containing martensite and austenite, the SRS was studied by varying the loading rate. It showed the high SRS value in the ultrafine grained steel and the effect of twinning and dislocation slip systems as the governing mechanisms[23].

A study on SRS of friction stir welded RAFM steel using nanoindentation has not been reported in any variant of RAFM steel till date. The present study deals with the friction stir welding of IN-RAFM plates of 6 and 12 mm thickness and its mechanical properties investigated using nanoindentation technique in the as-received and as-welded conditions. The results of the study are compared with bulk behavior of the sample as well.

4.3.2 Experimental Procedure:

IN-RAFM steel plates of thickness 6 and 12 mm were supplied in the rolled condition. The asreceived material is in tempered martensitic structure. The 6 mm plates were subjected to FSW at 200 rpm and 30mm.min⁻¹ and 12 mm plates were welded at 200 rpm and 15mm.min⁻¹ speed. The welded plates were subjected to a normalizing heat treatment at 1253 K for 30 minutes followed by a tempering heat treatment at 1033 K for 90 minutes.

Welded plates were sectioned in orthogonal direction using EDM to get all the weld zones for analysis. Samples in the as-welded (AW) and post weld normalized and tempered (PWNT) conditions were selected for the analysis. The sectioned samples were hot mounted in Bakelite powder using a QATM Opal 410 hot mounting press. The mounted samples were polished using SiC emery papers starting from grit size of 120 to 2000 and then with diamond paste of particle size 8.0 - 0.25 microns. The samples were subjected to vibratory polishing in colloidal silica of particle size 0.05 microns for a duration of 14 hours using a QATM Saphir Vibro. Vibratory polishing is a very gentle material removing polishing process which helps in removing the damaged grains from the surface and helps to prepare samples without deformation.

(A) Nanohardness estimation by high speed nanoindentation

The polished samples were subjected to high throughput nanoindentation using an iMicro Nanoindentor manufactured by M/s. Nanomechanics Inc., Oakridge, USA available at International Advanced Research Centre for Powder Metallurgy and New Materials (ARCI), Hyderabad, India. Nanoindentation maps of 50*50 matrix were performed using NanoBliz 3D fast indentation and property mapping technique. It uses the Inforce50 actuator to do 3D mapping on samples using a Berkovich tip. The time taken for each test is less than 1s which is inclusive of the time for positioning the tip over the sample, approaching the sample, loading, unloading and withdrawal of the tip. A load of 1.75mN was applied with a spacing of 1 micron given between the indents based on the study done by S. Phani et.al [24]. This study discusses about the least spacing to be given from indent to indent in-order to avoid effect of neighboring indents to get mechanical properties accurately. The locations for the mapping was chosen based on the Continuous Stiffness Method (CSM) indents performed at locations of 2mm distance. These indents were able to distinguish the regions with hardness variation which corresponds to different weld zones. This was done as it is difficult to distinguish the weld zones in a mirror finished sample without etching.

Chapter 4.3 Results and Discussion

(B) Strain rate sensitivity study using nanoindentation

Strain rate sensitivity was studied by performing nanoindentation on a M/s. Hysitron TI950 Triboindenter machine. The polished specimens were subjected to nanoindentation at the base-metal and stir zone (SZ) regions to study the strain rate sensitivity (SRS) in the as-welded and post weld heat treated condition. This is achieved by applying different loading rates while keeping the peak load constant. A 7x7 matrix consisting of a total 49 indents were performed in each loading rate and the average value was taken for the calculations. Figure 4.3.1 shows the trapezoidal load function used for the nanoindentation study at different loading rates. The loading rate and unloading rate is kept identical in each set. A dwell time (holding time) of 30 s was given in each loading cycle so as to reduce the effect of prior loading history on the unloading curve. Nanohardness is estimated from the unloading curves using the Oliver and Pharr method[18]. Mathematical calculations were used to evaluate the strain rate sensitivity (m) out of the nanohardness values. Strain Rate Sensitivity, m is obtained from the slope of $\ln (\sigma)$ vs. $\ln (\varepsilon)$ plot[25].

Where,

 $\sigma = H/3$ (H-Nanohardness in GPa)

 $\dot{\varepsilon}$ = Loading Rate/Peak Load

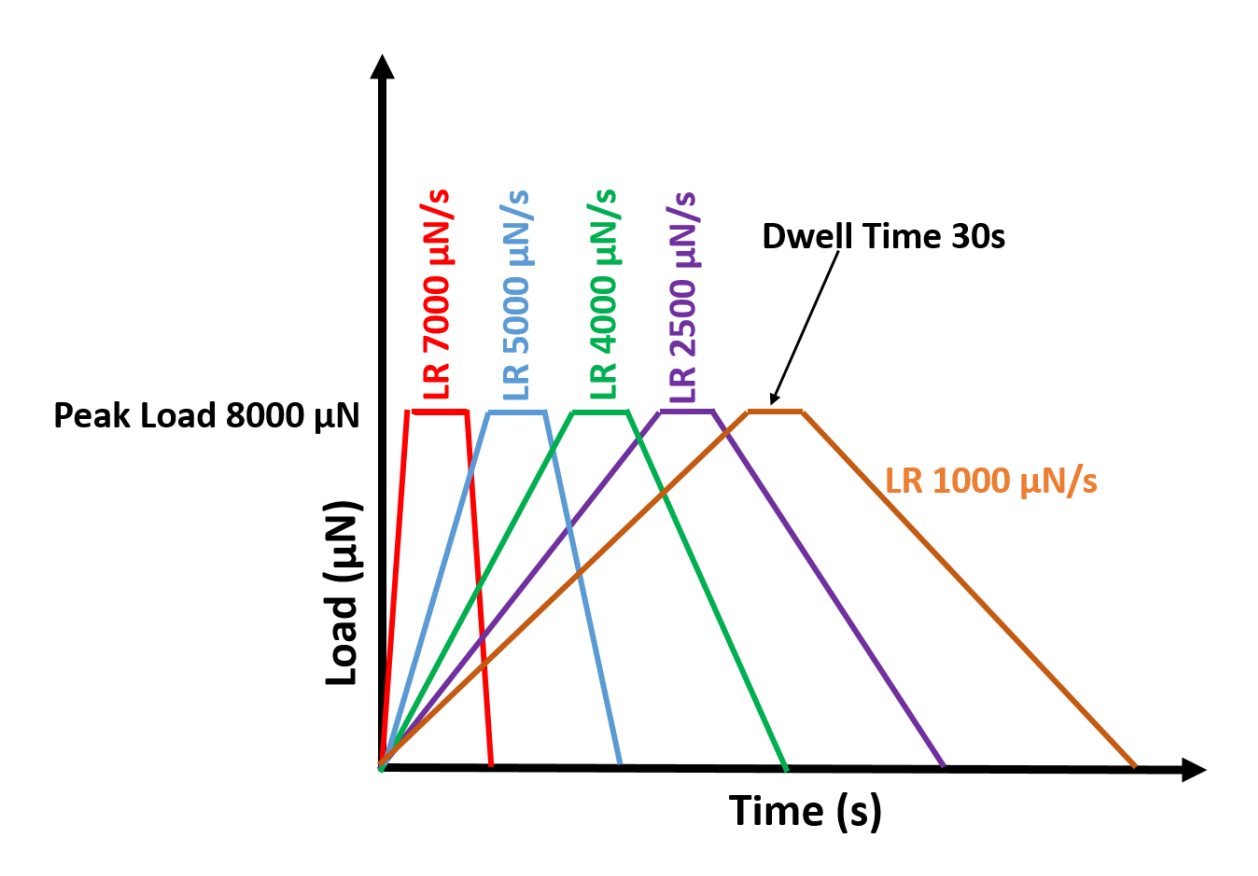


Figure 4.3.2. Trapezoidal load function used to study loading rate effect

(C) Strain rate sensitivity from bulk sample testing

Strain rate jump tests were performed on bulk tensile specimen machined from the IN-RAFM steel plate in the as-received (AR) and as-welded (AW) condition. This was performed by giving increments in the cross head speed (CHS) values of the UTM machine. Mathematical calculations (Eqn. 2) are done to estimate the strain rate sensitivity values out of the stress-strain curve obtained from the jump test. This kind of study dealing with bulk material property being compared to nanomechanical property is being reported for the first time.

Strain Rate Sensitivity, m=
$$\frac{\log \frac{\sigma_2}{\sigma_1}}{\log \frac{\dot{\epsilon}_2}{\dot{\epsilon}_1}}$$
(2)

Where,

 σ_1 , σ_2 - Stress before and after the jump respectively

 $\acute{\epsilon}_{1},\, \acute{\epsilon}_{2}\text{-}$ Strain rate before and after the jump respectively

4.3.3 Results and Discussion:

The as-received material has a tempered martensitic microstructure as shown in the Figure 4.3.2. The presence of MX type carbides within the grains which are rich in Ta, V and $M_{23}C_6$ carbides along the grain boundaries which are rich in Cr, play a vital role in controlling the deformation behavior of the steel. These carbides act as grain boundary pinning agents impeding the grain boundary sliding as well as block the dislocation movement and improve the creep properties of the material at elevated temperatures[11]. The average grain size of in the as-received condition was estimated to be 7 microns.

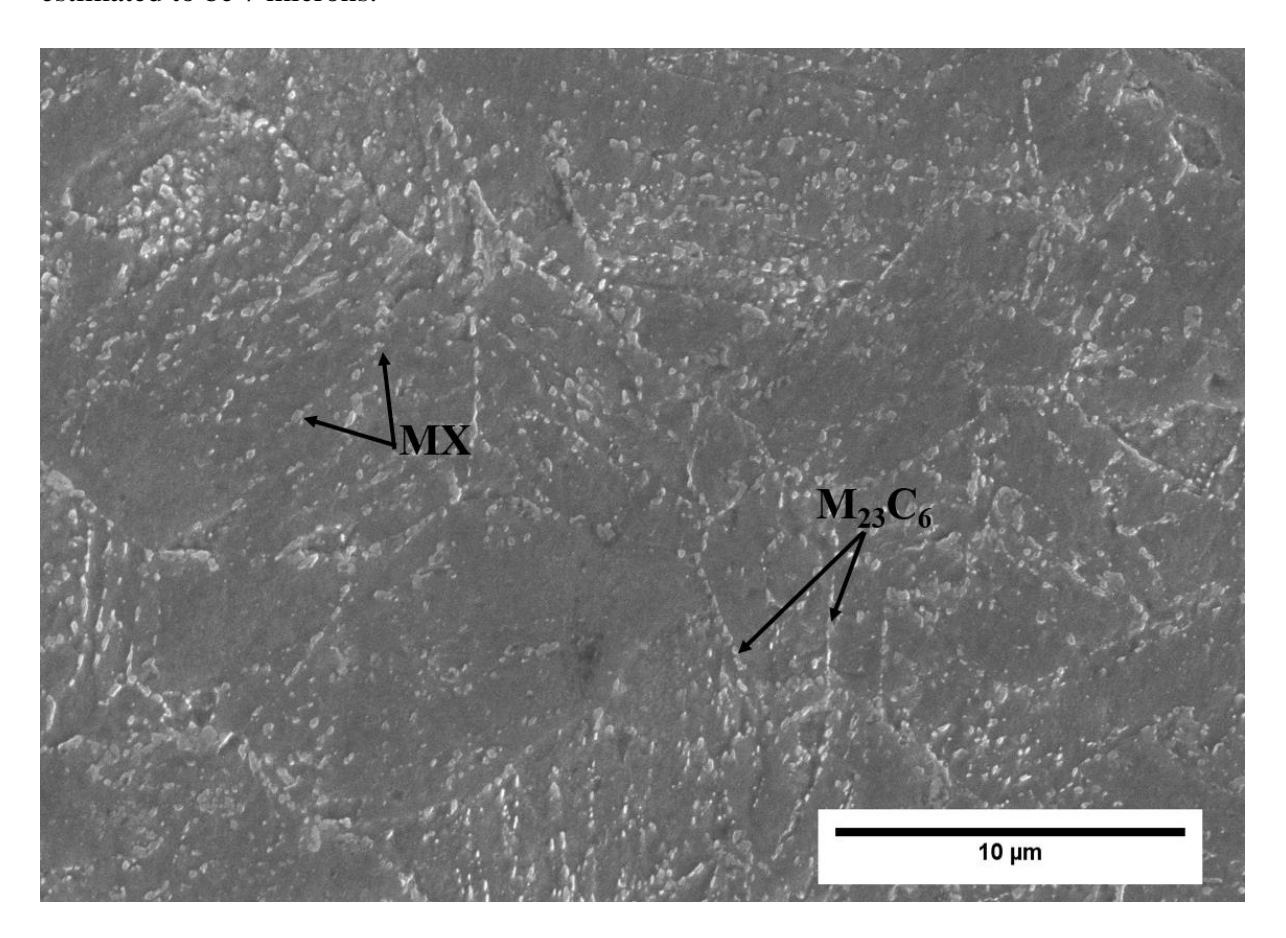


Figure 4.3.3. As-received microstructure of IN-RAFM steel

(A) Nanohardness from high speed nanoindentation

CSM tests were performed as a guide to fix the locations for high speed hardness mapping. The distinct zones of the weldment exhibiting variation in hardness values were located on the mirror finished sample using CSM tests. The nanohardness values are higher than the micro hardness

values obtained before. This is due to the effect of the precipitates which are in nano scale that are harder offering more resistance to the nano sized tip during indentation.

The results of the CSM indents performed on each sample at different weld zones are shown in Figure 4.3.4. Clear difference in the hardness values in the base-metal and the SZ region was observed. The hardness of the SZ region at the center of the weld is high and towards the BM region it falls. The trend resembles to the bell shaped curve. The SZ is observed to be hard compared to the BM due to the presence of the martensite, undissolved MX carbides, the newly formed Fe3C and increased dislocation density due to the FSW process. As the distance from the center of the weld increases and proceeds towards the unaffected BM region, there is a drop in the hardness value. In the 6mm welded sample, in the advancing side (AS) there is a drop in the hardness value near to the interphase between TMAZ and BM which is the HAZ region which is a thin region whereas in the case of thicker 12mm welded plates, this HAZ region is very evident. The AS side experiences prolonged exposure to the heating effects due to FSW which leads to over tempering of the microstructure and can create coarsening and coagulation of the grain boundary carbides. This can be attributed to the reason for the dip in the hardness profile. To homogenize the microstructural and mechanical properties, it's suggested to do appropriate post weld heat treatment to the weldment. The homogenization of the hardness after the PWNT is visible from the flattening of the hardness curve (Figure 4.3.4). After PWNT the hardness values follow the same trend as that of the as-received condition and has very slight variations in the SZ and BM region. The dissolved M₂₃C₆ carbides were re-precipitated on grain and martensite lath boundaries after PWNT. This is very much crucial in creating more homogeneous and uniform microstructure within SZ, TMAZ and HAZ zones. The microstructure in these zones resembled the AR condition after PWNT. The uniform hardness acquired after PWNT is concomitant with this homogenization process.

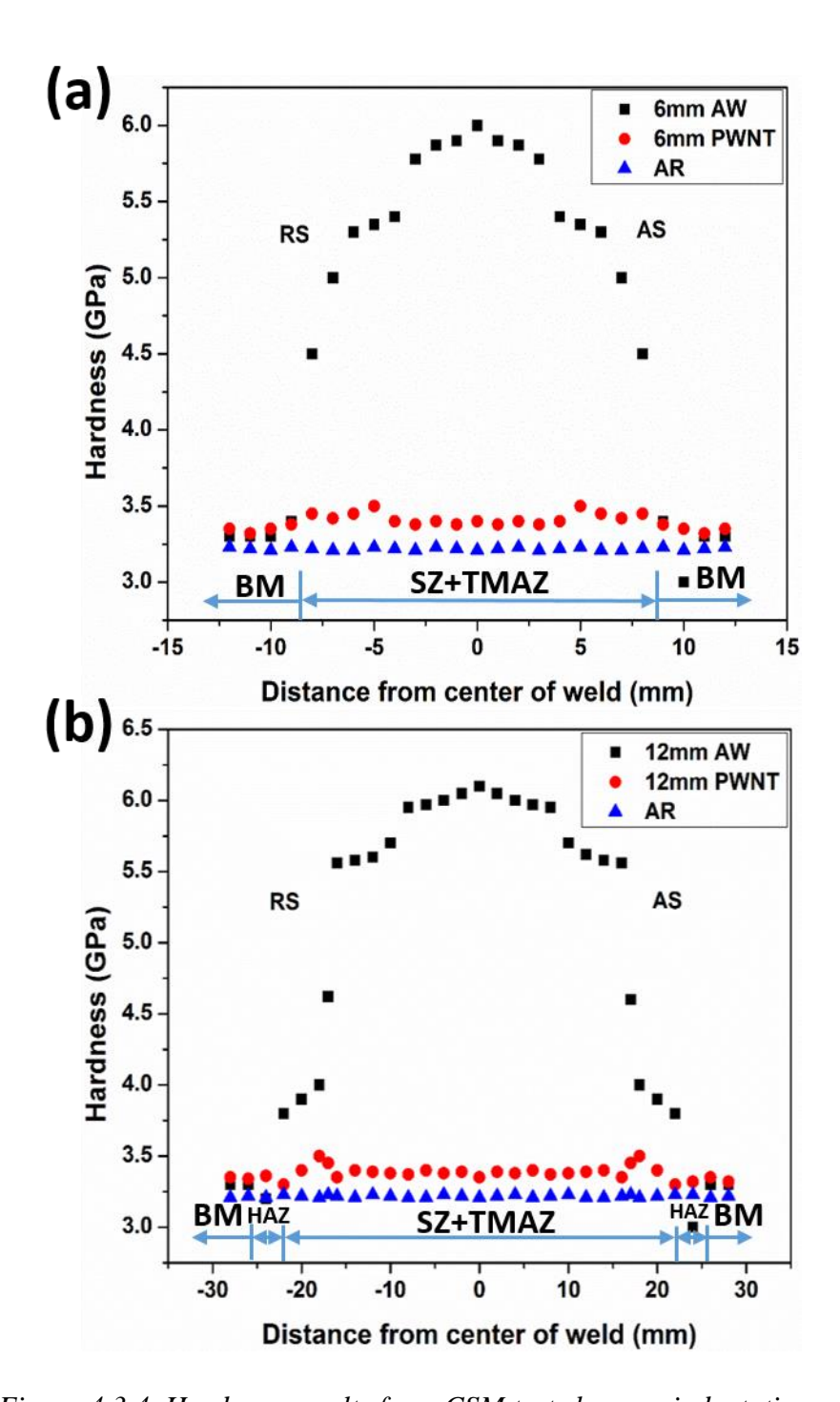


Figure 4.3.4. Hardness results from CSM tests by nanoindentation

(a) 6mm sample, (b) 12mm sample

The nanoindentation mapping was done at three locations corresponding to each region (SZ, TMAZ/HAZ & BM) based on the distance from the center of the weld taken from CSM tests.

The nanoindentation maps of 6 mm welded plates in the AW condition is shown in Figure 4.3.5. A detailed interphase temperature study in the SZ at 200 rpm speed by M. Vijayalakshmi et.al[14] established that it is below lower critical temperature, $Ac_1(818 \,^{\circ}\text{C})$. Even though this temperature is not enough for the formation of Fe₃C due to transformation of α - γ , the increased dislocation density and non-equilibrium vacancies created due to the plastic deformation during FSW accelerates the diffusion of solute atoms leading to the formation of Fe₃C. This is aided by the fragmentation of $M_{23}C_6$ carbides due to FSW to subcritical level leading to solid state dissolution that leaves the matrix supersaturated with carbon[14].

The FE-SEM micrographs of the mapped region is also shown along with the respective maps. On a comparative study of the FESEM micrographs of the SZ and the hardness map, it can be understood that, the region where the presence of martensite, Fe₃C and increased dislocation density is located are the regions which are exhibiting higher hardness. As indentation hardness is sensitive to depth of penetration, these harder phases impart more resistance to the penetration of the nano sized tip.

The TMAZ region can be observed to show few regions with higher hardness similar to SZ. This is due to the presence of dissolved carbides in regions near to the SZ where higher temperature was experienced. The BM shows region unaffected with the stirring/heating effects of the FSW that shows hardness values similar to the material in the AR condition.

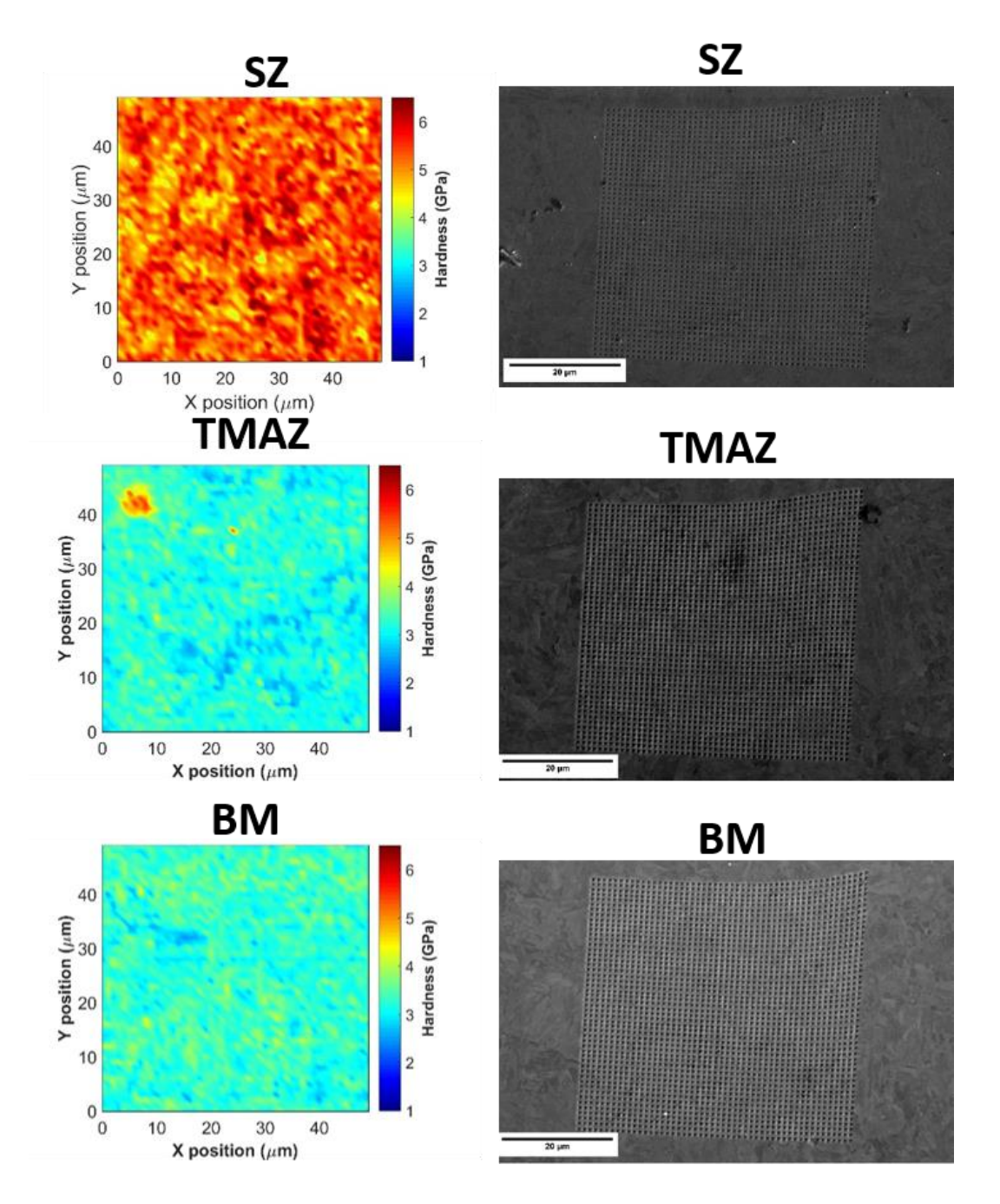


Figure 4.3.5. Nanoindentation maps of 6 mm AW plates

The nanoindentation maps of 6 mm welded plates in the PWNT condition is shown in Figure 4.3.6. The hardness of the weldment is observed to have homogenized after the heat treatment process with all the mapped regions exhibiting similar color codes. Certain regions of higher hardness can be observed in all the maps which correspond to the carbides in the grain boundary and the matrix. As these carbides are in nano size range, the mapping process is able to indent specifically on these carbides also which is observed as regions of higher hardness.

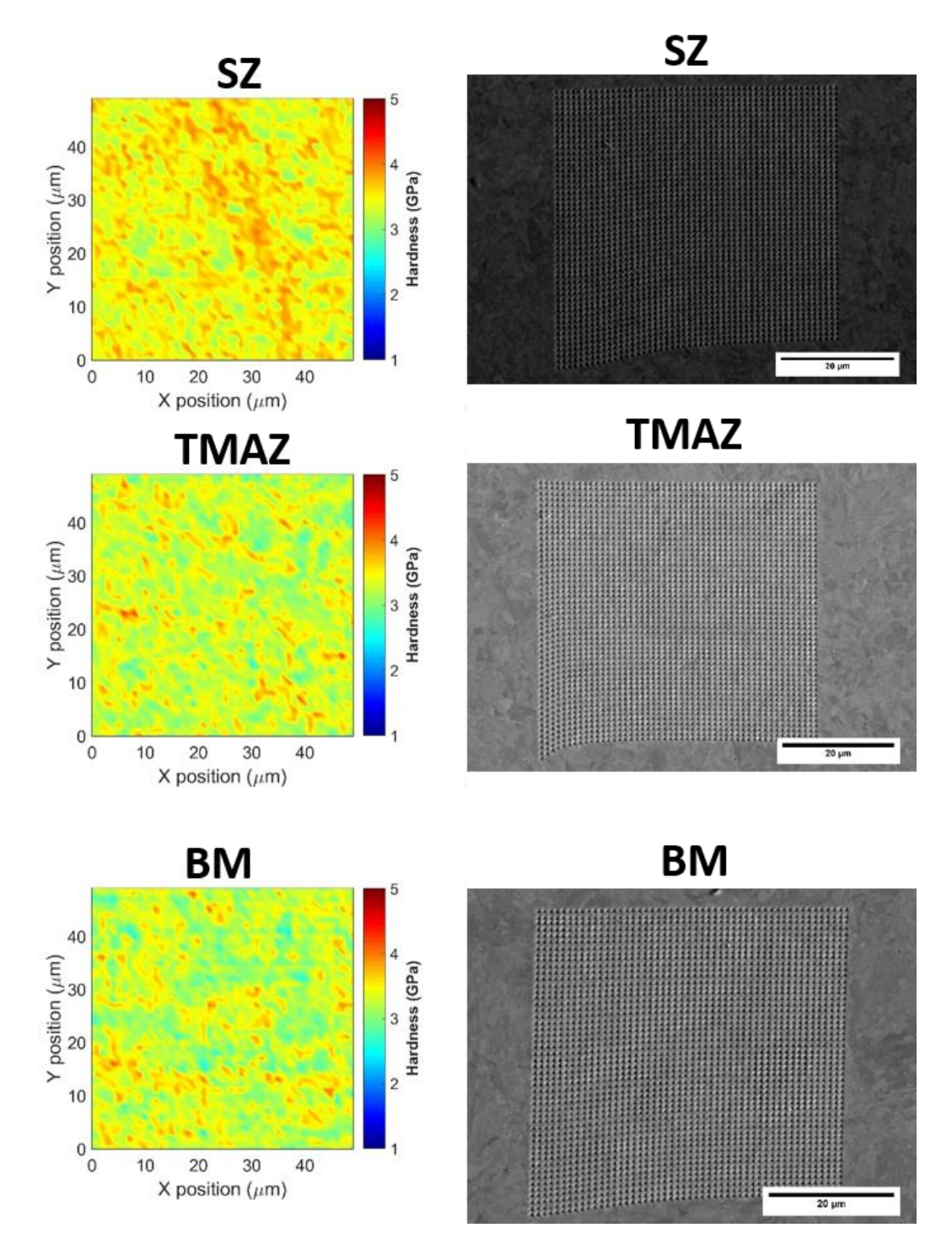


Figure 4.3.6. Nanoindentation maps of 6 mm PWNT plates

The nanoindentation maps of 12 mm welded plates in the AW condition is shown in Figure 4.3.7.

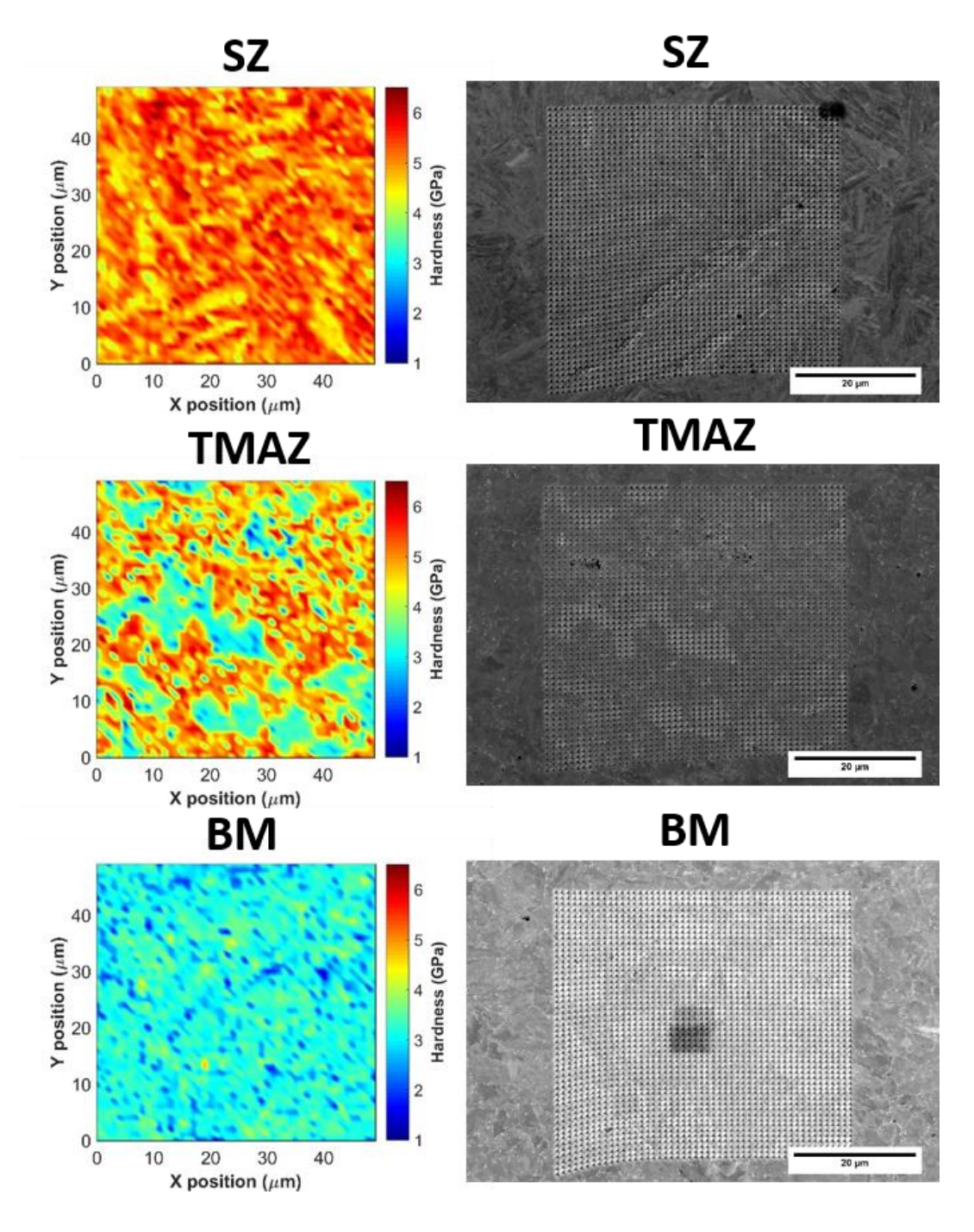


Figure 4.3.7. Nanoindentation maps of 12 mm AW plates

The nanoindentation maps of 12 mm welded plates in the PWNT condition is shown in Figure 4.3.8. The hardness of the weldment is observed to have homogenized after the heat treatment process.

The hardness of the 6 and 12 mm plates were observed to be nearly the same in the AW and PWNT conditions. This can be due to the similar temperature effects experienced in the plates during the welding process irrespective of the plate thickness.

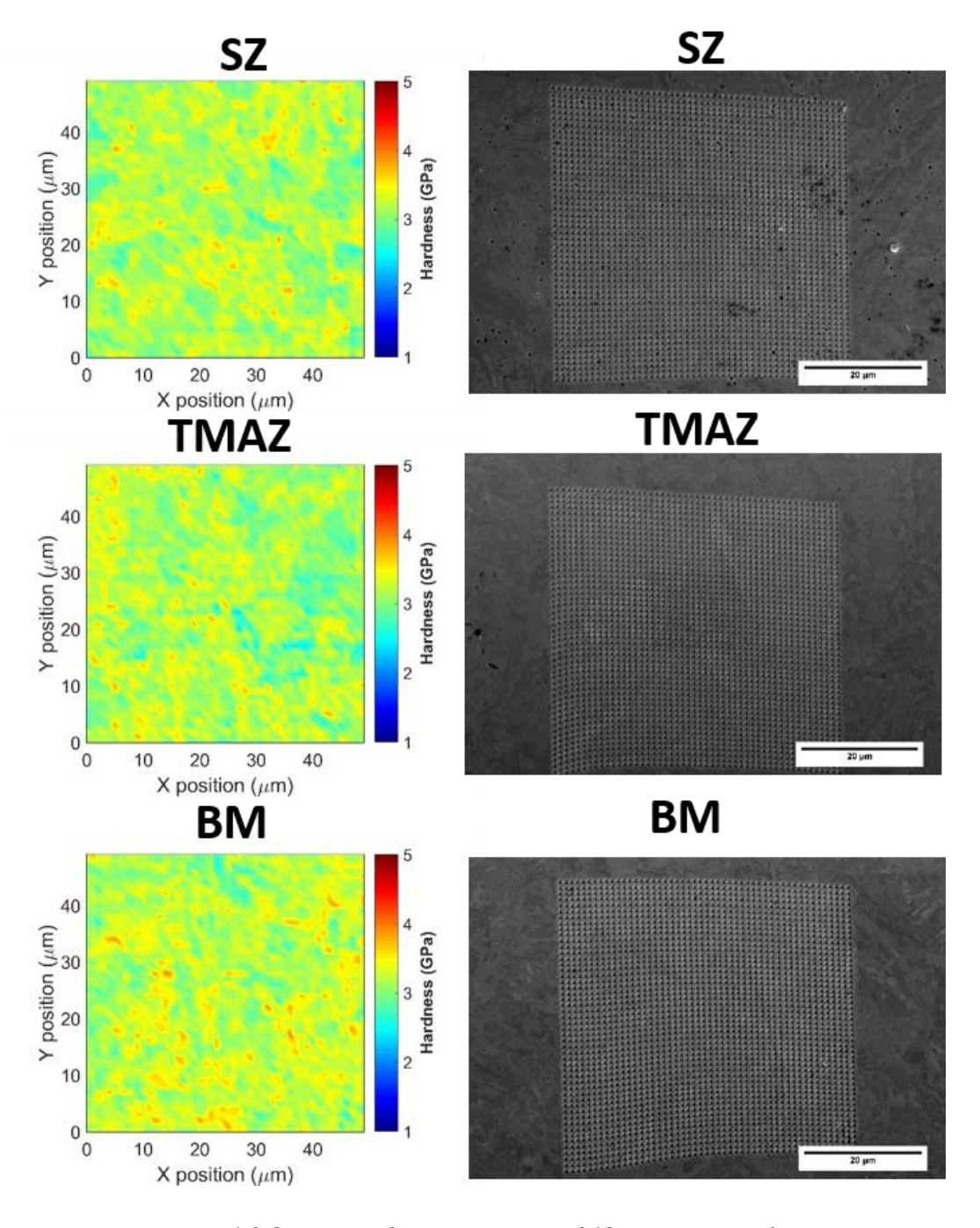


Figure 4.3.8. Nanoindentation maps of 12 mm PWNT plates

(B) Strain rate sensitivity from nanoindentation

The strain rate sensitivity of the BM region of the 6mm welded sample calculated from the nanoindentation results are shown in Figure 4.3.9. The SRS estimated from the slope of $\ln(\sigma)$ vs $\ln(\epsilon)$ plot gives a value of 0.02.

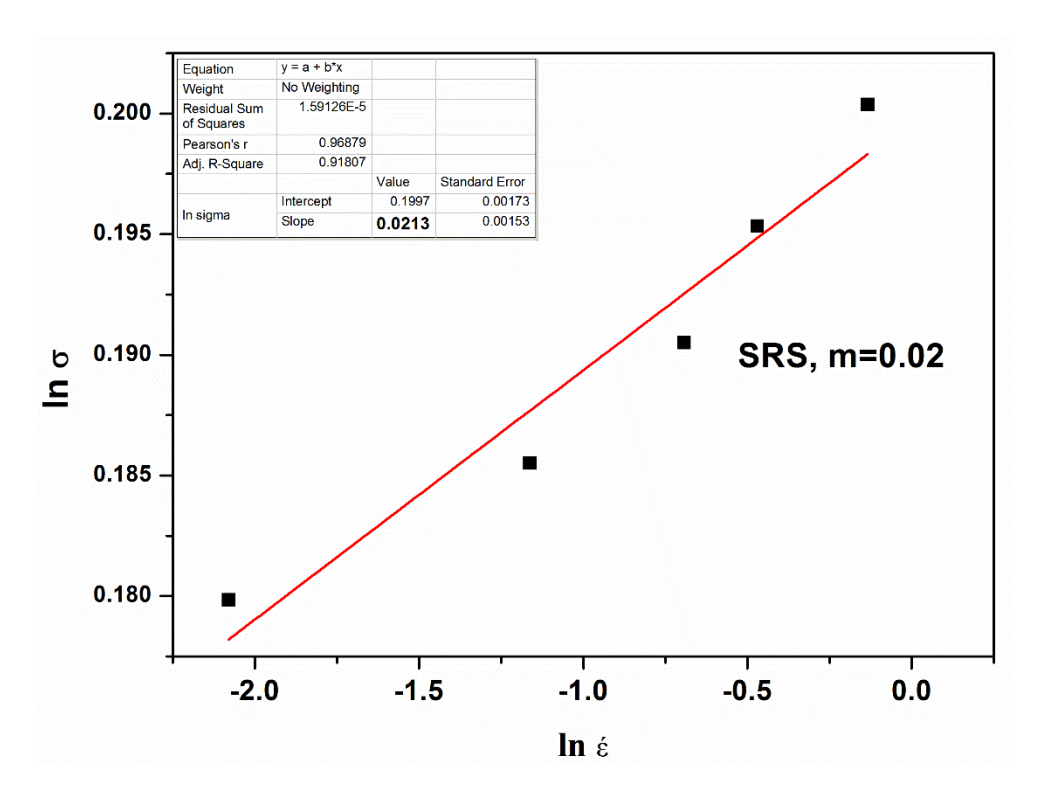


Figure 4.3.9. SRS estimated from $ln(\sigma)$ vs $ln(\dot{\varepsilon})$ plot of the AW sample in the BM region

Figure 4.3.10 shows the SRS estimation from slope of $ln(\sigma)$ vs $ln(\acute{\epsilon})$ plot of the nanoindentation tests done on the stir zone (SZ) region of the AW sample (6mm). The SRS has decreased in the SZ region and is 0.01. As SRS is a measure of the easiness in deforming the material, the reduction in its value attributes to the increased strength and hardness of the SZ in the weldment.

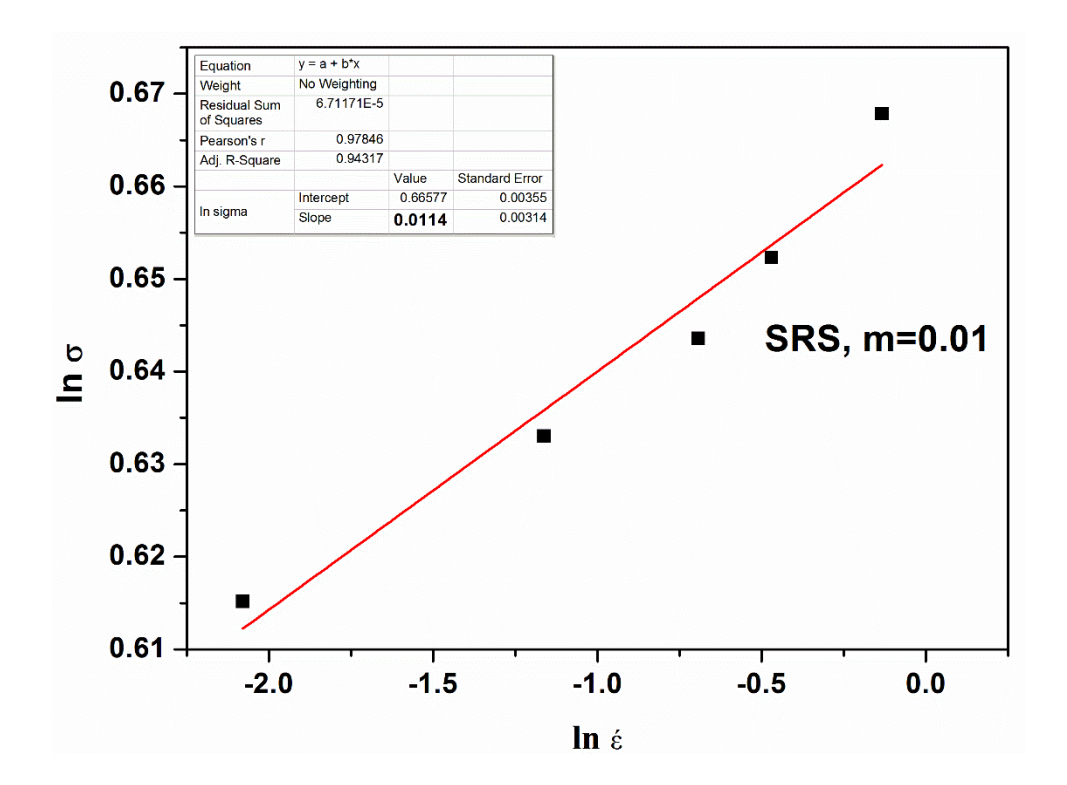


Figure 4.3.10. SRS estimated from $ln(\sigma)$ vs $ln(\dot{\epsilon})$ plot of the AW sample in the SZ region

(C) Strain rate sensitivity from bulk testing

The strain rate jump tests done on the UTM using tensile specimen in the as-received (AR) and as-welded (AW) condition was able to give an estimation of the strain rate sensitivity of the bulk sample. The Stress-strain plots and the estimated SRS values of the AR and AW material are shown in Figure 4.3.11. The values match closely with slightly higher value in the AR condition. The values fall much close because of the fracture that happened in the base metal (BM) region in the AW condition. As the sample has fractured outside the SZ region away from the weldment, the properties are much influenced by the BM region.

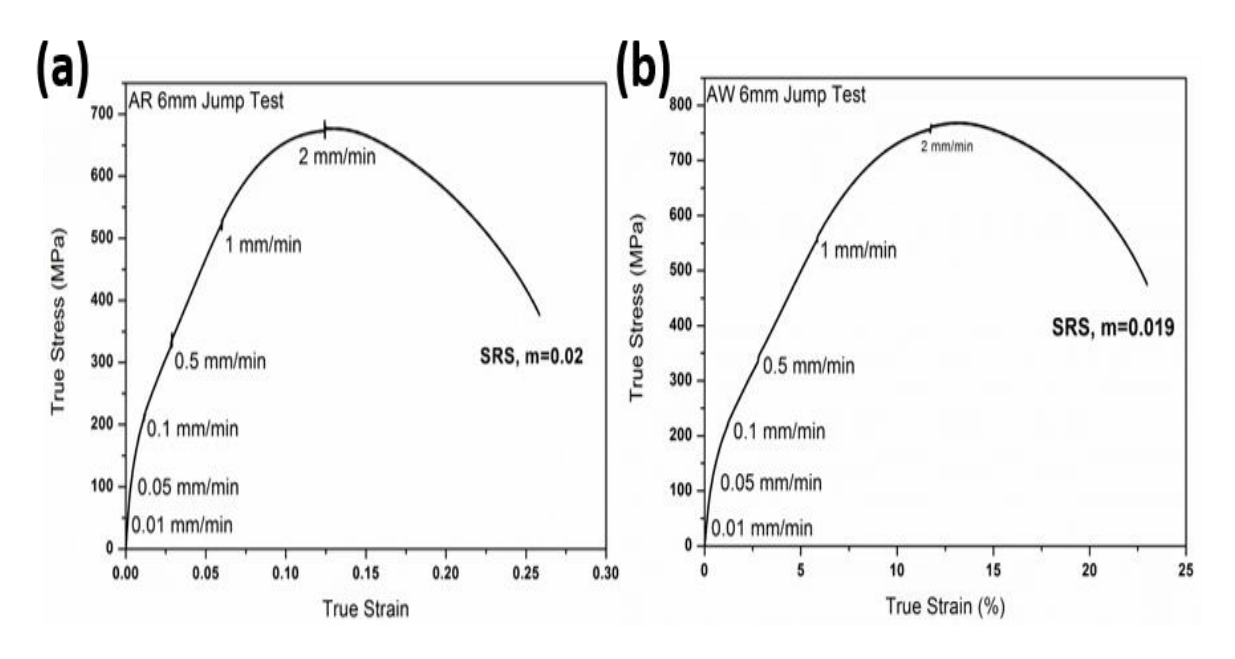


Figure 4.3.11. Stress-Strain plots and SRS value of (a) as-received material, (b) as-welded material

The SRS value of the BM region estimated using nanoindentation matches with that of the bulk behavior of the sample in the as-received condition. Whereas, there is difference in the values when compared between the SZ and BM region or the SZ and AR condition. During FSW process, the microstructure of the SZ region undergo recrystallization and refinement. The mechanical straining by the tool will induce stresses also in the SZ region. This has affected the SRS of the SZ region which was able to be detected by the nanoindentation method. But when it comes to the bulk behavior of the weldment, the deformation is happening in the BM region because of which the bulk behavior of the SZ region was not able to be estimated. The FSW process performed on the RAFM steel has reduced the formability of the material. Post weld heat treatments suggested for the weldment can be performed to homogenize the mechanical properties of the weldment.

The post weld normalizing and tempering (PWNT) treatment was done to homogenize the weld microstructure and thereby the mechanical properties on the weldment. Studies on the hardness and tensile properties have proved that this heat treatment process was successful in achieving the properties similar to the base-metal. The carbides which were dissolved in the SZ region got reprecipitated and the microstructure resembled that of the parent metal after PWNT process.

4.3.4 Conclusions:

- The IN-RAFM steel welded using FSW was subjected to high throughput nanoindentation mapping and maps were obtained in the AW and PWNT conditions in plates of 6 and 12 mm thickness from different regions of the weldment.
- The maps were able to show the hardness variation in different phases of the material in the AW and PWNT condition.
- Higher hardness region in the AW conditions indicate the increased hardness due to the dissolved carbides and it has been homogenized to the base metal condition after PWNT.
- Nanoindentation at constant peak load and different loading rates was used as a tool to estimate strain rate sensitivity at different weld regions.
- Strain rate sensitivity (SRS) estimated mathematically from the nanohardness values gave m=0.02 in the BM region and m=0.01 in the SZ region.
- The values of the SZ region has reduced because of the strain hardening due to FSW and grain refinement.
- The SRS estimated from strain rate jump test performed using bulk sample in a UTM gave a value of m=0.019 in the as-welded condition and m=0.02 in the as-received condition.
- The values of the bulk behavior fall nearly matching because of the fracture that has happened in the BM region in AW condition.
- The SRS estimated using nanoindentation and strain rate jump test match exactly in the AR condition and in the BM region.
- Post weld heat treatments are suggested to homogenize the mechanical behavior of the weldment.
- The post weld heat treatment process, PWNT is proved to have homogenized the weld mechanically. The nanohardness of the SZ region which was ~6.0 GPa has been brought to ~3.5-4 GPa (base metal hardness) through the PWNT process.
- An analysis of this kind comparing the nanomechanical response towards varying loading rate and bulk response towards varying strain rate is being reported for the first time in this alloy.

References:

- [1] J.M. Vitek, R.L. Klueh, Precipitation reactions during the heat treatment of ferritic steels, Metall. Trans. A. 14 (1983) 1047–1055. https://doi.org/10.1007/BF02670443.
- [2] N. Baluc, D.S. Gelles, S. Jitsukawa, A. Kimura, R.L. Klueh, G.R. Odette, B. van der Schaaf, J. Yu, Status of reduced activation ferritic/martensitic steel development, J. Nucl. Mater. 367-370 A (2007) 33–41. https://doi.org/10.1016/j.jnucmat.2007.03.036.
- [3] H. Tanigawa, K. Shiba, A. Möslang, R.E. Stoller, R. Lindau, M.A. Sokolov, G.R. Odette, R.J. Kurtz, S. Jitsukawa, Status and key issues of reduced activation ferritic/martensitic steels as the structural material for a DEMO blanket, J. Nucl. Mater. 417 (2011) 9–15. https://doi.org/10.1016/j.jnucmat.2011.05.023.
- [4] H. Tanigawa, T. Hirose, K. Shiba, R. Kasada, E. Wakai, H. Serizawa, Y. Kawahito, S. Jitsukawa, A. Kimura, Y. Kohno, A. Kohyama, S. Katayama, H. Mori, K. Nishimoto, R.L. Klueh, M.A. Sokolov, R.E. Stoller, S.J. Zinkle, Technical issues of reduced activation ferritic/martensitic steels for fabrication of ITER test blanket modules, Fusion Eng. Des. 83 (2008) 1471–1476. https://doi.org/10.1016/j.fusengdes.2008.07.024.
- [5] J. Yu, Q. Huang, F. Wan, Research and development on the China low activation martensitic steel (CLAM), J. Nucl. Mater. 367-370 A (2007) 97–101. https://doi.org/10.1016/j.jnucmat.2007.03.236.
- [6] Q. Huang, C. Li, Y. Li, M. Chen, M. Zhang, L. Peng, Z. Zhu, Y. Song, S. Gao, Progress in development of China Low Activation Martensitic steel for fusion application, J. Nucl. Mater. 367-370 A (2007) 142–146. https://doi.org/10.1016/j.jnucmat.2007.03.153.
- [7] B. Van Der Schaaf, D.S. Gelles, S. Jitsukawa, A. Kimura, R.L. Klueh, A. Möslang, G.R. Odette, Progress and critical issues of reduced activation ferritic/martensitic steel development, J. Nucl. Mater. 283–287 (2000) 52–59. https://doi.org/10.1016/S0022-3115(00)00220-8.
- [8] B. Raj, K.B.S. Rao, A.K. Bhaduri, Progress in the development of reduced activation ferritic-martensitic steels and fabrication technologies in India, Fusion Eng. Des. 85 (2010) 1460–1468. https://doi.org/10.1016/j.fusengdes.2010.04.008.

- [9] K. Laha, S. Saroja, A. Moitra, R. Sandhya, M.D. Mathew, T. Jayakumar, E. Rajendra Kumar, Development of India-specific RAFM steel through optimization of tungsten and tantalum contents for better combination of impact, tensile, low cycle fatigue and creep properties, J. Nucl. Mater. 439 (2013) 41–50. https://doi.org/10.1016/j.jnucmat.2013.03.073.
- [10] S. Raju, B. Jeya Ganesh, A.K. Rai, R. Mythili, S. Saroja, E. Mohandas, M. Vijayalakshmi, K.B.S. Rao, B. Raj, Measurement of transformation temperatures and specific heat capacity of tungsten added reduced activation ferritic-martensitic steel, J. Nucl. Mater. 389 (2009) 385–393. https://doi.org/10.1016/j.jnucmat.2009.02.030.
- [11] J. Vanaja, K. Laha, M.D. Mathew, T. Jayakumar, E. Rajendra Kumar, Effects of tungsten and tantalum on creep deformation and rupture properties of Reduced Activation Ferritic-Martensitic steel, Procedia Eng. 55 (2013) 271–276. https://doi.org/10.1016/j.proeng.2013.03.253.
- [12] C.R. Das, S.K. Albert, S. Sam, P. Mastanaiah, G.M.S.K. Chaitanya, A.K. Bhaduri, T. Jayakumar, C.V.S. Murthy, E.R. Kumar, Mechanical properties of 9Cr-1W reduced activation ferritic martensitic steel weldment prepared by electron beam welding process, Fusion Eng. Des. 89 (2014) 2672–2678. https://doi.org/10.1016/j.fusengdes.2014.07.001.
- [13] V.L. Manugula, K. V. Rajulapati, G.M. Reddy, R. Mythili, K. Bhanu Sankara Rao, Influence of Tool Rotational Speed and Post-Weld Heat Treatments on Friction Stir Welded Reduced Activation Ferritic-Martensitic Steel, Metall. Mater. Trans. A Phys. Metall. Mater. Sci. 48 (2017) 3702–3720. https://doi.org/10.1007/s11661-017-4143-5.
- [14] V.L. Manugula, K. V. Rajulapati, G. Madhusudhan Reddy, R. Mythili, K. Bhanu Sankara Rao, A critical assessment of the microstructure and mechanical properties of friction stir welded reduced activation ferritic-martensitic steel, Mater. Des. 92 (2016) 200–212. https://doi.org/10.1016/j.matdes.2015.12.019.
- [15] V.L. Manugula, K. V. Rajulapati, G.M. Reddy, E. Rajendra Kumar, K.B.S. Rao, Friction stir welding of thick section reduced activation ferritic–martensitic steel, Sci. Technol. Weld. Join. 23 (2018) 666–676. https://doi.org/10.1080/13621718.2018.1467111.
- [16] V.L. Manugula, K. V. Rajulapati, G.M. Reddy, K.B.S. Rao, Role of evolving

- microstructure on the mechanical properties of electron beam welded ferritic-martensitic steel in the as-welded and post weld heat-treated states, Mater. Sci. Eng. A. 698 (2017) 36–45. https://doi.org/10.1016/j.msea.2017.05.036.
- [17] J. Varghese, K. V. Rajulapati, K.B.S. Rao, A. Chavan N, S.D. Meshram, G.M. Reddy, Characterization of Microstructure and Mechanical Properties of Friction Stir Welded Reduced Activation Ferritic-Martensitic Steel in As-Received, As-Welded and Post Weld Heat Treated States, Trans. Indian Inst Met. (2022). https://doi.org/DOI: 10.1007/s12666-022-02628-z.
- [18] W.C. Oliver, G.M. Pharr, An improved technique for determining hardness and elastic modulus using load and displacement sensing indentation experiments, J. Mater. Res. 7 (1992) 1564–1583. https://doi.org/10.1557/JMR.1992.1564.
- [19] F. Bergner, G. Hlawacek, C. Heintze, Helium-ion microscopy, helium-ion irradiation and nanoindentation of Eurofer 97 and ODS Eurofer, J. Nucl. Mater. 505 (2018) 267–275. https://doi.org/10.1016/j.jnucmat.2017.07.054.
- [20] M. Roldán, P. Fernández, J. Rams, F.J. Sánchez, A. Gómez-Herrero, Nanoindentation and TEM to study the cavity fate after post-irradiation annealing of he implanted EUROFER97 and EU-ODS EUROFER, Micromachines. 9 (2018). https://doi.org/10.3390/mi9120633.
- [21] Y. Takayama, R. Kasada, Y. Sakamoto, K. Yabuuchi, A. Kimura, M. Ando, D. Hamaguchi, H. Tanigawa, Nanoindentation hardness and its extrapolation to bulk-equivalent hardness of F82H steels after single- and dual-ion beam irradiation, J. Nucl. Mater. 442 (2013). https://doi.org/10.1016/j.jnucmat.2012.12.033.
- [22] N.V. Nguyen, S.E. Kim, Experimental study to investigate microstructure and continuous strain rate sensitivity of structural steel weld zone using nanoindentation, Elsevier Ltd, 2020. https://doi.org/10.1016/j.ijmecsci.2020.105482.
- [23] R.D.K. Misra, P. Venkatsurya, K.M. Wu, L.P. Karjalainen, Ultrahigh strength martensite-austenite dual-phase steels with ultrafine structure: The response to indentation experiments, Mater. Sci. Eng. A. 560 (2013) 693–699. https://doi.org/10.1016/j.msea.2012.10.015.
- [24] P. Sudharshan Phani, W.C. Oliver, A critical assessment of the effect of indentation spacing

- on the measurement of hardness and modulus using instrumented indentation testing, Mater. Des. 164 (2019) 107563. https://doi.org/10.1016/j.matdes.2018.107563.
- [25] S. Varam, K. V. Rajulapati, K. Bhanu Sankara Rao, Strain rate sensitivity studies on bulk nanocrystalline aluminium by nanoindentation, J. Alloys Compd. 585 (2014) 795–799. https://doi.org/10.1016/j.jallcom.2013.09.116.



CHAPTER 5

Conclusions and Future Scope



5.1 Conclusions

The studies performed on India specific Reduced Activation Ferritic/Martensitic (IN-RAFM) steel was successful in welding thick sections of IN-RAFM steel plates using the FSW process and in establishing the mechanical properties of the weldment in the as-welded and post-weld heat-treated condition.

The major outcomes of the work can be summarised as follows.

- The friction stir welding of a reduced activation ferritic-martensitic steel has been successfully performed on 6 mm thick plates employing PcBN tool. At the tool rotational speed of 200 rpm defect-free bead-on-plate welds were obtained.
- The as-received base metal microstructure revealed tempered martensite (alpha-ferrite + carbides) comprising of prior austenite grain boundaries and martensite lath boundaries decorated with discrete M₂₃C₆ particles in addition to very fine MX precipitates in intragranular regions.
- FSW joint contained SZ, TMAZ and unaffected BM. In the SZ and TMAZ significant changes in microstructure occurred; solid state dissolution of M₂₃C₆ and precipitation of brittle Fe₃C took place. No fresh martensite could be found in SZ in the as-welded state though the dislocation density is high. BM structure remained unaffected in the as-welded state.
- In the as-welded state, the FSW joint displayed very high hardness in SZ with a rapid fall in hardness across TMAZ. Both SZ and TMAZ were softened to the level of BM by post weld normalising and tempering treatment. This treatment enabled the re-precipitation of desirable carbides on grain and martensite lath boundaries in SZ and TMAZ, with complete elimination of Fe₃C from SZ. The microstructure after PWNT was more homogeneous and resembled that of BM with perceptible change in grain size distribution in SZ due to the impact of recrystallization process.
- Tensile tests performed at room temperature and at 450 °C, 500 °C and 550 °C in AR, AW and PWNT states indicated the decrease in 0.2% offset yield strength and ultimate tensile strength with raise in temperature. Alloy showed higher strength in the AW state due to high dislocation density and the presence of Fe₃C in SZ. The ductility was low in AW state but improved after PWNT treatment. The low ductility in all the states at an intermediate

temperature has been ascribed due to intervention of dynamic strain ageing effects. Alloy displayed transgranular ductile fracture with signature of dimples irrespective of temperature and material state.

- In order to study the tensile behavior of the SZ specifically, tensile specimens were extracted separately from the stir zone region. The SZ-alone showed higher strength in AW state and high ductility (~50%) in the PWNT state at room temperature. The deformation in weld joint at room temperature was constrained by other constituents and the recovery and recrystallization effects contributing to high ductility of SZ-alone have not been fully realised.
- The yield strength of the SZ region was estimated using mathematical calculations of the operating strengthening mechanisms. These results match with the experimental results obtained.
- The 12mm thick as-received RAFM steel displayed a tempered martensite microstructure. TEM studies revealed M₂₃C₆ type carbides on prior austenite grain and martensite lath boundaries. The finer particles in the intra-lath regions were identified as Ta and V rich MX type of carbides and carbonitrides.
- Bead-on-Plate FSW was successfully accomplished by employing PCBN tool with a rotational speed of 200 rpm. In the as-welded state, the weld joint was composed of SZ, TMAZ, HAZ and unaltered base metal.
- SZ displayed very high hardness due to the presence of martensite, Fe₃C and high dislocation density. The SZ and TMAZ exhibited precipitate- free prior austenite grain boundaries which can act as preferential sites for the occurrence of grain boundary damage under creep conditions, while HAZ displayed ripening and agglomeration of carbides with concomitant decrease in hardness.
- The as-welded microstructure was completely modified and restored to the parent metal microstructure by PWNT treatment. The non-uniformity in hardness across the transverse section was also eliminated.
- Tensile tests conducted in different states over the wide temperature range indicated UTS to be in the order AW> PWNT>AR while ductility in the form of the percentage elongation is in the order AW<PWNT <AR. An exception to this generalisation was shown at 450 °C, where the ductility was in order AR<AW<PWNT.

Irrespective of the state, the minimum in ductility was displayed at 450 °C owing to the
prevalence of dynamic strain ageing. In all the states and at all the temperatures ductile
fracture prevailed.

- Tensile flow stress-strain response revealed a brief period of monotonic hardening in all the states at room temperature followed by softening. Elevated temperatures were found conducive for rapid softening. The variation in monotonic tensile stress response was rationalised on the basis of evolving substructure during tensile deformation.
- The tensile test samples were taken from the central portion of the bead-on-plate welds and represent the full penetration welds, as would also be expected from welding of two plates in a configuration of a butt joint. Thick sections may require FSW from both the sides when two plates joining is contemplated in butt configuration at very low rotational speeds; this is essential since tools of larger length would fail at low heat inputs associated with low rotational speeds.
- The IN-RAFM steel welded using FSW was subjected to high throughput nanoindentation mapping and maps were obtained in the AW and PWNT conditions in plates of 6 and 12 mm thickness from different regions of the weldment.
- The maps were able to show the hardness variation in different phases of the material in the AW and PWNT condition.
- Higher hardness region in the AW conditions indicate the increased hardness due to the dissolved carbides and it has been homogenized to the base metal condition after PWNT.
- Nanoindentation at constant peak load and different loading rates was used as a tool to estimate strain rate sensitivity at different weld regions.
- Strain rate sensitivity (SRS) estimated mathematically from the nanohardness values gave m=0.02 in the BM region and m=0.01 in the SZ region.
- The values of the SZ region has reduced because of the strain hardening due to FSW and grain refinement.
- The SRS estimated from strain rate jump test performed using bulk sample in a UTM gave a value of m=0.019 in the as-welded condition and m=0.02 in the as-received condition.
- The values of the bulk behavior fall nearly matching because of the fracture that has happened in the BM region in AW condition.

• The SRS estimated using nanoindentation and strain rate jump test match exactly in the AR condition and in the BM region.

- Post weld heat treatments are suggested to homogenize the mechanical behavior of the weldment.
- The post weld heat treatment process, PWNT is proved to have homogenized the weld mechanically. The nanohardness of the SZ region which was ~6.0 GPa has been brought to ~3.5-4 GPa (base metal hardness) through the PWNT process.
- An analysis of this kind comparing the nanomechanical response towards varying loading rate and bulk response towards varying strain rate is being reported for the first time in this alloy.

5.2 Scope of Future Work

Even though the current work was able to throw light to some technological gaps in the mechanical properties of the IN-RAFM steels, there are certain in depth analyses that can be done in future as an addition to this data.

The possible future works are,

- Impact studies on the weldment at room temperature and cryogenic temperatures
- TEM analysis of the specimens extracted from the TMAZ and HAZ regions can throw light on the deformation and microstructural details of these zones.
- Tensile tests at different strain rates and temperatures can give an idea about the strain rate sensitivity of the material at high temperatures.
- Nanoindentation at different zones of the weldment at different peak loads in the AW and PWNT conditions can be used to study the RT creep properties of each zone.
- Nanoindentation at different zones of the weld at constant peak load and different loading rates can be used to study the strain rate sensitivity (SRS) of each zone.
- Advanced analysis can be done on the EBSD maps to extract more details about the material
 in the welded condition.

Thank You

Declaration

The below mentioned sources (Sl. No. 1&2) of the plagiarism report (submission ID: 1876536622) generated for the Ph. D. Thesis entitled "Mechanical Properties of Friction Stir Welded Reduced Activation Ferritic-Martensitic Steel" submitted by Mr. Johny Varghese (Reg. No. 12ETMM03), Ph. D. scholar at School of Engineering Sciences and Technology, University of Hyderabad are his own publications.

Hence the net similarity index of the thesis will be 8% (30-22).

Mechanical Properties of Friction Stir Welded Reduced Activation Ferritic-Martensitic Steel

ORIGINA	ALITY REPORT			
3 SIMILA	O% ARITY INDEX	25% INTERNET SOURCES	29% PUBLICATIONS	1% STUDENT PAPERS
PRIMAR	Y SOURCES			
1	link.spri Internet Sour	nger.com		18
2	K. Bhan Meshra "Charac Mechan Reduced in As-Re Heat-Tre	arghese, Kotesw u Sankara Rao, I m, G. Madhusud terization of Mid ical Properties of d Activation Ferr eceived, As-Weld eated States", To nstitute of Meta	N. Chavan Akadhan Reddy. crostructure a of Friction Stireitic–Martensited and Post-wransactions of	nd Welded ic Steel veld

Supervisor,

30-07-2022 Prof. Koteswararao V. Rajulapati

Professor

School of Engineering Sciences and Technology University of Hyderabad

Dr. KOTESWARARAO V. RAJULAPATI

Professor
School of Engineering Sciences and Technology,
University of Hyderabad, Prof. C. R. Bao Road,
Gachibowli, Hyderabad - 500 046, INDIA.